

APPLICATION OF RATE DEPENDENT SOIL MODEL, MIT-SR, FOR EVALUATION OF LONG-TERM GROUND MOVEMENTS DUE TO CONSOLIDATION AND CREEP

By

Gonzalo Rellán

Civil Engineer (2012)

Universidad de Buenos Aires, Capital Federal, Argentina

Submitted to the Department of Civil and Environmental Engineering
in Partial Fulfillment of the Requirements for the Degree of
MASTER OF SCIENCE IN CIVIL AND ENVIRONMENTAL ENGINEERING
at the

MASSACHUSETTS INSTITUTE OF TECHNOLOGY

September, 2018

© 2018 Massachusetts Institute of Technology. All rights reserved


Signature redacted

Signature of Author: _____

Department of Civil and Environmental Engineering

August 17, 2018

Signature redacted

Certified by: _____

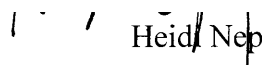
Andrew J. Whittle

Edmund K. Turner Professor of Civil and Environmental Engineering

Thesis Supervisor

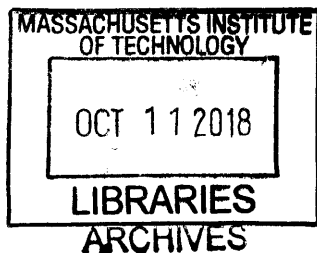
Signature redacted

Accepted by: _____


Heidi Nepf

Donald and Martha Harleman Professor of Civil and Environmental Engineering

Chair, Graduate Program Committee



This page intentionally left blank

APPLICATION OF RATE DEPENDENT SOIL MODEL, MIT-SR, FOR EVALUATION OF LONG-TERM GROUND MOVEMENTS DUE TO CONSOLIDATION AND CREEP

By

Gonzalo Rellán

Submitted to the Department of Civil and Environmental Engineering on August 17, 2018 in partial fulfillment of the requirements for the degree of Master of Science in Civil and Environmental Engineering.

ABSTRACT

Saturated clays exhibit rate-dependent behavior (i.e. their stress-strain-strength properties are significantly affected by the applied loading rate). This is of great significance for geotechnical projects, particularly when long-term predictions of settlements of compressible soil strata are based on results of laboratory element tests on small test specimens. Ladd et al. (1977) show that scaling of laboratory consolidation tests to field scale is strongly affected by assumed creep properties of the clay, leading to competing hypotheses of field performance (Hypotheses A and B). Most pre-existing soil models are based on isochrone theory which assumes a unique relationship between effective stress-strain and strain rate - such that the scaling of creep and consolidation conforms to Hypothesis B. Recently Yuan (2016) has developed a novel elasto-viscoplastic effective stress model, MIT-SR, that is capable of accurately predicting a wide range of rate-dependent characteristics of clay. The proposed formulation is able to represent both scaling hypotheses of coupled creep and consolidation.

This thesis analyzed the predictive capabilities of MIT-SR model by studying two projects: New Hamilton Partnership Levee Project (NHPL) and Marina Bay land reclamation projects, Singapore. MIT-SR materials were calibrated with laboratory and field tests only and numerical simulations of the projects were performed with the Finite Element Method (FEM).

The NHPL project consisted on an 11ft high embankment, constructed in 1996 in California, on +30ft of highly compressive San Francisco Bay Mud (SFBM). Our re-analyses included the MIT-SR calibration for SFBM and 2D FEM simulations that compare MIT-SR, Soft Soil Model and Soft Soil Creep Model predictions. The results show that MIT-SR offers superior predictions of the lateral spreading and settlement during both the construction and post-construction phases.

The Marina Bay area in Singapore was reclaimed by surcharged underlying marine clays with more than 13m of granular fill between 1979 and 1985. Construction of the new Thomson Line subway through the area has measured on-going free-field settlements from the reclamation during the period 2015-2018. We analyze these long-term settlements by calibrating MIT-SR parameters for Singapore marine clay and performing a series of 1D consolidation analyses to represent variations in the soil profile across the area. The model predicts settlement rates that vary with the thickness of marine clay, principally ranging from 10 to 20mm/yr at present time. The model tends to underestimate the measured settlement rates. This may reflect underestimation of creep properties of the clays or thickness of the fill.

The results from MIT-SR simulations in both projects were very encouraging and confirmed the strong predictive capabilities of the model with calibration procedures based on laboratory and site tests only. MIT-SR was able to accurately predict deformations and pore pressures in undrained, consolidation and creep stages with a unique set of parameters calibrated.

Thesis Supervisor: Prof. Andrew J. Whittle

Edmund K. Turner Professor of Civil and Environmental Engineering

This page intentionally left blank

ACKNOWLEDGMENTS

Completing graduate studies at the Massachusetts Institute of Technology (MIT) is the culmination of a dream that started in 2011. This is my humble and sincere recognition to all those who contributed to this personal, although collective, achievement.

First and foremost, I would like to thank my advisor Prof. Andrew J. Whittle for allowing me to join his research team and participate in these fascinating research projects. His continuous guidance and support were essential to accomplish my objectives and motivated me to fulfil all my interests. It was a real pleasure and privilege to work under his supervision during these two years and I will forever be grateful for opening the MIT doors to my life and career.

I wish to extend my sincere appreciation to all the MIT professors, colleagues and friends with whom I shared this experience. They truly shaped and helped my research throughout these years.

I would also like to express my deep gratitude to MIT, Prof. Whittle and Argentina's Bec.AR program for sponsoring my studies in USA. In addition, I am grateful to the people of my country, Argentina, for providing for my early academic education in our public universities where I earned my Civil Engineering diploma at the Universidad de Buenos Aires (UBA), my alma mater.

A special recognition for my mentor, Prof. Alejo. O. Sfriso. In 2011, he planted a seed that I transformed into a dream and now is a reality: completing graduate studies in USA. He is the cornerstone of my engineering career and his selfless guidance and truthful advice were decisive to forge and consolidate my career and character. I will forever be grateful for revealing me this life-changing experience and I look forward to imitate his generous mentorship in my future.

A warm and thoughtful recognition to my parents, Adriana and Pablo, my brother Ignacio and my sister Bárbara for their unconditional support and encouragement. As the youngest of our family, they have always taught me with their example, discipline and values making me very proud of my family.

Last but not least, I wish to thank Camila, my wife and best friend, for her endless love, friendship and patience and for joining me in this adventure with daily challenges and surprises. None of this would have been possible without her support and joy.

Thank you all for having helped me to accomplish this dream. The best is yet to come!

Gonzalo Rellán

This page intentionally left blank

CONTENTS

ABSTRACT	3
ACKNOWLEDGEMENTS	5
CONTENTS	7
LIST OF TABLES	9
LIST OF FIGURES	12
1. INTRODUCTION	17
1.1. OBJECTIVES AND SCOPE OF THE THESIS	17
2. MIT-SR EFFECTIVE STRESS CONSTITUTIVE SOIL MODEL	19
2.1. INTRODUCTION	19
2.2. EXISTING MODELS AND LIMITATIONS	21
2.3. 1D RATE DEPENDENT COMPRESSION MODEL FOR CLAY	22
2.4. GENERALIZED MIT-SR MODEL	24
2.4.1. 3D framework and surfaces	24
2.4.2. Plastic loading and hardening laws	26
2.4.3. Evolution of viscoplastic strains	28
2.4.4. Non-linear small strain behavior	29
2.4.5. Elastic stiffness and dilation of OC clays	31
2.5. MIT-SR MATERIAL CONSTANTS AND STATE VARIABLES	31
2.5.1. Determination of standard material constants	32
2.5.2. Determination of new material constants	33
2.5.3. Determination of initial state variables	34
3. NEW HAMILTON LEVEE PROJECT	50
3.1. OVERVIEW OF NEW HAMILTON LEVEE PROJECT	50
3.2. NOVATO CITY MONITORING PROGRAM	51
3.3. URS SITE INVESTIGATION & MONITORING PROGRAM	51
3.3.1. Laboratory tests	52
3.3.2. Field tests and preconsolidation profile	52
3.3.3. Subsurface conditions and geotechnical characteristics	53
3.3.4. Monitoring program	54
3.4. NGUYEN SM THESIS (2006)	55
3.5. RE-ANALYSIS OF NHPL PROJECT WITH MIT-SR	58

3.5.1.	Finite Element Model stages	59
3.5.2.	Comparison with field information	60
3.5.3.	MIT-SR calibration for San Francisco Bay Mud	60
3.5.4.	Soft Soil Creep Model for San Francisco Bay Mud	67
3.6.	SIMULATION OF SETTLEMENTS DUE TO LEVEE CONSTRUCTION	68
4.	LAND RECLAMATION SETTLEMENTS, MARINA BAY, SINGAPORE	104
4.1.	OVERVIEW OF MARINA BAY T228 & T302 PROJECTS	105
4.2.	MARINA BAY GEOTECHNICAL CONDITIONS	106
4.2.1.	Kallang Formation and Singapore Marine Clay	107
4.2.2.	Original seabed conditions and preconsolidation profile	108
4.3.	T228 & T302 SITE MONITORING INFORMATION	109
4.4.	ANALYSES OF MARINA BAY AREA WITH MIT-SR	110
4.4.1.	Selection of stratigraphies for analyses in T228 and T302	110
4.4.2.	Selection of hydraulic parameters	113
4.4.3.	Finite Element Model stages	113
4.4.4.	MIT-SR calibration for Kallang Formation Units (UMC, F2 & LMC)	114
4.5.	SIMULATION OF SETTLEMENTS DUE TO LAND RECLAMATION	121
5.	SUMMARY, CONCLUSIONS AND RECOMMENDATIONS	183
5.1.	SUMMARY	183
5.2.	CONCLUSIONS	184
5.3.	RECOMMENDATIONS	187
6.	REFERENCES	188
7.	APPENDICES	191
7.1.	APPENDIX A: NEW HAMILTON PARTNERSHIP LEVEE PROJECT	191
7.1.1.	URS (2003) site investigation and monitoring information	191
7.1.2.	Korchaiyapruk (2007)	196
7.1.3.	PLAXIS Contour plots	205
7.2.	APPENDIX B: MARINA BAY AREA PROJECTS	222
7.2.1.	Arup (2014) & Mott MacDonald (2015)	222
7.2.2.	Choi (1982)	223
7.2.3.	Kiso-Jiban (1978)	230

LIST OF TABLES

Table 2-1: Transformed quantities used in MIT models (Whittle and Kavvadas, 1994).	36
Table 2-2: 3D MIT-SR Material Parameters (Yuan, 2016).	37
Table 2-3: 3D MIT-SR Internal State Variables (Yuan, 2016).	38
Table 3-1: Parameters considered in D4 case (Nguyen, 2006).	71
Table 3-2: Stages considered in the NHPL PLAXIS 2D simulation.	71
Table 3-3: Material parameters for NHPL PLAXIS 2D simulation.	72
Table 3-4: SFBM MIT-SR material parameters for NHPL PLAXIS 2D simulation.	72
Table 3-5: SFBM MIT-SR state parameters for NHPL PLAXIS 2D simulation.	73
Table 3-6: SFBM Layers, OCR and K_0 considered in NHPL PLAXIS 2D simulation.	73
Table 3-7: Piezometers in TS3 and TS5 and PLAXIS points to compare pore pressures.	74
Table 3-8: Compressibility in the NC regime (ρ_c).	75
Table 3-9: Borehole CCB-25B: Total specific weight, moisture content and void ratios.	75
Table 3-10: Boreholes CCB-25B & CCB-22: V_s measurements and G_{max} calculated.	75
Table 3-11: Small strain elastic compressibility (C_b) calibration.	76
Table 3-12: Oedometer tests – Calculated values of secondary compression (ρ_α).	77
Table 3-13: Oedometer tests – Calculated values of reference strain rate (ϵ_{ref} , [%/min]).	77
Table 3-14: CRS tests, effective vertical stresses and void ratios and calculated β values.	77
Table 4-1: Extrapolated stratigraphies in markers (T228) and calculated settlement rates.	124
Table 4-2: Extrapolated stratigraphies in markers (T302) and calculated settlement rates.	124
Table 4-3: Histogram of layer's thicknesses in T228 and T302.	125
Table 4-4: Statistical results from histogram statistical analyses in data sets.	126
Table 4-5: Representative thicknesses considered in the PLAXIS analyses.	127
Table 4-6: Stratigraphies considered in PLAXIS analyses PLX01 to PLX14.	128
Table 4-7: Stratigraphies considered in PLAXIS analyses PLX15 to PLX28.	129
Table 4-8: Stratigraphies considered in PLAXIS analyses PLX29 to PLX42.	130
Table 4-9: Stratigraphies considered in PLAXIS analyses PLX43 to PLX54.	131
Table 4-10: Summary of reported hydraulic conductivities and selected.	132
Table 4-11: Stages considered in the PLAXIS simulations.	132
Table 4-12: Material parameters for OA in PLAXIS simulations.	133
Table 4-13: MIT-SR material parameters for UMC, F2 & LMC in PLAXIS.	133
Table 4-14: MIT-SR state parameters for UMC, F2 & LMC in PLAXIS.	134

Table 4-15: Small strain elastic compressibility (C_b) calibration.	134
Table 4-16: CRS tests, effective vertical stresses for specific void ratios and β values.	135
Table 4-17: Series 4 tests, calculated values for $\widehat{C}_{\alpha\varepsilon}$, $C_{\alpha\varepsilon}$ and ε_1 .	135
Table 4-18: Series 4 tests, OCR, $\widehat{C}_{\alpha\varepsilon}/C_{\alpha\varepsilon}$ and $\varepsilon_1/\varepsilon_{100}$ for β_2 calibration.	135
Table 4-19: Calibration of β_2 and β_3 .	136
Table 4-20: Calibration of secondary compression (ρ_α) and reference strain rate (ε_{ref}).	136
Table 4-21: PLAXIS 01-23 predictions of settlements and settlement rates, 1985-2012.	137
Table 4-22: PLAXIS 01-23 predictions of settlements and settlement rates, 2017-2047.	138
Table 4-23: PLAXIS 24-46 predictions of settlements and settlement rates, 1985-2012.	139
Table 4-24: PLAXIS 24-46 predictions of settlements and settlement rates, 2017-2047.	140
Table 4-25: PLAXIS 47-54 predictions of settlements and settlement rates, 1985-2012.	141
Table 4-26: PLAXIS 47-54 predictions of settlements and settlement rates, 2017-2047.	141
Table 4-27: PLAXIS predictions of settlements rates [mm/yr], 2017-2047.	142
Table 4-28: PLAXIS predictions of settlements [m], 2017-2047.	143
Table 4-29: PLAXIS average predictions of settlements and settlements rates, 1985-2012.	144
Table 4-30: PLAXIS average predictions of settlements and settlements rates, 2017-2047.	145
Table 7-1: Summary of field testing on Bay Mud for NHPL (Nguyen, 2006).	191
Table 7-2: Summary of laboratory testing on Bay Mud for NHPL (Nguyen, 2006).	192
Table 7-3: Monitoring information, settlement (URS, 2003).	192
Table 7-4: Monitoring information, inclinometers and Sondex (URS, 2003).	193
Table 7-5: Monitoring information, piezometers in Line 1 in TS3 (URS, 2003).	194
Table 7-6: Monitoring information, piezometers in Line 2 in TS3 (URS, 2003).	194
Table 7-7: Monitoring information, piezometers in Line 3 in TS3 (URS, 2003).	194
Table 7-8: Monitoring information, piezometers in Line 4 in TS3 (URS, 2003).	195
Table 7-9: Monitoring information, piezometers in Line 1 in TS5 (URS, 2003).	195
Table 7-10: Monitoring information, piezometers in Line 2 in TS5 (URS, 2003).	195
Table 7-11: Monitoring information, piezometers in Line 3 in TS5 (URS, 2003).	196
Table 7-12: Oedometer tests – Load applied, strain and void ratio (Korchaiyapruk, 2007).	196
Table 7-13: Oedometer test 112 – Secondary compression stages (Korchaiyapruk, 2007).	196
Table 7-14: Oedometer test 113 – Secondary compression stages (Korchaiyapruk, 2007).	197
Table 7-15: Oedometer test 116 – Secondary compression stages (Korchaiyapruk, 2007).	198
Table 7-16: Oedometer test 117 – Secondary compression stages (Korchaiyapruk, 2007).	199

Table 7-17: Oedometer test 122 – Secondary compression stages (Korchaiyapruk, 2007).	200
Table 7-18: CRS 654/656/662/674 tests information (Korchaiyapruk, 2007).	201
Table 7-19: CRS 680/683/686/687 tests information (Korchaiyapruk, 2007).	202
Table 7-20: CRS 672 test information (Korchaiyapruk, 2007).	203
Table 7-21: CRS 691 test information (Korchaiyapruk, 2007).	203
Table 7-22: Digitized σ'_v and preconsolidation pressure (Arup, 2014).	222
Table 7-23: Digitized undrained shear strength of F2 (Arup, 2014) and OCR values.	222
Table 7-24: CRS tests information (Choi, 1982).	223
Table 7-25: SC-12 test, creep stage at 1000psf (Choi, 1982).	224
Table 7-26: SC-12 test, creep stage at 2000psf (Choi, 1982).	224
Table 7-27: SC-12 test, creep stage at 4000psf (Choi, 1982).	225
Table 7-28: SC-12 test, creep stage at 8000psf (Choi, 1982).	225
Table 7-29: SC-13 test, creep stage at 1000psf (Choi, 1982).	226
Table 7-30: SC-13 test, creep stage at 2000psf (Choi, 1982).	227
Table 7-31: SC-13 test, creep stage at 4000psf (Choi, 1982).	227
Table 7-32: SC-13 test, creep stage at 8000psf (Choi, 1982).	228
Table 7-33: SC-14 test, creep stage at 1000psf (Choi, 1982).	228
Table 7-34: SC-14 test, creep stage at 2000psf (Choi, 1982).	229
Table 7-35: SC-14 test, creep stage at 4000psf (Choi, 1982).	229
Table 7-36: SC-14 test, creep stage at 8000psf (Choi, 1982).	230
Table 7-37: Consolidation test BH8-U4-S3 (Kiso-Jiban, 1978).	231
Table 7-38: Consolidation test BH8-U4-S4 (Kiso-Jiban, 1978).	231
Table 7-39: Consolidation test BH8-U6-S3 (Kiso-Jiban, 1978).	232
Table 7-40: Consolidation test BH8-U6-S4 (Kiso-Jiban, 1978).	232

LIST OF FIGURES

Figure 2-1: Typical consolidation curve ε -log(t) upon an incremental load in an (IL) oedometer test (Yuan, 2016).	39
Figure 2-2: Effect of strain rate in CRS tests on Batiscan clay (Leroueil et al., 1985).	39
Figure 2-3: Effective stress paths for CK ₀ UC tests on NC RBBC under different strain rates (after Sheahan, 1991).	40
Figure 2-4: Strain rate versus time for undrained creep in CIUC tests on Haney clay (after Vaid & Campanella, 1977).	40
Figure 2-5: Effective stress paths from multiple-phases relaxation test on Fujinomori clay in CIUC (after Murayama, 1974).	41
Figure 2-6: Consolidation curves of Hypothesis A and B (after Ladd et al., 1977).	41
Figure 2-7: Typical consolidation curve of strain - log (time) upon an incremental load in an (IL) oedometer test (Yuan, 2016).	42
Figure 2-8: Spectrum of duration or average strain rate for the consolidation at laboratory and field-scale (Yuan 2016).	42
Figure 2-9: Conceptual framework for describing compression behavior in the loge-log σ'_v space with compressibility parameters ρ_c and ρ_r (after Pestana & Whittle, 1999).	43
Figure 2-10: Effects of a) ϕ'_m and b) m on the shape of MIT-SR loading surface for isotropic consolidated clay with $b_1=0$ (Yuan 2016).	43
Figure 2-11: (cont.) Effects of c) ϕ'_m and d) m on the shape of MIT-SR loading surface for K ₀ -normally consolidated clay (Yuan 2016).	44
Figure 2-12: Plots of the proposed framework consisting of an isotropic critical state surface, a reference and a loading surface in 3-D principal effective stress space ($\sigma'_1, \sigma'_2, \sigma'_3$) (for illustration purpose only, from Yuan 2016).	44
Figure 2-13: Plots of the proposed framework in the triaxial stress space (Yuan 2016).	45
Figure 2-14: Effects of parameters D and r on the predictions of 1D unloading behavior (Yuan 2016).	45
Figure 2-15: Effects of w_s on the predicted nonlinear small strain behavior of CK ₀ UC tests on normally consolidated clay (Yuan 2016).	46
Figure 2-16: Parameter m and ϕ'_m on the predicted ESPs for CK ₀ UC and CK ₀ UE tests on normally consolidated clay (Yuan 2016).	46
Figure 2-17: Illustration of ESPs and the transformation of reference surface for a K ₀ consolidated specimen underwent 1/K ₀ consolidation (Yuan 2016).	47
Figure 2-18: Effects of parameter ψ on CK ₀ UC and CK ₀ UE predictions on normally consolidated clay (Yuan 2016).	47
Figure 2-19: Experimental evidence of dilative behavior in CK ₀ UC test on RBBC and model predictions with parameter DL (Yuan 2016).	48

Figure 2-20: Parameter β on the predicted ESPs for CK ₀ UC tests on normally consolidated clay (Yuan 2016).	48
Figure 2-21: (cont.) Parameter β on the predicted ESPs for CK ₀ UC tests on normally consolidated clay (Yuan 2016).	49
Figure 3-1: Location of the Hamilton Wetland Restoration Project (URS, 2003).	78
Figure 3-2: Longitudinal subsurface section along the NHPL (URS, 2003).	79
Figure 3-3: Typical transverse section and stratigraphy along NHPL (URS, 2003).	79
Figure 3-4: Novato City monitoring program (URS, 2003 and Ladd, 2002).	80
Figure 3-5: Settlement vs. Time at points 16 to 19, near TS3 and TS5 (URS, 2003).	80
Figure 3-6: Vane shear strength (FVT) & tip resistance (CPT) vs. ELs (URS, 2003).	81
Figure 3-7: NHPL σ'_p (FVT, $\mu=0.8$) & laboratory tests (URS, 2003 and Ladd, 2002).	82
Figure 3-8: Test section area with borings, field tests and instrumentation (URS, 2003).	83
Figure 3-9: Layout of installed instruments in TS3 (URS, 2003).	84
Figure 3-10: Layout of installed instruments in TS5 (URS, 2003).	84
Figure 3-11: NHPL free field soil profile and stress history (Nguyen, 2006).	85
Figure 3-12: NHPL mesh model and materials (Nguyen, 2006).	86
Figure 3-13: NHPL staged construction sequence (Nguyen, 2006).	86
Figure 3-14: Stress histories and predictions for case D4 (Nguyen, 2006).	87
Figure 3-15: Predicted & measured settlement of NHPL (URS, 2003 & Nguyen, 2006).	87
Figure 3-16: Predicted & measured pore pressure NHPL (URS, 2003 & Nguyen, 2006).	88
Figure 3-17: PLAXIS 2D Model: NHPL simulations with SSM, MITSR & SSCM.	89
Figure 3-18: PLAXIS 2D selected points and sections for results and comparisons.	90
Figure 3-19: ρ_c selection in $\log(e) - \log(\sigma'_v)$ space.	91
Figure 3-20: D & r selection in $\Delta\varepsilon_v - \sigma'_v/\sigma'_p$ and $\Delta\varepsilon - \sigma'_v/\sigma'_p$ spaces respectively.	92
Figure 3-21: ϕ'_m , m, w_s & ψ selection in q/σ'_{vc} vs. p'/σ'_{vc} and q/σ'_{vc} vs. ε_a spaces.	93
Figure 3-22: β selection in $\log(\varepsilon) - \log(\sigma'_{vc})$ space.	94
Figure 3-23: Vertical settlement of top of the clay in time.	95
Figure 3-24: Maximum horizontal displacement in clay in time.	96
Figure 3-25: Ratio of max. hor. displacement and max. vertical settlement in time.	97
Figure 3-26: Total pore pressure in reference centerline (Line 3) points in time.	98
Figure 3-27: Total pore pressure in reference toeline (Line 2) points in time.	99
Figure 3-28: Total pore pressure in reference free field line (Line 4) points in time.	100
Figure 3-29: Total pore pressure in reference free field line (Line 1) points in time.	101

Figure 3-30: Vertical settlement at centerline (Line 3), 17/Feb/02 to 11/Nov/02.	102
Figure 3-31: Vertical settlement at free field (Line 1), 17/Feb/02 to 11/Nov/02.	102
Figure 3-32: Horizontal u at toe line (Line 4'), 17/Feb/02 to 11/Nov/02.	103
Figure 4-1: Marina bay reclaimed areas and phases (Mott MacDonald, 2015).	146
Figure 4-2: Marina bay reclaimed areas (Arup, 2014).	147
Figure 4-3: Reclamation stages, areas and dates in the Marina bay Area (Arup, 2014).	148
Figure 4-4: Areas included in contracts T228 (left) and T302 (right).	149
Figure 4-5: Schematic geotechnical profile in Marina bay area (Adachi & Mizuni, 1979).	150
Figure 4-6: Typical soil profile encountered in T228 (Arup, 2014).	150
Figure 4-7: Typical soil profile encountered in T302 (Mott MacDonald, 2015).	151
Figure 4-8: Soil profile in the Marina Bay channel (Arup, 2014).	151
Figure 4-9: Undrained shear strength and OCR profile in the canal in T228 (Arup, 2014).	152
Figure 4-10: Undrained shear strength for F2 in T228 (Arup, 2014).	153
Figure 4-11: Location of settlement markers in TS22 (T228).	154
Figure 4-12: Location of settlement markers in TE22A (T302).	154
Figure 4-13: Settlement vs. time in markers in TS22 (T228).	155
Figure 4-14: Settlement vs. time in markers in TE22A (T302).	155
Figure 4-15: PLAXIS 2D Model, example of geometry and materials (PLX34).	156
Figure 4-16: ρ_c selection in $\log(e) - \log(\sigma'_{vc})$ space.	157
Figure 4-17: D & r selection for UMC and LMC and sensitivity analyses.	158
Figure 4-18: ϕ'_m , m, w_s & ψ selection for UMC in q/σ'_{vc} vs. p'/σ'_{vc} and q/σ'_{vc} vs. ϵ_a .	159
Figure 4-19: ϕ'_m , m, w_s & ψ selection for LMC in q/σ'_{vc} vs. p'/σ'_{vc} and q/σ'_{vc} vs. ϵ_a .	160
Figure 4-20: ϕ'_m , m, w_s & ψ parameters, ϕ'_m sensitivity analyses.	161
Figure 4-21: ϕ'_m , m, w_s & ψ parameters, m sensitivity analyses.	161
Figure 4-22: ϕ'_m , m, w_s & ψ parameters, w_s sensitivity analyses.	162
Figure 4-23: ϕ'_m , m, w_s & ψ parameters, ψ sensitivity analyses.	162
Figure 4-24: Creep tests, ρ_α determination for UMC and LMC.	163
Figure 4-25: β selection in $\log(\epsilon) - \log(\sigma'_{vc})$ space.	164
Figure 4-26: Series 4 IL tests on Marine Clay (Choi, 1982): $\epsilon' - \epsilon'$.	165
Figure 4-27: Calibration curves for β_2 (left) and β_3 (right).	166
Figure 4-28: PLAXIS results, total settlements and settlement rates from 1985 to 2047.	167
Figure 4-29: PLAXIS results, settlement and settlement rates at Dec/1985 and Dec/1987.	168

Figure 4-30: PLAXIS results, settlement and settlement rates at Dec/1992 and Dec/1997.	169
Figure 4-31: PLAXIS results, settlement and settlement rates at Dec/2002 and Dec/2005.	170
Figure 4-32: PLAXIS results, settlement and settlement rates at Dec/2007 and Dec/2012.	171
Figure 4-33: PLAXIS results, settlement and settlement rates at Dec/2017 and Dec/2022.	172
Figure 4-34: PLAXIS results, settlement and settlement rates at Dec/2027 and Dec/2032.	173
Figure 4-35: PLAXIS results, settlement and settlement rates at Dec/2037 and Dec/2042.	174
Figure 4-36: PLAXIS results, total settlement and settlement rates at Dec/2047.	175
Figure 4-37: PLAXIS settlements rates and settlement for 14m of marine clay.	176
Figure 4-38: PLAXIS excess pore pressure for 14m of marine clay.	176
Figure 4-39: PLAXIS settlements rates and settlement for 16m of marine clay.	177
Figure 4-40: PLAXIS excess pore pressure for 16m of marine clay.	177
Figure 4-41: PLAXIS settlements rates and settlement for 18m of marine clay.	178
Figure 4-42: PLAXIS excess pore pressure for 18m of marine clay.	178
Figure 4-43: PLAXIS settlements rates and settlement for 20m of marine clay.	179
Figure 4-44: PLAXIS excess pore pressure for 20m of marine clay.	179
Figure 4-45: PLAXIS settlements rates and settlement for 22m of marine clay.	180
Figure 4-46: PLAXIS excess pore pressure for 22m of marine clay.	180
Figure 4-47: PLAXIS settlements rates and settlement for 24m of marine clay.	181
Figure 4-48: PLAXIS excess pore pressure for 24m of marine clay.	181
Figure 4-49: Comparison between predictions at Dec/2017 and site measurements.	182
Figure 7-1: Geometries and meshes considered, SSM, SSCM & MIT-SR.	205
Figure 7-2: Vertical settlements (u_y) CD=215 (11/Nov/96), SSM, SSCM & MIT-SR.	206
Figure 7-3: Vertical settlements (u_y) CD=2140 (17/Feb/02), SSM, SSCM & MIT-SR.	207
Figure 7-4: Vertical settlements (u_y) CD=2417 (20/Nov/02), SSM, SSCM & MIT-SR.	208
Figure 7-5: Vertical settlements (u_y) CD=10960 (10/Apr/26), SSM, SSCM & MIT-SR.	209
Figure 7-6: Horizontal settlements (u_x) CD=215 (11/Nov/96), SSM, SSCM & MIT-SR.	210
Figure 7-7: Horizontal settlements (u_x) CD=2140 (17/Feb/02), SSM, SSCM & MIT-SR.	211
Figure 7-8: Horizontal settlements (u_x) CD=2417 (20/Nov/02), SSM, SSCM & MIT-SR.	212
Figure 7-9: Horizontal settlements (u_x) CD=10960 (10/Apr/26), SSM, SSCM & MIT-SR.	213
Figure 7-10: Exc. pore pressure (p_{excess}) CD=215 (11/Nov/96), SSM, SSCM & MIT-SR.	214
Figure 7-11: Exc. pore pressure (p_{excess}) CD=2140 (17/Feb/02), SSM, SSCM & MIT-SR.	215
Figure 7-12: Exc. pore pressure (p_{excess}) CD=2417 (20/Nov/02), SSM, SSCM & MIT-SR.	216
Figure 7-13: Exc. pore pressure (p_{excess}) CD=10960 (10/Apr/26), SSM, SSCM & MIT-SR.	217

- Figure 7-14: Act. pore pressure (p_{active}) CD=215 (11/Nov/96), SSM, SSCM & MIT-SR. 218
- Figure 7-15: Act. pore pressure (p_{active}) CD=2140 (17/Feb/02), SSM, SSCM & MIT-SR. 219
- Figure 7-16: Act. pore pressure (p_{active}) CD=2417 (20/Nov/02), SSM, SSCM & MIT-SR. 220
- Figure 7-17: Act. pore pressure (p_{active}) CD=10960 (10/Apr/26), SSM, SSCM & MIT-SR. 221

1. INTRODUCTION

Clays are elasto-viscoplastic materials characterized by their low hydraulic conductivity, high deformability, low shear strength and rate-dependent behavior; i.e., their stress-strain-strength behavior is significantly affected by the applied loading rate. Particular cases of rate-dependent behaviors are creep and relaxation. Creep occurs when strains develop in time under constant effective stresses while relaxation is the decrease in effective stresses under constant strains. Secondary compression refers to the drained creep observed in 1D consolidation tests.

Rate-dependency is of great significance for geotechnical projects, particularly when field scale long-term predictions require extrapolation of data from laboratory data. Although compressibility properties can be characterized with laboratory tests, controversies regarding the internal mechanisms governing their rate-dependency and the laboratory field behavior extrapolation persist.

The fundamental question has been whether the stress-strain relationship at the end of primary (EOP) consolidation is unique ($\sigma' - \varepsilon$) or also depends on the strain rate applied ($\sigma' - \varepsilon - \dot{\varepsilon}$). There is a long-standing controversy associated with two opposing hypothesis (Ladd et al., 1977): Hypothesis A, assumes that the strain at the end of primary consolidation is effectively independent of the thickness of the clay specimen while Hypothesis B, assumes that the strain at the end of primary consolidation increases with the thickness of the test specimen. Both hypothesis have been supported by different laboratory and field information. To date all pre-existing soil models assume that creep occurs concurrently with primary consolidation and hence, generate results consistent with Hypothesis B. Geotechnical engineering practice almost universally computes creep secondary settlements due to creep are independent of the magnitude of primary consolidation (Hypothesis A).

MIT-SR model developed in the PhD thesis by Yuan (2016) is an elasto-viscoplastic effective stress model capable of accurately predicting a wide range of rate-dependent characteristics of soft soils (e.g.: creep, relaxation and secondary compression) within a unified framework that includes anisotropic effective stress-strain-strength properties.

1.1. OBJECTIVES AND SCOPE OF THE THESIS

This thesis analyzed the capabilities of MIT-SR model as a predictive tool by studying two projects: New Hamilton Partnership Levee Project (NHPL) and Singapore Bay area project. MIT-SR input parameters were calibrated with laboratory and field tests only and numerical simulations of the projects were performed with the Finite Element Method (FEM, PLAXIS 2D v2017.01). The predicted results were compared against site measurements and MIT-SR predictive capability was assessed. No site measurements or monitoring information were considered in the MIT-SR calibrations.

The thesis is organized in five chapters: 1) Introduction; 2) MIT-SR model; 3) New Hamilton Partnership Levee Project; 4) Land Reclamation Settlements, Marina Bay, Singapore and 5) Summary, conclusions and recommendations.

Chapter 2 presents an introduction to rate-dependent behavior of clays and its influence in field-scale predictions and an overview of the MIT-SR model with an explanation of the main features, parameters and internal state variables.

Chapter 3 includes the first project analyzed with MIT-SR. The New Hamilton Partnership Levee is an 11 ft high embankment built on approximately 30ft of a highly compressive clay known as San Francisco Bay Mud (SFBM). The long-term performance of the embankment was reanalyzed using three different models to represent SFBM behavior (Soft Soil Model, Soft Soil Creep Model and MIT-SR). 2D FEM simulations of the construction process were executed with each model and the predictions of the embankment's performance were compared to each other and against available monitoring measurements to assess the predictive capabilities of MIT-SR.

Chapter 4 presents the second project analyzed with MIT-SR. The Marina Bay area in Singapore is the result of an offshore land reclamation process that occurred between 1979 and 1985 and where 13m of granular, dredged fill were deposited on the original seabed, principally composed by soft compressive clays (Singapore Marine Clay). Ongoing construction works in the area are observing considerable current creep rates in free field locations. MIT-SR was utilized to represent the clays of interest present in the area (Marine and Fluvial clays) and simulate the complete reclamation process to predict current and future creep rates. The performance of MIT-SR model was assessed by comparing the predicted current creep rates against site measurements.

2. MIT-SR EFFECTIVE STRESS CONSTITUTIVE SOIL MODEL

This chapter presents an overview of MIT-SR model developed in the PhD thesis by Yuan (2016).

2.1. INTRODUCTION

Saturated clays exhibit rate-dependent behavior, this means that their stress-strain-strength behavior is significantly affected by the applied loading rate. Some examples of these properties in compression and shearing can be summarized as follows:

1. Secondary compression in an incrementally loaded (IL) oedometer test: continuous deformation occurs after the end of primary consolidation (EOP; i.e., after all the excess pore pressure has dissipated) at constant effective stresses (Figure 2-1).
2. Variation of the effective stress-strain response in constant strain rate (CRS) consolidation tests with the imposed strain rate (Figure 2-2).
3. Increasing undrained shear resistance with strain rate for specimens in triaxial shear tests (Figure 2-3).
4. Creep or relaxation in shear tests (Figure 2-4 and Figure 2-5, respectively).

Rate-dependent behavior of clay has been subject of numerous experimental research studies (Wissa et al., 1971; Vaid and Campanella, 1977) including a series of theses in the MIT Geotechnical Laboratory (Sheahan, 1991; Ng, 1998; Gonzalez, 2000; Korchaiyapruk, 2007).

Rate-dependency is of great significance on geotechnical projects, particularly when field scale long-term predictions are based on short-term laboratory test measurements; the critical issue is the extrapolation methodology of laboratory-based information to predict field behavior.

Although rate-dependent properties can be characterized from laboratory tests, controversies regarding the internal mechanisms governing the rate-dependent properties and the extrapolation from lab to field scale remain issues of long-standing dispute within the geotechnical community.

Various research studies were focused on the creep-consolidation coupling to assess the challenges of creep influence in field-scale long-term consolidation prediction (e.g., Crawford, 1965; Berre & Iversen, 1972; Mesri & Choi, 1985; Kabbaj et al., 1988; Korchaiyapruk, 2007; Watabe et al., 2008).

The contradiction between the behavior evidenced in experimental and field measurements in different soils has been characterized by two competing hypotheses, A and B, as reported by Ladd et al. (1977) and presented in Figure 2-6.

Hypothesis A considers that the strain at the end of primary consolidation is effectively independent of the strain level in the clay ($e_{EOP\ lab} = e_{EOP\ field}$; Fig. 2-6). As a result the lab behavior can be estimated by scaling the lab time data by the squared-ratio of drainage path lengths in the lab and field situations. Laboratory results can be extrapolated to field-time scale by:

$$\frac{t_{field}}{(H_{field})^2} = \frac{t_{lab}}{(H_{lab})^2} \rightarrow t_{field} = \left(\frac{H_{field}}{H_{lab}}\right)^2 t_{lab} \quad (2.1)$$

Implicitly, this hypothesis assumes that the physical mechanisms causing creep are similar to those responsible for volume change due to an increase in effective stress: elastic deformation of particles, slippage at contacts and reorientation of particles, double layer compression and displacement of adsorbed water and particle crushing (Mesri and Godlewski, 1977; Ladd et al., 1977).

Hypothesis B assumes that creep processes are activated by the initial loading event and hence, larger creep strains occur in the field than in the small laboratory element test. Therefore, larger strains will develop in the field than in the lab and will be most clearly observed by a large strain level at the end of primary consolidation ($t_{EOP\ field}$; Fig. 2-6).

This hypothesis treats creep as a separate phenomenon independent of the primary consolidation process. The mechanisms responsible for secondary compression occurring during primary consolidation are often thought to be due to some type of “structural viscosity” or time dependent deformation of adsorbed water films (Bjerrum, 1973).

This enduring and existing controversy has been widely studied (Mesri, 2001; Leroueil, 2006; Watabe et al., 2008; Degago et al., 2011), illustrates the complexity of concurrent creep and consolidation of clays and the necessity for a more comprehensive constitutive framework to explain laboratory and field measured behaviors.

2.2. EXISTING MODELS AND LIMITATIONS

Existing time-dependent compression models for clay can be divided in five categories: i) Rheological models; ii) Isochrones (time-line) models; iii) Isotache models; iv) Microstructure and v) Unique EOP line models. Detailed description of these models, Analyses and comments on their capabilities and limitations can be found Yuan (2016). All of these existing consolidation formulations predict 1-D constitutive behavior corresponding to Hypothesis B (Yuan, 2016).

During the last four decades, various models have been proposed among which isochrone or isotache frameworks are the most popular. These formulations, limited to compression behavior under isotropic or K_0 conditions, consider that volumetric creep strain rate ($\dot{\epsilon}^{vp}$) is defined by current vertical effective stress (σ'_v/σ'_{pe}) and void ratio (e) and a constant reference strain rate ($\dot{\epsilon}_{ref}$). A typical expression is:

$$\dot{\epsilon}^{vp} = \dot{\epsilon}_{ref} \left(\frac{\sigma'_v}{\sigma'_{pe}} \right)^{\frac{C_c}{C_\alpha}} \quad (2.2)$$

Where σ'_{pe} is the equivalent stress on the virgin compression line (VCL) at the same void ratio as the current stress state (σ'_v), C_c is the compression index and C_α the coefficient of secondary compression (Figure 2-7). These models exhibited acceptable results when simulating laboratory time-dependent behavior (Yin et al., 2010; Bodas Freitas et al., 2011).

Experience has shown that laboratory-calibrated models tend to give unrealistically high initial creep strain rates of in-situ soil, leading to greater field compression strains than those found in the laboratory tests, (a result complying with Hypothesis B). The difference between the lab-calibrated initial field strain rate with the field values can be of several orders of magnitude (Figure 2-8).

A solution to the isotache-model limitation of considering a unique relationship between stress, strain and void ratio is to assume that viscoplastic strain evolution also depends on the history of strain rate.

2.3. ONE-DIMENSIONAL RATE DEPENDENT COMPRESSION MODEL FOR CLAY

Yuan (2016) proposed a new elasto-viscoplastic framework for 1D rate-dependent compression of clays. The key objectives that motivated this model include:

- Solve the existing limitations to determine initial creep rate and field-scale consolidation predictions.
- Describe a wide range of rate-dependent clay behavior, including isotache-type and temporary rate effects in CRS tests.
- Describe hypothesis A and B behaviors under a unique framework allowing a broader range of field-scale predictions based on laboratory data.
- Introduce a rational explanation to the physical mechanism controlling 1D rate-dependent compression behavior.

The proposed formulation decomposes total strain rate ($\dot{\epsilon}$) into elastic ($\dot{\epsilon}^e$) and viscoplastic ($\dot{\epsilon}^{vp}$) strain rate components:

$$\dot{\epsilon} = \dot{\epsilon}^e + \dot{\epsilon}^{vp} \quad (2.3)$$

The 1D compression behavior is defined in $\log e - \log \sigma'$ space following the MIT-S1 model formulation (Pestana and Whittle, 1995; Figure 2-9). Elastic recompression curve is linearized with a constant slope ($\rho_r = 0.434 C_r/e$) and the virgin compression (i.e., normally consolidated behavior) is also linearized with a constant slope ($\rho_c = 0.434 C_c/e$). Normally consolidated states are defined by the Limiting Compression Curve (LCC) shown in Figure 2-9.

The elastic strain rate ($\dot{\epsilon}^e$) is evaluated in terms of effective stress rate ($\dot{\sigma}'_v$), recompression slope (ρ_r) and porosity (n):

$$\dot{\epsilon}^e = \rho_r n \frac{\dot{\sigma}'_v}{\sigma'_v} \quad (2.4)$$

The evolution law for viscoplastic strain attributes macroscopic creep deformations to an internal strain rate representing the past straining effects on the microstructure. This innovative interpretation relates viscoplastic strain rate to the strain rate history opposed to past empirical formulations (e.g., isotache or isochorone models).

Viscoplastic strain rate ($\dot{\varepsilon}^{vp}$) is defined by strain rate history (R_a) and current effective stress state (σ'_{pe}):

$$\dot{\varepsilon}^{vp} = R_a \cdot f\left(\frac{\sigma'_v}{\sigma'_{pe}}\right) \quad (2.5)$$

Where R_a [1/time] is a non-negative new state parameter that represents the internal strain rate activated at the meso-scale (clay aggregate scale) due to the stimulation of historical straining (Yuan, 2016). Also, σ'_{pe} is the equivalent stress state on the LCC and is subjected to density hardening during compression:

$$\dot{\sigma}'_{pe} = \frac{\sigma'_{pe}}{\rho_c n} \dot{\varepsilon} \quad (2.6)$$

$$\dot{R}_a = [f(\dot{\varepsilon}) - R_a] m_t \quad (2.7)$$

The evolution of the internal state parameter (\dot{R}_a) utilizes an activation-decay mechanism; the first term corresponds to activation ($f(\dot{\varepsilon})$) and is caused by external mechanical perturbations while the second is an auto-decay function ($-R_a$) for automatic fading effects as time advances. The net change in R_a is scaled by a migration coefficient (m_t).

$$m_t = \left(\frac{\rho_c}{\rho_\alpha} - 1\right) \frac{\dot{\varepsilon}^{vp}}{\rho_r n} \quad (2.8)$$

Where ρ_α is an intrinsic viscosity property with a similar role to the conventional coefficient of secondary compression (C_α)¹.

$$f(\dot{\varepsilon}) = \frac{\rho_c - \rho_r}{\rho_c} \dot{\varepsilon} \left(\frac{\dot{\varepsilon}}{\dot{\varepsilon}_{ref}}\right)^{-\beta} \quad (2.9)$$

¹ It should be noted that the ratio, $\rho_\alpha/\rho_c = C_\alpha/C_c = Ca/Cc$ used in existing constitutive models of creep (such as the Soft Soil Creep, SSC, model in Plaxis; Vermeer and Neher, 1999).

2.4. GENERALIZED MIT-SR MODEL

Clay behavior prediction for geotechnical engineering problems involves complex loading conditions and coupling between volumetric and deviatoric stresses and strains, conditions that necessitate a general 3D representation of stress-strain relations.

Yuan (2016) developed a generalized rate-dependent soil model, MIT-SR, embedded within prior anisotropic 3D framework, previously presented by Pestana and Whittle. The key features of the MIT-SR model are the generalization of evolution law for the internal strain rate within a 3D framework and a generalized description of hysteretic behavior for unloading and reloading.

The generalized 3D MIT-SR formulation includes the following elements:

- 3D framework and surfaces.
- Plastic loading and hardening laws.
- Evolution of viscoplastic strains.
- Non-linear small strain behavior.
- Elastic stiffness and dilation of OC clays.

2.4.1. 3D framework and surfaces

MIT-SR divides the total strain tensor into a scalar volumetric strain component (ε) and a deviatoric strain tensor (\mathbf{E}) with up to 5 independent components; each of which can be further decomposed into elastic and viscoplastic contributions:

$$\begin{Bmatrix} \dot{\varepsilon} \\ \dot{\mathbf{E}} \end{Bmatrix} = \begin{Bmatrix} \dot{\varepsilon}^{el} + \dot{\varepsilon}^{vp} \\ \dot{\mathbf{E}}^{el} + \dot{\mathbf{E}}^{vp} \end{Bmatrix} \quad (2.10)$$

The proposed formulation uses the transformed stress and strain measures to simplify the formulation and numerical implementation of the model (after Whittle & Kavvas, 1994, Table 2-1).

Loading surface (f) is defined by current effective stress state (σ' , mean effective stress; $\boldsymbol{\eta} = \mathbf{S}/\sigma'$, deviatoric stress ratio vector) and two internal state variables (\mathbf{b} and α'_1). The tensor \mathbf{b} represents the orientation of the loading function and characterizes material anisotropy and α'_1 is an equivalent stress that represents the size of the loading surface size:

$$f = (\sigma')^2 \left\{ (\boldsymbol{\eta} - \mathbf{b}) : (\boldsymbol{\eta} - \mathbf{b}) - \zeta^2 \left(\frac{\alpha'_1}{\sigma'} - 1 \right) \left(\frac{\sigma'}{\alpha'_1} \right)^m \right\} \quad (2.11)$$

Parameters m and ζ^2 are introduced to control the shape of the surface: m (Figure 2-10 and Figure 2-11) varies from 0 to 1 and allows the function to describe loading surface with shape varying from ellipsoidal ($m = 0$, MIT-E3) to a lemniscate-shaped surface ($m = 1$, MIT-S1) whereas ζ^2 describes clay frictional characteristics and is defined by ϕ'_m (a material constant that controls the amplitude of the reference surface), the deviatoric stress ratio, $\boldsymbol{\eta}$ and anisotropy \mathbf{b} :

$$\zeta^2 = c^2 + \mathbf{b} : \mathbf{b} - \boldsymbol{\eta} : \mathbf{b} \quad (2.12)$$

$$c^2 = \frac{24 \sin^2 \phi'_m}{(3 - \sin \phi'_m)^2} \quad (2.13)$$

The reference surface (f^r), defined by image stresses ($\sigma'^r, \boldsymbol{\eta}$) and its size is determined by the state variable α' , is introduced in a similar form to the loading surface:

$$f^r = (\sigma'^r)^2 \left\{ (\boldsymbol{\eta} - \mathbf{b}) : (\boldsymbol{\eta} - \mathbf{b}) - \zeta^2 \left(\frac{\alpha'}{\sigma'^r} - 1 \right) \left(\frac{\sigma'^r}{\alpha'} \right)^m \right\} \quad (2.14)$$

The critical state condition (h_f) is represented by an isotropic failure criterion based on the generalization of Matsuoka and Nakai criterion (Panteghini and Lagioia, 2014):

$$h_f = k^2 - \boldsymbol{\eta} : \boldsymbol{\eta} = 0 \quad (2.15)$$

$$k^2 = k_a^2 + \left(3 - \frac{k_a^2}{2} \right) J_{3\boldsymbol{\eta}} \quad (2.16)$$

$$k_a^2 = \frac{8 \sin^2 \phi'_{cs}}{3 + \sin^2 \phi'_{cs}} \quad (2.17)$$

The factor k depends on the third invariant of the deviatoric stress ratio ($J_{3\boldsymbol{\eta}} = \det|\boldsymbol{\eta}|$) and the critical state friction angles (ϕ'_{cs}), measured at large strain in triaxial compression.

These surface (loading, reference and critical state) are illustrated in principal stress and triaxial stress space in Figure 2-12 and Figure 2-13, respectively.

2.4.2. Plastic loading and hardening laws

Previous MIT (Whittle & Kavvadas, 1994; Pestana & Whittle, 1999) models already introduced the concept of plastic loading in order to evaluate the contribution of plastic phenomena at the reference surface.

In the current formulation, the plastic multiplier (Λ) is determined from a consistency condition, used to obtain isotropic and kinematic hardening effects and is used as an external activation source for the internal strain rate; Λ does not directly contribute to plastic deformations. Macroscopic irrecoverable deformation is governed by a viscoplastic flow rule.

Plastic loading condition (CL) can be evaluated on the reference surface at a given image stress:

$$CL = (K^r Q^r \dot{\epsilon} + 2G^r \mathbf{Q}'^r : \dot{\mathbf{E}}) \quad (2.18)$$

where K^r and G^r are the elastic bulk and shear modulus evaluated at the reference surface, respectively. $Q^r (= \frac{\partial f^r}{\partial \sigma'^r})$ and $\mathbf{Q}'^r (= \frac{\partial f^r}{\partial \mathbf{S}^r})$ are the volumetric and deviatoric components of the gradient of the reference surface respectively:

$$\begin{Bmatrix} Q^r \\ \mathbf{Q}'^r \end{Bmatrix} = \sigma'^r \left\{ \begin{array}{l} \left[(m\zeta^2 + \boldsymbol{\eta} : \mathbf{b}) \left(1 - \frac{\alpha'}{\sigma'^r} \right) + \zeta^2 \frac{\alpha'}{\sigma'^r} \right] \left(\frac{\sigma'^r}{\alpha'} \right)^m - 2\boldsymbol{\eta} : (\boldsymbol{\eta} - \mathbf{b}) \\ 2(\boldsymbol{\eta} - \mathbf{b}) + \mathbf{b} \left(\frac{\alpha'}{\sigma'^r} - 1 \right) \left(\frac{\sigma'^r}{\alpha'} \right)^m \end{array} \right\} \quad (2.19)$$

If plastic loading occurs ($CL > 0$), then the plastic multiplier can be computed from the consistency condition considering that the image stress always is on the reference surface (i.e., $\dot{f}^r = 0$):

$$\Lambda = \frac{\langle CL \rangle}{H + K^r Q^r P + 2G^r \mathbf{Q}'^r : \mathbf{P}'} \quad (2.20)$$

Where $\langle \rangle$ are the Macaulay brackets, P and \mathbf{P}' are the volumetric and deviatoric components of flow direction (Table 2-1). H is the plastic modulus obtained from the consistency conditions and includes isotropic and kinematic hardening:

$$H = -\frac{\partial f^r}{\partial \alpha'} \frac{\dot{\alpha}'}{\Lambda} - \frac{\partial f^r}{\partial \mathbf{b}} : \frac{\dot{\mathbf{b}}}{\Lambda} \quad (2.21)$$

The proposed framework uses non-associated flow rule. Current stress point and the corresponding image point share the same P and \mathbf{P}' :

$$\begin{pmatrix} P \\ \mathbf{P}' \end{pmatrix} = \begin{bmatrix} (k^2 - \boldsymbol{\eta} : \boldsymbol{\eta}) \frac{\sigma'^r}{\alpha'} \\ \chi^P \boldsymbol{\eta} + \frac{\xi^2 \|\boldsymbol{\eta}\|}{\alpha'} \mathbf{Q}^r \end{bmatrix} \quad (2.22)$$

$$\chi = \left(\frac{\rho_c}{\rho_c - \rho_r} \right) \left[\frac{1}{3} \left(\frac{1 + 2K_{0NC}}{1 - K_{0NC}} \right) - \frac{K}{2G} \left(\frac{\rho_c}{\rho_r} \right) \right] \quad (2.23)$$

Lateral earth pressure ratio for K_0 -normally consolidated clays (K_{0NC}) is considered constant. Hardening can be isotropic (reference surface changes its size) or kinematic (reference surface is rotated). During loading ($CL > 0$), the size of the reference surface (α') varies and isotropic hardening is defined by:

$$\frac{\dot{\alpha}'}{\alpha'} = \frac{\Lambda P}{(\rho_c - \rho_r)n} - \frac{2\mathbf{b} : \dot{\mathbf{b}}}{a^2 + \mathbf{b} : \mathbf{b}} \quad (2.24)$$

$$a^2 = \frac{24 \sin^2 \phi'_{cs}}{(3 - \sin \phi'_{cs})^2} \quad (2.25)$$

If unloading occurs ($CL < 0$) and $\dot{\varepsilon} < 0$, the isotropic hardening is given by:

$$\frac{\dot{\alpha}'}{\alpha'} = \frac{\dot{\varepsilon}}{\rho_c \cdot n} \quad (2.26)$$

Kinematic hardening is defined by:

$$\dot{\mathbf{b}} = \psi \frac{\Lambda}{\alpha' \cdot n} \langle r_x \rangle \langle Q \cdot P \rangle (\boldsymbol{\eta} - \mathbf{b}) \quad (2.27)$$

$$r_x = (k^2 + \mathbf{b} : \mathbf{b} - 2\boldsymbol{\eta} : \mathbf{b}) / k_a^2 \quad (2.28)$$

Where ψ is a material constant property that controls the evolving rate of anisotropy, r_x bounds the maximum anisotropy within the critical state stress ratio and the anisotropy evolution rate depending on the shearing mode.

2.4.3. Evolution of viscoplastic strains

Volumetric ($\dot{\varepsilon}^{vp}$) and deviatoric ($\dot{\mathbf{E}}^{vp}$) viscoplastic strain rate components are computed by:

$$\begin{pmatrix} \dot{\varepsilon}^{vp} \\ \dot{\mathbf{E}}^{vp} \end{pmatrix} = \Lambda^{vp} \begin{pmatrix} P \\ \mathbf{P}' \end{pmatrix} \quad (2.29)$$

Where Λ^{vp} represents the viscoplastic strain rate magnitude (analogous to 1D formulation, Eqn. 2.5) and its 3D generalization is given by:

$$\Lambda^{vp} = R_a \cdot f \left(\frac{\alpha'_1}{\alpha'} \right) \quad (2.30)$$

$$f \left(\frac{\alpha'_1}{\alpha'} \right) = \left(\frac{\alpha'_1}{\alpha'} \right)^{\frac{1}{2}} \exp \left\{ \frac{1}{2\beta_2} \left[1 - \left(\frac{\alpha'_1}{\alpha'} \right)^{\beta_2} \right] \right\} \quad (2.31)$$

Therefore, viscoplastic multiplier (Λ^{vp}) is defined by the internal strain rate (R_a) and a stress ratio function, α'_1 / α' is the ratio between sizes of the loading and references surfaces respectively and β_2 is a material parameter that characterizes the decrease in the predicted rate-dependency and creep properties with stress history.

R_a is defined as an internal strain rate that represents the strain history influence on the general 3D case and has a strong influence on the Λ^{vp} magnitude. The general evolution law is:

$$\dot{R}_a = [f_A - R_a] \cdot m_t \quad (2.32)$$

When loading the soil in a 3D condition, general straining occurs (i.e., volumetric and deviatoric strains occur). The activation function (f_A) and the transient coefficient (m_t) are defined by:

$$f_A = \Lambda \left(\frac{\Lambda \cdot P_0}{\dot{\varepsilon}_{ref}} \right)^{-\beta} \quad (2.33)$$

$$P_0 = (k^2 - \mathbf{b} : \mathbf{b})_{\eta=\mathbf{b}} \quad (2.34)$$

$$m_t = \left(\frac{\rho_c}{\rho_\alpha} - 1 \right) \frac{\|\dot{\boldsymbol{\epsilon}}^{vp}\|}{\rho_r n} + O(\|\dot{\boldsymbol{\epsilon}}\|) \quad (2.35)$$

$O(\|\dot{\boldsymbol{\epsilon}}\|)$ small term is added to ensure m_t is positive when $\|\dot{\boldsymbol{\epsilon}}^{vp}\| \cong 0$. For unloading ($CL < 0$), R_a decreases and is determined as:

$$\dot{R}_a = (\beta_3 - 1) \left(\frac{\dot{\alpha}'_1}{\alpha'_1} \right) R_a \quad (2.36)$$

where β_3 is a material constant that controls the decreasing rate in R_a .

2.4.4. Non-linear small strain behavior

The proposed MIT-SR formulation includes a systematic description of general nonlinear small-strain behavior and its approach is similar to previous MIT soil models.

A maximum elastic stiffness, often observed after load reversal, is assumed to be represented by an intrinsic property (ρ_{r0}):

$$\rho_{r0} = \frac{1}{C_b \left(1 + \frac{K}{2G} \boldsymbol{\eta} : \boldsymbol{\eta} \right)^{\frac{1}{6}}} \left(\frac{\sigma'}{p_{atm}} \right)^{\frac{2}{3}} \quad (2.37)$$

where C_b is a dimensionless material constant and $K/2G$ is related to Poisson's ratio ($= \frac{1+\nu}{3(1-2\nu)}$). The degradation of elastic stiffness is then presented by a transition function:

$$\rho_r = \rho_{r0} \left(1 + \frac{D}{\rho_{r0}} \xi + w_s \xi_s \right) \quad (2.38)$$

Material constants D and w_s are included to scale volumetric and deviatoric components respectively. The equation multiplies ρ_{r0} by a factor that considers volumetric and deviatoric contributions defined by non-dimensional stress measures ξ and ξ_s :

$$\xi = \left\langle r \frac{\dot{\epsilon}}{\|\dot{\epsilon}\|} \ln \left(\frac{\sigma'}{\sigma^h} \right) \right\rangle \quad (2.39)$$

$$\xi_s = \left\langle \frac{\dot{\mathbf{E}}}{\|\dot{\epsilon}\|} : (\boldsymbol{\eta} - \boldsymbol{\eta}^h) \right\rangle \quad (2.40)$$

where r is a material constant. Hysteretic stress state variables $(\sigma^h, \boldsymbol{\eta}^h)$ evolution laws are:

$$\dot{\sigma}^h = \frac{\dot{\epsilon}^h}{D \cdot n} \sigma^h \quad (2.41)$$

$$\dot{\boldsymbol{\eta}}^h = \frac{2G \dot{\mathbf{E}}^h}{w_s \sigma'} + \frac{|\dot{\epsilon}|}{n \rho_{r0}} (\boldsymbol{\eta} - \boldsymbol{\eta}^h) \quad (2.42)$$

where $\dot{\epsilon}^h$ and $\dot{\mathbf{E}}^h$ are the volumetric and deviatoric components of the hysteretic strain rate, respectively. These components are assumed to be proportional to the elastic strain rate:

$$\dot{\epsilon}^h = \frac{D \xi}{\rho_r} \left(1 + \frac{\mathbf{b} : \mathbf{b}}{d_a^2} \right) (\dot{\epsilon} - \dot{\epsilon}^{vp}) \quad (2.43)$$

$$\dot{\mathbf{E}}^h = \frac{\rho_{r0} w_s \xi_s}{\rho_r} (\dot{\mathbf{E}} - \dot{\mathbf{E}}^{vp}) \quad (2.44)$$

$$d_a^2 = \frac{2 (1 - K_{0NC})^2}{(1 + K_{0NC} + K_{0NC}^2)} \quad (2.45)$$

2.4.5. Elastic stiffness and dilation of OC clays

Elastic bulk modulus (K) and shear modulus (G) are defined as:

$$K = \frac{\sigma'}{n \cdot \rho_r} \quad (2.46)$$

$$G = K \frac{3(1 - 2\nu')}{2(1 - \nu')} \quad (2.47)$$

Incremental effective stresses can be determined by multiplying the incremental strains in each direction by the respective stiffness:

$$\begin{pmatrix} \dot{\sigma}' \\ \dot{\mathbf{S}} \end{pmatrix} = \begin{pmatrix} K(\dot{\epsilon} - \dot{\epsilon}^{vp} + \dot{\epsilon}^{dil}) \\ 2G(\dot{\mathbf{E}} - \dot{\mathbf{E}}^{vp}) \end{pmatrix} \quad (2.48)$$

A strain rate term ($\dot{\epsilon}^{dil}$) is introduced to address clay dilative behavior of overconsolidated clays. D_L is a material constant that controls dilative strain rate magnitude and $\dot{\epsilon}^{dil}$ is defined as:

$$\dot{\epsilon}^{dil} = D_L \cdot (\dot{\mathbf{E}} - \dot{\mathbf{E}}^{vp}) : \boldsymbol{\eta} \left[1 - \frac{\sigma'}{\alpha'} \right] \quad (2.49)$$

2.5. MIT-SR MATERIAL CONSTANTS AND STATE VARIABLES

The generalized MIT-SR formulation includes 17 material constants (Table 2-2), and 5 internal state parameters (Table 2-3):

- 11 standard material constants, rate-independent parameters essentially inherited from the MIT-S1 model ($\rho_c, C_b, D, r, w_s, 2G/K, K_{0NC}, \phi'_{cs}, \phi'_m, m, \psi$).
- 6 new material constants, 5 are rate-dependent parameters ($\rho_\alpha, \beta, \dot{\epsilon}_{ref}, \beta_2, \beta_3$) and 1 material constant utilized to describe dilative behavior of OC clays (D_L).
- 5 internal state variables ($\alpha', R_\alpha, \sigma^h, \mathbf{b}, \boldsymbol{\eta}^h$), whose initial values must be calculated based in stress and strain rate history of the past consolidation process.

2.5.1. Determination of standard material constants

The calibration procedures for these parameters are essentially consistent with the original formulation (Pestana, 1994; Pestana and Whittle, 1999) and are listed as follows:

1. ρ_c can from 1D or isotropic consolidation under incrementally loads (IL) or constant rate of strain (CRS) and its value is obtained from the slope in the NC compression range plotted in $\log e - \log \sigma'_v$ (or $\log \sigma'_v$).
2. C_b governs small strain elastic compressibility and can be estimated from volumetric stress-strain measurement immediately after unloading and reloading. Considering the difficulty and inaccuracies generally present in these measurements, an alternative and suggested procedure is obtaining G_{max} value and by adopting a Poisson's ratio (ν) value (or $2G/K$), calculate C_b with the following equation that considers de porosity (n) and atmospheric pressure (p_a):

$$\frac{G_{max}}{p_a} n = \frac{3}{2} C_b \left(\frac{1 - 2\nu}{1 + \nu} \right) \left(\frac{\sigma'}{p_a} \right)^{1/3} \quad (2.50)$$

3. D and r control the nonlinearity of small strain volumetric behavior. Both parameters can be obtained by fitting 1D or hydrostatic unloading-reloading behavior in IL or CRS tests (Figure 2-14).
4. w_s controls the nonlinearity of small strain shear behavior and can be determined by fitting either the stress-strain curve for undrained shear tests at small strain range or the degradation curve of the shear modulus (Figure 2-15).
5. K_{0NC} determines lateral earth pressures in 1D compression in NC range and can be calculated from K_0 consolidation in triaxial cell or oedometer rigid wall with pressure measurements. It also can be estimated with several empirical relationships.
6. $2G/K$ is related to Poisson's ratio, which can be obtained from 1D swelling effective stress path in triaxial cell (Pestana and Whittle, 1999). These parameters are related by:

$$\frac{2G}{K} = 3 \left(\frac{1 - 2\nu}{1 + \nu} \right) \quad (2.51)$$

7. ϕ'_{cs} is the friction angle in critical state measured in compression at large strains. The model considers the same critical angle for compression and extension based on an isotropic Matsuoka-Nakai generalization.
8. ϕ'_m and m define the loading/reference surface shape (Figure 2-16). As m changes from 0 to 1, the surface geometry transforms from an ellipsoid to a lemniscate shape. ϕ'_m defines the surface friction coefficient.

For clays, both parameters can be calibrated by fitting CK₀UC and CK₀UE tests with standard strain rate. The selected strain rate should be the same as the test to be fitted (e.g., $\dot{\epsilon}_a = 0.5\%/hr$).

9. ψ determines reference surface rotation rate consequence of kinematic hardening. Figure 2-17 presents the evolution of the reference surface during a 1/K₀ consolidation test of a K₀ normally consolidated specimen test; it can be observed the rotation and expansion of the surface due to kinematic and isotropic hardening respectively. ψ can be obtained by fitting the measurements in CK₀UE tests (Figure 2-18); ψ has negligible influence on CK₀UC.

2.5.2. Determination of new material constants

The proposed model incorporates 6 new material constants: 1 material constant (D_L) and 5 rate-dependent parameters ($\rho_\alpha, \beta, \dot{\epsilon}_{ref}, \beta_2, \beta_3$) that are generalized from the 1D formulation and can be determined with 1D compression tests data:

1. D_L describes the dilative behavior of over consolidated clays during shearing. It can be calibrated by fitting the effective stress path and undrained strength exhibited in undrained triaxial tests for specimens with OCR higher than 2 (Figure 2-19); conditions in which clays are generally expected to exhibit dilation.
2. β describes the rate-dependency of the internal rate strain (R_a) steady state and has a significant influence in the shear behavior rate-dependency. It ranges from 0 to ρ_α/ρ_c and is independent from the viscous property ρ_α/ρ_c . Figure 2-20 and Figure 2-21 present effective stress paths in CK₀UC tests on NC clays executed at different strains rate for β values equal to 0 (=0.001) and $\beta = 0.02 = \rho_\alpha/\rho_c$ respectively.

3. ρ_α/ρ_c controls the transient process of R_α and can be determined by fitting a creep or relaxation curve under 1D compression. Another alternative to estimate this parameters is to fit the rate-dependent s_u in K_0 -normally consolidated specimens in CK_0UC tests.
4. $\dot{\epsilon}_{ref}$ is the reference volumetric strain rate, generally adopted from the strain rate measured at the 24hr interval in IL oedometer tests ($\dot{\epsilon}_{ref} \sim 1.10^7/\text{sec}$). It can also be obtained by calibrating CRS tests and when $\beta = 0$ is ineffective.
5. β_2 governs nonlinear creep properties variation and allows the variation of steady state rate-dependency behavior in different strain rate ranges. It can be obtained from creep rate reduction with OCR in different tests. Yuan (2016) suggests $\beta_2 \approx 6.8$ after fitting limited experimental data for Salt Lake City and in Chapter 4, with considerable information, $\beta_2 = 6.5$ was calibrated for Singapore Marine Clay.
6. β_3 controls R_α decreasing rate after unloading and can be determined by fitting decreasing creep rate with OCR during 1D swelling. It is important to have a realistic value of this parameter to ensure realistic creep rates in the clay before shearing from an OC state. Yuan (2016) suggests $\beta_3 \approx 19$ after fitting limited experimental data for Salt Lake City and in Chapter 4, with considerable information, $\beta_3 = 9.0$ was calibrated for Singapore Marine Clay.

2.5.3. Determination of initial state variables

The models considers 5 internal state variables including 3 scalars (α' , R_α , σ^h) and 2 tensors (\mathbf{b} , $\boldsymbol{\eta}^h$) whose initial values (α'_0 , $R_{\alpha 0}$, σ^{h0} , \mathbf{b}_0 , $\boldsymbol{\eta}^{h0}$) could be estimated by considering stress and strain rate history of past consolidation processes.

Their initial values can be estimated as follows:

1. The initial value of internal strain rate ($R_{\alpha 0}$) defines the initial viscoplastic strain rate ($\dot{\epsilon}_0^{vp}$) and influences NC clay compression. For $OCR \cong 1$, $R_{\alpha 0}$ can be estimated from the preceding consolidation process given a known drainage path. For high OCR, $R_{\alpha 0} \cong 0$ is a reasonable assumption considering that creep effects are negligible at such condition.
2. Initial size and orientation of the reference surface are represented by α'_0 and \mathbf{b}_0 , respectively; they both depend on the strain history of the soil. For clay at general stress state, initial estimates of these values require back analyses to reproduce recent stress paths.

For K_0 -normally consolidated conditions, $\mathbf{b}_0 = \boldsymbol{\eta}_0$ and can be calculated with K_{0NC} . Initial OCR is reflected by the initial value of α'_0/α'_1 .

3. Hysteretic state parameters initial values ($\sigma^{h0}, \boldsymbol{\eta}^{h0}$) are challenging to estimate from direct measurements. For practical conditions initial values can be inferred. For OC clays $\sigma^{h0} = \sigma'_0$ and $\boldsymbol{\eta}^{h0} = \boldsymbol{\eta}_0$ can be considered to establish a maximum initial elastic stiffness at the initial state. For NC clays, σ^{h0} can be settled at a steady state rate and $\boldsymbol{\eta}^{h0} \approx \boldsymbol{\eta}_0$.

Table 2-1: Transformed quantities used in MIT soil models (Whittle and Kavvas, 1994).

Effective stress	Stress ratio	Strain	Yield surface Gradient	Plastic flow direction	Anisotropy
(σ', S)	η	(ϵ, E)	(Q, Q')	(P, P')	b
$\sigma' = \frac{(\sigma'_x + \sigma'_y + \sigma'_z)}{3}$	1	$\epsilon = \epsilon_x + \epsilon_y + \epsilon_z$	$Q_s = Q_x + Q_y + Q_z$	$P = P_x + P_y + P_z$	1
$S_1 = \frac{(2\sigma'_y - \sigma'_x - \sigma'_z)}{\sqrt{6}}$	$\eta_1 = \frac{(2\eta_y - \eta_x - \eta_z)}{\sqrt{6}}$	$E_1 = \frac{(2\epsilon_y - \epsilon_x - \epsilon_z)}{\sqrt{6}}$	$Q_1 = \frac{(2Q_y - Q_x - Q_z)}{\sqrt{6}}$	$P_1 = \frac{(2P_y - P_x - P_z)}{\sqrt{6}}$	$b_1 = \frac{(2b_y - b_x - b_z)}{\sqrt{6}}$
$S_2 = \frac{(\sigma'_z - \sigma'_x)}{\sqrt{2}}$	$\eta_2 = \frac{(\eta_z - \eta_x)}{\sqrt{2}}$	$E_2 = \frac{(\epsilon_z - \epsilon_x)}{\sqrt{2}}$	$Q_2 = \frac{(Q_z - Q_x)}{\sqrt{2}}$	$P_2 = \frac{(P_z - P_x)}{\sqrt{2}}$	$b_2 = \frac{(b_z - b_x)}{\sqrt{2}}$
$S_3 = \sqrt{2}\sigma_{xy}$	$\eta_3 = \sqrt{2}\eta_{xy}$	$E_3 = \sqrt{2}\epsilon_{xy}$	$Q_3 = \sqrt{2}Q_{xy}$	$P_3 = \sqrt{2}P_{xy}$	$b_3 = \sqrt{2}b_{xy}$
$S_4 = \sqrt{2}\sigma_{yz}$	$\eta_4 = \sqrt{2}\eta_{yz}$	$E_4 = \sqrt{2}\epsilon_{yz}$	$Q_4 = \sqrt{2}Q_{yz}$	$P_4 = \sqrt{2}P_{yz}$	$b_4 = \sqrt{2}b_{yz}$
$S_5 = \sqrt{2}\sigma_{zx}$	$\eta_5 = \sqrt{2}\eta_{zx}$	$E_5 = \sqrt{2}\epsilon_{zx}$	$Q_5 = \sqrt{2}Q_{zx}$	$P_5 = \sqrt{2}P_{zx}$	$b_5 = \sqrt{2}b_{zx}$

Table 2-2: 3D MIT-SR Material Parameters (Yuan, 2016).

Parameters	Physical meaning	Suggested calibration method	
Parameters similar to MIT-S1	ρ_c	Compressibility of NC clay (LCC regime)	Measure from $\log e - \log \sigma'$ compression curve
	C_b	Small strain elastic compressibility	Derive from high quality small strain measurement of G
	D	Nonlinear volumetric and deviatoric hysteretic behavior	Measure from 1-D swelling $\log e - \log \sigma'$ curve
	r		Measure from shear stiffness degradation curve
	w_s	Alternative measure of Poisson's ratio at small strain	Measure from 1-D swelling stress path
	$2G/K$	Lateral earth pressure ratio in LCC regime	Measure for NC clays using SHANSEP consolidation
	K_{0NC}	(Large strain) critical state friction angle	Measure in triaxial compression tests
	ϕ'_{cs}	Friction coefficient of loading/reference surface	Fit undrained strengths for CK0UC on NC clays
	ϕ'_m	Geometry of loading/reference surface	Fit tendency of softening for CK0UC on NC clays
	m	Rate of evolution of anisotropy due to stress history	Fit CK0UE behavior over strain range >5%
	ψ	New parameters	Compressibility in secondary compression
ρ_α	Rate-sensitivity of steady state of R_α		Measure from the rate-sensitivity of CRS tests
β	Reference strain rate		Measure at the 24hr interval in IL oedometer tests ($\approx 1 \times 10^{-7}$ /sec)
$\dot{\epsilon}_{ref}$	Nonlinear variation of rate-dependency with stress history		Measure reduction of the post-unloading creep property with OCR in 1-D swelling
β_2	Reduction of creep rate during unloading		Measure decrease in creep rate with OCR in 1-D swelling
β_3	Dilation behavior		Fit effective stress path for CK0UC with OCR >2
D_L			

Table 2-3: 3D MIT-SR Internal State Variables (Yuan, 2016).

Symbol	Physical Meaning	Estimation of initial values
α'	Size of bounding surface	$\alpha'_0/\alpha'_1 = \text{OCR}$
b	Orientation of anisotropic bounding surface in stress space	$\mathbf{b}_0 = \boldsymbol{\eta}_0$ for K_0 -normally consolidated clay
R_a	Activated Rate [1/time] due to historic straining	Strain rate from the preceding consolidation on a clay layer with known drainage length
σ^h	Volumetric hysteretic state parameter	For NC: Eqns. 2.37-2.43; For OC: $\sigma^{h0} = \sigma'_0$
$\boldsymbol{\eta}^h$	Deviatoric hysteretic state parameter	$\boldsymbol{\eta}_0^h = \boldsymbol{\eta}_0$ for NC and OC clays

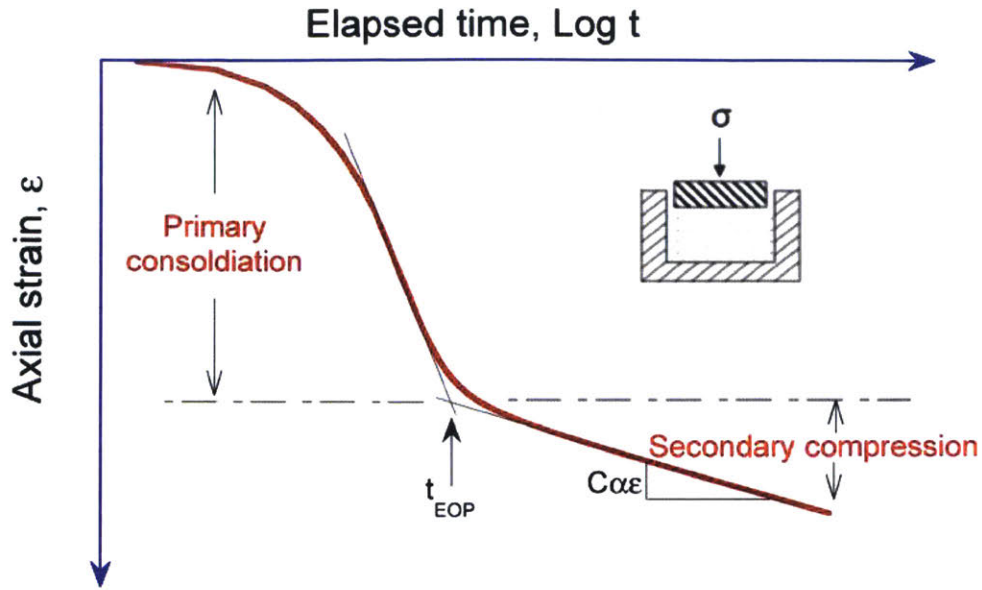


Figure 2-1: Typical consolidation curve of strain - log (time) upon an incremental load in an (IL) oedometer test (Yuan, 2016).

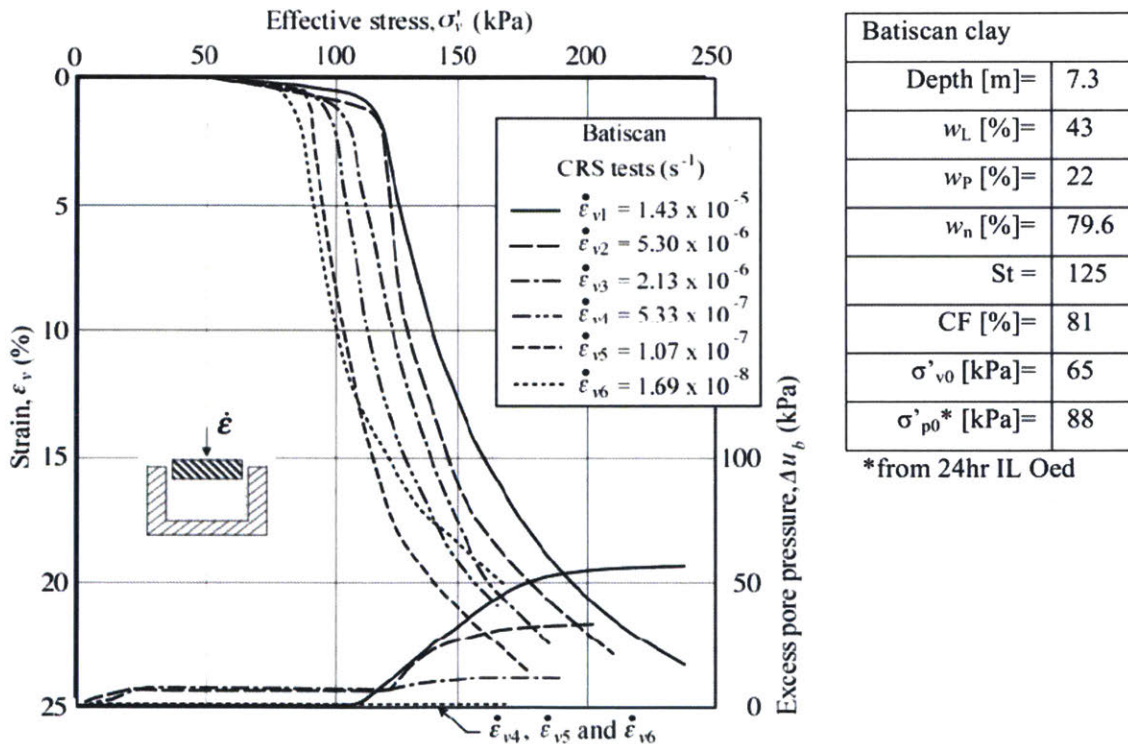


Figure 2-2: Effect of strain rate in CRS consolidation tests on Batiscan clay (Leroueil et al., 1985).

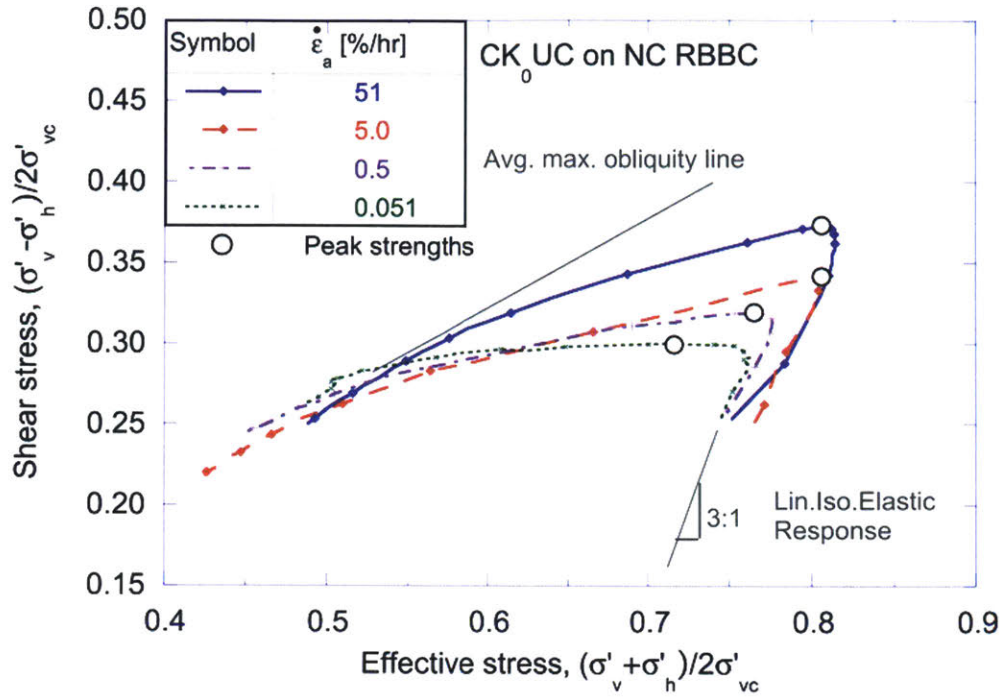


Figure 2-3: Effective stress paths for CK0UC tests on NC RBBC under different strain rates (after Sheahan, 1991).

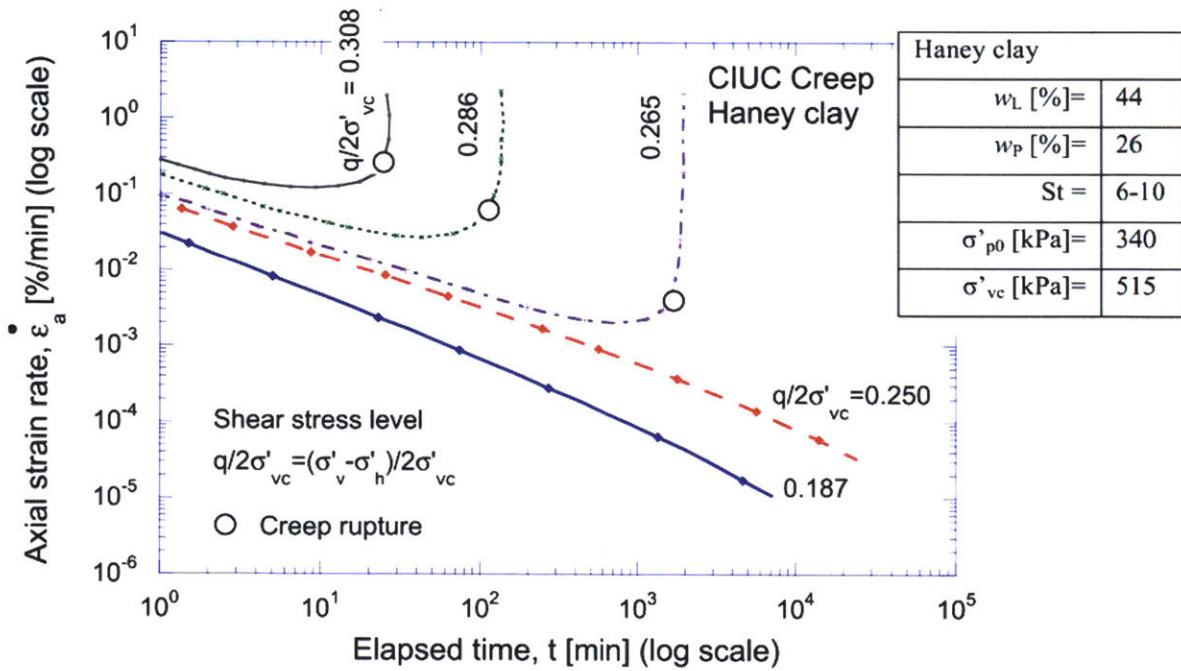


Figure 2-4: Strain rate versus time for undrained creep in CIUC tests on Haney clay (after Vaid & Campanella, 1977).

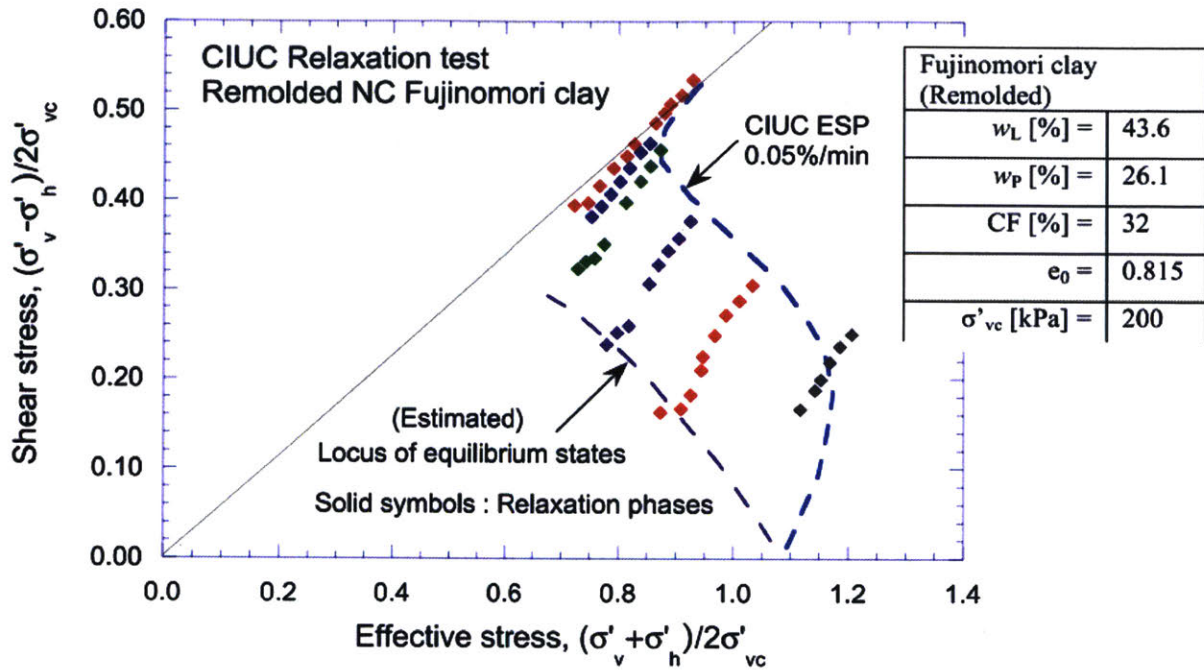


Figure 2-5: Effective stress paths from multiple-phases relaxation test on Fujinomori clay in CIUC (after Murayama, 1974).

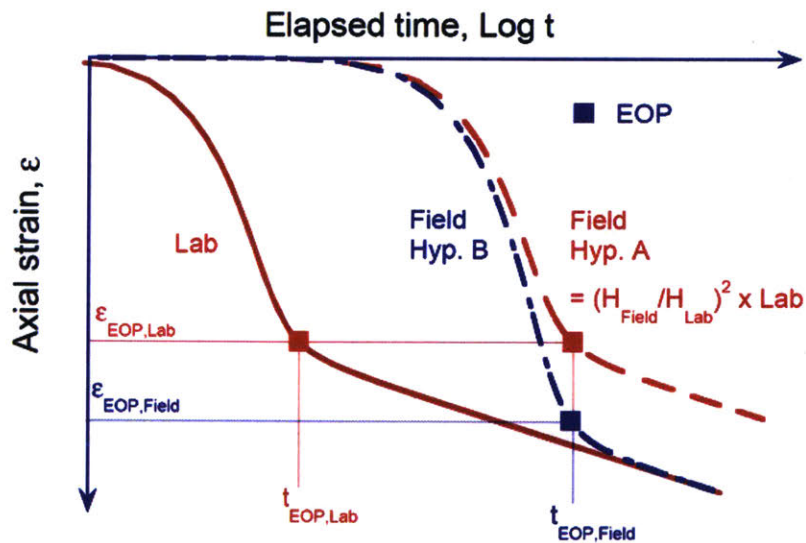


Figure 2-6: Consolidation curves of Hypothesis A and Hypothesis B (after Ladd et al., 1977).

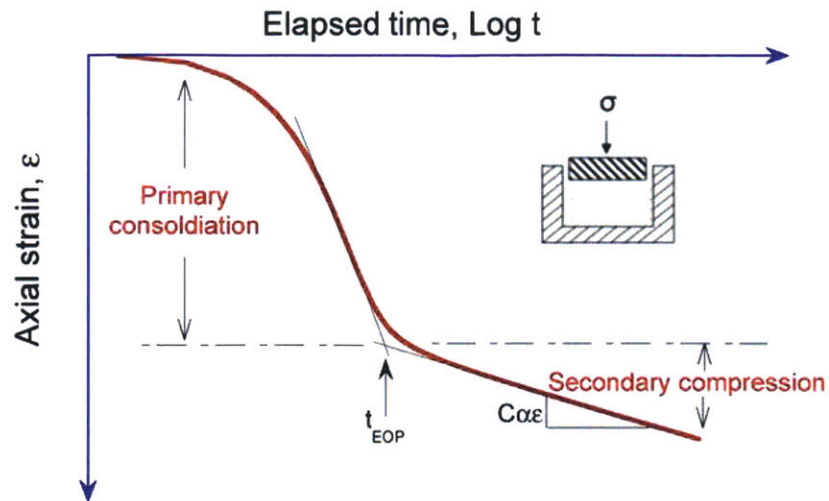


Figure 2-7: Typical consolidation curve of strain - log (time) upon an incremental load in an (IL) oedometer test (Yuan, 2016).

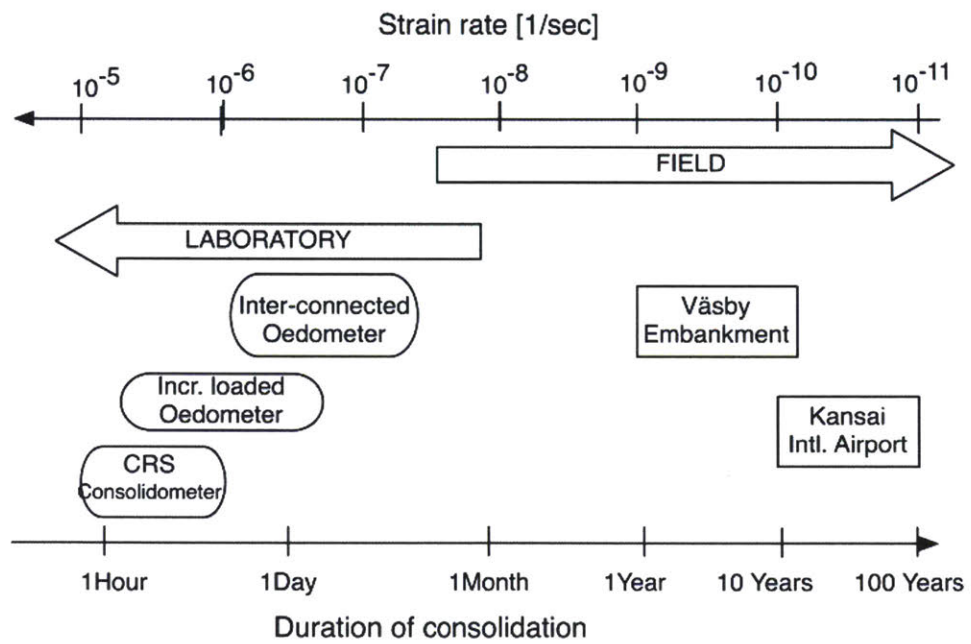


Figure 2-8: Spectrum of duration or average strain rate for the consolidation at laboratory and field-scale (Yuan 2016).

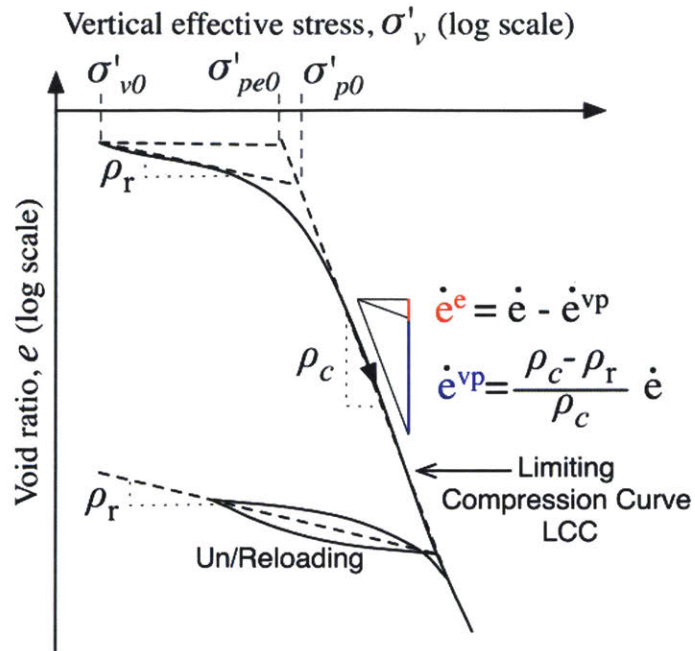


Figure 2-9: Conceptual framework for describing compression behavior in the loge-log σ'_v space with compressibility parameters ρ_c and ρ_r (after Pestana & Whittle, 1999).

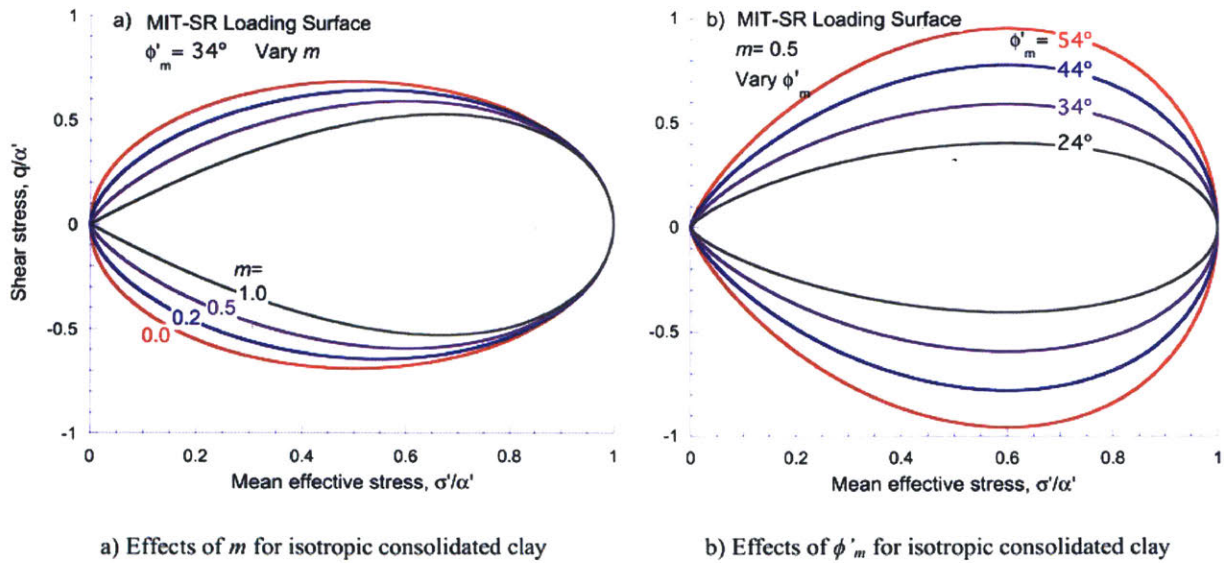
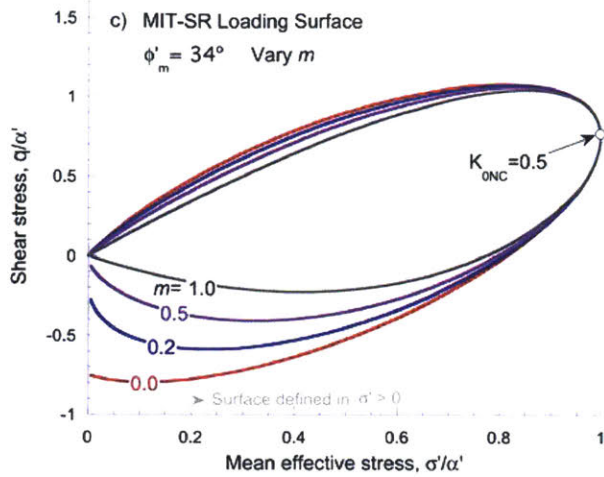
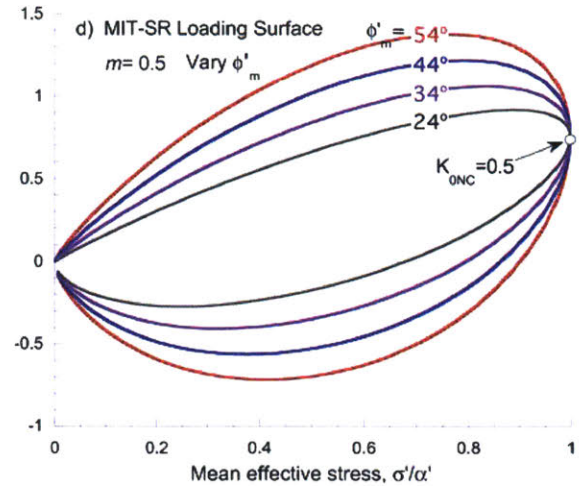


Figure 2-10: Effects of a) ϕ'_m and b) m on the shape of MIT-SR loading surface for isotropic consolidated clay with $b_1=0$ (Yuan 2016).

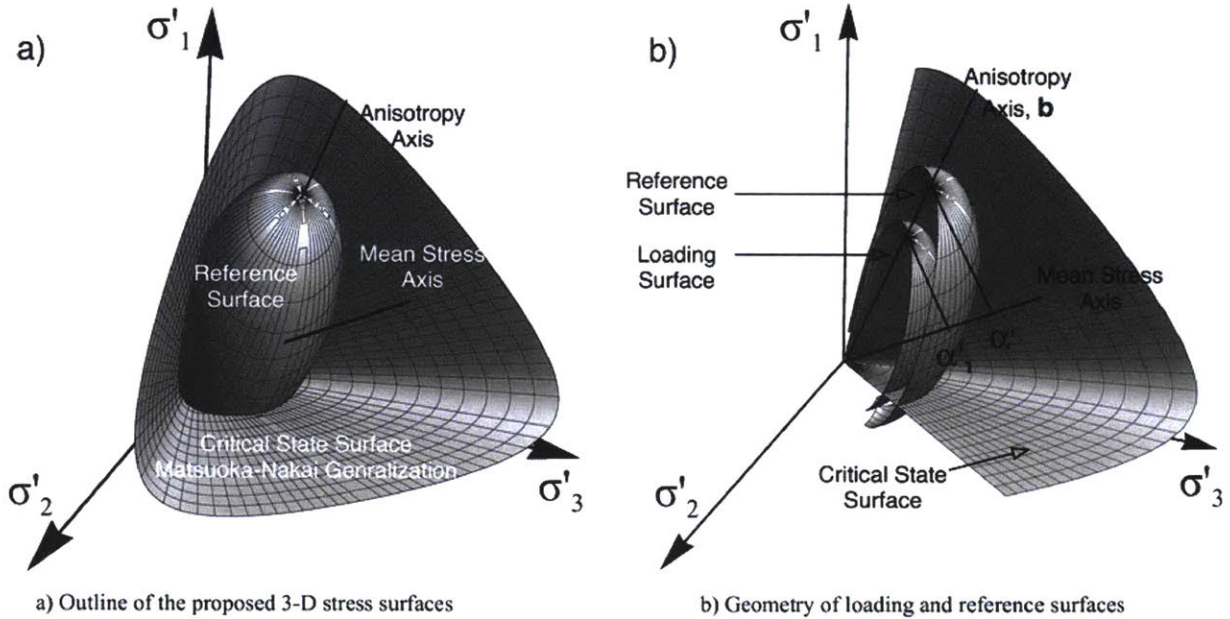


c) Effects of m for K_0 -normally consolidated



d) Effects of ϕ'_m for K_0 -normally consolidated clay

Figure 2-11: (cont.) Effects of c) ϕ'_m and d) m on the shape of MIT-SR loading surface for K_0 -normally consolidated clay (Yuan 2016).



a) Outline of the proposed 3-D stress surfaces

b) Geometry of loading and reference surfaces

Figure 2-12: Plots of the proposed framework consisting of an isotropic critical state surface, a reference and a loading surface in 3-D principal effective stress space ($\sigma'_1, \sigma'_2, \sigma'_3$) (for illustration purpose only, from Yuan 2016).

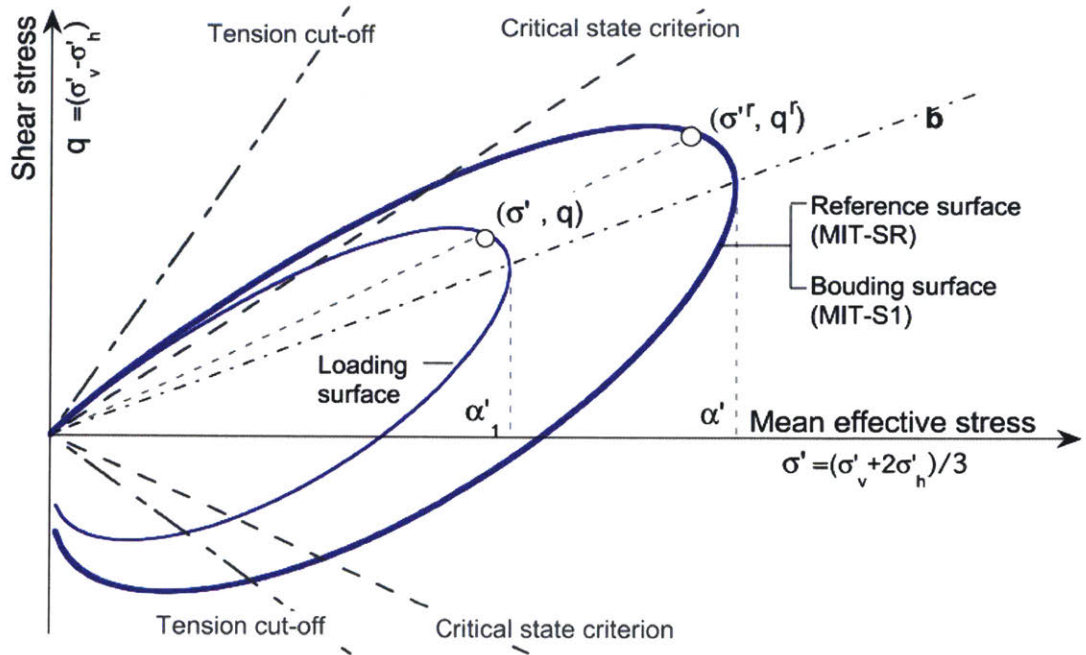


Figure 2-13: Plots of the proposed framework in the triaxial stress space (Yuan 2016).

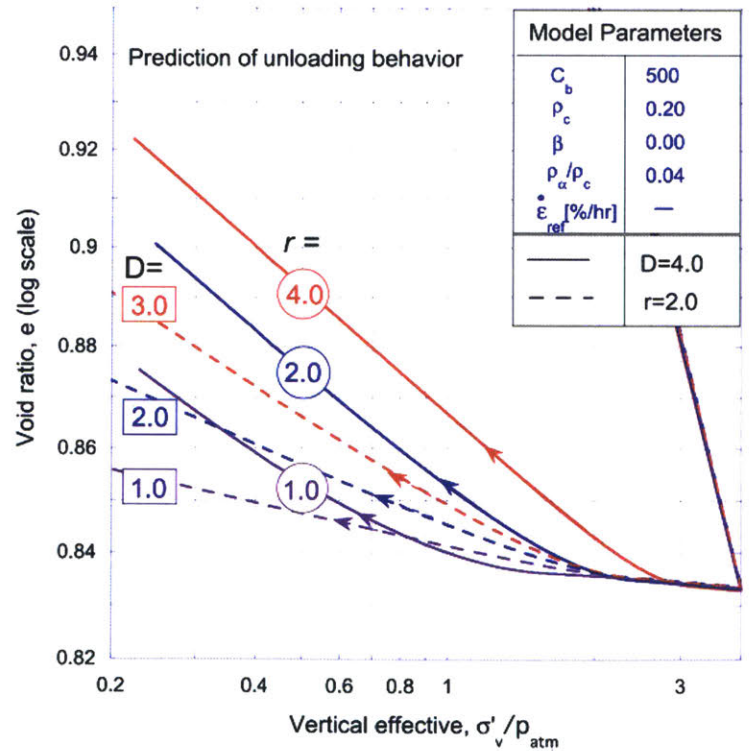


Figure 2-14: Effects of parameters D and r on the predictions of 1D unloading behavior (Yuan 2016).

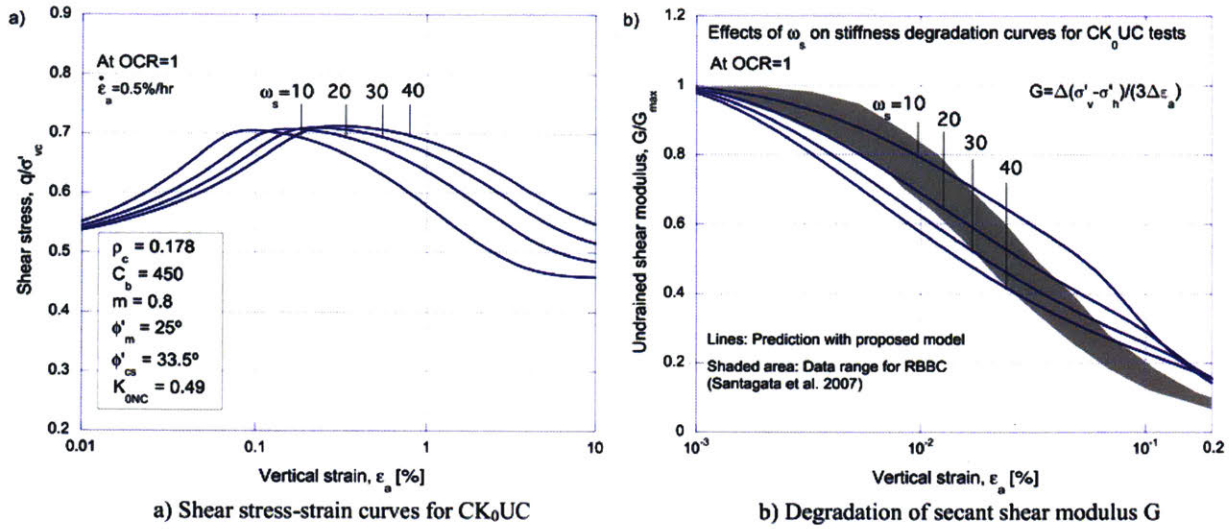


Figure 2-15: Effects of w_s on the predicted nonlinear small strain behavior of CK₀UC tests on normally consolidated clay (Yuan 2016).

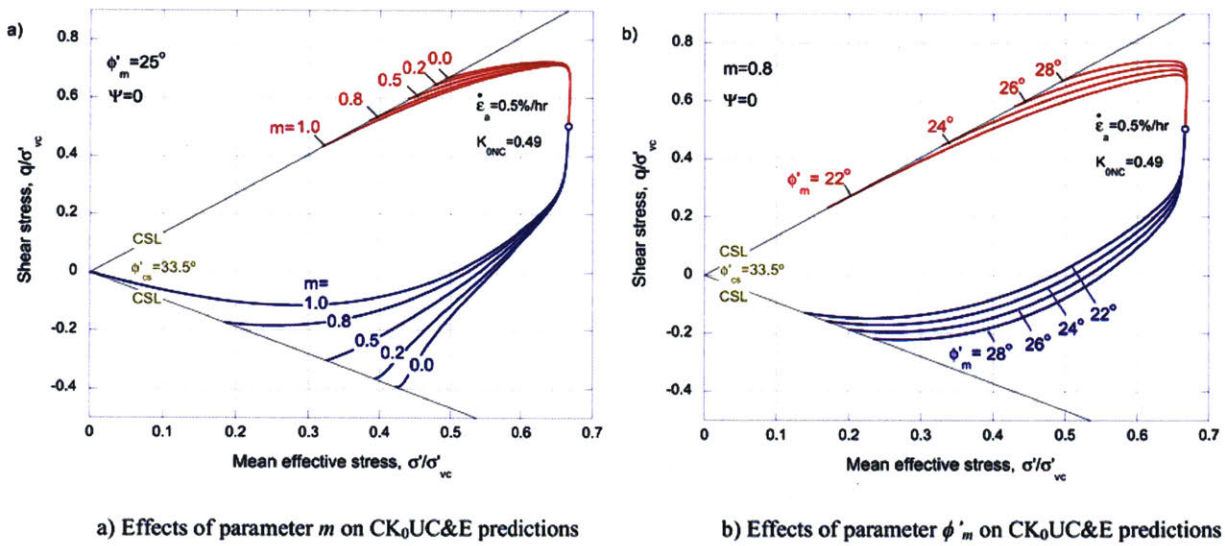


Figure 2-16: Parameter m and ϕ'_m on the predicted ESPs for CK₀UC and CK₀UE tests on normally consolidated clay (Yuan 2016).

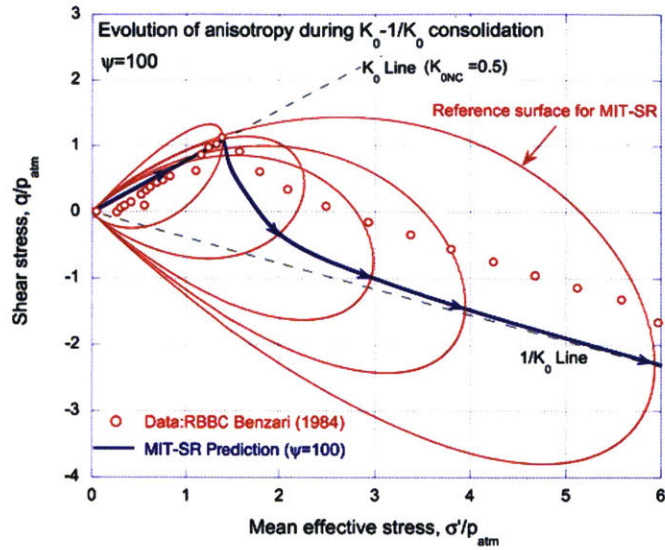


Figure 2-17: Illustration of ESPs and the transformation of reference surface for a K_0 consolidated specimen underwent $1/K_0$ consolidation (Yuan 2016).

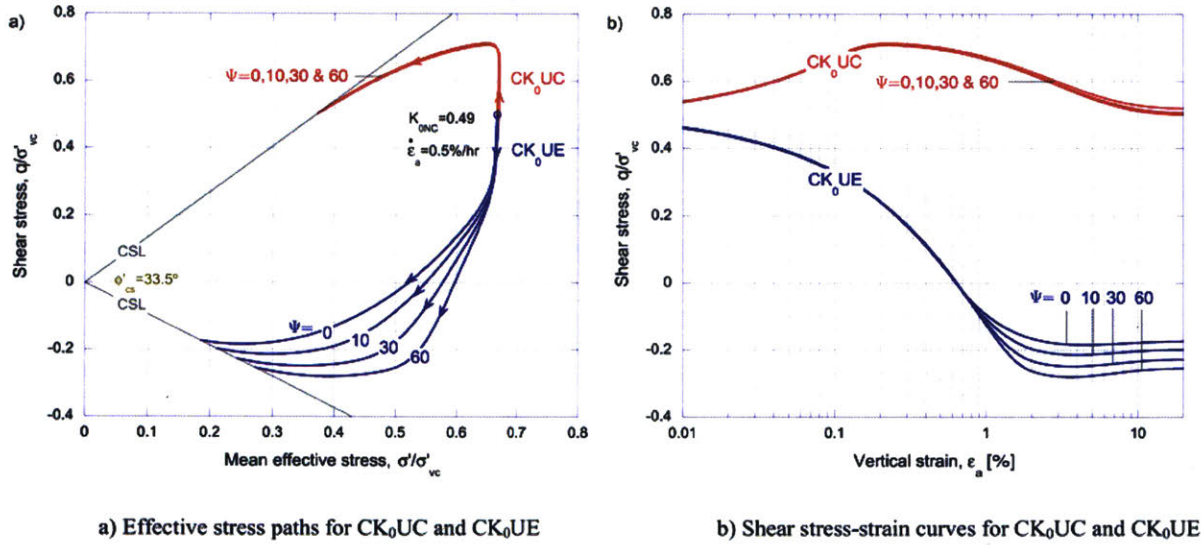


Figure 2-18: Effects of parameter ψ on CK_0UC and CK_0UE predictions on normally consolidated clay (Yuan 2016).

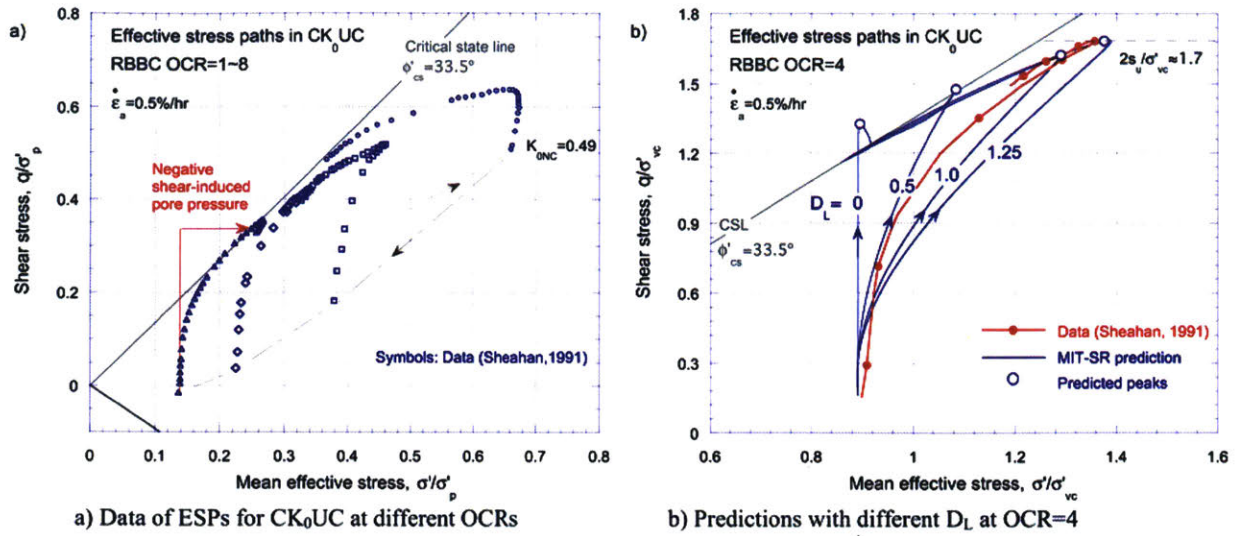


Figure 2-19: Experimental evidence of dilative behavior in CK₀UC test on RBBC and model predictions with parameter D_L (Yuan 2016).

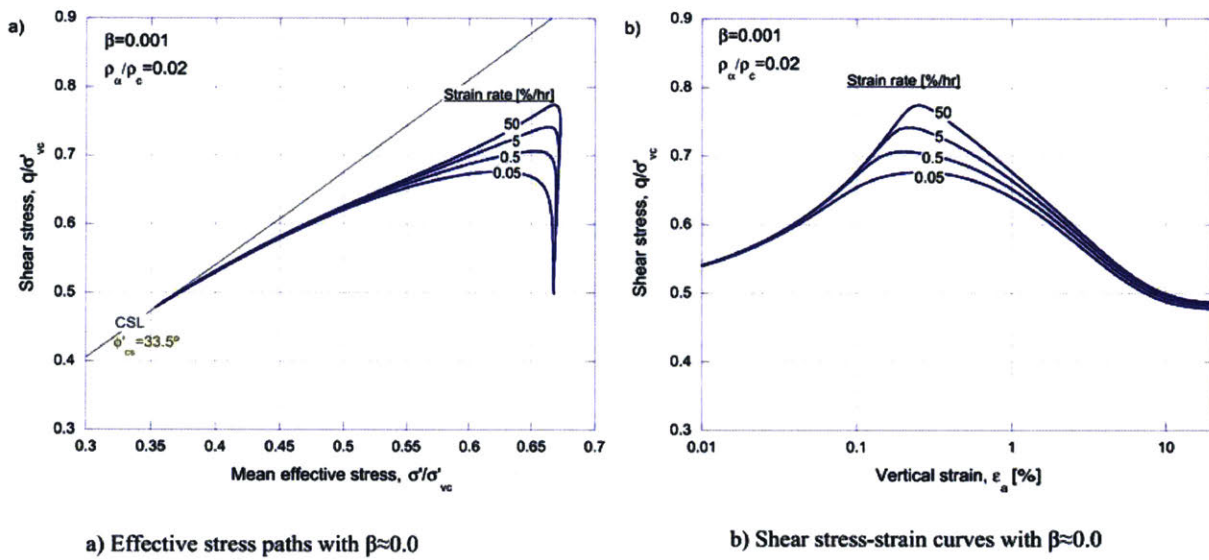


Figure 2-20: Parameter β on the predicted ESPs for CK₀UC tests on normally consolidated clay (Yuan 2016).

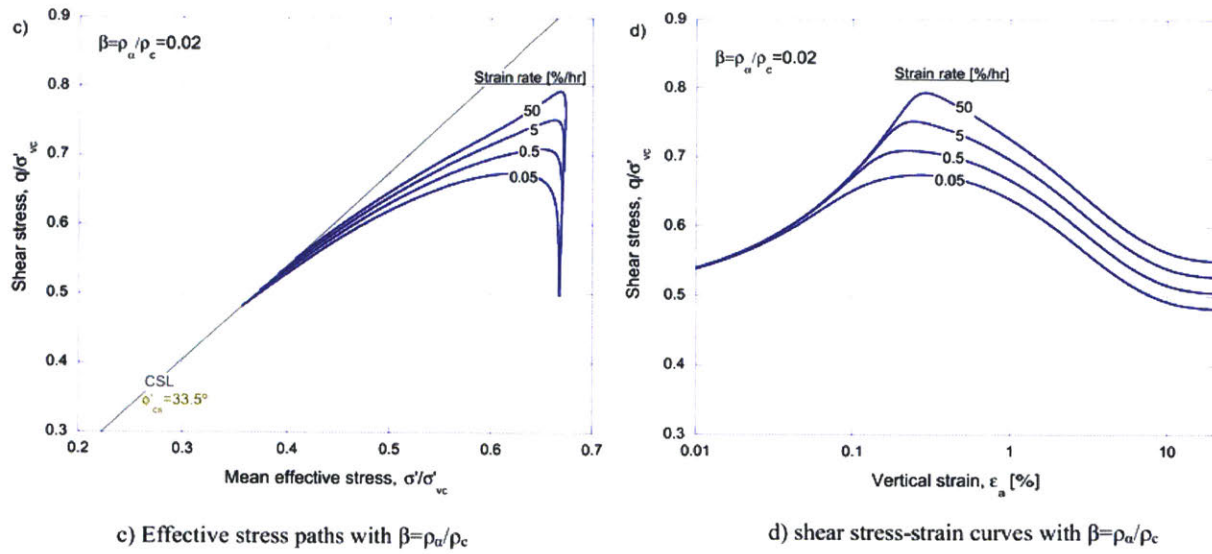


Figure 2-21: (cont.) Parameter β on the predicted ESPs for CK₀UC tests on normally consolidated clay (Yuan 2016).

3. NEW HAMILTON LEVEE PROJECT

3.1. OVERVIEW OF NEW HAMILTON LEVEE PROJECT

The Hamilton Wetland Restoration Project¹ (HWRP) is a wetlands habitat restoration project at the former Hamilton Army Air Field (HAAF) and the Bel Marin Keys shoreline. The location of this site is within the City of Novato, north of San Francisco, California.

The airfield operated from 1930 until 1974 and began a closure process under the Defense Base Realignment and Closure Act in 1988. The base was redeveloped following a 1996 Reuse Plan, the City of Novato's Master Plan and subsequent plans and processes. Much of the base was converted to residential and commercial use, with a significant balance set aside for parks and open space.

The plan of the HWRP is to create a system of seasonal and tidal wetlands by placing approximately 10.6 million cubic yards of dredged material to raise site elevation, which is now several feet below sea level. This requires the construction of levees all around the perimeter of the new wetlands, including enlargement of the existing New Hamilton Partnership Levee (NHPL) by constructing a new embankment overlapping the outboard (east) side of the levee. The New Hamilton Partnership Levee (NHPL) is one of several existing levees that surround the HAAF Base Wetlands Restoration project (Figure 3-1).

The existing NHPL was built between March and October 1996 and functions as a flood control embankment structure for the New Hamilton Partnership residential area. It consists of well-compacted, slightly cohesive granular fill, 7200ft long, 11-12ft high, 23ft wide crest, 89ft wide base and 1V:3H slopes.

The existing NHPL alignment is located on a thick layer (30-40ft) of recent San Francisco Bay Mud (SFBM). Free field average ground surface elevation is EL. -1.6ft (NGVD), levee crest average elevation is EL. +9.4ft (NGVD) and water table average elevation is EL. -4.5ft (NGVD). Note that NGVD elevation zero approximates mean sea level (MSL). Typical

¹ Nowadays known as the Hamilton/Bel Marin Keys Wetlands Restoration

longitudinal and transverse profiles of the levee and subsurface conditions are presented in Figure 3-2 and Figure 3-3, respectively.

3.2. NOVATO CITY MONITORING PROGRAM

Shortly after the completion of the NHPL construction, Novato City instituted a settlement monitoring program using 32 survey points along the crest of the levee at 200ft intervals; no pore water pressure or lateral deformations were measured in this program (Figure 3-4). Settlement markers were installed on the floodwall and monitored periodically; time zero is between 10/07/96 to 12/12/96, depending on the point considered.

The NHPL levee was monitored from Nov/96 to Jan/02 (5.2yrs after construction approximately). The survey measured settlements (ρ_m) in the range 1.6 to 2.5ft, with a minimum of 1.1ft and a maximum of 2.7ft. Eleven set of readings were taken during these years. The measured settlements are much larger than were originally predicted (0.6ft) based on 1D consolidation analyses with σ'_p measured in laboratory oedometer tests (at End of Primary consolidation).

Figure 3-5 shows the settlement-log time data for 4 control points P16, P17, P18 and P19 that are located close to two test sections of interest (Figure 3-8): Test Section 3 (TS3) and Test Section 5 (TS5). These data suggest that primary consolidation is far from complete (indeed conventional 1-D consolidation analyses suggest the time for primary consolidation could exceed 50 years); settlements for TS3 and TS5 were 1.65 and 1.57ft respectively (Ladd, 2002). Unfortunately, observed changes in the elevation of the pavement suggested that the total settlement is higher than the monitored settlement which only covers post-construction settlement.

3.3. URS SITE INVESTIGATION & MONITORING PROGRAM

During 2002, United States Army Corps of Engineers (USACE) engaged URS to conduct an intensive site investigation program and analysis that included additional field and laboratory tests, instrumentation and monitoring program. The purpose was to calibrate analytical and finite element models (FEM) for further use in design of other levees that were planned to be constructed as part of the HWRP.

The key objective of this site investigation and monitoring program was to improve the existing geotechnical characterization of SFBM, the most compressible layer in the subsurface and which

played a critical role in the general settlement of the area. Summaries of the executed field and laboratory tests are included in Appendix A.

The following sections highlight the key elements of URS report (2003) that served for this research.

3.3.1. Laboratory tests

Laboratory tests were executed on samples obtained from all around the project. Data from samples at TS3 and TS5 included the following:

- 7 CRS tests: CRS-430/431/432/435/440/441/443/444;
- 3 CK_0UC tests: TXC-575/584/590 and
- 2 CK_0UE tests: TXE-576/603.

These tests were of key importance for the later MIT-SR calibration for the SFBM. Detailed information about the tests executed at MIT and their results can be found in Nguyen (2006).

3.3.2. Field tests and preconsolidation profile

Several FVT and CPT tests were executed all around the project. URS (2003) compared results from FVT performed 3ft away from each CPT locations and concluded that results showed good agreement. In addition, overall consistency of all the FVT and CPT results (Figure 3-6) suggested that the SFBM is relatively uniform along the alignment of the NHPL levee.

Another key element of this field investigation was the calculation of an OCR profile: from FV tests and by using SHANSEP equation and Bjerrum's field vane correction method (Ladd and DeGroot, 2003), an OCR profile is calculated:

$$OCR = \frac{\sigma'_p}{\sigma'_v} = \left(\frac{s_u}{S} / \sigma'_v \right)^{1/m} = \left(\frac{\mu s_{u(FV)}}{S} / \sigma'_v \right)^{1/m} \quad (3.1)$$

Where OCR is the overconsolidation ratio, σ'_p is the preconsolidation stress, σ'_v is vertical effective stress, s_u is the undrained shear strength, $s_{u(FV)}$ is the measured peak field vane strength, μ is the empirical correction factor (Bjerrum, 1972), S is the undrained strength ratio for NC soil and m is the stress-strength dependency power factor. URS (2003) selected $\mu = 0.80$ based on an

average Plastic Index ($I_p = 0.50$) for SFBM, $S = 0.25$ based on prior experience with SFBM and results from direct shear tests and $m = 0.85$.

Results obtained from this methodology were compared with results from CRS and oedometer tests to establish a unified OCR profile of the site; all methods exhibited reasonable agreement and resulted in a consistent σ'_p profile. Figure 3-7 presents the results together with an effective overburden profile (σ'_{v0}) for reference.

Bay Mud Crust (top few feet of Bay Mud) is highly overconsolidated with OCR in the range of about 6.5 down to 3.5 whereas the rest of the SFBM has OCR between 3.5 and 1.45; most of the SFBM, more than 25ft, has OCR lower than 2.0. OCR profile decreases continuously in depth with minimum OCR~1.45 at the base of the layer.

Last but not least, SFBM was found to exhibit normalized behavior when comparing Direct Shear tests on samples from all around the project (URS, 2003).

3.3.3. Subsurface conditions and geotechnical characteristics

As shown in Figure 3-2 and Figure 3-3, the typical soil profile of the area, from top to bottom:

- Levee material: consists of compacted fill placed directly over the airfield pavement and quite variable in its composition. The fill is generally 11-12ft high in areas where the material was placed on top of the pavement; in areas with no pavement, the thickness of the fill varies between 14 and 18ft.
- Airfield concrete pavement: thickness of 3ft, composed by 1ft of reinforced concrete followed by 1ft of lightly reinforced concrete that rests on 1ft of gravel.
- San Francisco Bay Mud Crust: 2 to 7ft of stiff clay composed of desiccated Bay Mud; most of the alignment present thicknesses lower than 5ft.
- San Francisco Bay Mud: 30 to 40ft of highly plastic, slightly organic, overconsolidated, soft to medium stiff clay known as San Francisco Bay Mud. Variables amounts of organic material and numerous small shell fragments are commonly incorporated into the Bay Mud.
- +20ft of various, essentially incompressible and highly permeable soil strata (alluvial soil, stiff to very stiff clay, colluvium) overlying bedrock.

Water table varies seasonally and is generally located several feet below the ground surface; elevations of the water table vary between EL. -3.0 to -5.0.

3.3.4. Monitoring program

The monitoring program implemented by URS extended between Jan/02 to Dec/02. Instrumentation included piezometers, inclinometers and subsurface Sondex settlement devices. Most of the instrumentation was concentrated in two test sections (TS3 and TS5) considering the future construction of a test fill that would provide a full scale test of the proposed construction of the containment dikes and wetlands.

Figure 3-8 presents a plan view with a detail of the elements installed in each section, Figure 3-9 and Figure 3-10 present transverse sections with the detailed, final layout of the instruments installed.

In sections TS3 and TS5 were installed:

- Piezometers: 3 lines with 4 to 5 piezometers each, 14 piezometers in total, to measure free field conditions (TS3-P1-1/4, TS3-P4-1/5 and TS5-P1-1/5); 2 lines with 8 and 5 piezometers each to measure toe conditions (TS3-P2-1/8 and TS5-P2-1/5) and 2 lines in the center of the levee, with 6 piezometers each, to measure central conditions (TS3-P3-1/6 and TS5-P3-1/6). Measurements started around Jan/02 and registers continued until later Nov/2002.
- Sondex Profile devices: 1 device in line 1 and 1 in line 3 to measure free field and crest conditions respectively (TS3-S1 and TS3-S3). Measurements started the 6/Feb/2002 and registers continued until later Nov/2002.
- Inclinometers: 2 were installed at line 4' to measure toe conditions (TS3-I4' and TS5-I4') and also two at line 3 for crest conditions (TS3-I3 and TS5-I3). Measurements started the 28/Feb/2002 and registers continued until later Nov/2002.

The registered information is presented in Appendix A and will later be utilized to assess the performance of different constitutive models in the prediction of settlements and pore pressure of the NHPL project.

3.4. NGUYEN SM THESIS (2006)

Nguyen (2006) conducted a detailed independent reanalysis of the settlement of the NHP levee. Information utilized for these analyses included the URS (2003) report and additional data from an extensive program of tests carried out at MIT (Germaine, 2002 and 2004). The considered soil profile and stress history profile are presented in Figure 3-11.

One important aspect of this work is that it was not a predictive assessment of the behavior of the levee but a calibration of parameters to determine the best set that would had predicted with most accuracy the measured settlement and pore pressures.

The poor accuracy of previous predictions on the NHPL settlement and overall behavior of SFBM motivated many aspects of Nguyen (2006) work. Therefore, his work mainly focused on:

1. Reinterpretation of the mechanical properties and preconsolidation stress of the SFBM based on the available field and laboratory data.
2. Reanalyses of conventional 1D consolidation settlement with revised soil properties and reduced preconsolidation profiles.
3. Parametric, non-linear 2D FEM analyses using the Soft Soil Model (SSM; Neher, Wehnert and Bonnier, 2001) to represent the behavior of the SFBM.

The first two phases of his work resulted in several conclusions. Following are the most important details that were later addressed in the 2D simulations:

- $c_{V(NC)}$ values (around 0.06ft²/day) of the SFBM exceeded DM-7 mean line suggesting that it would experience high rates of consolidation in comparison to other clays with similar characterization and site conditions.
- There was a lack of prior investigation and interpretation of the hydraulic conductivity properties (k_{v0} , k_{h0} , c_k) of the Bay Mud and especially for the SFBM Crust and Alluvium soils which are the boundary layer and directly affect the consolidation of the SFBM.
- Most of the SFBM profile was still under recompression and therefore, the importance of investigating recompression behavior and RR values and the reevaluation of the 7 CRS provided RR values generally much larger (0.06-0.12) than RR=0.04 selected by URS (2003).

- The application of the 1D methodology for the calculation of the settlement presented several drawbacks due to uncertainties from piezometer scattered data, pavement stiffness and its distribution of load and recompression properties of the BM.
- In order to fit the measured settlement, the preconsolidation pressure profile had to be reduced 20% ($\sigma'_{p_{red}} = 0.8 \sigma'_p$), a conclusion already proposed by URS in 2003.

The limitations of the 1D calculations methodology together with the many variables that induced uncertainties (principally the preconsolidation pressure, the recompression ratio and the measured excess pore pressure) led to the parametric, non-linear 2D FEM simulations.

The detailed 2D parametric study of the NHPL sections TS3 and TS5 was executed in PLAXIS 2D software v8.2 (Figure 3-12). The simulation consisted on the staged construction of an embankment in 6 phases and the later consolidation stage. From the available information, it was deduced that construction lasted around 6-7 months and started in Apr/96. Figure 3-13 presents Nguyen's (2006) assumption of the construction process. PLAXIS v8.2 limited the construction stages and each layer was modeled with 2 separate stages: a plastic stage where the cluster is activated and undrained responses occurs followed by a consolidation stage which allows coupled deformation and seepage. Newer versions of PLAXIS present features that enable concurrent modeling of ramped loading and consolidation, representing more closely the actual construction events.

The parametric study consisted on the analysis of ten scenarios, divided in four group of cases (A, B, C, and D) to evaluate the effects of: i) the pavement under the NHPL (Cases A1 and A2); ii) the Alluvium hydraulic conductivity (Case B); iii) rate of consolidation, i.e., $c_{V(NC)}$ of Bay Mud (Cases C1, C2, and C3); iv) the effect of preconsolidation stress profiles (Cases D1 and D2); and v) the combined effects of σ'_p , $c_{V(NC)}$ and hydraulic conductivities of Bay Mud Crust and Alluvium (Cases D3 and D4). Further information on each case, its parameters and the detailed results obtained are included in Nguyen (2006).

D4 was the last and best scenario reached and predicted settlement very close to that reported by URS (2003). Parameters considered in this case are presented in Table 3-1 and results are presented in Figure 3-15 and Figure 3-16. D4 case considered a 20% reduction in the OCR profile obtained by URS from equation 3.1 ($\sigma'_{p_{D4}} = 0.8 \sigma'_{p_{URS}}$), $C_{V(NC)}^{SFBM} = 0.04 ft^2/day$ and high

permeability boundaries in the Alluvium and SFBM Crust with hydraulic conductivities equal to 0.005ft/day.

The 2D Finite Element analyzes using Soft Soil Model (SSM) for the SFBM presented several shortcomings:

- Predictive limitations of SSM: The SSM model does not include creep and hence, the reduction of the preconsolidation pressure profile is introduced as a method to represent the measured settlement-time behavior. This condition seriously limits the predictive capability of the model and therefore, its application for engineering design and construction.
- Undrained response: unrealistically high undrained initial settlements (and therefore, too high horizontal displacements) were obtained when Nguyen (2006) calibrated the model for the consolidation phase. The reason is that when the SSM model is calibrated to match the consolidation behavior, the resulting undrained stiffness (E_u) is too low and undrained response of the simulation is exaggerated. SSM is not able to reproduce reasonable predictions of undrained and consolidation settlement with a unique set of parameters.
- Horizontal displacements during consolidation: SSM was not able to reproduce accurately the overall increasing horizontal displacements during consolidation, after the end of construction. In fact, the analysis results show that remains almost constant or exhibit slight increment or reductions depending on the elevation considered (Nguyen, 2006).

Overall conclusion after the 1D and 2D results was SSM is a limited model that: i) did not provide a feature to capture creep behavior during and after construction and a reduced preconsolidation pressure had to be considered for this purpose; ii) had limited potential to describe undrained and consolidation behavior with a unique parameter set and therefore, undrained and consolidation responses were analyzed separately and iii) continuing lateral spreading, which also incremented the settlement, was still not captured by the model. Last but not least, Nguyen (2006) was not able to determine the validity of Hypothesis B for the Bay Mud.

3.5. RE-ANALYSIS OF NHPL PROJECT WITH MIT-SR

We have reanalyzed the NHPL project utilizing the MIT-SR constitutive model (Yuan, 2016) to represent the SFBM behavior and assess the performance of the model as a predictive tool by using a calibration procedure based on laboratory element tests.

Results obtained with MIT-SR are compared against results obtained with SSM and also, with Soft Soil Creep Model (SSCM; Vermeer and Neher, 1999). This model, which includes one parameter (μ^*) to define creep phenomena in the material, serves as an intermediate case between SSM (no creep phenomena is considered in the parameters) and MIT-SR (5 parameters related to creep).

The followed working methodology was:

1. Geometry, boundary conditions and material parameters for all materials, with the exception of the SFBM, were obtained from D4 case (Nguyen, 2006). Geometry was simplified considering the symmetry of the problem; i.e., only half of the section is simulated.
2. Calibration of SFBM material parameters with available laboratory and field tests and, once all material parameters are determined, the calibration of SFBM state parameters for the OCRs considered in the NHPL project. The calibration of the MIT-SR parameters for the SFBM parameters was entirely an ex-ante procedure; i.e., no information related to the performance of the NHPL levee was considered in this stage.
3. FEM simulation of the construction procedure and later consolidation with PLAXIS 2D software (Version v2017.01) with the models already mentioned: SSM, SSCM and MIT-SR.
4. Comparison of predictions against monitoring data and assessment of the performance of the soil models considered.

Model geometry, boundary conditions, materials and mesh are presented in Figure 3-17. Simulated stages of the model are detailed in Table 3-2. Materials parameters from Nguyen (2006) are presented in Table 3-3 whereas SFBM material and state parameters are presented separately in Table 3-4 and Table 3-5, respectively. The explanation and calibration procedure for each of the parameters is detailed in a later section. Considering that MIT-SR and SSCM consider creep phenomena, the defined OCR for each of these materials corresponded to the original

preconsolidation profile defined for the site by URS (2003). This contrasts with Nguyen (2006) D4 analysis case that uses a 20% reduction in σ'_p . Table 3-6 presents the OCR and K_0 considered for each SFBM layer.

In addition, SFBM is separated in 7 layers to introduce the different OCRs of the material while Nguyen (2006) considered 8 layers. This difference was adopted to improve the quality of the mesh. No significant consequences are expected from this change considering that it merged two layers with low and very similar OCRs.

Last but not least, Nguyen (2006) used PLAXIS v8.2 while all the new simulations present in this document were executed in PLAXIS v2017.01 to be able to obtain the required results at specific points for the later comparisons (e.g.: settlement, horizontal displacement and total pore pressure). Slight differences in the settlement were observed between SSM simulations with PLAXIS v8.2 (Nguyen, 2006) and SSM simulations with PLAXIS v2017.01.

The origin of these differences is not addressed in the present document considering that the main objectives are the comparison of the performance of different constitutive models and testing their capabilities and not a strict comparison with related previous research projects.

3.5.1. Finite Element Model stages

Main stages of the model consisted on:

- Initial phase where model is initialized and initial stresses are generated.
- Construction phase with a duration of 7 months (215 days), from 11/Apr/96 to 10/Nov/96 (CD=0 to CD=215). This stage is a consolidation stage in which the 11ft high levee is activated linearly in time; a new feature available in PLAXIS v.2017.01.
- Consolidation stage of 1925 days, until the 17/Feb/ 02 (CD=216 to CD=2140). This date serves as an average installation date of the Sondex (installed the 6/Feb/02) and inclinometers (installed the 28/Feb/02); i.e., this date is the baseline for Sondex and inclinometers for later comparisons.
- Consolidation stage of 277 days, until the 20/Nov/02 (CD=2141 to CD=2417). This date serves as the last, and also the unique, measurement of Sondex and inclinometers devices; i.e., values obtained from this date are compared to monitoring data using baseline information of CD=2140.

- Consolidation stage of 8543 days (CD=2418 to CD=10960) to complete predictions in a time window of 30 years in 10/Apr/26.

Detailed information of the model phases is included in Table 3-2.

3.5.2. Comparison with field information

In order to be able to compare directly the simulations results against field monitoring data, several points were selected in the mesh to track their results in time. Figure 3-18 presents in detail all the points considered.

General, maximum settlement ($u_{y \max}$) of the levee was obtained from point A ($x=0.0\text{ft}$, $y=-3.0\text{ft}$) and was compared against monitoring information from tracking points P17 and P18.

Maximum horizontal displacement ($u_{x \max}$) was obtained from point B ($x=27.3\text{ft}$, $y=-17.0\text{ft}$). The objective was to determine the ratio ($u_{x \max}/u_{y \max}$) in. The coordinates of point B were calculated as the average of the coordinates were each of the models exhibited the maximum horizontal displacement. SSM, SSCM and MIT-SR maximum horizontal displacement were at the following coordinates: (26.2, -18.4)ft, (27.4, -17.7)ft and (28.3, -15.0)ft, respectively.

Total pore pressures were compared directly against the piezometers measured values. As described in URS (2003) monitoring program, and presented in Figure 3-9 and Figure 3-10, piezometers were located in sections TS3 and TS5 under 3 lines: under the crest (Line 3), toe (Lines 2 and 4') and free field conditions (Lines 1 and 4). The exact location of each of the piezometers were identified and average location were defined to track result in PLAXIS models. The detail of the location of the piezometers in TS3 and TS5 and the specified point in PLAXIS model is detailed in Table 3-7. In Figure 3-18 were presented the points that were considered for the pore pressures comparison and informed results.

3.5.3. MIT-SR calibration for San Francisco Bay Mud

MIT-SR contains parameters that are calibrated separately and with different methodologies. Some parameters can be calculated with equations and laboratory tests while other parameters, including all the state parameters, require the numerical simulation of laboratory tests to later compare the results against real measurements. For this purpose, the point-level laboratory test simulator “Modlab” (originally developed by Kavvas, 1982), adapted by Yuan (2016) to include

MIT-SR model, was utilized. In Modlab, all stresses are normalized by the atmospheric pressure ($p_{atm}=100\text{kPa}$) and therefore, are dimensionless.

The calibration procedure of the MIT-SR for the SFBM was divided in two separate and sequenced stages:

1. Calibration of material parameters with existing laboratory and field data.
2. Determination of state parameters for SFBM layers for the NHPL OCR profile selected with the all the material parameters calibrated.

3.5.3.1. Sources of information for MIT-SR calibration

Main sources of available information to calibrate San Francisco Bay Mud were:

- Germaine (2002 and 2004): An extensive laboratory testing program executed on SFBM samples carried out at MIT facilities. The key information used for the calibration was 7 CRS tests (CRS-430/431/432/435/440/441/443/444) performed on samples from TS3-B1 (i.e., free field conditions) and 5 triaxial tests (CK₀UC-575/584/590 and CK₀UE-576/603) on samples from TS3-B1, TS3-S3 and TS5-B3.
- Nguyen (2006): “Reanalysis of the Settlement of a Levee on Soft Bay Mud”.
- Korchaiyapruk (2007): “Experimental and numerical study of primary consolidation of soft clay”. PhD thesis with 5 IL oedometer tests (Oed-112/113/116/117/122) and 10 CRS tests (CRS-654/656/662/672/674/680/683/686/687/691) on SFBM samples.
- Shear wave velocity, natural water content and total density profiles on Bay Mud from reports on boreholes CCB-25B and CCB-22.
- Yuan (2016): “A new elasto-viscoplastic model for rate dependent behavior of clays”. PhD thesis where the calibration procedures are described.

3.5.3.2. Material parameters

Material parameters were calibrated with the assistance of Dr. Yuan and utilized laboratory triaxial tests data executed at MIT (Germaine, 2002 and Korchaiyapruk, 2007) and field shear wave tests.

The simulation methodology for 1D consolidation, unloading and CK_0UC/E triaxial tests followed the procedure described by Sheahan (1991):

1. A hypothetical sample with initial $K_0=1.0$, $\sigma'_p=100\text{kPa}$ and $OCR=4$ is considered; the isotropic, effective stress state is $\sigma'_v/\sigma'_p = \sigma'_h/\sigma'_p=0.25$ ($\sigma'_p=p_{atm}$). This initial condition is assumed to have negligible creep effects.
2. K_0 -consolidation at a vertical strain rate of $0.10\%/hr$ from the initial stress state to a vertical effective stress $\sigma'_v/p_{atm}=4.0$. At this state, the soil reaches a normally consolidated state.
3. 1D Creep is allowed during a period of 24 hours at a constant effective stress state.

The next stage depends on the type of test simulated:

- For undrained triaxial compression or extension tests, the shearing is displacement-controlled type, where vertical displacements are imposed until reaching critical state. For SFBM, triaxial tests were simulated at strain rates equal to $0.05\%/hr$ according to Nguyen (2006).
- For consolidation tests with $OCR=1.0$ followed by an unloading stage, the 24hr creep stage is followed by an unloading stage where vertical effective stresses are imposed allowing the sample to swell and track stresses and strains.

The detailed procedure for the calibration of each of parameter was:

1. The compressibility in the NC regime (ρ_c) was calculated in 5 IL oedometer tests and 10 CRS tests from Korchaiyapruk (2007) and 6 CRS tests from Germaine (2002). Figure 3-19 presents some of the CRS tests considered whereas Table 3-8 presents all the calculated values of ρ_c . The resulting average of the 21 values obtained was $\rho_c=0.26$ and this value was adopted for the SFBM.
2. From Nguyen (2006): $K_{0NC}=0.47$ and $2G/K=1.13$. K_{0NC} was obtained from the pre-shear stress state in the K_0 -triaxial tests and $2G/K$ result in a Poisson's ratio equal to 0.26 considering equation 2.51.
3. Small strain elastic compressibility (C_b) is obtained from information provided in boreholes CCB-25B and CCB-22. The analysis was concentrated between elevations -10ft to -45ft, elevations corresponding to SFBM in the NHPL project of interest. Field measurements of shear velocity (V_s), moisture content (ω_n) and in-situ total specific weight (γ_t) in depth are

available in borehole CCB-25B whereas borehole CCB-22 only provides measurements of V_s in depth. Assuming a saturated condition and a specific gravity (G_s) for SFBM of 2.70, void ratios are calculated from water content measurements. Additionally, total density (ρ_t) is calculated from the average specific weight and gravity. For the elevations of interest, an average specific weight equal to 100pcf was calculated resulting in a total density of 3.11slug/ft³. Small strain shear stiffness (G_{max}) is calculated from shear wave and total density. Effective stress state is calculated in depth considering the known height of the fill, the specific weight of the fill equal to 130pcf and a $K_0=0.47$, already reported. Finally, small strain elastic compressibility (C_b) is a function of effective stress state (σ'), Poisson's ratio (ν'), void ratio (e) and small strain shear stiffness (G_{max}). Equations utilized for the estimation of this parameter are:

$$e = \omega_n G_s \quad (3.2)$$

$$\frac{2G}{K} = \frac{3(1 - 2\nu')}{1 + \nu'} \quad (3.3)$$

$$G_{max} = \rho_t V_s^2 \quad (3.4)$$

$$C_b = \frac{2}{3} \frac{e}{1 + e} \frac{1 + \nu'}{1 - 2\nu'} \frac{G_{max}/p_{atm}}{(\sigma'/p_{atm})^{1/3}} \quad (3.5)$$

For borehole CCB-25B, all these calculations are straightforward. For borehole CCB-22, considering there is no information on void ratio, they were estimated from borehole CCB-25B based on V_s values measured in CCB-22. Once determined the void ratios, C_b calculations were executed.

Calculated C_b values for CCB-25B varied between 152 and 232 whereas values calculated in CCB-22 ranged between 195 and 253. Measurements and calculated values are included in

Table 3-9 to Table 3-11. The average of all the calculations was 207 and therefore, the selected rounded value was $C_b=210$.

4. D and r parameters are simultaneously calibrated by fitting the unloading stages of several CRS tests: 431/432/435/441/443/444 (Germaine, 2002) and CRS-672/674/686/687/691 (Korchaiyapruk, 2007). As described above, consolidation and unloading simulations

followed Sheahan (1991) procedure. Unloading stage is presented in $\sigma'_v/\sigma'_{v0}-\Delta\varepsilon_v$ and $\sigma'_v/\sigma'_{v0}-\Delta e$ spaces. Stresses are normalized by the last vertical stress before unloading (σ'_{v0}), $\Delta\varepsilon_v$ is the incremental vertical strain and Δe is incremental void ratio. Considering samples that were compressed into NC regime, the initial point of the unloading stage is $\sigma'_v/\sigma'_{v0} = 1$ (OCR=1) and $\Delta\varepsilon_v=\Delta e=0$ and progresses towards lower σ'_v/σ'_{v0} values with positive $\Delta\varepsilon_v$ and Δe due to swelling. The accuracy of the fitting is focused in the range of σ'_v/σ'_{v0} 0.1-1.0 (corresponding to OCR between 1 and 10). Although parameters are calibrated simultaneously, fitting first the r parameter and second the D parameter proved to be efficient: r parameters governs the general trend of the unloading and while D governs the swelling at $\sigma'_v/\sigma'_{v0}<0.5$ approximately. One fact that must be considered during these calibrations is that samples tested in laboratory have different initial void ratios, a condition directly translated to different void ratios prior to unloading. This spreading in the void ratio prior to unloading is also exhibited in the unloading stage when presenting results in the $\sigma'_v/\sigma'_{v0}-\Delta e$ space. Therefore, in this calibration procedure where a unique void ratio can be considered in the hypothetical sample, most of the effort during the fitting procedure was focused in the $\sigma'_v/\sigma'_{v0}-\Delta\varepsilon_v$ space and $\sigma'_v/\sigma'_{v0}-\Delta e$ space was used as a second check. The unloading simulation corresponding to the selected values of $D=0.05$ and $r=1.00$ are illustrated in Figure 3-20.

5. ϕ'_{cs} from the CK₀UC tests with calculated friction angles in 38.7° and 54.0°. An average $\phi'_{cs}=45^\circ$ value was adopted.
6. ϕ'_m , m, w_s and ψ parameters are calibrated by fitting effective stress paths and shear stress strain curves in CK₀UC/E tests (Germaine, 2002) by simulating the consolidation procedure used in tests by Sheahan (1991). Parameters were sequentially calibrated: i) ϕ'_m was calibrated first by fitting the compression curve to the measured shear stress-strain during undrained shearing; ii) m was calibrated by fitting simultaneously the compression and extension curves from the measured effective stress paths; iii) w_s was calibrated by fitting the stiffness in the extension curve in the $\varepsilon_a-(\sigma'_v-\sigma'_v)/2\sigma'_{vc}$ space and iv) ψ was calibrated by refining the fitting of the extension curves in the $(\sigma'_v+\sigma'_v)/2\sigma'_{vc}-(\sigma'_v-\sigma'_v)/2\sigma'_{vc}$. The simulations corresponding to the selected values are presented in Figure 3-21. The selected values are $\phi'_m=29.0^\circ$, $m=0.2$, $w_s=15$ and $\psi=10$.

7. Dilation behavior assumed to be zero, therefore: $D_L=0$. No CK_0UC/E tests with samples with $OCR>2$ available to calibrate this parameter. In addition, this parameter was of little importance for the consolidation and creep cases that were analyzed with FEM models.
8. Compressibility in secondary compression (ρ_α) values were calculated from IL tests from Korchaiyapruk (2007). Each of the 5 tests considered had 4 secondary compression stages. Digitized information of the secondary compression stages are presented in Appendix A. For each of these stages a ρ_α value was calculated (Table 3-12). Values obtained ranged from 0.0080 to 0.0141 with an average ρ_α value of 0.0110. The average value was selected, resulting in a selected ρ_α/ρ_c equal to 0.04 ($\rho_c=0.26$).
9. Reference strain rate ($\dot{\epsilon}_{ref}$) was obtained from IL tests from Korchaiyapruk (2007). Each of the 5 tests considered had 4 secondary compression stages. Digitized information of the secondary compression stages are presented in Appendix A. In those stages where the duration was longer than 1 day, the reference strain rate ($\dot{\epsilon}_{ref}$) was determined as the strain rate at 1 day (Table 3-13). Values obtained ranged from 1.6E-4%/min to 3.8E-4%/min with an average value of 2.5E-4%/min; a $\dot{\epsilon}_{ref}=2.5E-4\%/min$ ($=4.1E-8 \text{ sec}^{-1}= 3.6E-3 \text{ day}^{-1}$) was selected.
10. Rate-sensitivity of steady state of R_a (β) was calculated from CRS tests from Korchaiyapruk (2007); some CRS tests were not considered due to the existence of induced, elevated pore pressure which reduced effective stresses making their result not comparable to the considered tests with low pore pressure. Base information are CRS tests in the $\sigma'_v - e$ space (digitized information of the secondary compression stages are presented in Appendix A), each with a different strain rate ($\dot{\epsilon}$). For different void ratios that correspond to the NC regime exhibited in the CRS tests, the corresponding σ'_v level for that strain rate is identified. This information is replotted in a $\dot{\epsilon} - \sigma'_v$ space where it is illustrated the different levels of effective vertical stress for each void ratio, depending on the strain rate imposed in the test (Figure 3-22). For each void ratio, the slope of the fitting line is a potential value of β . Considering that at higher strain rates, higher effective stresses for the same level of void ratio are expected, the slope of the fitting line is expected to be positive. The scatter and quality of data strongly conditioned the selection of a β value; certain slopes were negative. By fitting 6 tests (CRS-654/662/672/ 686/687/691) for void ratio values

between 1.6 and 2.0 (where most of the tests exhibited NC behavior), the average slope after discarding negative values was $\beta=0.051$. All the considered information regarding void ratios, stress levels and calculated slopes is included in Table 3-14. Considering that MIT-SR was developed under the assumption that β should generally lie in the range of 0 to ρ_α/ρ_c (already calibrated and selected $\rho_\alpha/\rho_c=0.040$), the current analyses assume a $\beta=0.040$.

11. There was no information to calibrate the non-linear variation of rate dependency with stress history (β_2) and the reduction of creep rate during unloading parameter (β_3). Therefore, values calibrated by Yuan (2016) for Salt Lake City were considered. The selected values are $\beta_2=6.8$ and $\beta_3=19.0$. These two parameters (β_2 and β_3) were calibrated for Singapore Marine Clay; the detailed procedure is presented in Chapter 4.

3.5.3.3. State parameters

MIT-SR is a rate-dependent model and strain rate effects are defined by state variables which depend on the stress history of the soil. To accurately describe creep phenomena, it is critical the methodology utilized to define and specify initial state variables.

The OCRs considered for the SFBM were 3.10, 2.05, 1.70, 1.60, 1.55, 1.50 and 1.45 and the simulation methodology followed the procedure described by Sheahan (1991):

1. A hypothetical sample with initial $K_0=1.0$, $\sigma'_p=100\text{kPa}$ and $\text{OCR}=4$ is considered; the isotropic, effective stress state is $\sigma'_v/\sigma'_p = \sigma'_h/\sigma'_p=0.25$ ($\sigma'_p=p_{\text{atm}}$). This initial condition is assumed to have negligible creep effects.
2. K_0 -consolidation at a vertical strain rate of 0.10%/hr from the initial stress state to a vertical effective stress $\sigma'_v/p_{\text{atm}}=4.0$. At this state, the soil reaches a normally consolidated state.
3. 1D Creep is allowed during a period of 24 hours at a constant effective stress state.
4. Unloading at a 0.05%/hr rate to a certain vertical effective stress to materialize the pretended OCR in the sample; e.g., final $\sigma'_v/p_{\text{atm}}=1.29$ for an $\text{OCR}=3.10$.
5. 1D Creep is allowed during a period of 20 years hours at a constant effective stress state. State parameters were obtained at the end of this stage. For longer periods of time, there were no visible differences in the state variables obtained; 20 years was a period long enough to simulate field conditions of the soil.

Table 3-5 provides detailed information on the state parameters obtained for the SFBM for each OCR.

3.5.4. Soft Soil Creep Model for San Francisco Bay Mud

In order to model SFBM behavior with a constitutive model with lower complexity and still consider creep phenomena, Soft Soil Creep Model was considered as a third, intermediate case between SSM with a reduced OCR profile and MIT-SR with original OCR profile and 5 creep parameters.

This model contains the original framework of SSM and includes an additional parameter (μ^*) that allows to consider creep phenomena:

$$\lambda^* = \frac{C_c}{2.3 (1 + e_0)} \quad (3.6)$$

$$\kappa^* = \frac{2 C_s}{2.3 (1 + e_0)} \quad (3.7)$$

$$\mu^* = \frac{C_\alpha}{2.3 (1 + e_0)} \quad (3.8)$$

Where C_α is the coefficient of secondary compression and e_0 is the initial void ratio considered. As stated in the previous section with SFBM calibration parameters, the ratio $\rho_\alpha/\rho_c = 0.04$ was adopted. Considering $\rho_\alpha/\rho_c = C_\alpha/C_c$, then $C_\alpha/C_c = 0.04$. From Nguyen (2006), $\lambda^* = 0.174$ and $e_0 = 2.5$ which results in $C_c = 1.401$. Then $C_\alpha = 0.056$ and the parameter $\mu^* = 0.007$.

Last but not least, by considering creep phenomena in the model, it not required to reduce the preconsolidation profile of the soil. Therefore, simulations with SSCM consider the original OCR profile, same situation as the described in simulations with MIT-SR.

Considering $K_0^{NC} = 0.47$ and $m = 0.35$ (Nguyen, 2006), then K_0^{OC} is calculated as:

$$K_0^{OC} = K_0^{NC} OCR^m \quad (3.9)$$

3.6. SIMULATION OF SETTLEMENTS DUE TO LEVEE CONSTRUCTION

Figure 3-23 to Figure 3-32 present the results for the SSM, MIT-SR and SSCM models simulations and compare them against monitoring data. Where required, total and post-construction values are plotted separately to evidence the different behavior during the undrained and consolidation stage of the problem. Contour plots of vertical and horizontal displacements as well as active and excess pore pressures were obtained from PLAXIS and are included in Appendix A.

Figure 3-23 present the maximum vertical settlement versus time, from the beginning of the construction of the levee (April/1996) until 30 years later (April/2026); post-construction settlement is plotted separately to enable the comparison of consolidation behavior separately.

The models predict very different long-term settlement responses (April/2026): 3.47ft (SSM), 4.91ft (SSCM) and 3.07ft (MIT-SR). SSM and MIT-SR converge to long-term response while SSCM continues to exhibit increment in settlement due to creep.

There are large discrepancies in the models predictions during the levee construction phase. MIT-SR predicted at the end of construction a settlement of 0.51m while SSM and SSCM predicted settlements equal to 1.49 and 1.54ft, respectively. These additional discrepancies reflect the differences in the modelling of the undrained shear behavior of the models. Unfortunately there are no data to validate which is more accurate.

The computed post-construction settlements were compared directly against measured data. Again, the models predict very different long-term, post-construction settlement responses (April/2026): 1.98ft (SSM), 3.37ft (SSCM) and 2.57ft (MIT-SR).

By analyzing the total response, SSM and SSCM exhibit their limitations to match undrained and consolidation stages with a unique set of parameters. Both cases had parameters originally calibrated by Nguyen (2006) for the SSM to match the consolidation phase and accurately predict the monitored settlements (Points P17 and P18). On the other hand, MIT-SR, with a unique parameter set and an ex-ante calibration procedure that did not consider any NHPL site measurement, perfectly matches the monitored settlements in the post-construction curve. It was not possible to compare MIT-SR prediction of total settlement from the beginning of the construction since no information was available.

In addition, when comparing long term prediction between MIT-SR and SSCM, it can be observed that SSCM consider a constant creep deformation in the long term while MIT-SR creep rate is reduced. This condition limits the predictive capacity of a model since it strongly depends on the time window considered whereas if using MIT-SR, creep rate evolves and eventually reaches a zero condition.

Maximum horizontal displacement and the ratio between maximum horizontal displacement and vertical settlement were included in Figure 3-24 and Figure 3-25, respectively. These figures were the best examples of the SSM and SSCM limitations to predict undrained and consolidation behavior. Both models were directly conditioned by displacements calculated during construction stage. SSM and SSCM models predicted at the end of construction maximum horizontal displacements of 0.70ft. These differences were also observed in the ratio (u_{xB}/u_{yA}). If considering total values, at the end of construction SSM and SSCM predicted relations around 0.45 that later decayed to values between 0.20 and 0.25. If considering only the post-construction phase, then these ratios were mostly between 0.07 and 0.10. It must be noted that SSCM ratio keeps increasing which would be explained only if the creep considered generated a horizontal displacement rate higher than the vertical settlement rate.

On the other hand, MIT-SR can correctly track the continuous increment of horizontal displacement due to construction and consolidation progression and therefore, the ratio u_{xB}/u_{yA} can correctly be tracked even during construction. MIT-SR simulation predicted after at the end of construction a u_{xB} of 0.1ft (in contrast to 0.7ft from SSM and SSCM) and a u_{xB}/u_{yA} ratio of 0.20 which later decreased and settled at a value of 0.174. These values did not present considerable differences when analyzing the post-construction deformations separately and settled at a value of 0.168.

Empirical data by Ladd (1991) showed that $u_{xB}/u_{yA} \sim 0.20$ are normal while higher ratios are abnormal for most embankments. MIT-SR was able to track these displacements and provide a ratio around this reference value while SSM and SSCM exhibited their limitations and their ratios directly depended on whether the deformations during construction were considered or not.

Total pore pressures from the monitoring program were compared against models predictions (Figure 3-26 to Figure 3-29). As already stated in Table 3.18, PLAXIS points were specifically selected at the same locations of the piezometers to make a straightforward comparison. There is

a general trend: SSCM predicts the higher pore pressures, followed by SSM and MIT-SR always predicted the lowest pore pressures. SSM and MIT-SR predictions were very similar, only slight differences were present in the centerline of the levee. SSM and MIT-SR predictions match closely piezometer measurements.

Last but not least, when comparing vertical settlement and horizontal displacements between Feb/02 and Nov/02 (installation date and unique reading, respectively) against site measurements, all models performed similarly (Figure 3-30 to Figure 3-32). It must be noted the limitations of these comparison considering the small amount of time (277 days) and the existence of a unique set of values to compare with.

The information provided by the vertical settlement (Figure 3-23), horizontal displacement (Figure 3-24), their ratio (Figure 3-25) and total pore pressure (Figure 3-26 to Figure 3-29) proved to be the most important elements to exhibit the robustness and consistency of the calibration methodology and MIT-SR predictive capabilities. Obtained results with MIT-SR correctly matched monitored information without any parametric refinement of original calibrations and a unique set of parameters can be utilized for the complete representation of the loading and consolidation process of the SFBM under the levee.

Table 3-1: Parameters considered in D4 case (Nguyen, 2006).

Top EL.	[ft]	9.4	-1.6	-1.6	-4.5	-6.2	-10	-20	-41.5
Bottom EL.	[ft]	-1.6	-4.5	-4.5	-6.2	-10	-20	-41.5	-60
Soil layer	[-]	Levee Fill	Pav.	Cracked Pav.	Base Course	Bay Mud Crust	Bay Mud 1	Bay Mud 2	Alluvium
Soil Model	[-]	MC	MC	MC	MC	SSM	SSM	SSM	Linear Elastic
Type	[-]	Drained	Drained	Drained	Drained	Undrained	Undrained	Undrained	Undrained
γ_t	[pcf]	130	150	150	145	99.8	92.7	92.7	130
e_o	[-]	-	-	-	-	2.5	2.5	2.5	-
ν_{ur}	[-]	0.3	0.15	0.2	0.2	0.26	0.26	0.26	0.3
E_{ref}	[ksf]	30	1000	200	200	-	-	-	1000
c'	[ksf]	0.02	0.02	0.025	0.025	0.025	0.025	0.025	-
ϕ'	[°]	37	35	35	35	25	25	25	-
ψ'	[°]	0	5	2	2	0	0	0	-
K_{0NC}	[-]	0.5	0.5	0.5	0.5	0.47	0.47	0.47	0.7
M	[-]	-	-	-	-	1.693	1.693	1.55	-
λ^*	[-]	-	-	-	-	0.174 (CR=0.40)	0.174 (CR=0.40)	0.174 (CR=0.40)	-
κ^*	[-]	-	-	-	-	0.035 (RR=0.04)	0.035 (RR=0.04)	0.07 (RR=0.08)	-
k_{vo}, k_{ho}	[ft/day]	0.1	1.0	1.0	1.0	0.005	4E-4; 8E-4	4E-4; 8E-4	0.005
C_k	[-]	''	''	''	''	1.143	1.143	1.143	-

Table 3-2: Stages considered in the NHPL PLAXIS 2D simulation.

Stage name	Stage type	Date, start	Date, finish	Δt	CD	H_{Levee}
[-]	[-]	[-]	[-]	[day]	[day]	[ft]
S00-CD=0 (11/04/1996)	Consolidation	11/04/1996	11/04/1996	0	0	0
S01-CD=215 (11/11/1996)	Consolidation	11/04/1996	10/11/1996	215	215	0 to 11
S02-CD=2140 (17/02/2002)	Consolidation	11/11/1996	17/02/2002	1925	2140	11
S03-CD=2417 (20/11/2002)	Consolidation	18/02/2002	20/11/2002	277	2417	11
S04-CD=10960 (10/04/2026)	Consolidation	21/11/2002	10/04/2026	8543	10960	11

Table 3-3: Material parameters for NHPL PLAXIS 2D simulation..

From EL.	[ft]	9.4	-1.6	-4.5	-6.2	-10	-41.5
To EL.	[ft]	-1.6	-4.5	-6.2	-10	-41.5	-60
Soil layer	[-]	Levee Fill	Cracked Pavement	Base Course	Bay Mud Crust	SFBM	Alluvium
Soil Model	[-]	MC	MC	MC	SSM	MIT-SR Model	Linear Elastic
Type	[-]	Drained	Drained	Drained	Undrained		Undrained
γ_t	[pcf]	130	150	145	100		130
e_0	[-]	-	-	-	2.5		-
v_{ur}	[-]	0.3	0.2	0.2	0.26		0.3
E_{ref}	[ksf]	30	200	200	-		1000
c'	[ksf]	0.02	0.025	0.025	0.025		-
ϕ'	[°]	37	35	35	25		-
ψ'	[°]	0	2	2	0		-
K_{0NC}	[-]	0.5	0.5	0.5	0.47		0.7
M	[-]	-	-	-	1.693		-
λ^*	[-]	-	-	-	0.174		-
κ^*	[-]	-	-	-	0.035		-
k_{vo}, k_{ho}	[ft/day]	0.1	1.0	1.0	0.005		0.005
C_k	[-]	0.1	1.0	1.0	1.143		-

Table 3-4: SFBM MIT-SR material parameters for NHPL PLAXIS 2D simulation.

Symbols	Values	Used Data of SFBM	Reference	
ρ_c	0.26	LCC curves from CRS and oedometer tests	Nguyen (2006), Korchaiyapruk (2007)	
K_{0NC}	0.47	Preshear stress states of triaxial tests		
C_b	210	Field shear wave velocity tests		
$2G/K$	1.13	- (Inferred from data of RBBC)		
D	0.05	1D swelling curves from CRS tests		
r	1.0			
w_s	15	Degradation of shear stiffness of triaxial tests		
ϕ'_{cs}	45°	Shear stress at large strain in triaxial compression tests		
ϕ'_m	29	Effective stress paths for triaxial compression/extension tests		
m	0.2			
ψ	10			
D_L	0.0	- (Inferred from data of RBBC)		
ρ_α/ρ_c	0.04	Secondary compression of oedometer tests		Korchaiyapruk (2007)
β	0.04	CRS tests		
$\dot{\epsilon}_{ref}$	4.2x10 ⁻⁸ /sec	Strain rate at 24hr of consolidation in oedometer tests		
β_2	6.8	- (Inferred from data of SLC clay)		
β_3	19	- (Inferred from data of SLC clay)		

Table 3-5: SFBM MIT-SR state parameters for NHPL PLAXIS 2D simulation.

State Par.	Unit	OCR=3.10	OCR=2.05	OCR=1.70	OCR=1.60	OCR=1.55	OCR=1.50	OCR=1.45
p_{atm}	[kPa]	101	101	101	101	101	101	101
α' / σ'	[-]	2.288	1.753	1.553	1.495	1.467	1.438	1.412
e_0	[-]	1.763	1.750	1.744	1.740	1.738	1.735	1.731
b_0	[-]	0.734	0.735	0.735	0.735	0.736	0.736	0.736
b_1	[-]	1.531	1.531	1.530	1.529	1.529	1.529	1.528
b_2	[-]	0.734	0.735	0.735	0.735	0.736	0.736	0.736
b_3	[-]	0	0	0	0	0	0	0
b_4	[-]	0	0	0	0	0	0	0
b_5	[-]	0	0	0	0	0	0	0
σ^h / σ'	[-]	1.285	1.035	0.903	0.859	0.838	0.814	0.792
η^{h_0}	[-]	0.851	0.775	0.763	0.761	0.760	0.759	0.757
η^{h_1}	[-]	1.297	1.450	1.474	1.478	1.480	1.483	1.486
η^{h_2}	[-]	0.851	0.775	0.763	0.761	0.760	0.759	0.757
η^{h_3}	[-]	0	0	0	0	0	0	0
η^{h_4}	[-]	0	0	0	0	0	0	0
η^{h_5}	[-]	0	0	0	0	0	0	0
R_{a0}	[1/day]	5.6E-09	1.5E-07	2.7E-07	3.2E-07	3.5E-07	3.9E-07	4.3E-07

Table 3-6: SFBM Layers, OCR and K_0 considered in NHPL PLAXIS 2D simulation.

Top EL.	Bottom EL.	OCR	K_0	OCR	K_0	OCR	K_0
[ft]	[ft]	[-]	[-]	[-]	[-]	[-]	[-]
-10	-12	2.379	0.637	3.1	Initial state variables	3.1	0.70
-12	-15	1.577	0.551	2.05		2.05	0.60
-15	-20	1.341	0.521	1.7		1.7	0.57
-20	-25	1.278	0.512	1.6		1.6	0.55
-25	-30	1.231	0.505	1.55		1.55	0.55
-30	-35	1.192	0.500	1.5		1.5	0.54
-35	-40	1.164	0.496	1.45		1.45	0.54
-40	-41.5	1.147	0.493				

Table 3-7: Piezometers in TS3 and TS5 and PLAXIS points to compare pore pressures.

Line	TS3 Piezometers				TS5 Piezometers				PLAXIS points		
	Name	Layer	X [ft]	Y [ft]	Name	Layer	X [ft]	Y [ft]	Point	X [ft]	Y [ft]
Centerline	TS3P3-1	BMC-BM	3.0	-10.1	TS5P3-1	BMC-BM	0.0	-11.6	C	0.0	-11.0
	TS3P3-2	BM	3.0	-17.1	TS5P3-2	BM	0.0	-17.6	D	0.0	-17.5
	TS3P3-3	BM	3.0	-24.1	TS5P3-3	BM	0.0	-24.1	E	0.0	-24.0
	TS3P3-4	BM	3.0	-31.1	TS5P3-4	BM	0.0	-30.6	F	0.0	-30.9
	TS3P3-5	BM	3.0	-38.1	TS5P3-5	BM	0.0	-36.6	G	0.0	-37.4
	TS3P3-6	BM	3.0	-45.1	TS5P3-6	OA	0.0	-43.1	H	0.0	-44.0
Toe Line	TS3P2-1	BMC-BM	57.0	-10.8	TS5P2-1	BMC-BM	51.5	-9.8	I	54.3	-11.0
	TS3P2-2	BM	57.0	-17.8	TS5P2-2	BM	51.5	-17.8	J	54.3	-17.8
	TS3P2-3	BM	57.0	-24.8	TS5P2-3	BM	51.5	-26.3	K	54.3	-25.6
	TS3P2-4	BM	57.0	-32.8	TS5P2-4	BM	51.5	-34.3	L	54.3	-33.6
	TS3P2-5	OA	57.0	-39.8	TS5P2-5	OA	51.5	-41.8	M	54.3	-40.0
Toe Line	TS3P4-1	BMC-BM	65.0	-10.1	-	-	-	-	N	65.0	-10.0
	TS3P4-2	BM	65.0	-19.1	-	-	-	-	O	65.0	-19.1
	TS3P4-3	BM	65.0	-27.1	-	-	-	-	P	65.0	-27.1
	TS3P4-4	BM	65.0	-35.9	-	-	-	-	Q	65.0	-36.0
Free Field	TS3P1-1	BM	80.0	-13.5	TS5P1-1A	BMC-BM	76.5	-11.5	R	78.3	-12.5
	TS3P1-2	BM	80.0	-23.5	TS5P1-1	BM	76.5	-20	S	78.3	-21.8
	TS3P1-3	BM	80.0	-33.5	TS5P1-2	BM	76.5	-35	T	78.3	-34.3
	TS3P1-4	OA	80.0	-44.5	TS5P1-3A	BM	76.5	-40	-	-	-
	-	-	-	-13.5	TS5P1-3	OA	76.5	-46.5	-	-	-

Table 3-8: Compressibility in the NC regime (ρ_c).

Germaine (2002)		Korchaiyapruk (2007)			
CRS	ρ_c	CRS	ρ_c	Oed.	ρ_c
[-]	[-]	[-]	[-]	[-]	[-]
CRS-441	0.301	CRS-654	0.252	Oed-112	0.291
CRS-432	0.270	CRS-656	0.214	Oed-113	0.280
CRS-431	0.319	CRS-662	0.204	Oed-116	0.244
CRS-435	0.324	CRS-672	0.251	Oed-117	0.249
CRS-443	0.243	CRS-674	0.255	Oed-122	0.304
CRS-440	0.274	CRS-680	0.276	-	-
-	-	CRS-683	0.264	-	-
-	-	CRS-686	0.246	-	-
-	-	CRS-687	0.259	-	-
-	-	CRS-691	0.242	-	-

Table 3-9: Borehole CCB-25B: Total specific weight, moisture content and void ratios.

EL	Depth	γ_t	ω	e
[ft]	[ft]	[pcf]	[-]	[-]
-9.9	18.0	109.3	0.47	1.27
-13.0	21.1	90.6	0.78	2.31
-16.3	24.4	99.7	0.66	1.81
-17.8	25.9	95.5	0.80	2.18
-21.5	29.6	100.7	0.66	1.78
-23.8	31.9	97.3	0.80	2.12
-24.4	32.5	91.6	0.90	2.50
-28.7	36.8	94.1	0.76	2.15
-28.7	36.8	98.8	0.70	1.90
-28.9	37.0	104.8	0.61	1.59
-30.0	38.1	107.8	0.60	1.50
-35.9	44.0	101.7	0.60	1.65
-39.9	48.0	99.7	0.64	1.77
-42.4	50.5	104.5	0.63	1.63

Table 3-10: Boreholes CCB-25B & CCB-22: V_s measurements and G_{max} calculated.

CCB-25B				CCB-22			
EL	Depth	V_s	G_{max}	EL	Depth	V_s	G_{max}
[ft]	[ft]	[ft/sec]	[psf]	[ft]	[ft]	[ft/sec]	[psf]
-19.5	27.6	367.7	420200	-15.4	25.8	350.4	381700
-21.8	29.9	344.7	369300	-18.2	28.6	392.4	478500
-24.2	32.3	324.9	328000	-19.5	29.9	375.1	437300
-26.1	34.2	348.6	377700	-22.7	33.1	373.2	432900
-28.3	36.4	321.2	320600	-25.2	35.6	378.2	444600
-30.6	38.7	349.6	380000	-25.9	36.3	400.2	497700
-32.4	40.5	350.8	382400	-28.1	38.5	403.2	505400
-34.2	42.3	328.7	335800	-29.3	39.7	375.8	439000
-35.7	43.8	355.2	392200	-30.1	40.5	409.9	522100

-37.7	45.8	371.7	429400
-40.3	48.4	394.3	483100
-41.3	49.4	367.3	419400
-43.2	51.3	400.6	498700
-44.6	52.7	379.9	448500

-32.3	42.7	417.1	540800
-33.8	44.2	393.2	480591

Table 3-11: Small strain elastic compressibility (C_b) calibration.

Borehole	EL.	Depth	σ'_{v0}	σ'	e	G_{max}	C_b
[-]	[-]	[ft]	[psf]	[psf]	[-]	[psf]	[-]
CCB-25B	-19.5	27.6	3357	2171	1.99	420216	232
CCB-25B	-21.8	29.9	3589	2321	1.82	369280	193
CCB-25B	-24.2	32.3	3826	2474	2.33	328015	182
CCB-25B	-26.1	34.2	4023	2602	2.36	377738	207
CCB-25B	-28.3	36.4	4235	2739	2.19	320601	169
CCB-25B	-30.6	38.7	4474	2893	1.52	379970	173
CCB-25B	-32.4	40.5	4647	3005	1.56	382449	173
CCB-25B	-34.2	42.3	4831	3124	1.61	335836	152
CCB-25B	-35.7	43.8	4977	3218	1.64	392239	177
CCB-25B	-37.7	45.8	5179	3349	1.70	429435	194
CCB-25B	-40.3	48.4	5438	3517	1.75	483130	217
CCB-25B	-41.3	49.4	5536	3580	1.69	419397	185
CCB-25B	-43.2	51.3	5731	3706	1.67	498707	216
CCB-25B	-44.6	52.7	5866	3794	1.73	448484	196
CCB-22	-15.4	25.8	3276	2119	1.55	381719	194
CCB-22	-18.2	28.6	3555	2299	1.82	478479	251
CCB-22	-19.5	29.9	3693	2388	1.71	437271	222
CCB-22	-22.7	33.1	4012	2595	1.71	432897	213
CCB-22	-25.2	35.6	4263	2757	1.72	444591	215
CCB-22	-25.9	36.3	4326	2797	1.81	497738	244
CCB-22	-28.1	38.5	4549	2941	1.81	505394	244
CCB-22	-29.3	39.7	4669	3019	1.71	438953	206
CCB-22	-30.1	40.5	4747	3070	1.81	522113	248
CCB-22	-32.3	42.7	4970	3214	1.80	540794	253
CCB-22	-33.8	44.2	5121	3311	1.82	480591	223
						Average	207

Table 3-12: Oedometer tests – Calculated values of secondary compression (ρ_α).

Stage	Oed 112	Oed 113	Oed 116	Oed 117	Oed 122	Average
1-2ksc	0.0119	0.0141	0.0097	0.0090	0.0093	0.0108
2-4ksc	0.0108	0.0092	0.0113	0.0107	0.0118	0.0108
4-8ksc	0.0132	0.0132	0.0080	0.0083	0.0116	0.0109
8-16ksc	0.0118	0.0108	0.0097	0.0105	0.0141	0.0114
Average	0.0119	0.0118	0.0096	0.0096	0.0117	0.0110

Table 3-13: Oedometer tests – Calculated values of reference strain rate ($\dot{\epsilon}_{ref}$, [%/min]).

Stage	Oed 112	Oed 113	Oed 116	Oed 117	Oed 122	Average
1-2ksc	N/A	N/A	3.0E-04	3.8E-04	2.0E-04	3.0E-04
2-4ksc	3.5E-04	2.5E-04	N/A	N/A	N/A	3.0E-04
4-8ksc	N/A	N/A	2.1E-04	1.6E-04	N/A	1.9E-04
8-16ksc	1.9E-04	1.8E-04	N/A	N/A	N/A	1.8E-04
Average	2.7E-04	2.1E-04	2.6E-04	2.7E-04	2.0E-04	2.5E-04

Table 3-14: CRS tests, effective vertical stresses and void ratios and calculated β values.

CRS Test	654	662	672	672	672	686	687	691	691	691	β
$\dot{\epsilon}$ [%/hr]	0.09	0.09	0.10	0.75	1.50	3.00	1.45	0.75	1.50	3.00	
e	σ'_v	σ'_v	σ'_v	σ'_v	σ'_v	σ'_v	σ'_v	σ'_v	σ'_v	σ'_v	
[-]	[ksc]	[ksc]	[ksc]	[ksc]	[ksc]	[ksc]	[ksc]	[ksc]	[ksc]	[ksc]	[-]
2.00	1.49					1.30	1.60	1.58	1.64	1.72	0.006
1.90	1.83		1.49	1.64	1.70	1.60	1.95	1.97	2.05	2.13	0.038
1.80	2.24		1.85	2.04	2.10	1.99	2.42	2.47	2.55	2.66	0.040
1.70	2.75		2.35	2.59	2.67	2.51	3.06	3.15	3.25	3.39	0.045
1.60	2.74	1.86	3.05	3.36	3.45	3.26	3.53	4.05	4.07	4.10	0.125
1.50	2.57	1.74	3.28	3.53	3.95	4.27	3.31	3.83	3.84	3.85	0.150

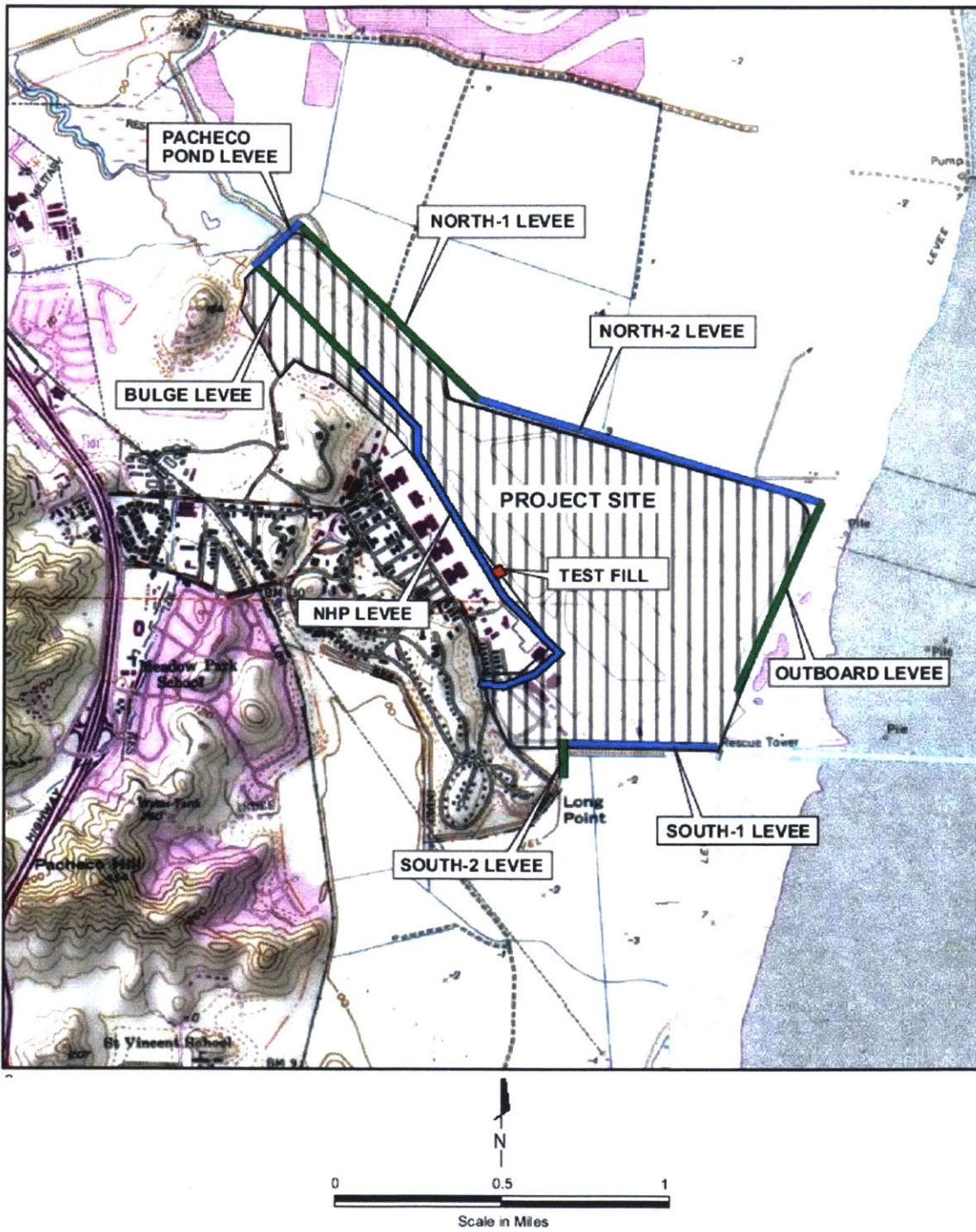


Figure 3-1: Location of the Hamilton Wetland Restoration Project (URS, 2003).

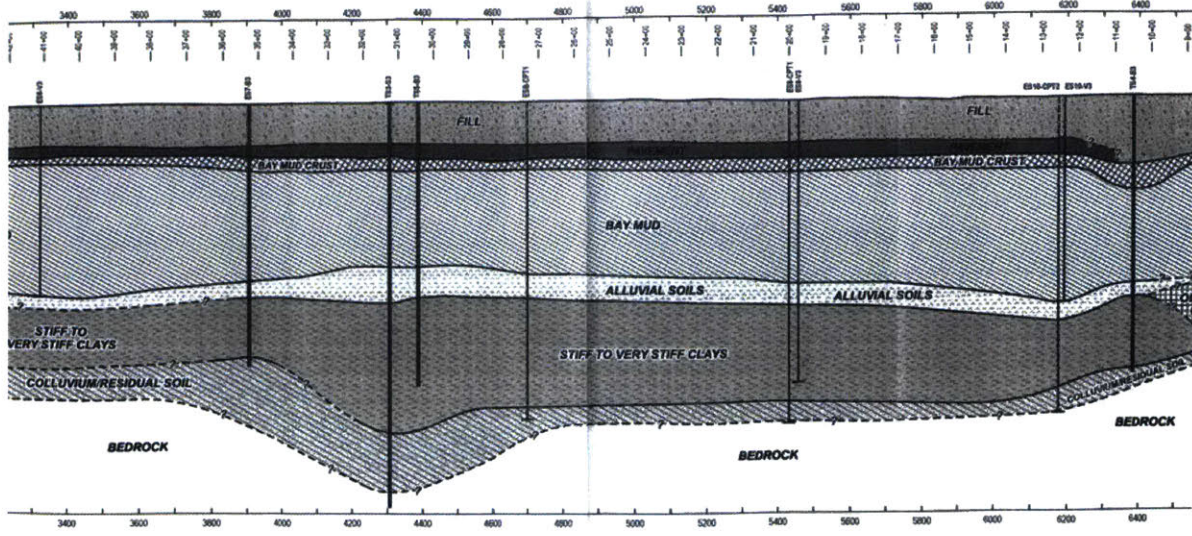


Figure 3-2: Longitudinal subsurface section along the NHPL (URS, 2003).

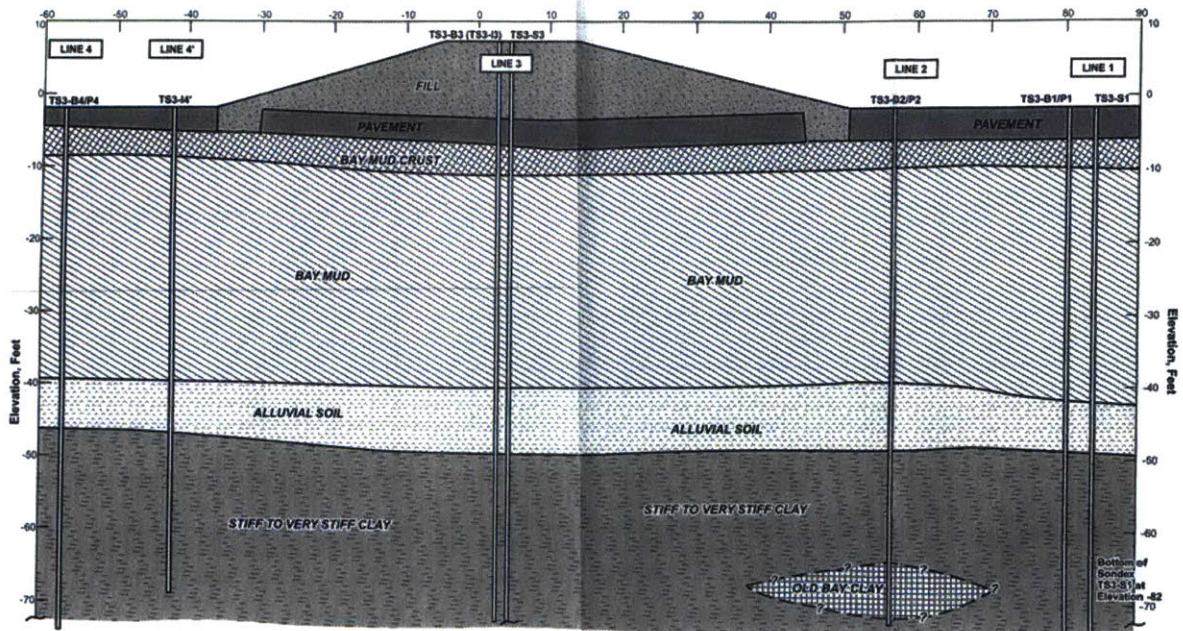


Figure 3-3: Typical transverse section and stratigraphy along NHPL (URS, 2003).

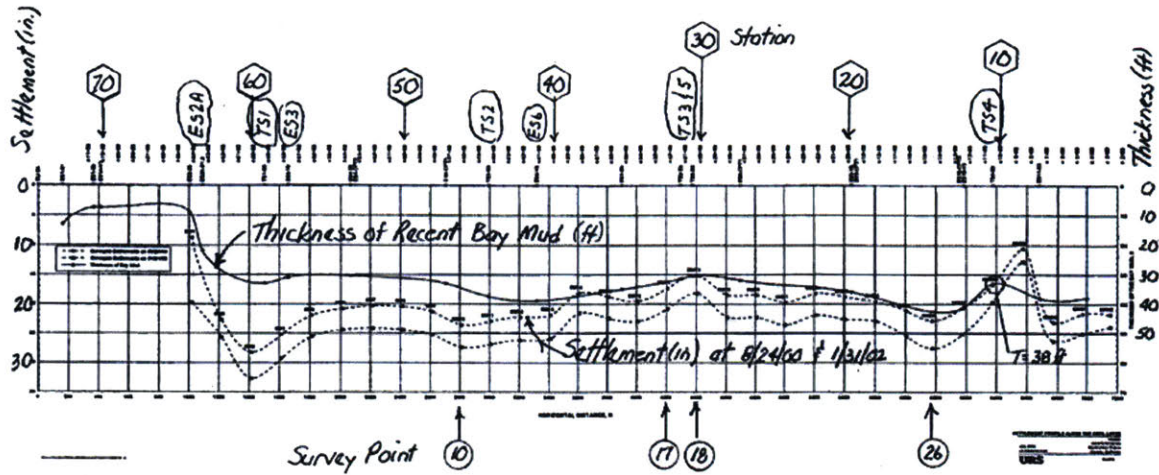


Figure 3-4: Novato City monitoring program (URS, 2003 and Ladd, 2002).

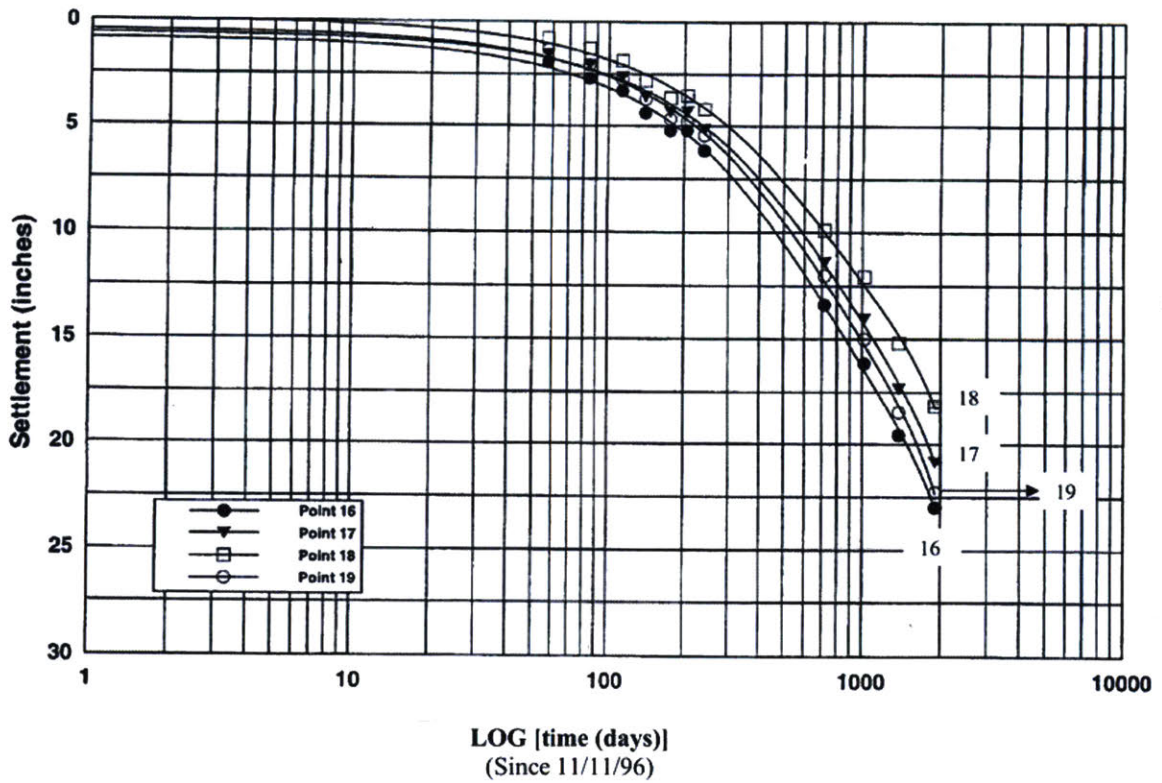


Figure 3-5: Settlement vs. Time at points 16 to 19, near TS3 and TS5 (URS, 2003).

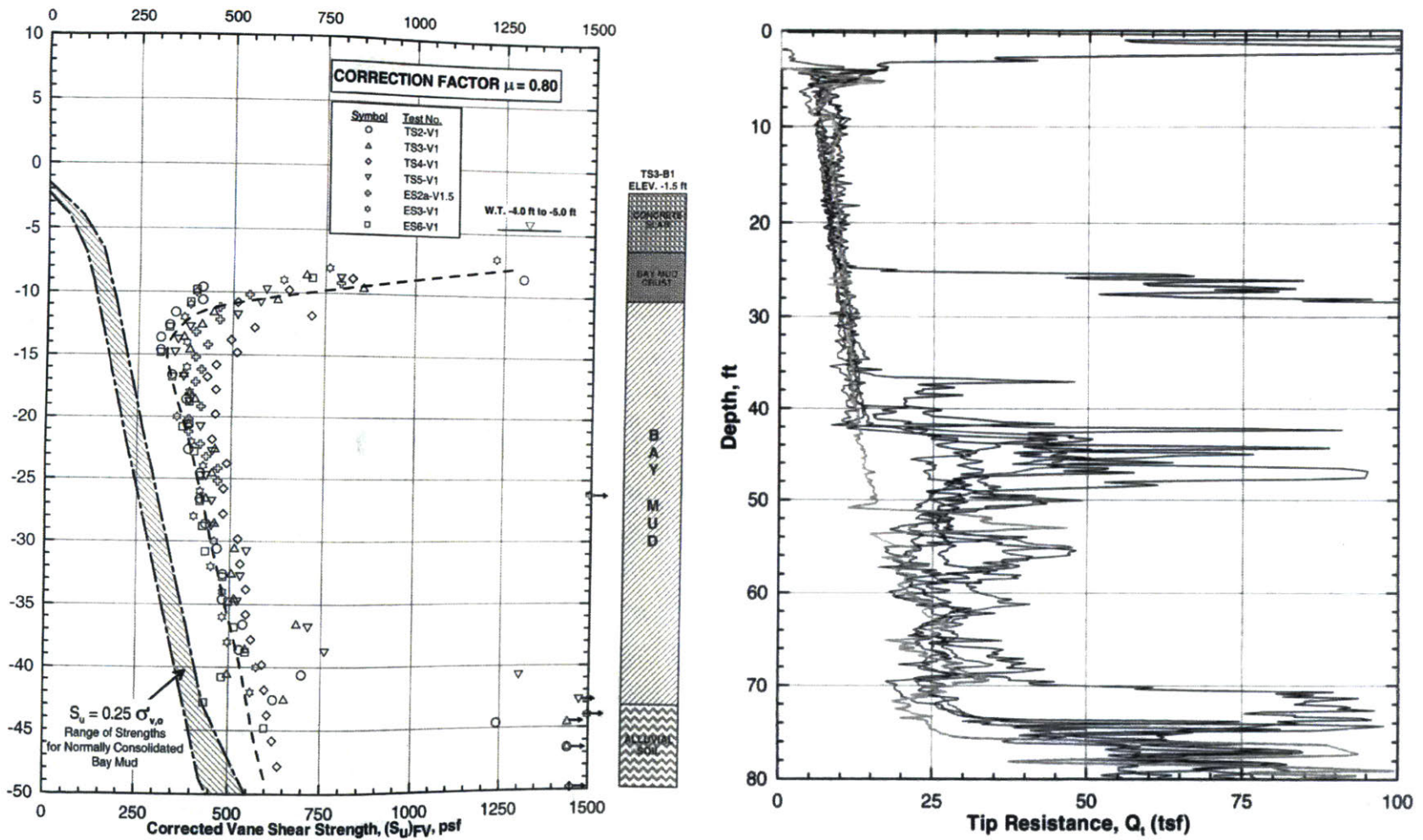


Figure 3-6: Corrected vane shear strength from FVT (left) and tip resistance from CPT (right) vs. Elevation (URS, 2003).

FIELD VANE CORRECTION FACTOR = 0.8

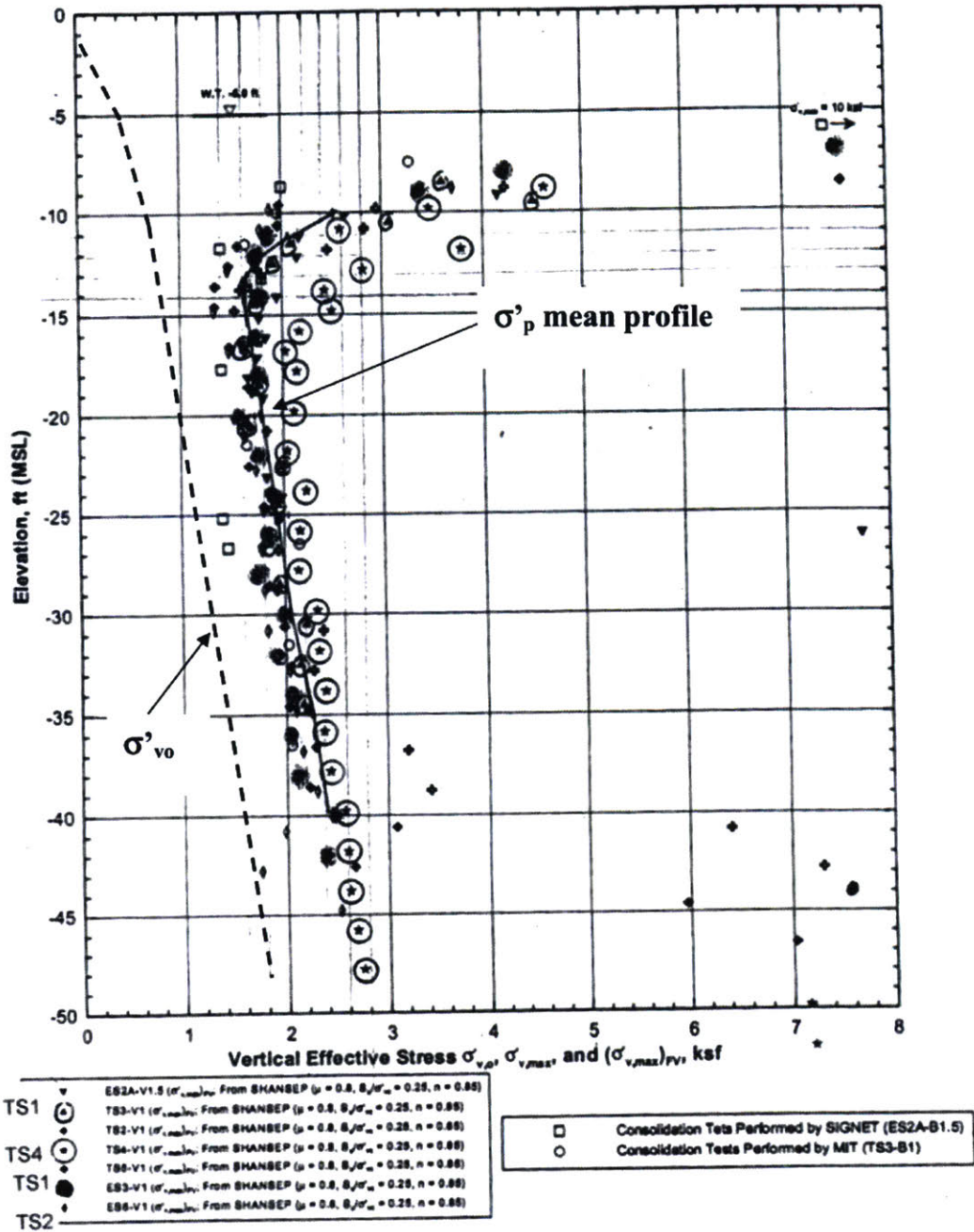


Figure 3-7: Summary of NHPL free field σ'_p from FVT ($\mu = 0.8$) and laboratory tests (URS, 2003 and Ladd, 2002).



Figure 3-8: Test section area with borings, field tests and instrumentation (URS, 2003).

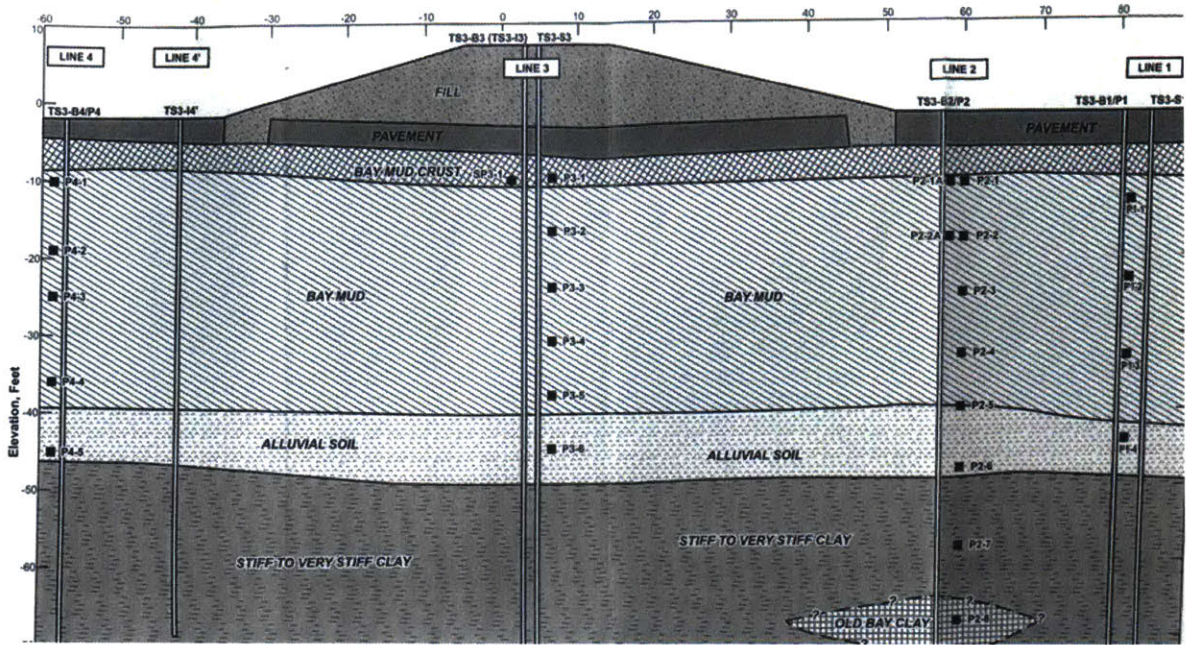


Figure 3-9: Layout of installed instruments in TS3 (URS, 2003).

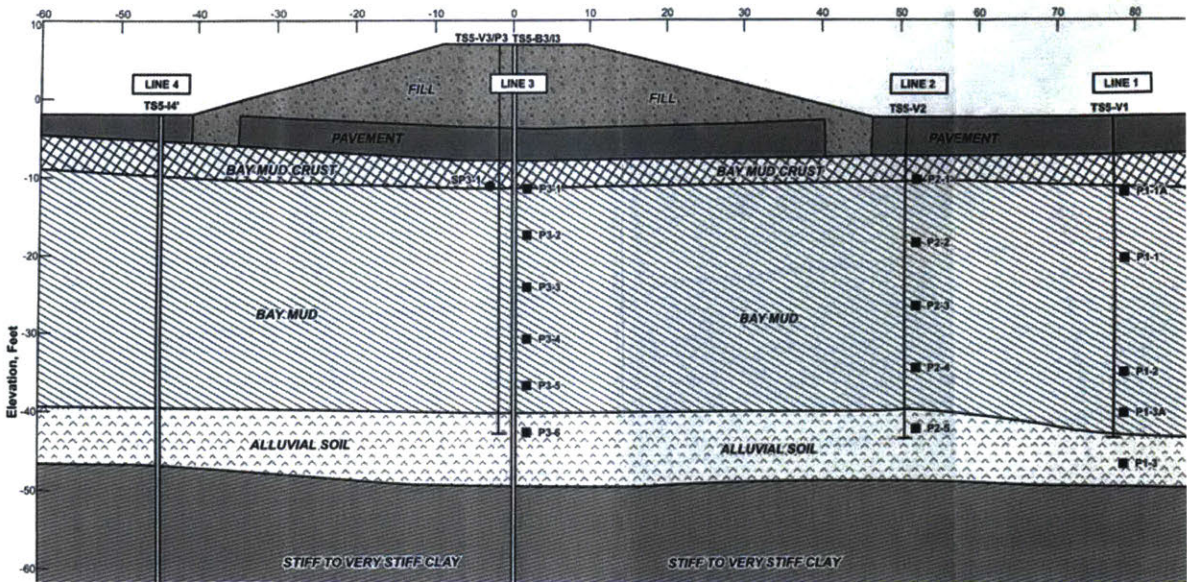


Figure 3-10: Layout of installed instruments in TS5 (URS, 2003).

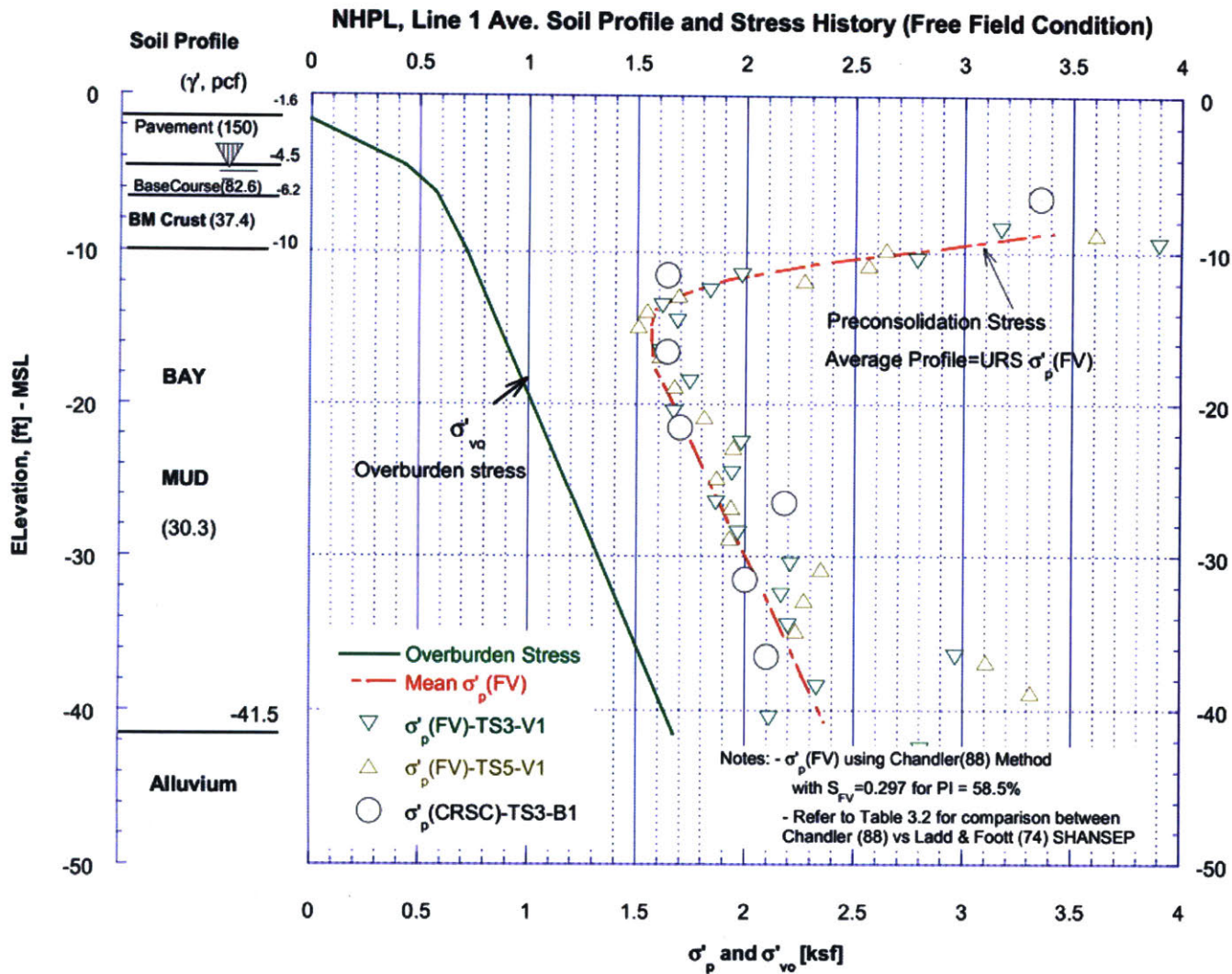


Figure 3-11: NHPL free field soil profile and stress history (Nguyen, 2006).

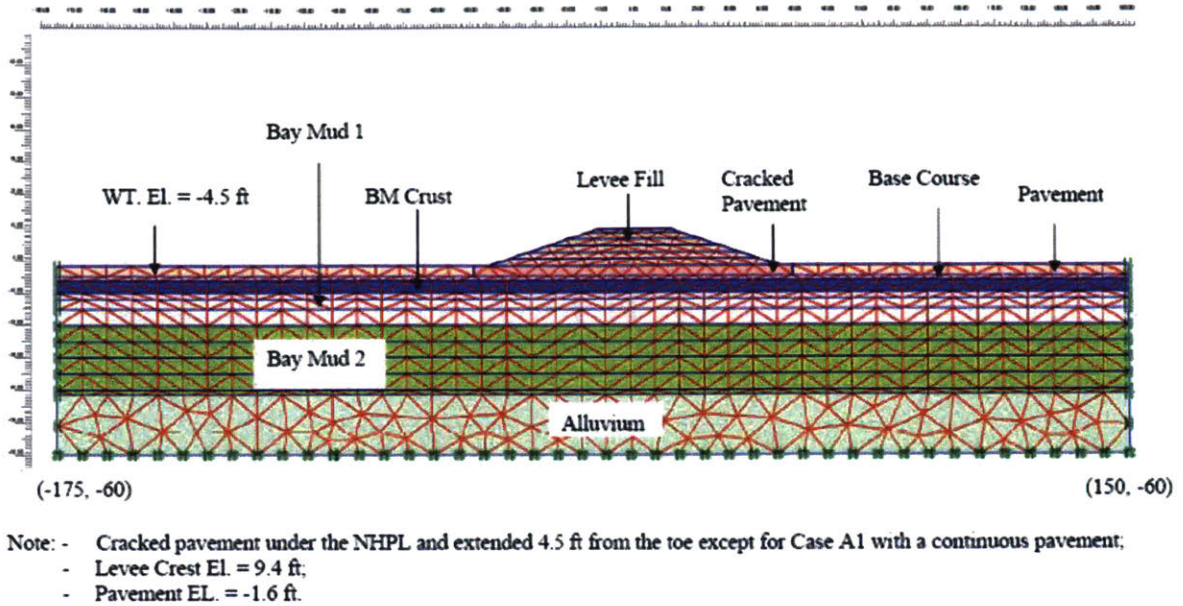


Figure 3-12: NHPL Mesh model and materials (Nguyen, 2006).

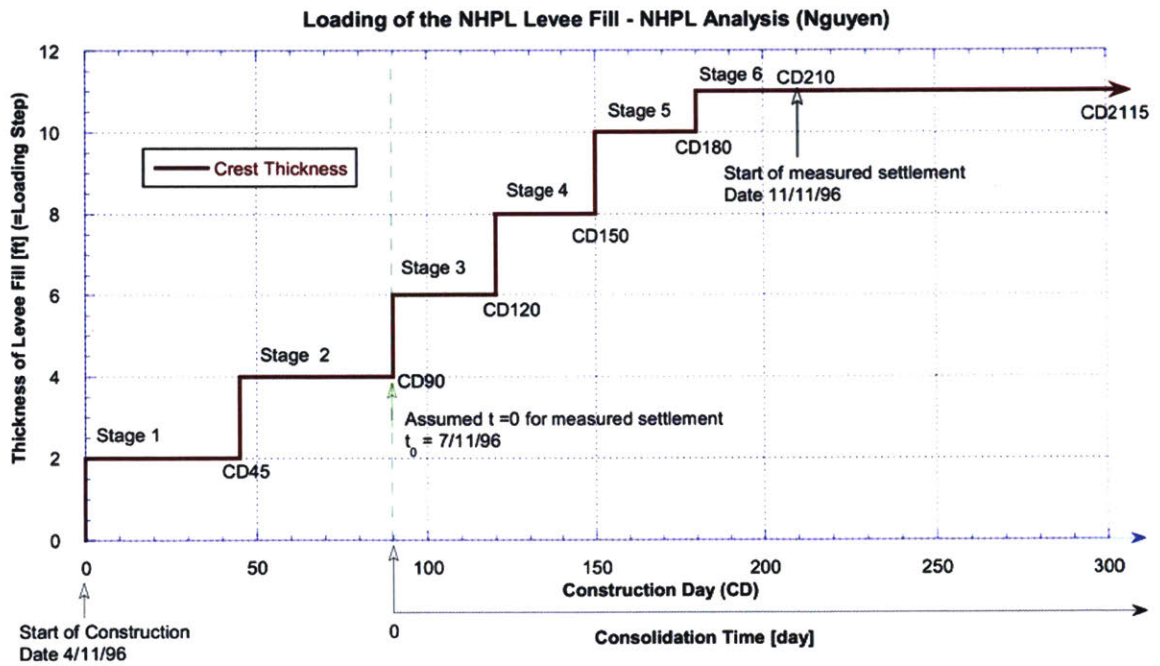


Figure 3-13: NHPL staged construction sequence (Nguyen, 2006).

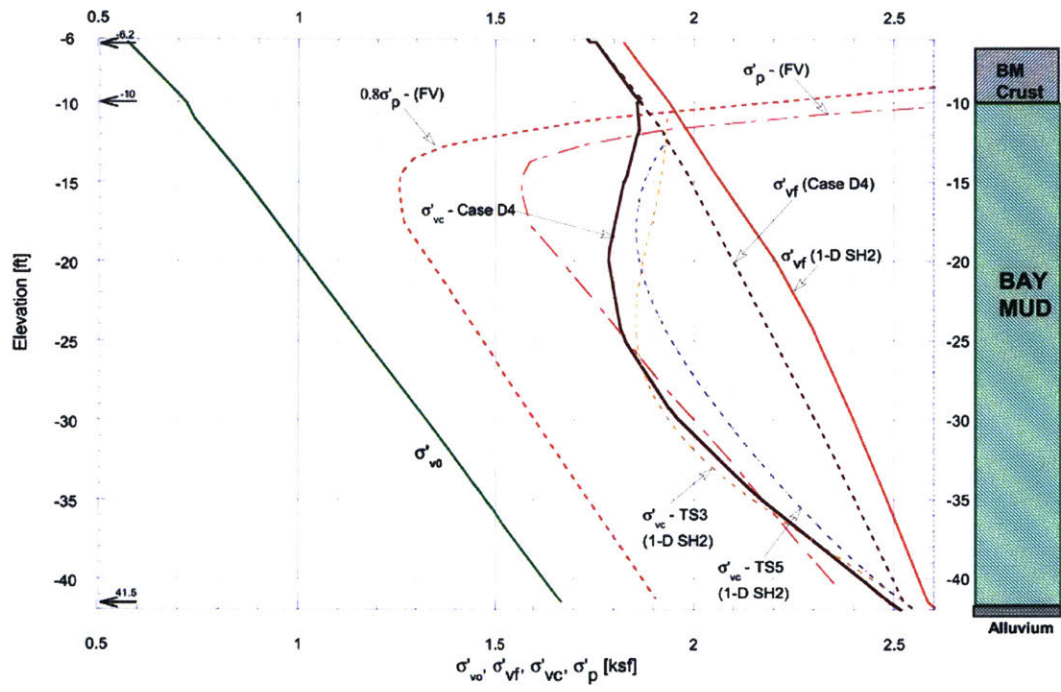


Figure 3-14: Stress histories and predictions for case D4 (Nguyen, 2006).

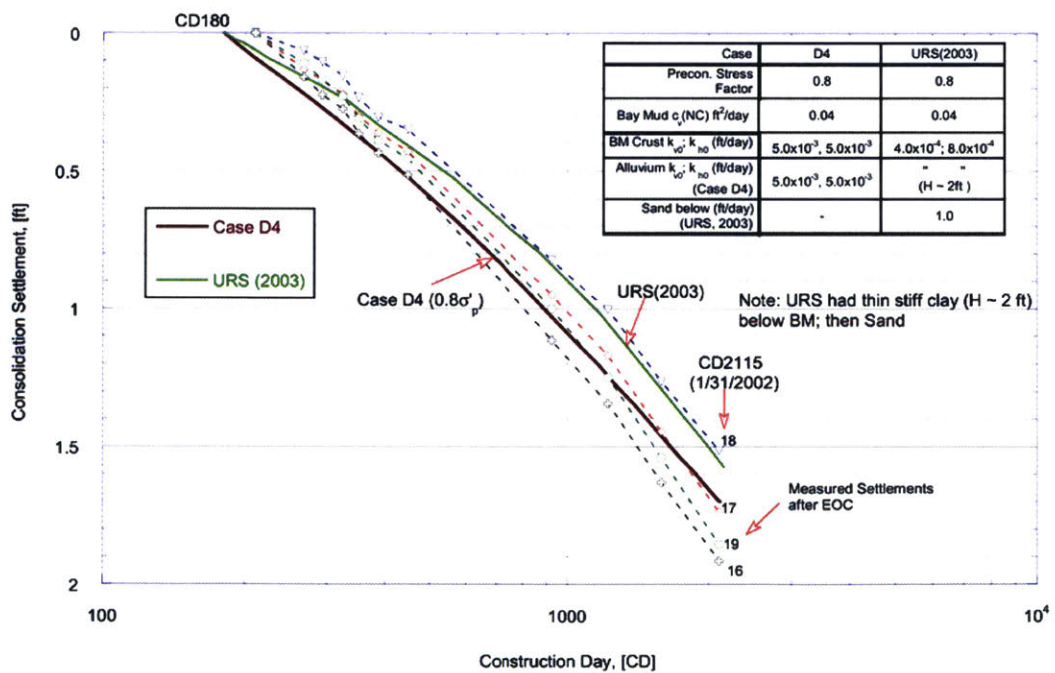


Figure 3-15: Predicted and measured consolidation settlement of the NHPL for cases URS (2003) and D4 (Nguyen, 2006).

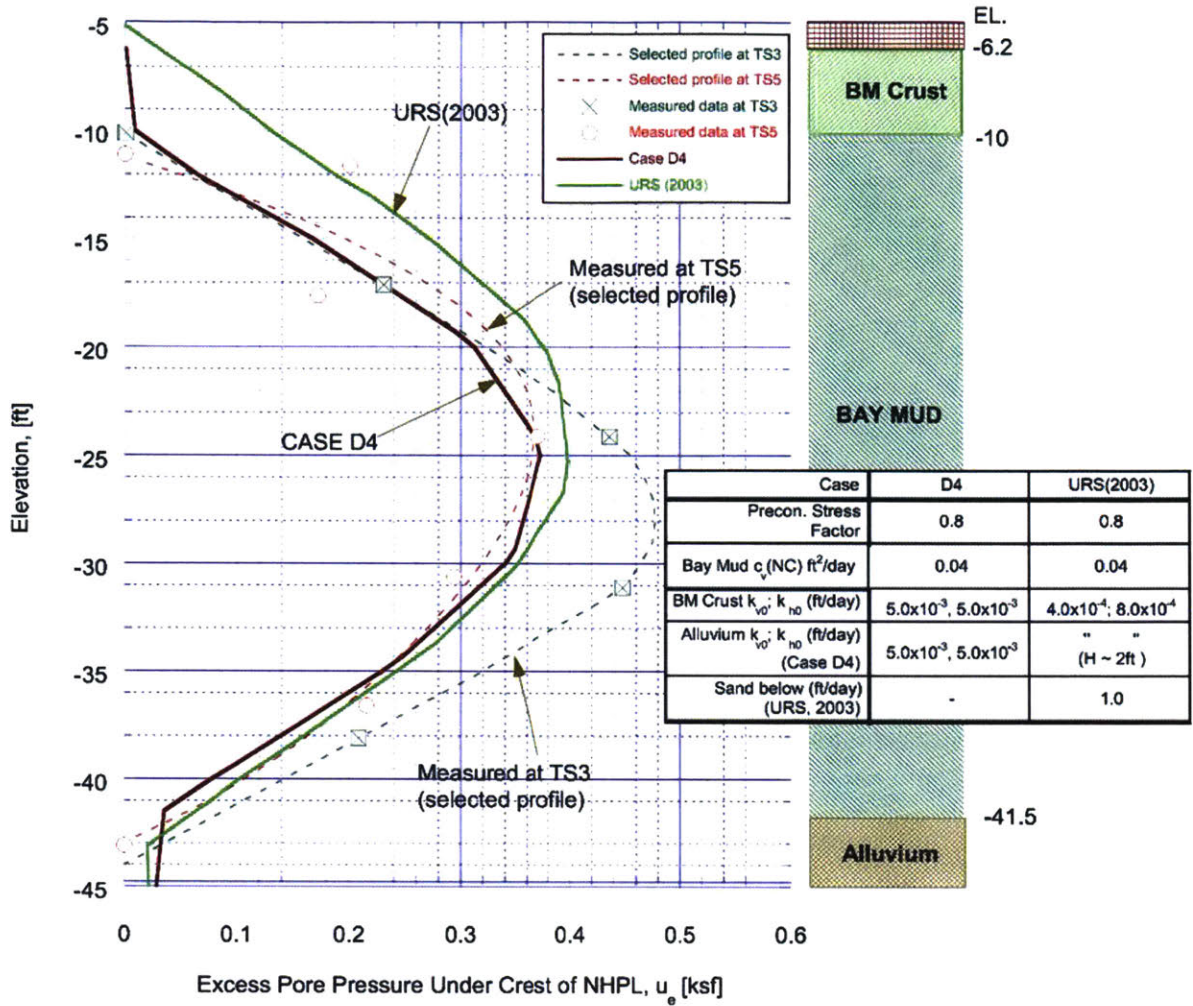


Figure 3-16: Predicted and measured excess pore pressure at centerline of the NHPL at CD2115 for URS (2003) and D4 (Nguyen, 2006).

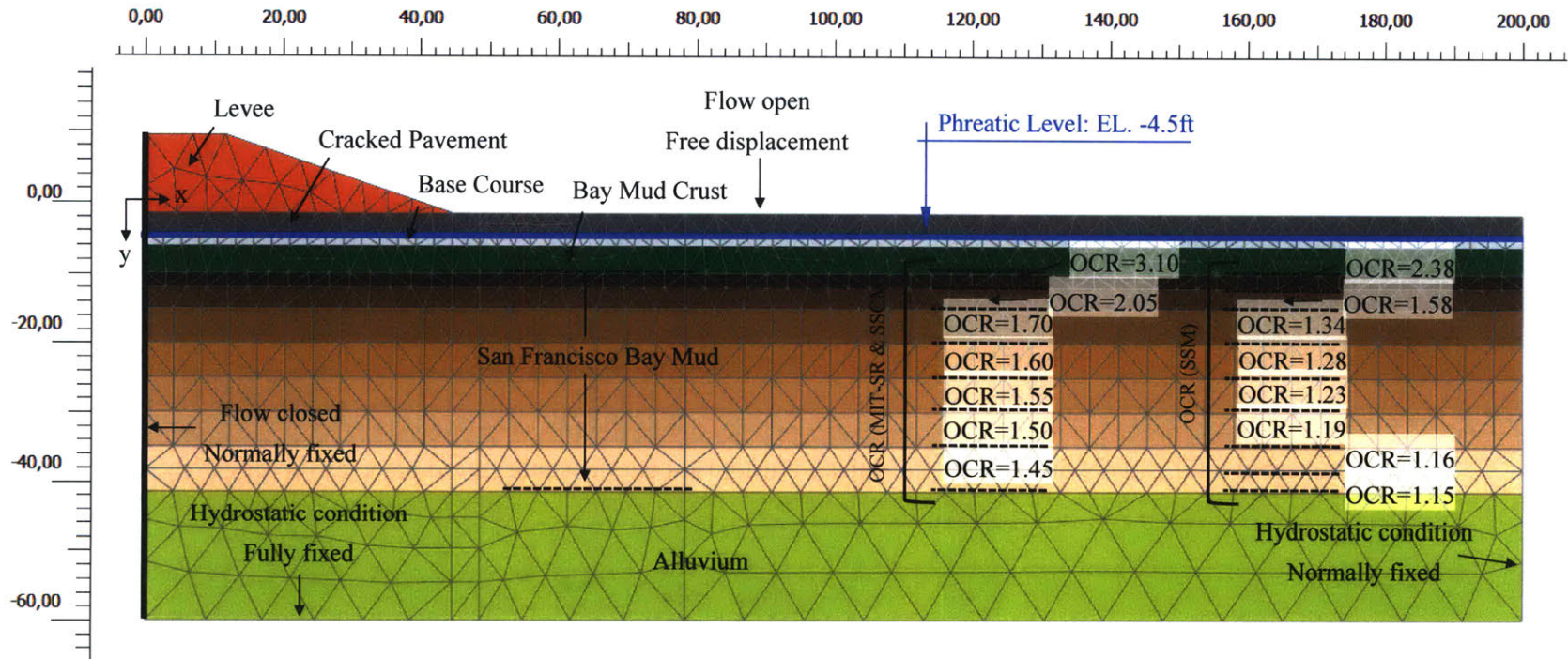


Figure 3-17: PLAXIS 2D Model: NHPL simulations with SSM, MITSR & SSCM.

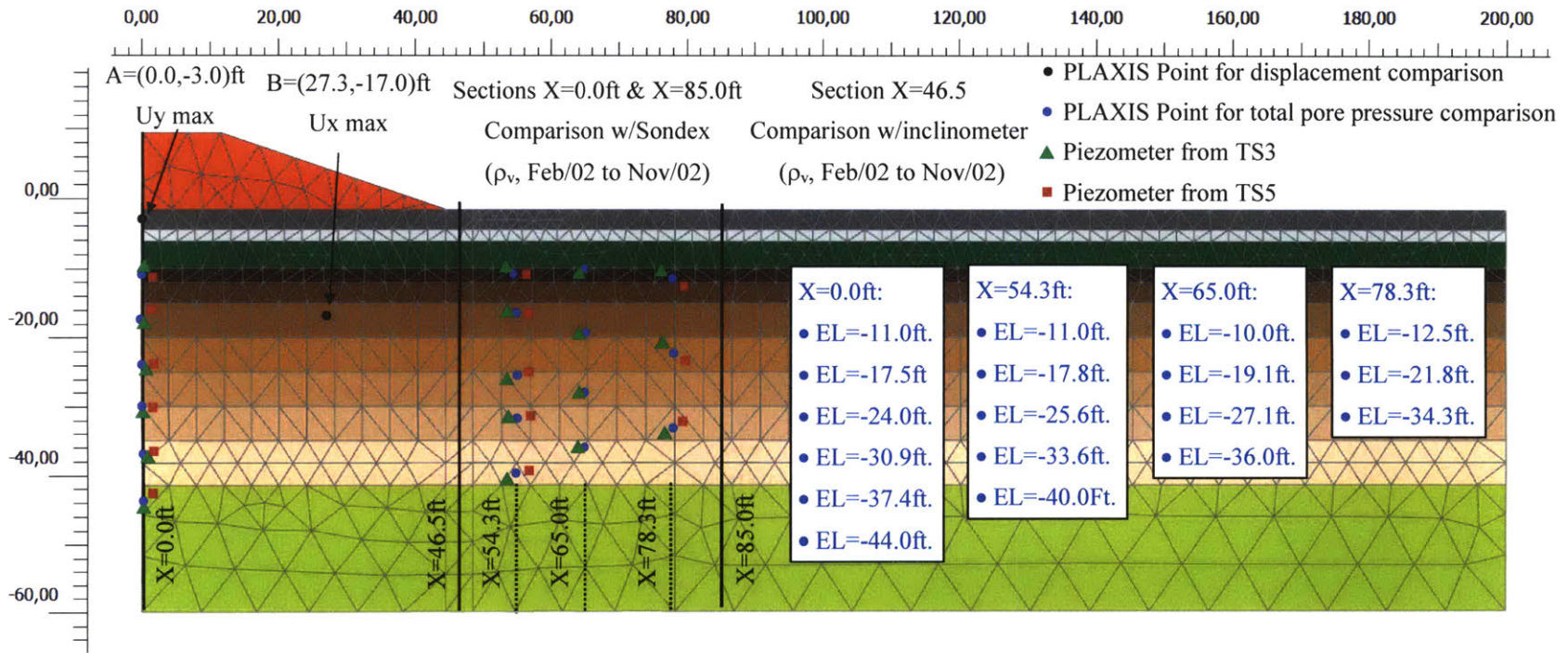


Figure 3-18: PLAXIS 2D selected points and sections for plotting results and comparing against field measurements.

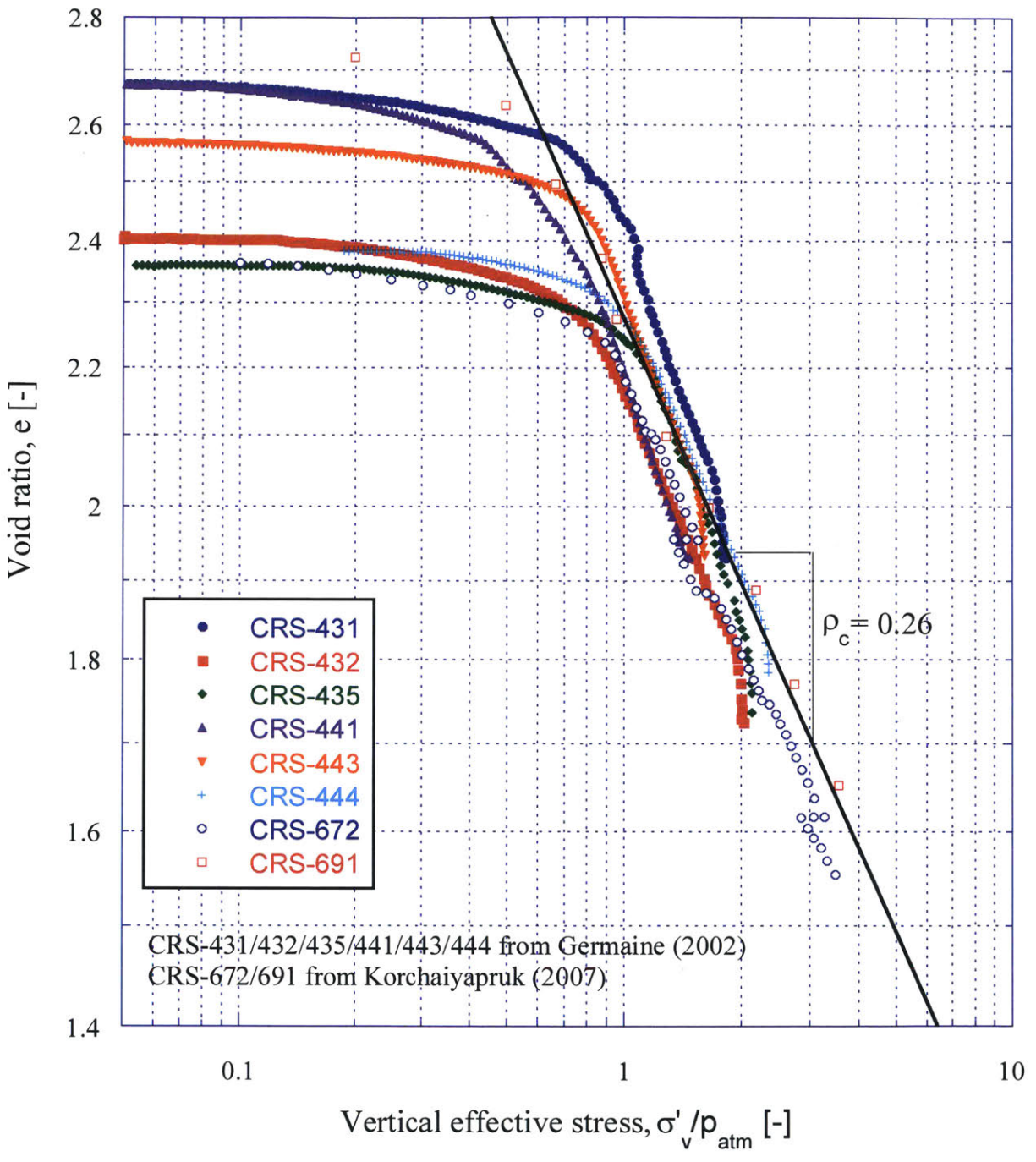


Figure 3-19: ρ_c selection in $\log(e) - \log(\sigma'_v)$ space.

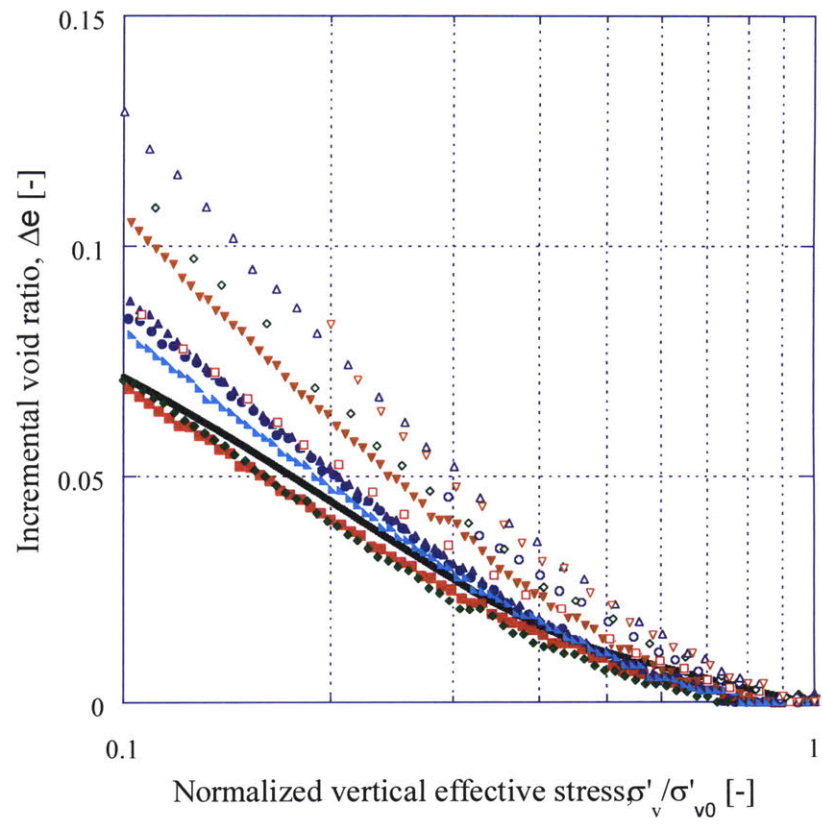
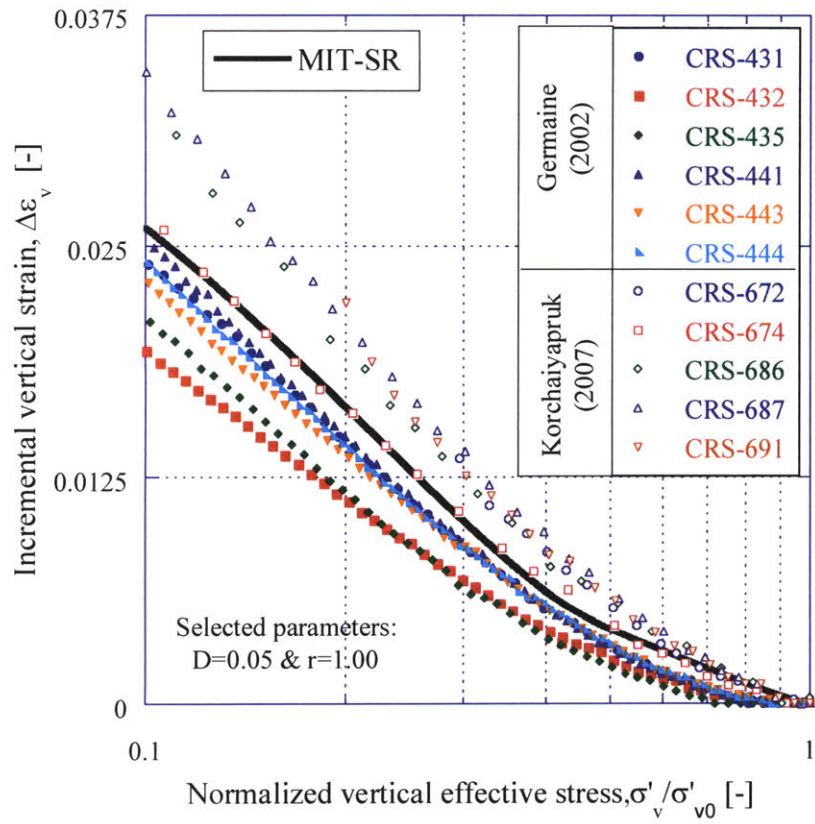


Figure 3-20: D & r selection in $\Delta\varepsilon_v-\sigma'_v/\sigma'_p$ and $\Delta e-\sigma'_v/\sigma'_p$ spaces respectively.

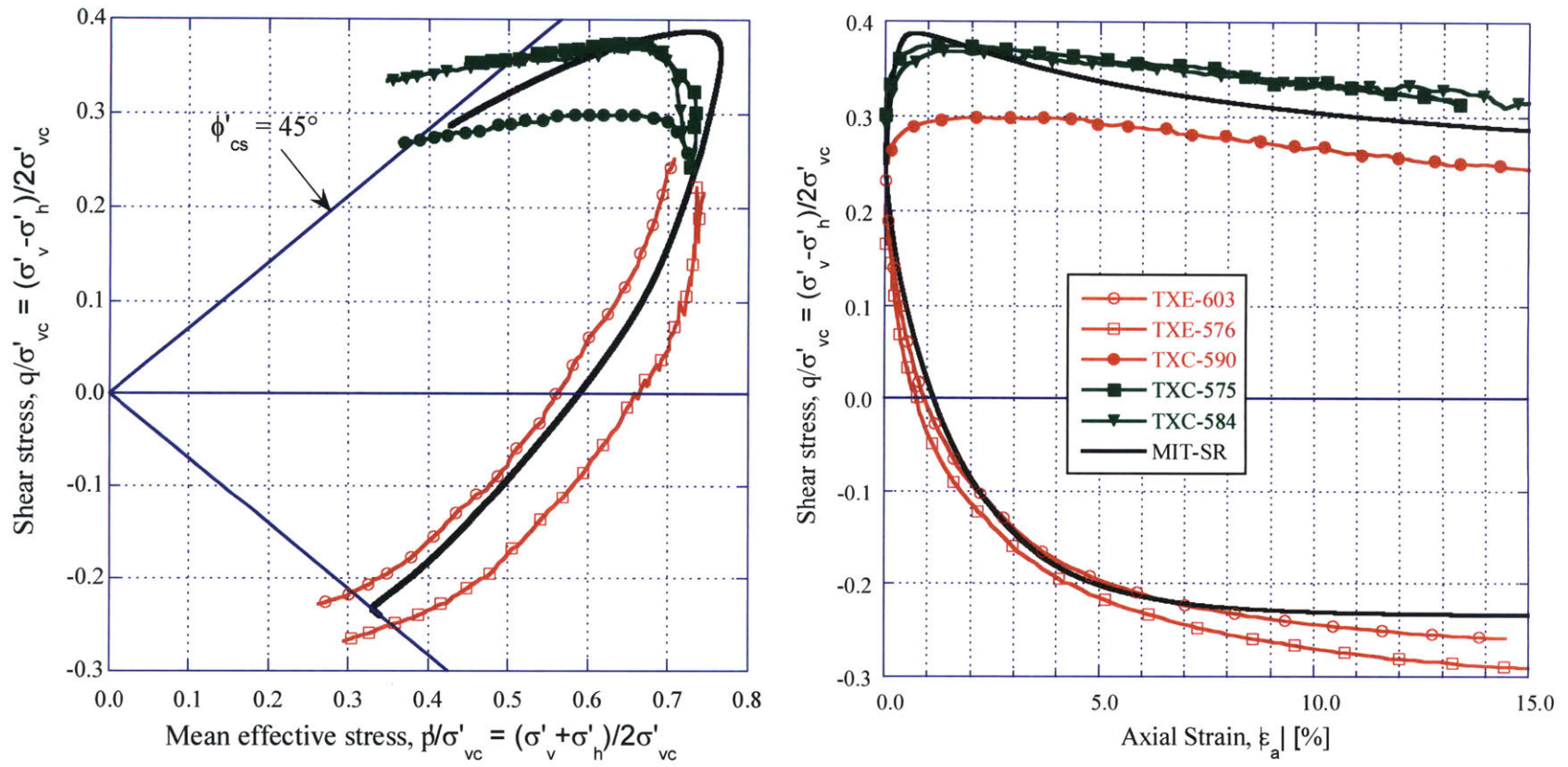


Figure 3-21: ϕ'_m , m , w_s & ψ selection in q/σ'_{vc} vs. p/σ'_{vc} and q/σ'_{vc} vs. ϵ_a spaces respectively.

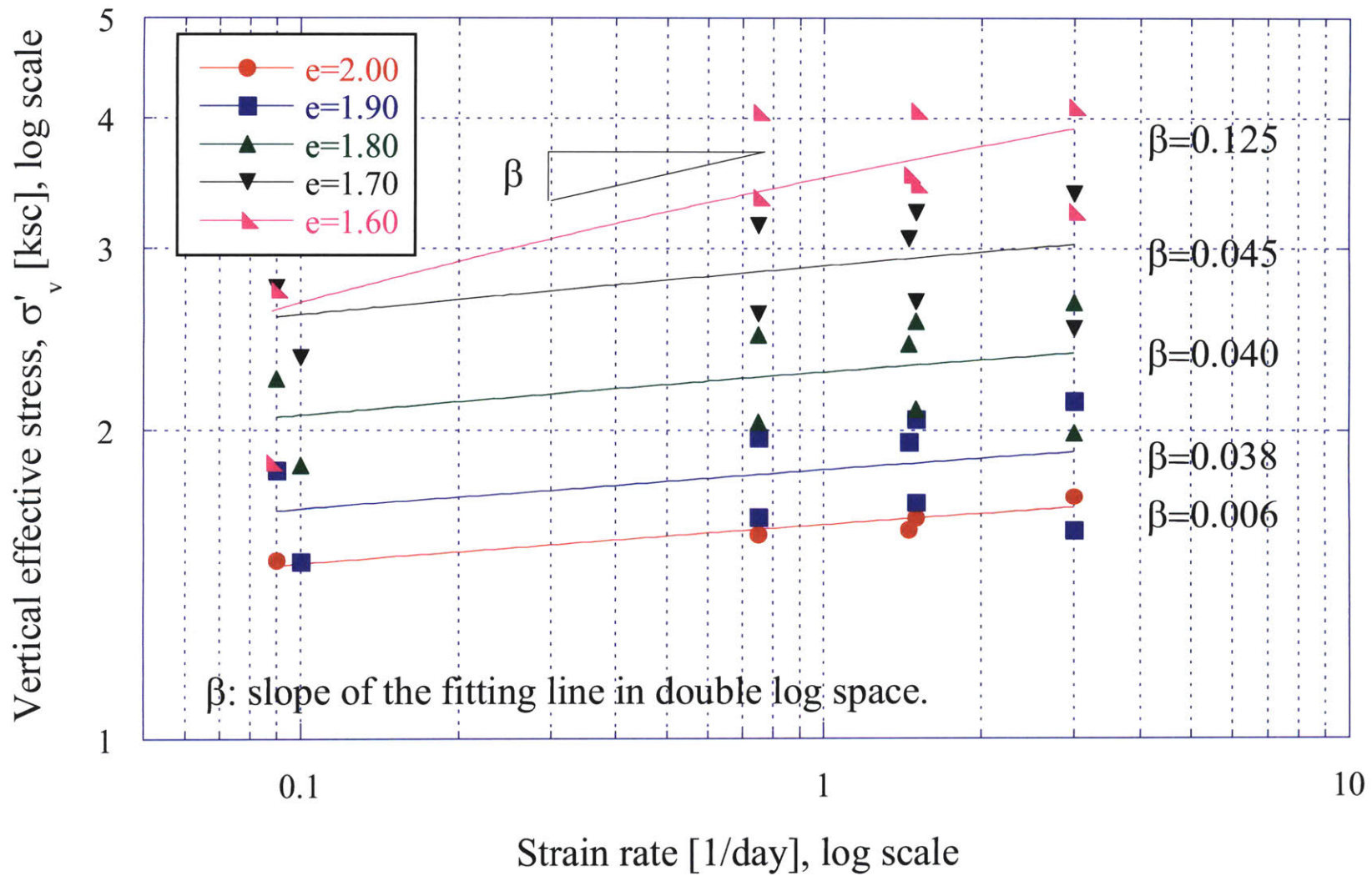


Figure 3-22: β selection in $\log(\dot{\epsilon}) - \log(\sigma'_{vc})$ space.

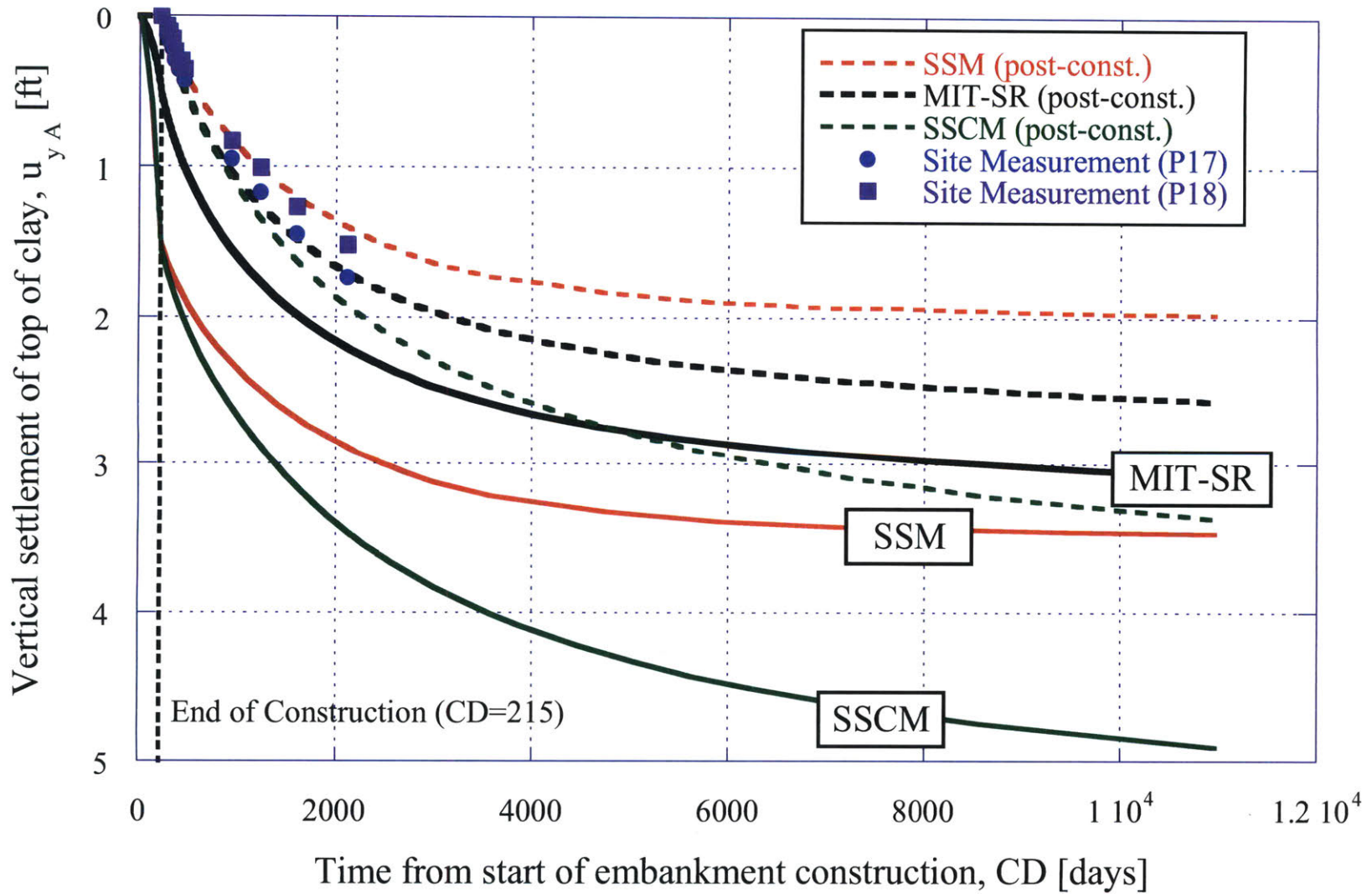


Figure 3-23: Vertical settlement of top of the clay in time.

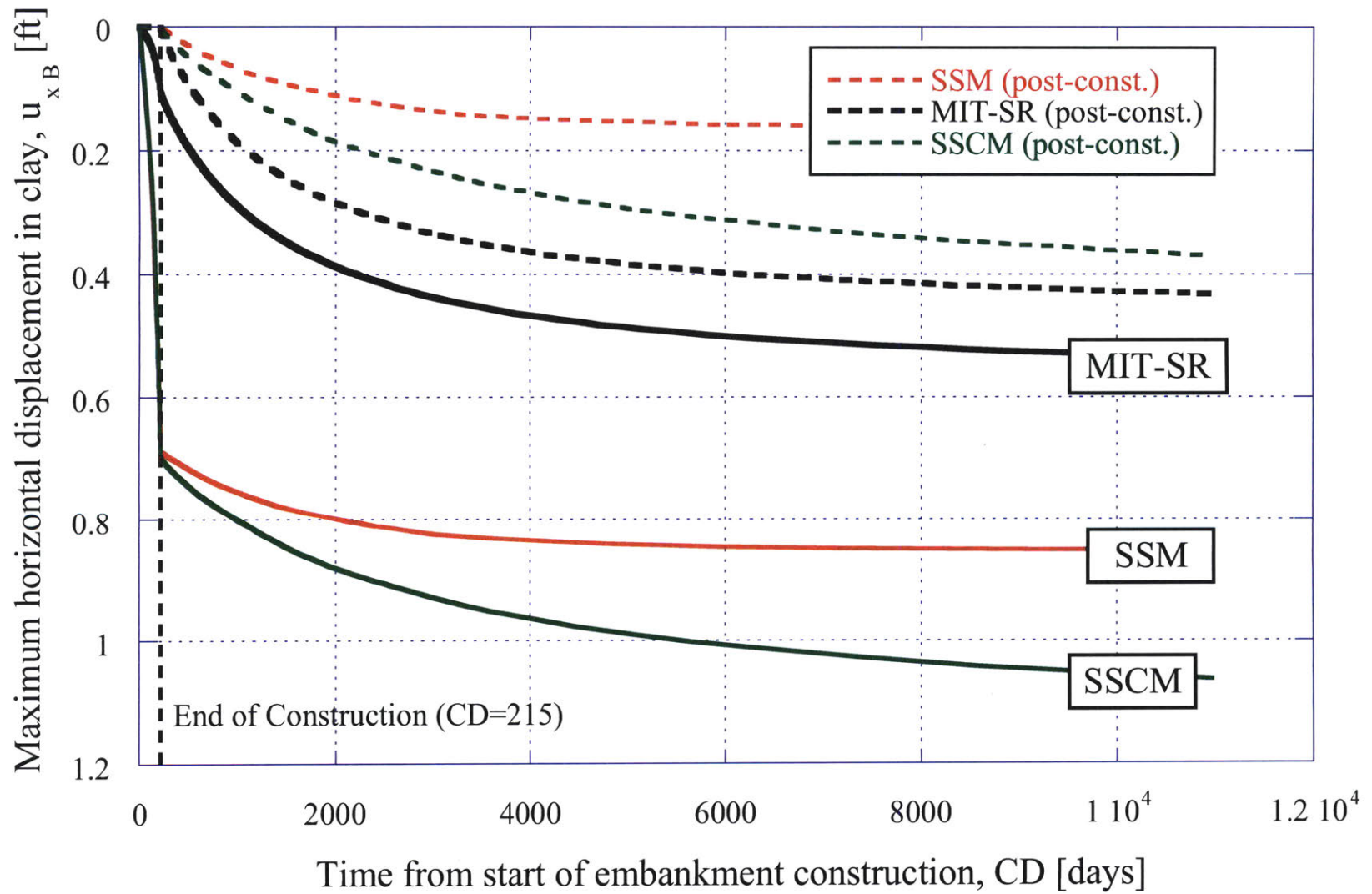


Figure 3-24: Maximum horizontal displacement in clay in time.

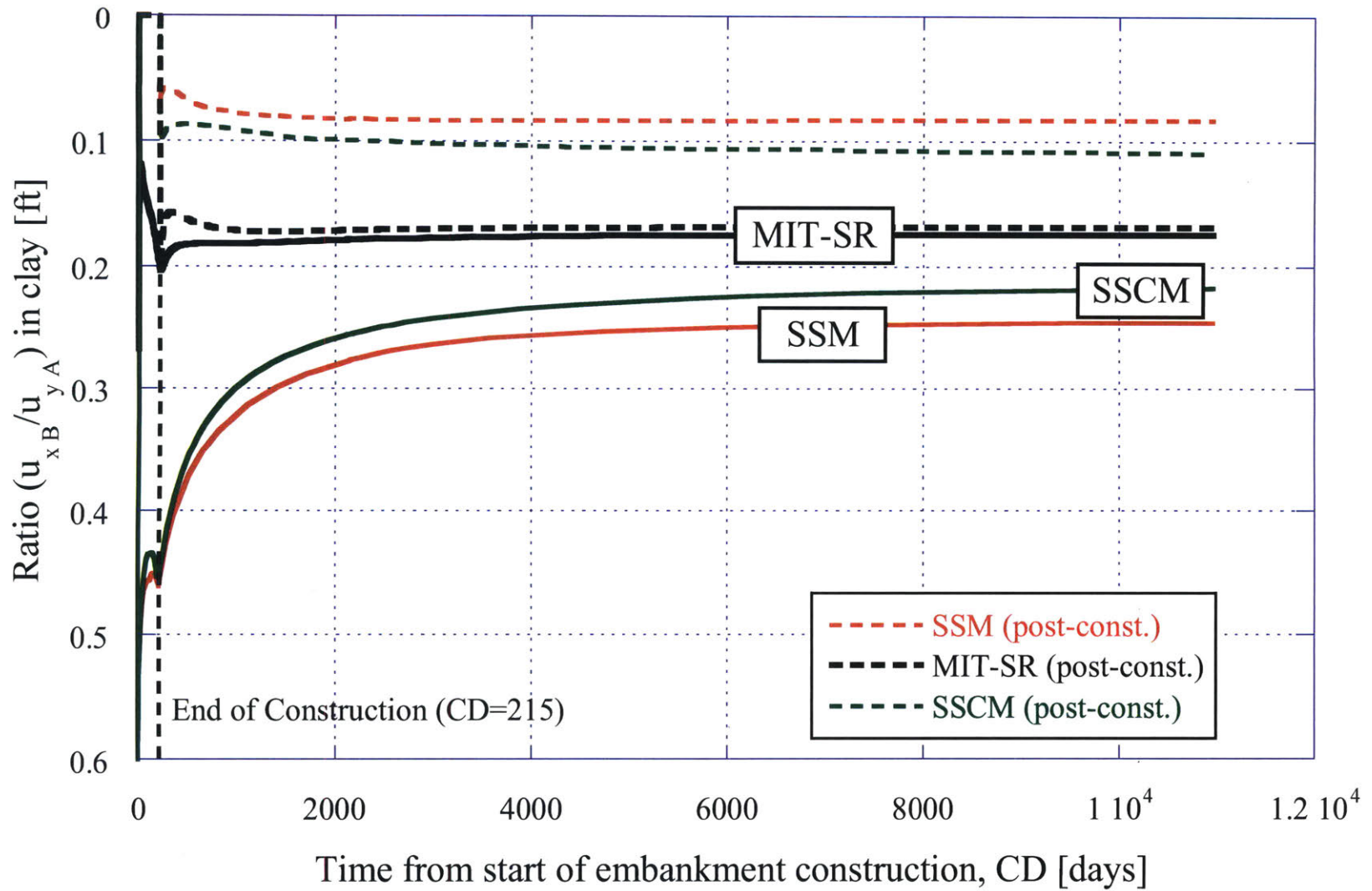


Figure 3-25: Ratio of maximum horizontal displacement and maximum vertical settlement in clay in time.

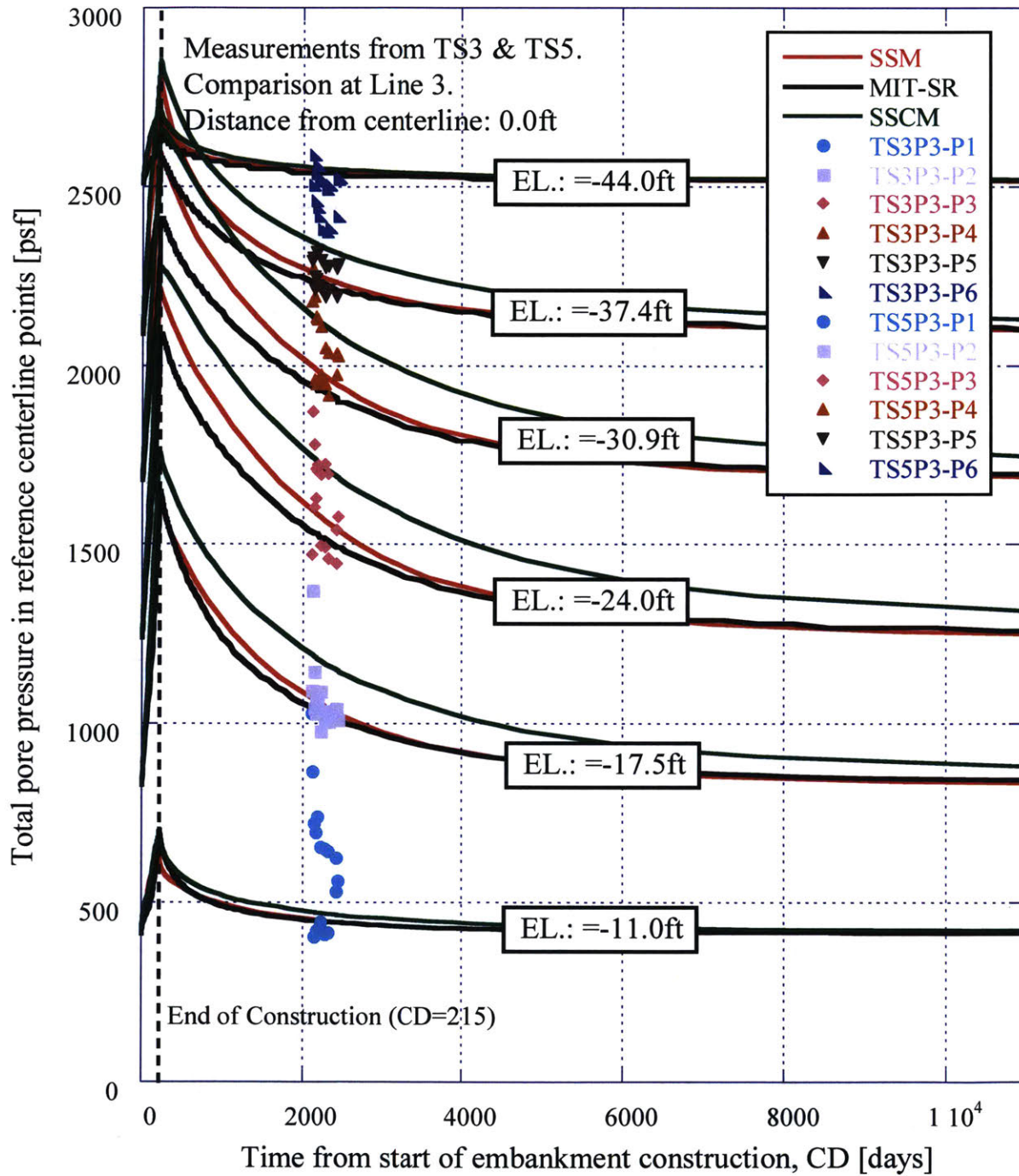


Figure 3-26: Total pore pressure in reference centerline (Line 3) points in time.

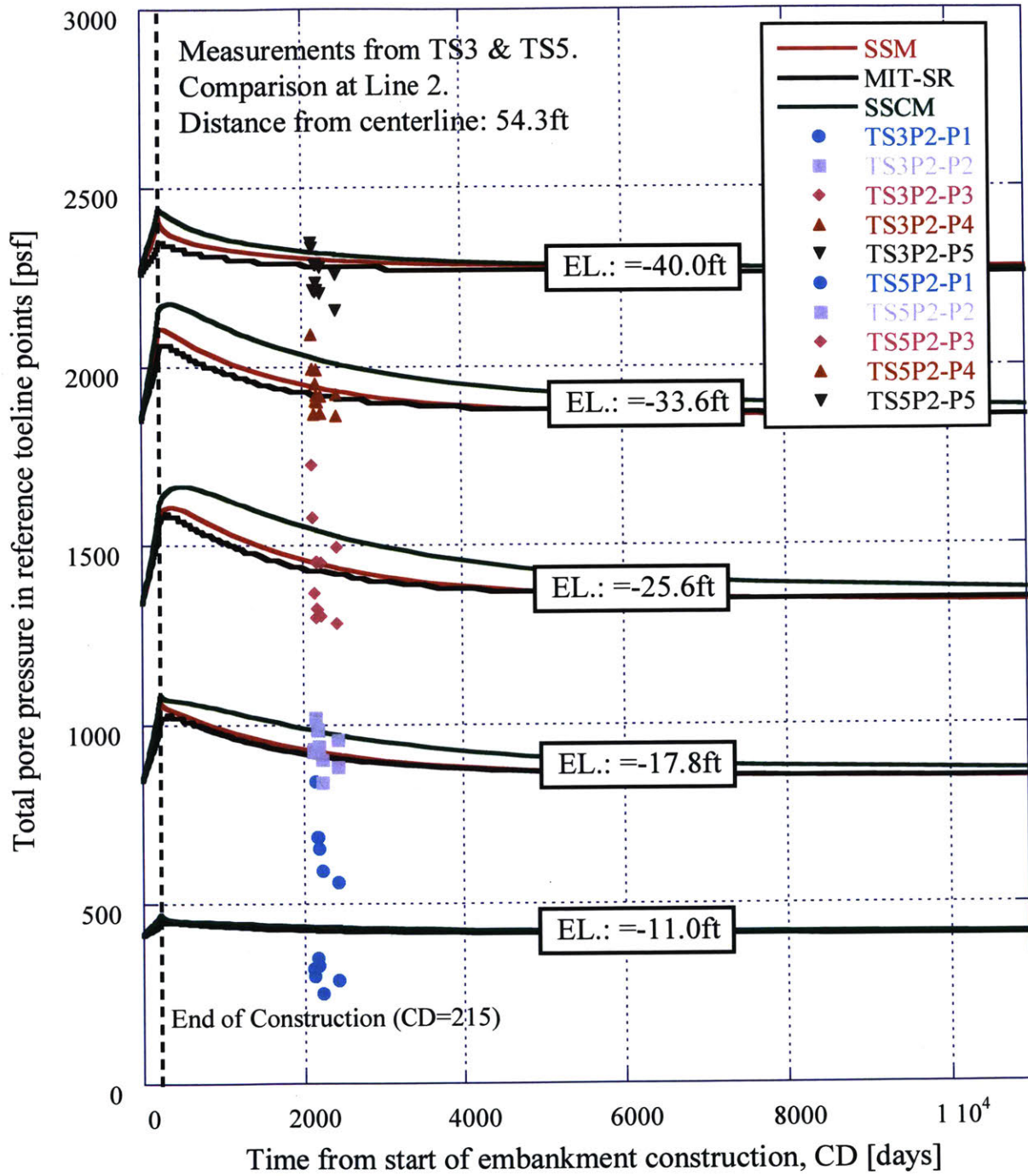


Figure 3-27: Total pore pressure in reference toeline (Line 2) points in time.

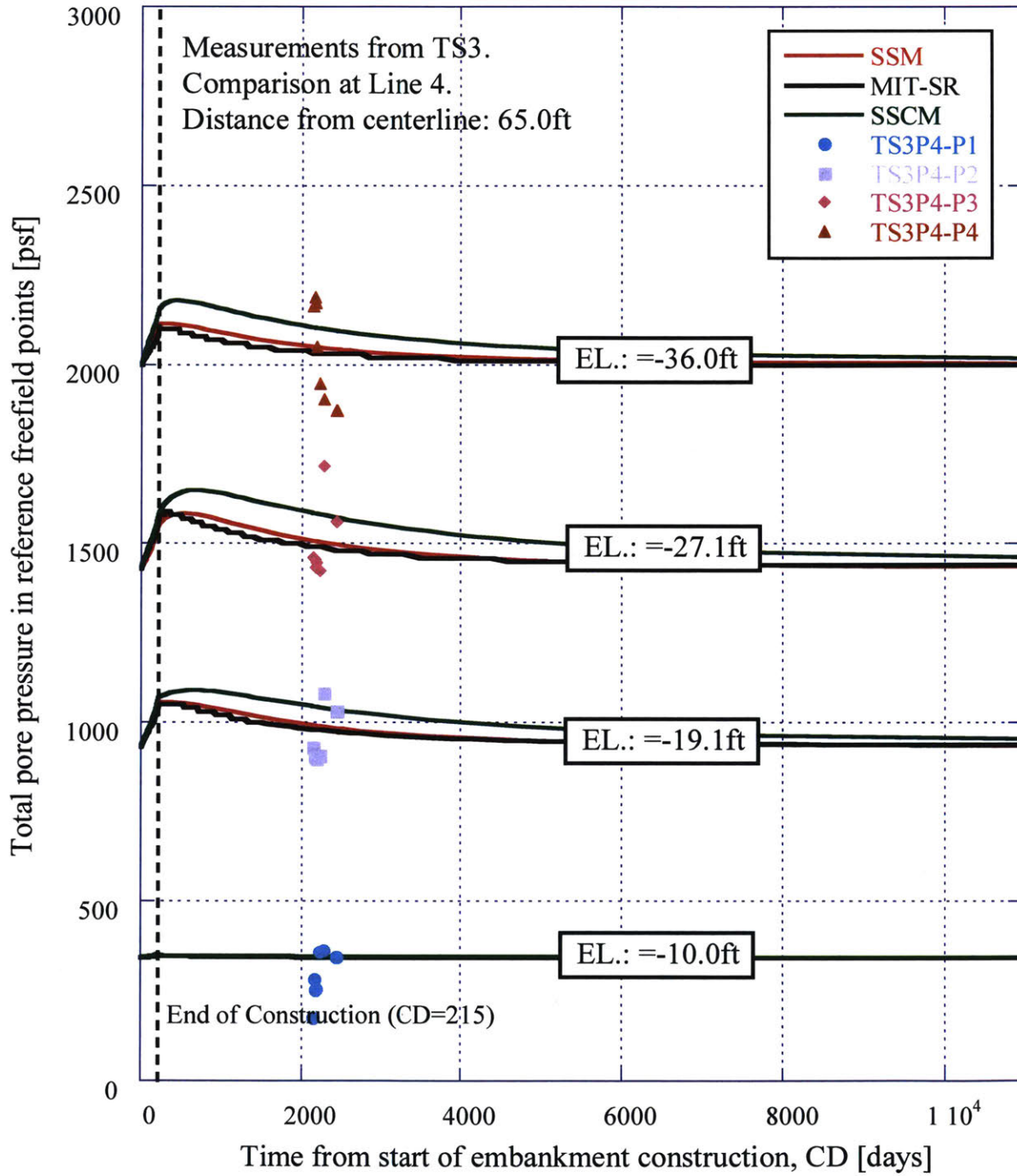


Figure 3-28: Total pore pressure in reference free field line (Line 4) points in time.

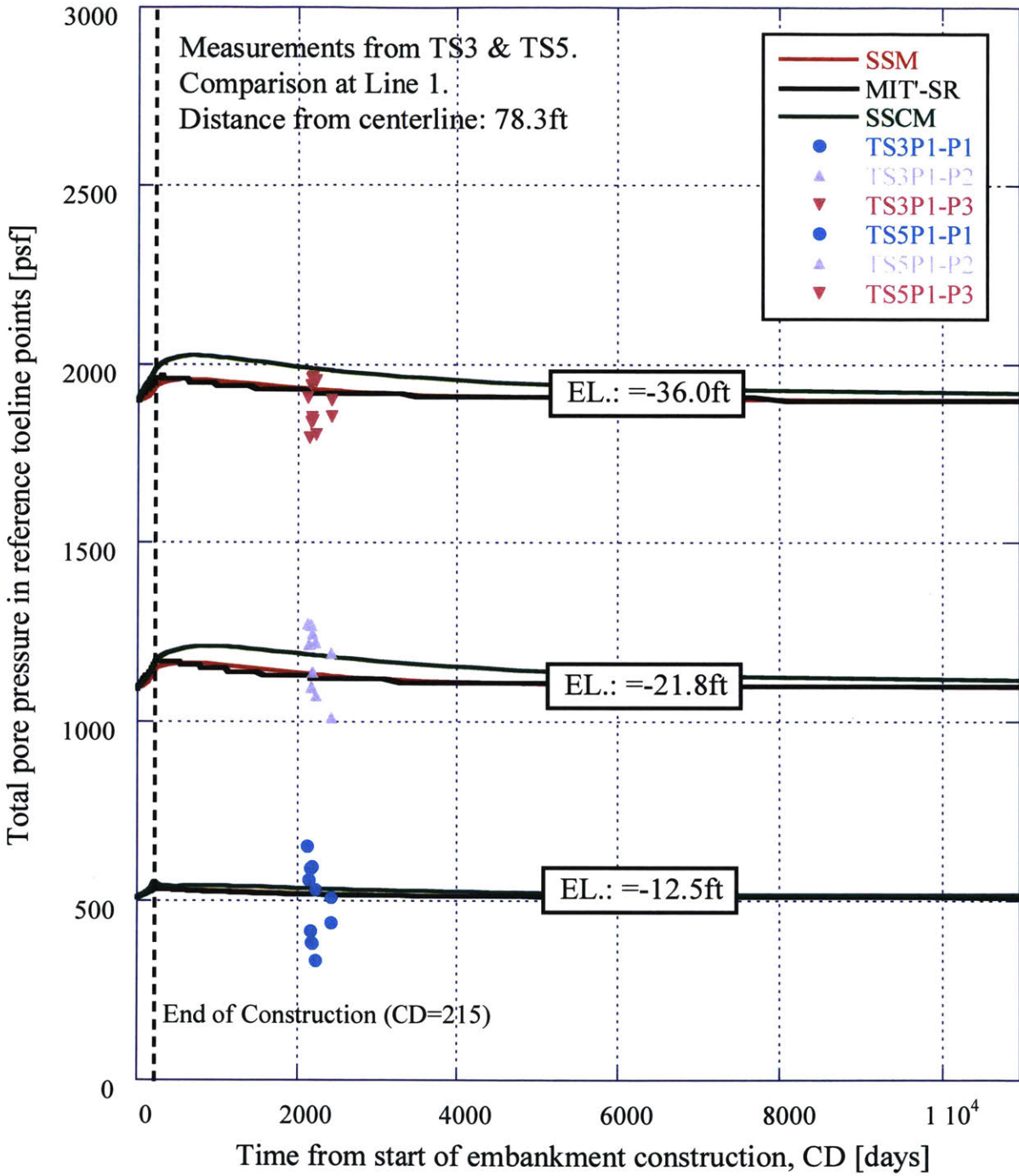


Figure 3-29: Total pore pressure in reference free field line (Line 1) points in time.

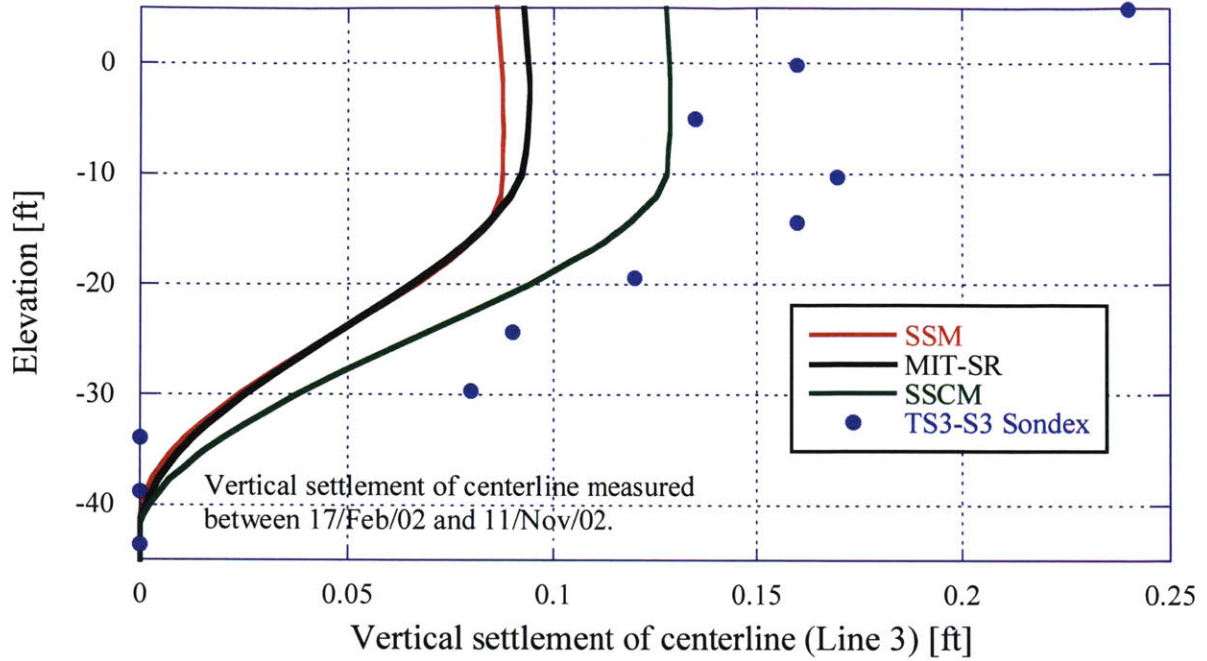


Figure 3-30: Vertical settlement at centerline (Line 3), between 17/Feb/02 and 11/Nov/02.

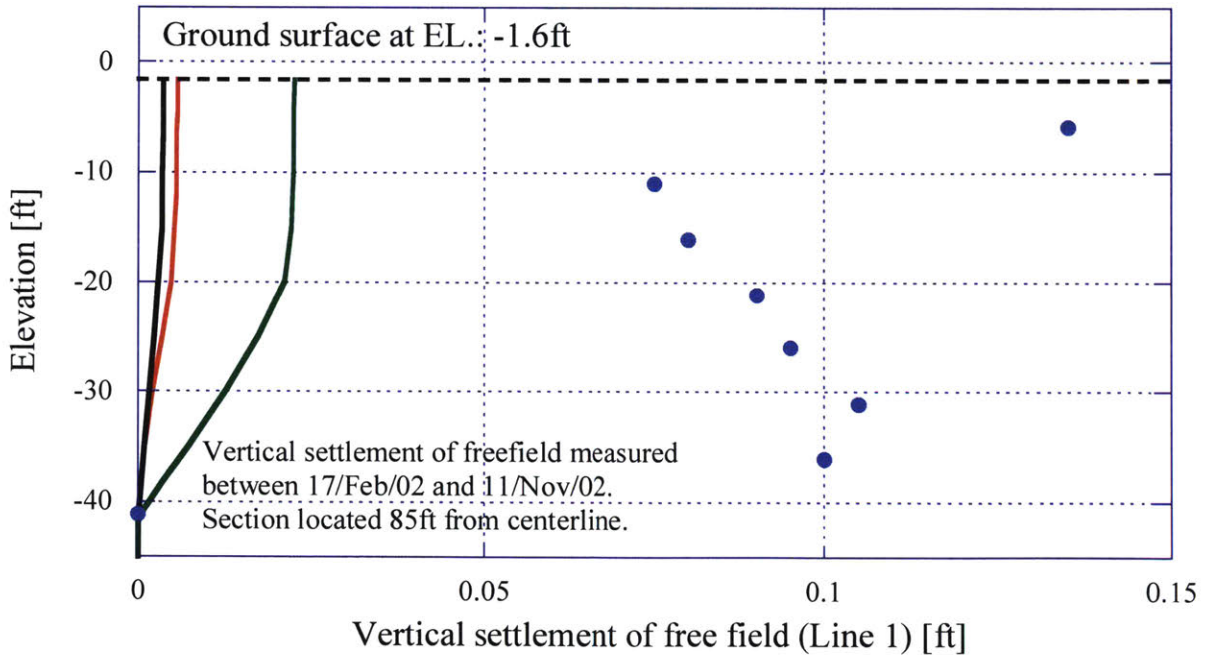


Figure 3-31: Vertical settlement at free field (Line 1), between 17/Feb/02 and 11/Nov/02.

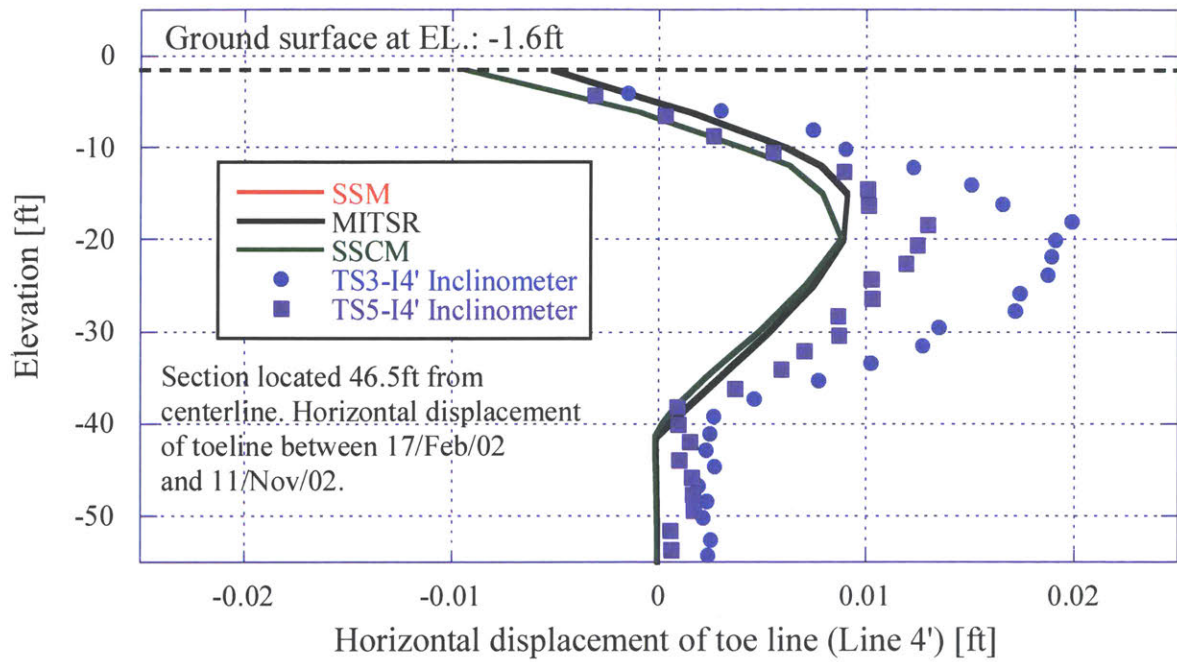


Figure 3-32: Horizontal displacement at toe line (Line 4'), measured between 17/Feb/02 and 11/Nov/02.

4. LAND RECLAMATION SETTLEMENTS, MARINA BAY, SINGAPORE

The current Marina Bay area has been formed at the mouth of the Kallang and Singapore rivers, through a program of offshore land reclamation that started in the 1950's and was executed in several separate stages and locations (Figure 4-1). Figure 4-2 presents a more detailed plan view of the bay area of interest for this chapter and in white the reclaimed territories.

This offshore land reclamation was carried out by first placing dredged sand fill to form an embankment onto the original seabed (sediments below the pre-existing mudline comprise marine clays of the Kallang formation and Pleistocene Old Alluvium). While many more recent reclamation projects in Singapore have used full depth PV drains to accelerate consolidation in the highly compressible marine clays, no such provisions were used at the sites around Marina Bay. The date, duration and reclaimed area of these processes is detailed in Figure 4-3. The current chapter considers the on-going consolidation settlements of the sites around Marine Bay using monitoring data from two recent subway station projects; T228 (Gardens by the Bay) and T302 (Gardens East facilities building) for the MRT Thomson Line.

Main sources of information for this chapter were:

- Arup (2014): Geotechnical Interpretative Baseline Report for contract T228. Report with subsurface interpretation of the ground conditions of the site and a summary of the soil properties for the design of Station TS22, twin bored tunnels from TS21 to TS22 and twin bored tunnels from TS22 to Marina East Bay.
- Mott MacDonald (2015): Geotechnical Interpretative Baseline Report for contract T302. Report with subsurface interpretation of the ground conditions of the site and a summary of the soil properties for the design of the facility building TE22A, twin bored tunnels from GBME Shaft to TE22A and twin bored tunnels from TE22A heading to the north interface with contract T303 and its cut and cover section.
- Amberg & TTI (2004): Final Geotechnical Interpretative Report for the reconstruction of the braced excavation system at Nicoll Highway. Report with subsurface interpretation of the ground conditions of the site and a summary of the soil properties for the design of the proposed reconstruction.
- Corral & Whittle (2010): Re-analysis of deep excavation collapse using a generalized effective stress soil model. This paper re-analyzed a well-documented failure of a 30m

deep braced excavation in underconsolidated marine clay using MIT-E3 effective stress soil model. The analyzed site in the paper is close to T228 and T302 areas and the information contained is considered to be representative of marine clay in the areas of interested of this research. MIT-E3 calibration for the marine clay served as a source of information to determine several MIT-SR parameters.

- Kiso-Jiban report (1978): Laboratory soil test results for B747 Hangar complex at Changi Airport, Volume I. The report includes different laboratory tests for soils present in the area. Regarding Marine Clay, consolidation tests BH8-U4-S3, BH8-U4-S4, BH8-U6-S3 and BH8-U6-S4 were considered for this research considering that the test loads were higher than the original in-situ stress and ensured a NC behavior and minimized sample disturbance influences.
- Choi (1982): Consolidation behavior of natural clays. This PhD thesis included tests on many clays, Singapore Marine Clay included. Executed consolidation tests included CRS (SC-15 to SC-18, rates ranged from 0.45%/hr to 0.13%/hr), IL without surcharge (samples SC-1 to SC-6) and IL with surcharges (SC-7 to SC-14 and SC-19 to SC-22). Series 3 (SC-7 to SC-10) allowed in each surcharge step a determined consolidation degree (60%, 80%, 60% and 90%) before unloading and allowing a creep stage. Series 4 (SC-11 to SC-14) and Series 6 (SC-19 to SC-22) reached EOP in each surcharge step, unloaded and allowed creep. In each Serie, first sample was tested without surcharge and used as baseline comparison to assess surcharge effects in consolidation and creep behavior. The most useful source of information for the MIT-SR calibration was provided by Series 4 and the CRS tests.
- Tan et al. (2003): “A characterisation study of Singapore Lower Marine Clay.” This paper contains, among other information, the variation of G_{max} in depth in the Singapore Arts Centre (SAC).

4.1. OVERVIEW OF MARINA BAY T228 & T302 PROJECTS

The Land Transport Authority is currently developing the proposed Thomson Line of the Singapore Mass Rapid Transit system. The area analyzed in this chapter was enclosed in contracts T228 and T302 (Figure 4-4). The ground levels within these contracts, taken from topographical surveys and site investigations, range mostly between +103 and +105mRL.

Contract T228 includes the construction of station TS22 with a launch shaft, twin bored tunnels driven from station TS21 towards TS22 and twin bored tunnels from station TS22 to the escape shaft at Marina Bay East. Contract T302 comprises a cut and cover underground facility building and two bored tunnel drives either side of the building. Contract T228 area is underlain by reclamation fill placed from 1979 to 1985 and includes “Phases VII”, “Marina Channel” and “Phase VI” and contract T302 reclamation area included “Phase II” (1970 to 1971) and “Phase VI”. Little to no information was available on the materials utilized for the reclamation process.

The present chapter is focused on the characterization of the compressive and creep behavior of the materials to later simulate the reclamation process and estimate current creep rates. These predictions were compared against current settlement rates in markers which areas are considered to be unaffected by construction works. In addition, predicted creep rates are expected to serve as baseline values for ongoing engineering design where no creep phenomena is considered in the numerical models.

4.2. MARINA BAY GEOTECHNICAL CONDITIONS

The main geotechnical units present at these sites can be summarized as follows:

- Reclamation Fill: encountered from the surface in all boreholes and can be described as very loose to medium dense fine to coarse sand with gravels and sea shell fragments, generally poorly graded, clean and highly permeable. The material is highly heterogeneous, composed of various granular and cohesive materials. The larger portion of this material is considered to be sandy and sourced from past dredged works. Thicknesses range from 8.0m to more than 20m with an average of 13.0m; the higher thicknesses are found along the current shoreline of Marina Channel (note that the bay was impounded by a barrage that was completed in 2008).
- Kallang Formation: consists of recent alluvial and marine deposits of Holocene and late Pleistocene Age and can be found on the southern and eastern parts of Singapore, near the Singapore River and other river valleys. It overlies the eroded upper surface of the Old Alluvium Formation and rapid changes in thickness of the stratum are common across the site. The existing and substantial variations of the Kallang Formation thickness are principally due to deeply incised channels in the underlying Old Alluvium (see Figure 4-5)

and dredging of Marine Clay in some locations in connection with construction of former marine works.

- Old Alluvium: typically described as a dense to very dense silty gravelly sand and very stiff to hard sandy clay and sandy silt. The Old Alluvium (OA) is a partially lithified, dense deposit of interbedded sands, silts and clays laid down in a slowly subsiding basin during one of the Pleistocene interglacial periods. It is weathered in the upper few meters, typically becoming weakly cemented in the unweathered state. Due to its depositional environment, the OA is laterally and vertically highly variable with rapid and frequent variations.

Figure 4-6 and Figure 4-7 present typical profiles encountered in T228 and T302, respectively.

4.2.1. Kallang Formation and Singapore Marine Clay

Marine Clay is the dominant member of the Kallang Formation and the deposition sequence contained two separate units: Lower Marine Clay (LMC) and Upper Marine Clay (UMC).

Between these stages, the decrease in sea level exposed to the LMC and allowed for desiccation processes to generate a crust and consolidate the upper portion of LMC. The formation of the UMC took place at a later stage with a higher sea level.

The Upper Marine Clay is a dark greenish grey clay with occasional shell fragments, organic materials and traces of fine sand and is usually very soft to medium stiff. LMC is similar to UMC but generally has a soft to firm or firm consistency, a higher density and an overconsolidation lower than the encountered in UMC. The desiccated crust of LMC, up to 6m thick, presents OCR higher values than UMC.

The intermediate unit between UMC and LMC is a complex mixture of dense sandy silts or silty clay layers, variously reported as either fluvial clays (F2) or estuarine clays (E), with OCR values as high as 8. In some places, an intermediate sand layer (i.e.: fluvial sands, F1) could be found instead of a desiccated layer; thus the stiff intermediate crust is not continuous in the Marina Bay area. Also, depending on the area, layers of F1 and E can be found on top of the UMC and below the LMC.

4.2.2. Original seabed conditions and preconsolidation profile

In order to be able to represent the reclamation process and simulate the consolidation and creep phenomena from the beginning, it was necessary to determine the original geotechnical profile of the area, prior to the reclamation.

As can be observed in Figure 4-2 to Figure 4-3, the current Marina Channel area has no fill and current seabed would strongly resemble to seabed conditions prior to the placement of the reclamation fill. Information obtained from Arup (2014) was presented in Figure 4-8 and Figure 4-9; a simplified profile from top to bottom would comprise UMC, F2, LMC and OA.

In Figure 4-9 (Arup, 2014), preconsolidation pressures were obtained from oedometer tests; values that plotted below current vertical effective stress were discarded. There is considerable scatter in the measurements of σ'_p . However, the data do consistently suggest that the Marine clay is lightly overconsolidated. Arup (2014) proposed that the upper limit of OCR could be obtained by assuming excavation/dredging equivalent to 40kPa (Figure 4-9a), leading to the OCR profile shown in Figure 4-9b. Digitized and analyzed information from Figure 4-9 is presented in Appendix B. OCR values for UMC range between 8.70 and 1.50 whereas for LMC these values are between 1.46 and 1.22. Figure 4-9c compares the undrained shear strength profile from field vane tests, with SHANSEP derived profiles using reference parameters $S=0.22$ and $m=0.8$. The measured data shows that the measured strengths are significantly higher than those predicted for $OCR=1.0$, but fit very closely with the assumption of a prior 40kPa overburden.

There is no direct information on undrained shear strength properties for the F2 (intermediate) layer within the Marina Channel. This required information was obtained from Figure 4-10 where points corresponding to the boreholes of the Marina channel (RE0003 to RE0008) were identified and digitized. The undrained shear strength values were utilized together with the estimated vertical effective stress to calculate OCR values according to SHANSEP methodology (equation 3.1) and the already quoted values of $S=0.22$ and $m=0.8$ (Figure 4-9). The average OCR obtained for F2 layers was 7.30.

A summary of the stratigraphy encountered in the canal, and which is considered as the baseline for pre-reclamation analyses, is:

1. UMC layer from +93.0mRL to +83.5m (ELs +93.0 to +90.0mRL with OCR=5.70, ELs +90.0 to +87.0mRL with OCR=2.40, ELs +87.0mRL to +84.0mRL with OCR=1.85 and ELs +84.0mRL to +83.5mRL with OCR=1.60).
2. F2 layer from +83.5mRL to +80.0mRL with OCR=7.30.
3. LMC layer from +80.0mRL to +64.0mRL (ELs +80.0 to +77.0 with OCR=1.40, ELs +77.0mRL to +74.0mRL with OCR=1.35, ELs +74.0mRL to +70.0mRL with OCR=1.30 and ELs +70.0mRL to +64.0mRL with OCR=1.25).

4.3. T228 & T302 SITE MONITORING INFORMATION

Current site measurements in these sites evidence ongoing settlement on markers installed far away from station TS22 (T228) and facility building TE22A (T302); these markers are assumed to provide a free field condition.

Information corresponding to 17 markers were available for comparison, 10 from TS22 (T228) and 7 from TE22A (T302). The detail of the monitored points and their distance to ongoing construction works are:

- TS22: LG28A019 (66m), LG28A020 (105m), LG28A055 (66m), LG28A056 (105m), LG28B019 (115m), LG28B020 (70m), LG28C035 (66m), LG28C036 (40m), LG28C055 (115m) and LG28C056 (105m).
- TE22A: LG290020 (20m), LG290030 (38m), LG290065 (38m), LG290070 (38m), LG290075 (38m), LG290080 (38m) and LG290085 (38m).

Figure 4-11 and Figure 4-12 present plan views of TS22 and TE22A with the considered markers and their distances from ongoing construction works. Figure 4-13 and Figure 4-14 present the measured settlement in time. Settlement measurements in TS22 date from Aug/15 to present while in TEA22 measurements start in Jul/17.

Stratigraphies in markers locations near TS22 and TE22A had to be estimated from the ground conditions observed in these particular locations; 3D extrapolation based on boreholes in TS22 and TE22A was provided by Dr. Yuepeng Dong. The reliability of the methodology implemented is limited considering that the extrapolation distance was generally between 30 to 70m, sometimes +100m.

Settlements rates were calculated as the slope of the best fitting line. The periods considered varied depending on the available information. Rates considering all the information were calculated. The extrapolated stratigraphies for each settlement marker and the calculated settlement rates for T228 and T302 are informed in Table 4-1 and Table 4-2.

4.4. ANALYSES OF MARINA BAY AREA WITH MIT-SR

The reclamation process in the Marina bay area was analyzed utilizing the MIT-SR constitutive model (Yuan, 2016) to represent the compression behavior of the UMC, F2 and LMC units and assess the performance of the model as a predictive tool for estimating long-term settlement rates.

The followed working methodology was:

1. Determination of specific stratigraphies to represent the cases encountered in T228 and T302. Geometry was simplified considering the symmetry of the problem (i.e., only 1D simulations were considered).
2. Calibration of UMC, F2 and LMC material parameters with available laboratory and field tests. Then, calibration of UMC, F2 and LMC state parameters for the OCRs considered in the Marina Bay area. The calibration of the MIT-SR parameters for these 3 materials was entirely based on laboratory tests.
3. FEM simulation of the reclamation process and later consolidation with PLAXIS 2D software (Version v2017.01).
4. Comparison of predictions against monitoring data and assessment of the performance of the MIT-SR model.

4.4.1. Selection of stratigraphies for analyses in T228 and T302

4.4.1.1. Soil thicknesses in T228 and T302

All the available information from the boreholes was analyzed to establish the thicknesses of all the layers and define stratigraphies that represent typical cases.

For this purpose, boreholes were digitized and thicknesses of Fill, UMC, F2 and LMC were calculated. To obtain a robust representation of the site, a simplified methodology was followed and materials above UMC were considered as Fill, materials between UMC and LMC were unified as F2 and all materials below LMC were defined as OA. Therefore, from top to bottom the soil layers were: Fill, UMC, F2, LMC and OA.

With all the boreholes digitized, a histogram of layer's thicknesses were calculated for each site; 62 and 114 boreholes were considered in T228 and T302, respectively. Since total settlement and creep rate are directly related to total Marine Clay thickness, the histogram also considered total Marine Clay (MC) as the summation of UMC and LMC. Table 4-3 presents the histograms for each site separately and also, a histogram of marine clay for both sides.

A summary of the information provided by these histograms:

- Fill layer varies principally between 10 to 14m in T228 whereas in T302 it varies between 8 to 16m. There are some isolated cases with Fill layers of +19m and the most representative value is 13.0m.
- UMC layer varies principally between 7 to 12m in T228 whereas in T302 it varies between 6 to 15m. The larger observed thickness was around 15.5m.
- F2 layer varies principally between 1 to 5m in T228 whereas in T302 it varies between 1 to 6m. This layer exhibits a strong concentration in the range between 2 and 4m in both areas; the most representative value is 3.5m.
- LMC varies principally between 3 to 17m in T228 whereas in T302 it varies between 3 to 20m. LMC variation and height is larger than the observed in UMC.
- MC, defined as the addition of UMC and LMC, varies principally between 10 to 25m (peak in 16.5m) in T228 whereas in T302 it varies between 12 to 29m (peaks in 21.5 and 23.5m). Marine clay thicknesses in T302 are generally slightly larger than in T228. When considering both areas together, marine clay varies between 10 to 30m with a concentration in heights between 21 to 26m.

4.4.1.2. Statistical analyses of stratigraphy and representative thicknesses of layers

The information provided by the boreholes in T228 and T302 was statistically analyzed by assuming that their probability density function was normal and fitting values to the available data sets. Mean (μ) and standard deviations (σ) were calculated for 3 data sets (T228, T302 and T228+T302) and the 95% confidence interval were determined ($\mu \pm 2\sigma$). The results from these fitting procedures are informed in Table 4-4.

From these analyses, the following facts were extracted:

- Fill: $H_{avg}=13.0m$ (T228 & T302) and the 95% confidence interval is 8.2-17.6m.

- UMC: $H_{avg}=9.6\text{m}$ (T228 & T302) and the 95% confidence interval is 5.5-13.8m.
- F2: $H_{avg}=3.5\text{m}$ (T228 & T302) and the 95% confidence interval is 1.2-5.9m.
- LMC: $H_{avg}=10.3\text{m}$ (T228 & T302) and the 95% confidence interval is 2.1-18.5m.
- MC: $H_{avg}=19.3\text{m}$ (T228 & T302) and the 95% confidence interval is 9.0-29.7m.

To analyze the settlement and creep rates in both areas, a set of representative stratigraphies was defined to address the potential thicknesses of UMC and LMC based on the statistically defined 95% confidence intervals. Therefore, UMC and LMC thicknesses were varied to account for the observed changes in the area.

The selected thicknesses for the Fill and F2 were 13.0 and 3.5m, respectively; these values correspond to the most representative values observed in the thickness histograms (Table 4-3) and the mean value for T228 & T302 (Table 4-4).

As regards UMC and LMC, the representative ranges considered were very similar to the calculated 95% confidence intervals: 4.5 to 14.5m for the UMC and 1.5 to 17.5m for the LMC. For both materials a 2.0m step between cases was considered resulting in 6 cases for UMC (4.5m, 6.5m, 8.5m, 10.5m, 12.5m and 14.5m) and 9 cases for LMC (1.5m, 3.5m, 5.5m, 7.5m, 9.5m, 11.5m, 13.5m, 15.5m and 17.5m). The combination of the thicknesses selected for UMC and LMC resulted in total marine clay thicknesses varying between 6.0-32.0m, addressing the 95% confidence interval of MC.

The summary of the thicknesses considered is: i) Fill: 13.0m; ii) UMC: 4.5m, 6.5m, 8.5m, 10.5m, 12.5m and 14.5m; iii) F2: 3.5m and iv) LMC: 1.5m, 3.5m, 5.5m, 7.5m, 9.5m, 11.5m, 13.5m, 15.5m and 17.5m. The combination of the quoted thicknesses resulted in 54 cases of interest.

4.4.1.3. Preconsolidation profile and stratigraphies for FEM analyses

Following section 4.2.2 and Figure 4-9, a profile was defined in the channel and adopted as the representative, baseline, pre-reclamation profile for the Bay area. Considering this base case and the 54 cases already defined by the UMC and LMC thicknesses (Table 4-5), the elevations and OCR of the units were determined.

Since the objective of these analyses were to determine a robust set of results to predict creep rates, the definition of the 54 stratigraphies and models was simplified:

1. Top of the UMC layer was assumed at EL. +93.0mRL, as observed in boreholes executed in the channel (Figure 4-8). The fill height was 13.0m and represented as a uniform charge.
2. The base of UMC was calculated from the UMC thickness corresponding to each case.
3. The base of F2 was calculated considering a constant 3.5m thickness for all cases.
4. The base of LMC was calculated from the LMC thickness corresponding to each case.
5. Old Alluvium was included in the geometry of the FEM model. The influence of the thickness of the OA in the numerical simulations was analyzed separately and proved to have negligible influence in the total settlement and creep rate.

Within the UMC and LMC layers, the individual OCRs were selected considering the original preconsolidation profile (Figure 4-9) and the baseline profile defined. The detailed stratigraphies are summarized from Table 4-6 to Table 4-9.

4.4.2. Selection of hydraulic parameters

The hydraulic conductivities for the materials were obtained from Arup (2014), Mott MacDonald (2015), Amberg & TTI (2004) and Choi (1982). The summary of all the available information is detailed in Table 4-10. Where possible, values based on field tests were adopted; all c_k values were adopted based on information reported in Choi (1982).

The summary of the selected values is: i) UMC: $k_y=2.1 \cdot 10^{-8}$ m/s and $c_k=0.82$; ii) F2: $k_y=1.0 \cdot 10^{-8}$ m/s and $c_k=0.82$; iii) LMC: $k_y=6.4 \cdot 10^{-9}$ m/s and $c_k=0.82$ and iv) OA: $k_y=1.0 \cdot 10^{-7}$ m/s and $c_k=0.82$.

4.4.3. Finite Element Model stages

Simulated stages of the model are detailed in Table 4-11 and consisted on:

1. Initial phase (pre-reclamation) where model is initialized and initial stresses are generated (Figure 4-15).
2. Construction phase with a duration of 7 years (2555 days), from Jan/78 to Jan/85 (CD=0 to CD=2555). This stage is a consolidation stage in which the 260kPa distributed load (equal to 13.0m of fill with a specific weight of 20kN/m³) is activated linearly in time (a new feature available in PLAXIS v.2017.01).
3. Consolidation stage of 33 years (12050 days), until 31/Dec/17 (CD=2555 to CD=14605).
4. Consolidation stage of 30 years (10950 days), until 31/Dec/47 (CD=14605 to CD=25555).

Model geometry, boundary conditions, materials and mesh are presented in Figure 4-15; this figure corresponded to PLX34, a typical case of the 54 stratigraphies analyzed. Considering the symmetry of the problem studied, 1D simulations were executed. The hydraulic boundary conditions were open at the top (y_{\max}), closed in both sides (x_{\min} and x_{\max}) and closed at the bottom (y_{\min}). OA included in the simulations corresponded to OA(E), the most weathered portion of the OA (Arup, 2014 and Mott MacDonalds, 2015), and below would be the OA(D) which hydraulic conductivity was reported to be 10 times lower in comparison to OA(E). Therefore, the bottom of the OA(E) was considered to be closed.

Old Alluvium (OA) parameters were obtained from Arup (2014) and Mott MacDonald (2015) and are presented in Table 4-12; selected parameters were average values from these reports. UMC, F2 and LMC material and state parameters are presented separately in Table 4-13 and Table 4-14. The explanation and calibration procedure for each of the parameters is detailed in a later section.

4.4.4. MIT-SR calibration for Kallang Formation Units (UMC, F2 & LMC)

MIT-SR contains some parameters that can be calculated with equations and laboratory tests while other parameters, including all the state parameters, require the numerical simulation of laboratory tests to later compare the results against real measurements. For this purpose, the point-level laboratory test simulator “Modlab” (originally developed by Kavvas, 1982), adapted by Yuan (2016) to include MIT-SR model, was utilized. In Modlab, all stresses are normalized by the atmospheric pressure ($p_{\text{atm}}=100\text{kPa}$) and therefore, are dimensionless.

MIT-SR was calibrated for UMC and LMC, while the F2 material was considered as LMC with a higher OCR. The calibration procedure for each material was divided in two separate stages:

1. Calibration of material parameters with existing laboratory and field data.
2. Determination of state parameters for each material for the OCR profile selected with the all the material parameters calibrated.

4.4.4.1. Material parameters

Material parameters were calibrated utilizing laboratory tests from Corral and Whittle (2010), Kiso-Jiban (1978), Choi (1982) and field shear wave tests. Corral and Whittle (2010) specified tests executed on UMC and LMC while the rest of the sources did not specify which Marine Clay

was tested. Therefore, they were supposed to be representative of the behavior of both materials and used for their calibrations.

The simulation methodology for 1D consolidation, unloading and CK_0UC/E triaxial tests followed the procedure described by Sheahan (1991):

1. A hypothetical sample with initial $K_0=1.0$, $\sigma'_p=100\text{kPa}$ and $OCR=4$ is considered; the isotropic, effective stress state is $\sigma'_v/\sigma'_p = \sigma'_h/\sigma'_p=0.25$ ($\sigma'_p=p_{atm}$). This initial condition is assumed to have negligible creep effects.
2. K_0 -consolidation at a vertical strain rate of $0.10\%/hr$ from the initial stress state to a vertical effective stress $\sigma'_v/p_{atm}=4.0$. At this state, the soil reaches a normally consolidated state.
3. 1D Creep is allowed during a period of 24 hours at a constant effective stress state.

The next stage depends on the type of test simulated:

- For undrained triaxial compression or extension tests, the shearing is displacement-controlled type, where vertical displacements are imposed until reaching critical state. Triaxial tests were simulated at strain rates equal to $0.05\%/hr$ since no information of the strain rates utilized for these tests.
- For consolidation tests with $OCR=1.0$ followed by an unloading stage, the 24hr creep stage is followed by an unloading stage where vertical effective stresses are imposed allowing the sample to swell and track stresses and strains.

The detailed procedure for the calibration of each of parameter was:

1. The compressibility in the NC regime (ρ_c) was calculated in several IL oedometer tests and CRS tests from Choi (1982) and Kiso-Jiban (1978). Only samples tested in the NC regime were considered: SC-1/2/5/6/11/12/13/14/19/20/21/22 (IL tests from Choi, 1982), SC-15/16/17/18 (CRS tests from Choi, 1982) and BH8-U4/U6 (IL tests from Kiso-Jiban, 1978). Figure 4-16 presents void ratios against vertical effective stress for tests from Choi (1982), by fitting all values a general value was calculated, $\rho_c=0.28$. Kiso-Jiban tests were executed at lower stresses and could not be included in the same plot; ρ_c values of 0.29 and 0.28 were calculated separately for each of these tests. An average value, $\rho_c=0.28$ was selected to be representative of UMC and LMC considering the results from all the samples.

2. From Corral & Whittle (2010): $K_{0NC}=0.52$, $2G/K=0.94$ and $\phi'_{cs}=32.4^\circ$ (UMC), 27.0° (LMC). As stated previously, proximity of the Nicoll Highway (C824) site (Corral and Whittle, 2010) enables us to assume similar properties of the marine clays for T228 and T302.
3. Small strain elastic compressibility (C_b) is obtained from information provided in Tan et al. (2003). Field measurements of maximum shear stiffness (G_{max}), moisture content (w_n) and in-situ stress state (σ'_{v0}) in depth are available. Assuming a specific gravity (G_s) for marine clay of 2.75 and a saturated condition, void ratios are calculated for UMC and LMC. As described above, $2G/K=0.94$ and this value is utilized to determine Poisson's ratio. Small strain elastic compressibility (C_b) is a function of effective stress state (σ'), Poisson's ratio (ν'), void ratio (e) and small strain shear stiffness (G_{max}). Equations utilized for the estimation of this parameter are:

$$e = \omega_n G_s \quad (4.1)$$

$$\frac{2G}{K} = \frac{3(1 - 2\nu')}{1 + \nu'} \quad (4.2)$$

$$C_b = \frac{2}{3} \frac{e}{1 + e} \frac{1 + \nu'}{1 - 2\nu'} \frac{G_{max}/p_{atm}}{(\sigma'/p_{atm})^{1/3}} \quad (4.3)$$

This calculation procedure is analogous to the proposed in Yuan (2016) where the porosity (n) is calculated from the void ratio and a normalized shear stiffness (G_n) is calculation by equation 7.1 (Yuan, 2016). Then calculate C_b from G_n and ν' with equation 7.2 (Yuan, 2016):

$$n = \frac{e}{1 + e} \quad (4.4)$$

$$G_n = n \frac{G_{max}/p_{atm}}{(\sigma'/p_{atm})^{1/3}} \quad (4.5)$$

$$C_b = \frac{2}{3} G_n \frac{1 + \nu'}{1 - 2\nu'} \quad (4.6)$$

Calculated C_b values for UMC and LMC were 486 and 534 respectively (Table 4-15). Considering the similarity of these, the selected value for this parameter, for both UMC and LMC, is $C_b=510$.

4. D and r parameters are calibrated by fitting the unloading stages of several consolidation tests (Corral & Whittle, 2010). Consolidation and unloading simulations followed Sheahan (1991) procedure. Unloading stage is presented in $\sigma'_v/\sigma'_{v0}-\Delta\varepsilon_v$ space (no void ratio during unloading were available for this calibration). Stresses are normalized by the last vertical stress before unloading (σ'_{v0}) and $\Delta\varepsilon_v$ is the incremental vertical strain. Considering samples that were compressed into NC regime, the initial point of the unloading stage is $\sigma'_v/\sigma'_{v0}=1$ (OCR=1) and $\Delta\varepsilon_v$ progresses towards lower σ'_v/σ'_{v0} values with positive $\Delta\varepsilon_v$ due to swelling. The accuracy of the fitting is focused in the range of σ'_v/σ'_{v0} 1.0-0.2 (corresponding to OCR between 1 and 5). Although parameters are calibrated simultaneously, fitting first the r parameter and second the D parameter proved to be efficient: r parameters governs the general trend of the unloading and while D governs the swelling at $\sigma'_v/\sigma'_{v0}<0.5$ approximately. The influence of D and r parameters are presented in Figure 4-17. The selected values for UMC and LMC are $D=0.12$ and $r=3.80$.
5. ϕ'_m , m , w_s and ψ parameters are calibrated by fitting effective stress paths and shear stress strain curves in CK_0UC/E tests (Corral & Whittle, 2010) by simulating the consolidation procedure used in tests by Sheahan (1991). Parameters were sequentially calibrated: i) ϕ'_m was calibrated first by fitting the compression curve to the measured shear stress-strain during undrained shearing; ii) m was calibrated by fitting simultaneously the compression and extension curves from the measured effective stress paths; iii) w_s was calibrated by fitting the stiffness in the extension curve in the $\varepsilon_a-(\sigma'_v-\sigma'_v)/2\sigma'_{vc}$ space and iv) ψ was calibrated by refining the fitting of the extension curves in the $(\sigma'_v+\sigma'_v)/2\sigma'_{vc}-(\sigma'_v-\sigma'_v)/2\sigma'_{vc}$. The simulations corresponding to the selected values are presented in Figure 4-18 and Figure 4-19. The influence of each parameter are presented from Figure 4-20 to Figure 4-23 (parameters correspond to UMC). The selected values for UMC and LMC are $\phi'_m=22.0^\circ$, 18.0° (UMC, LMC), $m=0.2$, $w_s=60$ and $\psi=15$.

6. Dilation behavior assumed to be zero, therefore: $D_L=0$. No CK_0UC/E tests with samples with $OCR>2$ available to calibrate this parameter. In addition, this parameter was of little importance for the consolidation and creep cases that were analyzed with FEM models.
7. Compressibility in secondary compression (ρ_α) values were calculated from IL tests from Kiso-Jiban report (1978); digitized information was included in Appendix B. For each of the four tests considered, a ρ_α value was calculated considering all the secondary compression (Table 4-20 and Figure 4-24). Values obtained ranged from 0.0056 to 0.0079 with an average ρ_α value of 0.007. The average value was selected, resulting in a selected $\rho_\alpha/\rho_c=0.025$. Choi (1982) reported $C_\alpha/C_c=0.025-0.040$ and therefore, the selected value is at the lower range.
8. Rate-sensitivity of steady state of R_a (β) was calculated from CRS tests from Choi (1982). Base information are the CRS tests in the $\sigma'_v - e$ space (digitized information was included in Appendix B), each with a different strain rate ($\dot{\epsilon}$). For different void ratios that correspond to the NC regime exhibited in the CRS tests, the corresponding σ'_v level for that strain rate is identified and β values calculated (Table 4-16). This information is replotted in a $\dot{\epsilon} - \sigma'_v$ space where it is illustrated the different levels of effective vertical stress for each void ratio, depending on the strain rate imposed in the test (Figure 4-25); for each void ratio, the slope of the fitting line is a potential value of β . Considering that MIT-SR was developed under the assumption that β should generally lie in the range of 0 to ρ_α/ρ_c (already calibrated and selected $\rho_\alpha/\rho_c=0.025$), the selected value was $\beta=0.025$.
9. Non-linear variation of rate dependency with stress history (β_2) was calculated from consolidation tests from Choi (1982). Tests SC-11, SC-12, SC-13 and SC-14 have each four creep stages: 1000, 2000, 4000 and 8000psf. Surcharge stages previous to creep stages generate OCR in the samples: $OCR=1.20-1.25$ (SC-12), $OCR=1.40-1.50$ (SC-13) and $OCR=1.60-1.75$ (SC-14).
Creep stages, initially informed in $t - \epsilon$ space are re-scaled in $t - \epsilon'$ space where $\epsilon' = 0$ at the peak of the rebound resulting in $\epsilon' > 0$, always compressive. From $t - \epsilon'$ space, strain rates can be calculated from the incremental strain in time ($\dot{\epsilon}'$) and the same test can be plotted in a $\dot{\epsilon}' - \epsilon'$ space. From the information plotted in this space, two values of interest for the MIT-SR calibration can be obtained. By fitting a straight line to the test

points in this space, $\hat{C}_{\alpha\varepsilon}$ is the slope of the line and $\dot{\varepsilon}_1$ is strain rate at $\varepsilon' = 0$; i.e., creep rate right after the rebound finishes. $\hat{C}_{\alpha\varepsilon}$ is utilized for the calibration of β_2 whereas $\dot{\varepsilon}_1$ will be utilized for β_3 calibration.

Figure 4-26 presents tests SC-12 to SC-14 in the $\dot{\varepsilon}' - \varepsilon'$ space. From SC-11, the sample tested without surcharge, C_α is determined for each creep stage and, by dividing C_α by the $1+e_0$ (initial void ratio at the creep stage), $C_{\alpha\varepsilon}$ is obtained. The equation utilized for the β_2 parameter calibration is:

$$\frac{\hat{C}_{\alpha\varepsilon}}{C_{\alpha\varepsilon}} = \frac{2}{OCR^{\beta_2} + 1} \quad (4.7)$$

Table 4-17, Table 4-18 and Table 4-19 present the calculated values from the line fitting and β_2 calibration values. Figure 4-27 presents the calibration curves utilized for the selection. The selected value is $\beta_2=6.5$.

10. Reduction of creep rate during unloading parameter (β_3) was obtained from creep tests from Choi (1982) and consolidation tests from Kiso-Jiban (1978). As detailed in the β_2 determination, $\dot{\varepsilon}_1$ is obtained from the line fitting in the $\dot{\varepsilon}' - \varepsilon'$ space of the creep tests on samples SC-12 to SC-14; strain rate at EOP ($\dot{\varepsilon}_{100}$) was not reported by Choi (1982). Therefore, this parameter was calculated from Kiso-Jiban report (1978) where for each of the four consolidation tests considered, $\dot{\varepsilon}_{100}$ was obtained from the curves informed. Values obtained ranged from 0.0018 to 0.0054 hr^{-1} with an average value of 0.0038 hr^{-1} . The selected value was the average, resulting in $\dot{\varepsilon}_{100}=0.0038 \text{ hr}^{-1}$. The equation utilized for the β_3 parameter calibration is:

$$\frac{\dot{\varepsilon}_1}{\dot{\varepsilon}_{100}} = OCR^{-\beta_3} \quad (4.8)$$

Table 4-17, Table 4-18 and Table 4-19 present the calculations and values considered for the β_3 calibration. Figure 4-27 presents the calibration curves utilized for the selection. The selected value is $\beta_3=9.0$.

11. Reference strain rate ($\dot{\varepsilon}_{ref}$) was obtained from Kiso-Jiban report (1978), for each of the four consolidation tests considered (digitized information was included in Appendix B).

The strain rate at 1 day ($\dot{\epsilon}_{ref}$), from the start of the test, were calculated. Available values were at 8, 24 and 48hrs from the start of the test. Strain rates were calculated between 8 to 24hr ($\dot{\epsilon}_{8-24}$), and from 24 to 48hr ($\dot{\epsilon}_{24-48}$). The average from these two values ($\dot{\epsilon}_{8-24}$ and $\dot{\epsilon}_{24-48}$) was considered as the reference strain rate of the test ($\dot{\epsilon}_{ref}$). Values obtained ranged from 3.8E-3 to 5.1E-3 day⁻¹ with an average value of 4.4E-3 day⁻¹ (Table 4-20). The selected value was the average, resulting in $\dot{\epsilon}_{ref}=4.4E-3$ day⁻¹.

4.4.4.2. State parameters

MIT-SR is a rate-dependent model and strain rate effects are defined by state variables which depend on the stress history of the soil. To accurately describe creep phenomena, it is critical the methodology utilized to define and specify initial state variables.

The OCRs considered for the UMC were 5.70, 2.40, 1.85 and 1.60 while the OCRs considered for the LMC were 1.40, 1.35, 1.30 and 1.25; F2 was assumed to have an OCR=7.30.

The simulation methodology followed the procedure described by Sheahan (1991):

1. A hypothetical sample with initial $K_0=1.0$, $\sigma'_p=100\text{kPa}$ and $\text{OCR}=4$ is considered; the isotropic, effective stress state is $\sigma'_v/\sigma'_p = \sigma'_h/\sigma'_p=0.25$ ($\sigma'_p=p_{\text{atm}}$). This initial condition is assumed to have negligible creep effects.
2. K_0 -consolidation at a vertical strain rate of 0.10%/hr from the initial stress state to a vertical effective stress $\sigma'_v/p_{\text{atm}}=4.0$. At this state, the soil reaches a normally consolidated state.
3. 1D Creep is allowed during a period of 24 hours at a constant effective stress state.
4. Unloading at a 0.05%/hr rate to a certain vertical effective stress to materialize the target OCR in the sample; e.g., final $\sigma'_v/p_{\text{atm}}=1.29$ for an $\text{OCR}=3.10$.
5. 1D Creep is allowed during a period of 20 years hours at a constant effective stress state. State parameters were obtained at the end of this stage. For longer periods of time, there were no visible differences in the state variables obtained; 20 years was a period long enough to simulate field conditions of the soil.

Table 4-14 provides detailed information on the state parameters obtained for UMC, F2 and LMC for each OCR.

4.5. SIMULATION OF SETTLEMENTS DUE TO LAND RECLAMATION

The results of the simulations modelling the reclamation process in the 54 stratigraphies that represented underground conditions in T228 and T302 are presented from Table 4-21 to Table 4-26.

The progression of total settlement in time was recorded from the beginning of the reclamation process (for which a duration of 7 years was assumed) until December/2047. For each of the 54 models, the total settlement and settlement rate were determined at the 31st of December of 1987 until 2047, at a 5 year step. Additionally, values at the end of 1985 and 2005 are considered.

Table 4-27 and Table 4-28 present minimum, average and maximum results between 2017 and 2047 organized by marine clay thickness. As originally supposed, settlement and creep rates directly depend on the total thickness of the marine clay: higher thicknesses result in higher settlements and creep rates. At constant marine clay thicknesses, slight differences were sometimes encountered between minimum, average and maximum settlement and creep rates calculated for the cases considered. Considering the robustness of the analyses and the quality of the site information, each average value was considered as the representative value for later comparisons against monitoring information.

The calculated average results were condensed in Table 4-29 and Table 4-30 and presented in Figure 4-28. Calculated values for each stage are presented separately from Figure 4-29 to Figure 4-36. For 9m and 30m of marine clay (values that define the calculated 95% confidence interval), current settlement and creep rate would be 2.62m and 2mm/yr and 4.23m and 18mm/yr, respectively. For 19.3m (the mean thickness of marine clay) current settlement and creep rate would be 3.67m and 10mm/yr. In other words, most of the observed creep rates in free field conditions in the Bay area are expected to be between 2 and 18mm/yr.

The progression in time of settlement, settlement rate and excess pore pressure for six cases are presented from Figure 4-37 to Figure 4-48. By the end of the reclamation, maximum excess pore pressure is approximately 150kPa while in 2017 the excess pore pressure is lower than 20kPa. Therefore, the settlement rate from 2017 onwards can be attributed principally to creep.

As can be observed in Figure 4-13, settlement rates in T228 are more consistent and data shows settlement increasing linearly with time. For the majority of points, annual rates of settlement are

consistent (i.e., show little inter-annual variation) over the 3 year monitoring period 2015–2018. Their elevations vary between EL. +103.2 and +104.5mRL.

On the other hand, Figure 4-14 shows settlement information from markers in T302 and they show behaviors that are not directly explained by free field consolidation and creep. Markers LG290020 and LG290030 (EL. +104.4mRL) correspond to the west side of TE22A while the rest (LG290065 to LG290085, EL. +105.2 to +106.5mRL) are located to the east and belong to a golf course which construction was finished by 2006 and included additional fillings. Markers in the golf course have higher elevations, in average 1.0 to 2.0m higher than elevations of the other markers. Markers to the west (LG290020 and LG290030) exhibit behaviors similar to T228 while markers near or in the golf course (LG290065 to LG290085) exhibit a higher settlement rate until in November 2017. Then, around May 2018, some points show rebound which could be explained by material removed in the golf course. Therefore, the comparison is focused against T228 markers while T302 markers are considered to be strongly affected by the golf course and do not represent free field conditions. It also must be noted that the stratigraphies corresponding to the markers were not informed and had to be assumed from extrapolations.

When comparing current information provided by site measurements against predictions, the first comparison is the current ground elevation. The cases analyzed considered an upper UMC elevation of +93mRL and 13m; initial ground elevation would be +106mRL. If lowering these values by the settlement predicted by the simulations, current predicted elevations would be between +101.7 and +103.9mRL; lower values for cases with larger marine clay and higher values for cases with lower marine clay thickness. The reference level informed in T228 markers ranged between +103.2 and +104.5mRL and those for T302 ranged between +104.4 and +106.5mRL.

The second comparison against current measurements is between settlement rates and also depends on the total thickness of the marine clay. Markers in T228 have marine clay thicknesses between 10.1 and 23.1m and calculated settlement rates were 24-62mm/yr while the markers considered in T302, LG290020 and LG290030, have 22.5 and 20.1m of marine clay and calculated settlement rates were 40 and 32mm/yr. For these marine clay values, predictions estimate current settlement rate between 9 and 15mm/yr. Figure 4-49 presents the predicted current settlement rates and the calculated values.

In both comparisons, predictions fall short to accurately describe current ground elevations and creep rates. There are some factors that could contribute to explain these differences. The main issue to be addressed is that the 1D problem modelled is sensitive to the hydraulic conductivities of UMC, F2 and LMC. The limitation of the information available to select this parameter conditioned the analysis. If selecting lower values than the considered in these analyses ($k_v=2.1E-8$ m/s for UMC and $k_v=6.4E-9$ m/s for F2 and LMC), predictions by 2017 would change and lower settlements and higher rates would be expected. These values would better compare with site measurements in T228 and markers in T302 not affected by the golf course.

With the hydraulic conductivities appropriately determined, additional factors that could enhance predictions could be:

1. Consider the correct fill height for each area. The selected height of 13m represented an average condition.
2. Stratigraphies considered always the top of UMC at EL. +93mRL. Refinements in this value would directly result in better estimates of current ground elevation.
3. The analyzed stratigraphies represented a simplified soil profile with only 5 geotechnical units (Fill, UMC, F2, LMC and OA). The presence of other compressible units like fluvial sands (F1), fluvial clays (F2) or estuarine clays (E) above UMC or below LMC were not included in these simulations. These simplifications were not conservative in terms of settlement rates. Therefore, if pursuing more detailed analyses, these materials should be included in the simulations.

Table 4-1: Extrapolated stratigraphies in markers near TS22 (T228) and calculated settlement rates.

Marker	Ref. Level	H FILL	H UMC	H F2	H LMC	H MC	$\Delta u/\Delta t$ ALL
[-]	[EL]	[m]	[m]	[m]	[m]	[m]	[mm/yr]
LG28A019	103.7	11.3	9.5	1.2	0.6	10.1	25.7
LG28A020	104.4	14.6	7.3	4.0	12.5	19.8	53.7
LG28A055	103.7	11.7	9.2	1.7	3.3	12.5	23.9
LG28A056	104.0	13.5	6.6	4.3	12.7	19.3	38.1
LG28B019	104.1	12.2	10.2	2.0	8.7	18.9	28.9
LG28B020	104.0	13.6	5.9	4.8	11.4	17.3	26.2
LG28C035	103.3	11.3	10.7	2.8	11.9	22.6	29.8
LG28C036	104.3	13.2	8.6	4.8	11.2	19.8	61.8
LG28C055	104.5	12.5	11.0	2.4	10.8	21.8	35.6
LG28C056	103.2	12.3	8.2	4.1	14.9	23.1	30.1

Table 4-2: Extrapolated stratigraphies in markers near TE22A (T302) and calculated settlement rates.

Marker	Ref. Level	H FILL	H UMC	H F2	H LMC	H MC	$\Delta u/\Delta t$ ALL
[-]	[EL]	[m]	[m]	[m]	[m]	[m]	[mm/yr]
LG290020	104.4	13.2	10.4	3.0	12.1	22.5	39.7
LG290030	104.4	13.4	9.9	5.8	10.2	20.1	31.9
LG290065	105.2	12.9	8.9	4.4	12.1	21.0	21.0
LG290070	106.0	12.9	8.7	5.0	12.1	20.8	37.5
LG290075	105.8	13.0	8.4	5.2	12.0	20.4	55.3
LG290080	105.7	13.1	8.2	5.2	11.5	19.7	57.8
LG290085	106.5	13.1	8.1	4.9	10.5	18.6	71.6

Table 4-3: Histogram of layer's thicknesses in T228 and T302.

Havg	T228						T302						Both	
	FILL	UMC	F2	LMC	MC*		FILL	UMC	F2	LMC	MC*		MC*	
[m]	[-]	[-]	[-]	[-]	[-]	[%]	[-]	[-]	[-]	[-]	[-]	[%]	[-]	[%]
0.5	0	0	0	0	0	0	0	0	0	0	0	0	0	0
1.5	0	0	7	0	0	0	0	0	7	1	0	0	0	0
2.5	0	1	14	1	0	0	0	1	36	1	0	0	0	0
3.5	0	0	29	8	0	0	0	0	39	3	0	0	0	0
4.5	0	0	8	2	2	3	0	2	13	4	0	0	2	1
5.5	0	0	3	5	0	0	0	1	17	9	1	1	1	1
6.5	0	0	3	4	0	0	0	5	2	7	0	0	0	0
7.5	0	9	0	7	1	2	0	7	0	7	0	0	1	1
8.5	0	22	0	3	0	0	4	19	0	4	0	0	0	0
9.5	0	6	0	2	0	0	11	28	0	9	0	0	0	0
10.5	2	10	0	6	3	5	4	21	0	2	1	1	4	2
11.5	15	3	0	5	5	8	10	12	0	10	1	1	6	3
12.5	15	2	0	6	5	8	34	11	0	24	2	2	7	4
13.5	19	1	0	3	1	2	18	3	0	13	5	4	6	3
14.5	0	1	0	7	5	8	21	3	0	6	4	4	9	5
15.5	2	0	0	1	3	5	9	1	0	6	6	5	9	5
16.5	0	0	0	2	9	15	1	0	0	3	4	4	13	7
17.5	0	0	0	0	3	5	1	0	0	1	6	5	9	5
18.5	0	0	0	0	1	2	1	0	0	2	7	6	8	5
19.5	1	0	0	0	2	3	0	0	0	2	7	6	9	5
20.5	1	0	0	0	2	3	0	0	0	0	7	6	9	5
21.5	1	0	0	0	5	8	0	0	0	0	13	11	18	10
22.5	1	0	0	0	6	10	0	0	0	0	9	8	15	9
23.5	0	0	0	0	5	8	0	0	0	0	14	12	19	11
24.5	1	0	0	0	2	3	0	0	0	0	12	11	14	8
25.5	0	0	0	0	0	0	0	0	0	0	8	7	8	5
26.5	0	0	0	0	0	0	0	0	0	0	2	2	2	1
27.5	0	0	0	0	2	3	0	0	0	0	2	2	4	2
28.5	0	0	0	0	0	0	0	0	0	0	2	2	2	1
29.5	0	0	0	0	0	0	0	0	0	0	1	1	1	1
30.5	0	0	0	0	0	0	0	0	0	0	0	0	0	0

*: $H_{MC} = H_{UMC} + H_{LMC}$.

Table 4-4: Statistical results from histogram statistical analyses in data sets.

VARIABLE	T228 & T302					T228					T302				
	FILL	UMC	F2	LMC	MC*	FILL	UMC	F2	LMC	MC*	FILL	UMC	F2	LMC	MC*
[-]	[m]	[m]	[m]	[m]	[m]	[m]	[m]	[m]	[m]	[m]	[m]	[m]	[m]	[m]	[m]
MIN	8.4	2.1	1.2	1.2	0.0	11.0	2.1	1.2	2.6	0.0	8.4	2.2	1.3	1.2	5.4
μ	12.9	9.6	3.5	10.3	19.3	13.3	9.2	3.4	9.3	16.9	12.7	9.9	3.6	10.8	20.6
MAX	24.2	15.0	6.2	20.5	29.4	24.2	14.0	6.1	20.5	27.5	18.9	15.0	6.2	19.4	29.4
σ	2.4	2.1	1.2	4.1	5.2	2.8	1.8	1.1	4.2	5.7	2.1	2.1	1.2	4.0	4.4
$\mu-1.\sigma$	10.6	7.6	2.4	6.2	14.1	10.5	7.4	2.3	5.1	11.2	10.7	7.7	2.4	6.8	16.3
$\mu+1.\sigma$	15.3	11.7	4.7	14.4	24.5	16.1	11.1	4.5	13.5	22.6	14.8	12.0	4.8	14.7	25.0
$\mu-2.\sigma$	8.2	5.5	1.2	2.1	9.0	7.7	5.5	1.2	1.0	5.6	8.6	5.6	1.2	2.8	11.9
$\mu+2.\sigma$	17.6	13.8	5.9	18.5	29.7	18.9	12.9	5.6	17.7	28.2	16.9	14.1	6.0	18.7	29.4
$\mu-3.\sigma$	5.9	3.5	0.0	-2.0	3.8	4.9	3.7	0.1	-3.2	-0.1	6.5	3.5	0.0	-1.1	7.5
$\mu+3.\sigma$	20.0	15.8	7.1	22.6	34.8	21.7	14.7	6.7	21.9	33.9	18.9	16.2	7.2	22.7	33.7

*: $H_{MC}=H_{UMC}+H_{LMC}$.

Table 4-5: Representative thicknesses considered in the PLAXIS analyses.

PLAXIS	FILL [m]	UMC [m]	F2 [m]	LMC [m]	MC [m]	PLAXIS	FILL [m]	UMC [m]	F2 [m]	LMC [m]	MC [m]
PLX01	13.0	4.5	3.5	1.5	6.0	PLX28	13.0	10.5	3.5	1.5	12.0
PLX02	13.0	4.5	3.5	3.5	8.0	PLX29	13.0	10.5	3.5	3.5	14.0
PLX03	13.0	4.5	3.5	5.5	10.0	PLX30	13.0	10.5	3.5	5.5	16.0
PLX04	13.0	4.5	3.5	7.5	12.0	PLX31	13.0	10.5	3.5	7.5	18.0
PLX05	13.0	4.5	3.5	9.5	14.0	PLX32	13.0	10.5	3.5	9.5	20.0
PLX06	13.0	4.5	3.5	11.5	16.0	PLX33	13.0	10.5	3.5	11.5	22.0
PLX07	13.0	4.5	3.5	13.5	18.0	PLX34	13.0	10.5	3.5	13.5	24.0
PLX08	13.0	4.5	3.5	15.5	20.0	PLX35	13.0	10.5	3.5	15.5	26.0
PLX09	13.0	4.5	3.5	17.5	22.0	PLX36	13.0	10.5	3.5	17.5	28.0
PLX10	13.0	6.5	3.5	1.5	8.0	PLX37	13.0	12.5	3.5	1.5	14.0
PLX11	13.0	6.5	3.5	3.5	10.0	PLX38	13.0	12.5	3.5	3.5	16.0
PLX12	13.0	6.5	3.5	5.5	12.0	PLX39	13.0	12.5	3.5	5.5	18.0
PLX13	13.0	6.5	3.5	7.5	14.0	PLX40	13.0	12.5	3.5	7.5	20.0
PLX14	13.0	6.5	3.5	9.5	16.0	PLX41	13.0	12.5	3.5	9.5	22.0
PLX15	13.0	6.5	3.5	11.5	18.0	PLX42	13.0	12.5	3.5	11.5	24.0
PLX16	13.0	6.5	3.5	13.5	20.0	PLX43	13.0	12.5	3.5	13.5	26.0
PLX17	13.0	6.5	3.5	15.5	22.0	PLX44	13.0	12.5	3.5	15.5	28.0
PLX18	13.0	6.5	3.5	17.5	24.0	PLX45	13.0	12.5	3.5	17.5	30.0
PLX19	13.0	8.5	3.5	1.5	10.0	PLX46	13.0	14.5	3.5	1.5	16.0
PLX20	13.0	8.5	3.5	3.5	12.0	PLX47	13.0	14.5	3.5	3.5	18.0
PLX21	13.0	8.5	3.5	5.5	14.0	PLX48	13.0	14.5	3.5	5.5	20.0
PLX22	13.0	8.5	3.5	7.5	16.0	PLX49	13.0	14.5	3.5	7.5	22.0
PLX23	13.0	8.5	3.5	9.5	18.0	PLX50	13.0	14.5	3.5	9.5	24.0
PLX24	13.0	8.5	3.5	11.5	20.0	PLX51	13.0	14.5	3.5	11.5	26.0
PLX25	13.0	8.5	3.5	13.5	22.0	PLX52	13.0	14.5	3.5	13.5	28.0
PLX26	13.0	8.5	3.5	15.5	24.0	PLX53	13.0	14.5	3.5	15.5	30.0
PLX27	13.0	8.5	3.5	17.5	26.0	PLX54	13.0	14.5	3.5	17.5	32.0

*: Top EL of UMC=+93.0m.

Table 4-6: Stratigraphies considered in PLAXIS analyses PLX01 to PLX14.

PLAXIS	PLX01	PLX02	PLX03	PLX04	PLX05	PLX06	PLX07	PLX08	PLX09	PLX10	PLX11	PLX12	PLX13	PLX14
MC [m]	6	8	10	12	14	16	18	20	22	8	10	12	14	16

Layer	Layer thickness [m]													
FILL [m]	13.0	13.0	13.0	13.0	13.0	13.0	13.0	13.0	13.0	13.0	13.0	13.0	13.0	13.0
UMC [m]	4.5	4.5	4.5	4.5	4.5	4.5	4.5	4.5	4.5	6.5	6.5	6.5	6.5	6.5
F2 [m]	3.5	3.5	3.5	3.5	3.5	3.5	3.5	3.5	3.5	3.5	3.5	3.5	3.5	3.5
LMC [m]	1.5	3.5	5.5	7.5	9.5	11.5	13.5	15.5	17.5	1.5	3.5	5.5	7.5	9.5

Interface	Elevation [mRL]													
TOP UMC 5.70	93.0	93.0	93.0	93.0	93.0	93.0	93.0	93.0	93.0	93.0	93.0	93.0	93.0	93.0
UMC 5.70-2.40	90.0	90.0	90.0	90.0	90.0	90.0	90.0	90.0	90.0	90.0	90.0	90.0	90.0	90.0
UMC 2.40-1.85	88.5	88.5	88.5	88.5	88.5	88.5	88.5	88.5	88.5	86.5	86.5	86.5	86.5	86.5
UMC 1.85-1.60	-	-	-	-	-	-	-	-	-	-	-	-	-	-
UMC 1.60-F2	-	-	-	-	-	-	-	-	-	-	-	-	-	-
UMC-F2	88.5	88.5	88.5	88.5	88.5	88.5	88.5	88.5	88.5	86.5	86.5	86.5	86.5	86.5
F2-LMC 1.40	85.0	85.0	85.0	85.0	85.0	85.0	85.0	85.0	85.0	83.0	83.0	83.0	83.0	83.0
LMC 1.40-1.35	83.5	81.5	79.5	77.5	77.0	77.0	77.0	77.0	77.0	81.5	79.5	77.5	77.0	77.0
LMC 1.35-1.30	-	-	-	-	75.5	74.0	74.0	74.0	74.0	-	-	-	75.5	73.5
LMC 1.30-1.25	-	-	-	-	-	73.5	71.5	69.5	67.5	-	-	-	-	-
LMC-OA	83.5	81.5	79.5	77.5	75.5	73.5	71.5	69.5	67.5	81.5	79.5	77.5	75.5	73.5

Table 4-7: Stratigraphies considered in PLAXIS analyses PLX15 to PLX28.

PLAXIS	PLX15	PLX16	PLX17	PLX18	PLX19	PLX20	PLX21	PLX22	PLX23	PLX24	PLX25	PLX26	PLX27	PLX28
MC [m]	18	20	22	24	10	12	14	16	18	20	22	24	26	12

Layer	Layer thickness [m]													
FILL [m]	13.0	13.0	13.0	13.0	13.0	13.0	13.0	13.0	13.0	13.0	13.0	13.0	13.0	13.0
UMC [m]	6.5	6.5	6.5	6.5	8.5	8.5	8.5	8.5	8.5	8.5	8.5	8.5	8.5	10.5
F2 [m]	3.5	3.5	3.5	3.5	3.5	3.5	3.5	3.5	3.5	3.5	3.5	3.5	3.5	3.5
LMC [m]	11.5	13.5	15.5	17.5	1.5	3.5	5.5	7.5	9.5	11.5	13.5	15.5	17.5	1.5

Interface	Elevation [mRL]													
TOP UMC 5.70	93.0	93.0	93.0	93.0	93.0	93.0	93.0	93.0	93.0	93.0	93.0	93.0	93.0	93.0
UMC 5.70-2.40	90.0	90.0	90.0	90.0	90.0	90.0	90.0	90.0	90.0	90.0	90.0	90.0	90.0	90.0
UMC 2.40-1.85	86.5	86.5	86.5	86.5	87.0	87.0	87.0	87.0	87.0	87.0	87.0	87.0	87.0	87.0
UMC 1.85-1.60	-	-	-	-	84.5	84.5	84.5	84.5	84.5	84.5	84.5	84.5	84.5	84.0
UMC 1.60-F2	-	-	-	-	-	-	-	-	-	-	-	-	-	82.5
UMC-F2	86.5	86.5	86.5	86.5	84.5	84.5	84.5	84.5	84.5	84.5	84.5	84.5	84.5	82.5
F2-LMC 1.40	83.0	83.0	83.0	83.0	81.0	81.0	81.0	81.0	81.0	81.0	81.0	81.0	81.0	79.0
LMC 1.40-1.35	77.0	77.0	77.0	77.0	79.5	77.5	77.0	77.0	77.0	77.0	77.0	77.0	77.0	77.5
LMC 1.35-1.30	74.0	74.0	74.0	74.0	-	-	75.5	73.5	74.0	74.0	74.0	74.0	74.0	-
LMC 1.30-1.25	71.5	69.5	67.5	65.5	-	-	-	-	71.5	69.5	70.0	70.0	70.0	-
LMC-OA	71.5	69.5	67.5	65.5	-	-	-	-	-	-	67.5	65.5	63.5	-

Table 4-8: Stratigraphies considered in PLAXIS analyses PLX29 to PLX42.

PLAXIS	PLX29	PLX30	PLX31	PLX32	PLX33	PLX34	PLX35	PLX36	PLX37	PLX38	PLX39	PLX40	PLX41	PLX42
MC [m]	14	16	18	20	22	24	26	28	14	16	18	20	22	24

Layer	Layer thickness [m]													
FILL [m]	13.0	13.0	13.0	13.0	13.0	13.0	13.0	13.0	13.0	13.0	13.0	13.0	13.0	13.0
UMC [m]	10.5	10.5	10.5	10.5	10.5	10.5	10.5	10.5	12.5	12.5	12.5	12.5	12.5	12.5
F2 [m]	3.5	3.5	3.5	3.5	3.5	3.5	3.5	3.5	3.5	3.5	3.5	3.5	3.5	3.5
LMC [m]	3.5	5.5	7.5	9.5	11.5	13.5	15.5	17.5	1.5	3.5	5.5	7.5	9.5	11.5

Interface	Elevation [mRL]													
TOP UMC 5.70	93.0	93.0	93.0	93.0	93.0	93.0	93.0	93.0	93.0	93.0	93.0	93.0	93.0	93.0
UMC 5.70-2.40	90.0	90.0	90.0	90.0	90.0	90.0	90.0	90.0	90.0	90.0	90.0	90.0	90.0	90.0
UMC 2.40-1.85	87.0	87.0	87.0	87.0	87.0	87.0	87.0	87.0	87.0	87.0	87.0	87.0	87.0	87.0
UMC 1.85-1.60	84.0	84.0	84.0	84.0	84.0	84.0	84.0	84.0	84.0	84.0	84.0	84.0	84.0	84.0
UMC 1.60-F2	82.5	82.5	82.5	82.5	82.5	82.5	82.5	82.5	80.5	80.5	80.5	80.5	80.5	80.5
UMC-F2	82.5	82.5	82.5	82.5	82.5	82.5	82.5	82.5	80.5	80.5	80.5	80.5	80.5	80.5
F2-LMC 1.40	79.0	79.0	79.0	79.0	79.0	79.0	79.0	79.0	77.0	77.0	77.0	77.0	77.0	77.0
LMC 1.40-1.35	77.0	77.0	77.0	77.0	77.0	77.0	77.0	77.0	77.0	77.0	77.0	77.0	-	-
LMC 1.35-1.30	75.5	73.5	74.0	74.0	74.0	74.0	74.0	74.0	75.5	73.5	74.0	74.0	74.0	74.0
LMC 1.30-1.25	-	-	71.5	69.5	70.0	70.0	70.0	70.0	-	-	71.5	69.5	70.0	70.0
LMC-OA	-	-	-	-	67.5	65.5	63.5	61.5	-	-	-	-	67.5	65.5

Table 4-9: Stratigraphies considered in PLAXIS analyses PLX43 to PLX54.

PLAXIS	PLX43	PLX44	PLX45	PLX46	PLX47	PLX48	PLX49	PLX50	PLX51	PLX52	PLX53	PLX54
MC [m]	26	28	30	16	18	20	22	24	26	28	30	32

Layer	Layer thickness [m]											
FILL [m]	13.0	13.0	13.0	13.0	13.0	13.0	13.0	13.0	13.0	13.0	13.0	13.0
UMC [m]	12.5	12.5	12.5	14.5	14.5	14.5	14.5	14.5	14.5	14.5	14.5	14.5
F2 [m]	3.5	3.5	3.5	3.5	3.5	3.5	3.5	3.5	3.5	3.5	3.5	3.5
LMC [m]	13.5	15.5	17.5	1.5	3.5	5.5	7.5	9.5	11.5	13.5	15.5	17.5

Interface	Elevation [mRL]											
TOP UMC 5.70	93.0	93.0	93.0	93.0	93.0	93.0	93.0	93.0	93.0	93.0	93.0	93.0
UMC 5.70-2.40	90.0	90.0	90.0	90.0	90.0	90.0	90.0	90.0	90.0	90.0	90.0	90.0
UMC 2.40-1.85	87.0	87.0	87.0	87.0	87.0	87.0	87.0	87.0	87.0	87.0	87.0	87.0
UMC 1.85-1.60	84.0	84.0	84.0	84.0	84.0	84.0	84.0	84.0	84.0	84.0	84.0	84.0
UMC 1.60-F2	80.5	80.5	80.5	78.5	78.5	78.5	78.5	78.5	78.5	78.5	78.5	78.5
UMC-F2	80.5	80.5	80.5	78.5	78.5	78.5	78.5	78.5	78.5	78.5	78.5	78.5
F2-LMC 1.40	77.0	77.0	77.0	75.0	75.0	75.0	75.0	75.0	75.0	75.0	75.0	75.0
LMC 1.40-1.35	-	-	-	-	-	-	-	-	-	-	-	-
LMC 1.35-1.30	74.0	74.0	74.0	73.5	74.0	74.0	74.0	74.0	74.0	74.0	74.0	74.0
LMC 1.30-1.25	70.0	70.0	70.0	-	71.5	69.5	70.0	70.0	70.0	70.0	70.0	70.0
LMC-OA	63.5	61.5	59.5	-	-	-	67.5	65.5	63.5	61.5	59.5	57.5

Table 4-10: Summary of reported hydraulic conductivities and selected values for PLAXIS simulations.

Layer	Selected		Arup (2014), T228			Mott MacDonald (2015), T302				AMBERG & TTI (2004)			Choi (1982)	
	kavg	kdesign	kmin	kmax	kdesign	kmin	kmax	kavg	kdesign	kmin	kmax	kdesign	kmin	kmax
[-]	[m/s]	[m/day]	[m/s]	[m/s]	[m/s]	[m/s]	[m/s]	[m/s]	[m/s]	[m/s]	[m/s]	[m/s]	[m/s]	[m/s]
Fill*	4.1E-06	3.5E-01	-	-	1.0E-06	3.0E-09	2.0E-05	4.1E-06	1.0E-05	-	-	1.0E-07	-	-
F1*	5.0E-06	4.3E-01	-	-	1.0E-06	1.2E-08	2.8E-05	5.0E-06	1.0E-05	-	-	1.0E-05	-	-
UMC	2.1E-08	1.8E-03	-	-	1.0E-08	5.5E-09	6.0E-08	2.1E-08	1.0E-09	-	-	5.0E-09	1.0E-10	1.0E-09
F2	6.4E-09	5.5E-04	1.0E-08	2.8E-08	1.0E-08	6.0E-09	2.8E-08	-	1.0E-08	-	-	1.0E-09	-	-
LMC	6.4E-09	5.5E-04	-	-	1.0E-08	1.3E-09	1.4E-08	6.4E-09	1.0E-09	-	-	5.0E-09	6.0E-11	3.0E-10
E*	1.0E-08	8.6E-04	-	-	1.0E-08	-	-	-	1.0E-08	-	-	1.0E-09	-	-
O(E)	1.0E-07	8.6E-03	-	-	-	-	-	-	1.0E-08	1.0E-07	5.5E-06	-	-	-
O(D)*	Impermeable		-	-	1.0E-07	-	-	-	1.0E-08	1.0E-08	1.0E-06	-	-	-
O(C)*	Impermeable		-	-	1.0E-07	-	-	-	1.0E-08			-	-	-
O(B)*	Impermeable		-	-	1.0E-07	-	-	-	1.0E-08			-	-	-
O(A)*	Impermeable		-	-	1.0E-08	-	-	-	1.0E-08			-	-	-

*: Materials not included in the simplified stratigraphies analyzed in PLAXIS simulations.

Table 4-11: Stages considered in the Marina Bay Area PLAXIS simulations.

Stage name	Stage type	Date, start	Date, finish	Δt	CD _i	CD _f
[-]	[-]	[-]	[-]	[day]	[day]	[day]
S0-Initial Phase	Consolidation	jan-78	jan-78	0	0	0
S1-Fill construction 7yrs	Consolidation	jan-78	jan-85	2555	0	2555
S2-Creep 33yrs	Consolidation	jan-85	dec-17	12050	2555	14605
S3-Creep 30yrs	Consolidation	dec-17	dec-47	10950	14605	25555

Table 4-12: Material parameters for OA in PLAXIS simulations of Marina bay area.

Material	Type	Behavior	γ	E'	ν	ϕ'	c'	$k_x=k_y$	c_k
[-]	[-]	[-]	[kN/m ³]	[MPa]	[-]	[deg]	[kPa]	[m/day]	[-]
OA	Mohr-Coulomb	Undrained (A)	20	240	0.2	35	10	$8.6 \cdot 10^{-3}$	0.82

Table 4-13: MIT-SR material parameters for UMC, F2 & LMC in PLAXIS simulations of Marina bay area.

Symbols	UMC	F2 & LMC	Used Data of SFBM	Reference
ρ_c	0.28	0.28	LCC curves from oedometer and CRS and oedometer tests	Kiso-Jiban (1978)
K_{ONC}	0.52	0.52	Preshear stress states of triaxial tests	
C_b	510	510	Field shear wave velocity tests	
$2G/K$	0.94	0.94	From Corral & Whittle (2010)	Choi (1982)
D	0.12	0.12	1D swelling curves from CRS tests (Corral & Whittle, 2010)	Corral & Whittle (2010)
r	3.8	3.8		
w_s	60	60	Degradation of shear stiffness of triaxial tests	Tan et al. (2003)
ϕ'_{cs}	32.4	27.0	Shear stress at large strain in triaxial compression tests	
ϕ'_m	22	18	Effective stress paths for triaxial compression/extension tests	
m	0.2	0.2		
ψ	15	15		
D_L	0	0	Assumed zero, little importance in analyses of interest	
ρ_a/ρ_c	0.025	0.025	Secondary compression of oedometer tests	Choi (1982)
β	0.025	0.025	CRS tests with different strain rates	Kiso-Jiban (1978)
β_2	6.5	6.5	Oedometer tests with surcharge, unloading and creep stages	
β_3	9.0	9.0	Oedometer tests with surcharge, unloading and creep stages	
$\dot{\epsilon}_{ref}$ [day ⁻¹]	4.4E-03	4.4E-03	Strain rate at 24hr of consolidation in oedometer tests	

Table 4-14: MIT-SR state parameters for UMC, F2 & LMC in PLAXIS simulations of Marina bay area.

State Par.	Unit	UMC				F2	LMC			
		OCR=5.70	OCR=2.40	OCR=1.85	OCR=1.60	OCR=7.30	OCR=1.40	OCR=1.35	OCR=1.30	OCR=1.25
p_{atm}	[kPa]	101	101	101	101	101	101	101	101	101
α' / σ'	[-]	2.58	1.84	1.64	1.52	2.86	1.41	1.37	1.34	1.30
e_0	[-]	1.33	1.23	1.20	1.19	1.04	0.91	0.91	0.90	0.90
b_0	[-]	0.78	0.78	0.78	0.78	0.78	0.78	0.78	0.78	0.78
b_1	[-]	1.44	1.44	1.44	1.44	1.44	1.44	1.44	1.44	1.44
b_2	[-]	0.78	0.78	0.78	0.78	0.78	0.78	0.78	0.78	0.78
b_3	[-]	0	0	0	0	0	0	0	0	0
b_4	[-]	0	0	0	0	0	0	0	0	0
b_5	[-]	0	0	0	0	0	0	0	0	0
σ^h / σ'	[-]	1.20	1.20	1.18	1.16	1.23	1.12	1.11	1.08	1.06
η^{h_0}	[-]	1.01	0.86	0.83	0.81	1.06	0.79	0.79	0.78	0.78
η^{h_1}	[-]	0.98	1.28	1.35	1.38	0.89	1.42	1.42	1.44	1.44
η^{h_2}	[-]	1.01	0.86	0.83	0.81	1.06	0.79	0.79	0.78	0.78
η^{h_3}	[-]	0	0	0	0	0	0	0	0	0
η^{h_4}	[-]	0	0	0	0	0	0	0	0	0
η^{h_5}	[-]	0	0	0	0	0	0	0	0	0
R_{a0}	[1/day]	3.3E-07	2.8E-07	1.2E-07	8.9E-08	1.7E-07	1.2E-07	1.2E-07	1.3E-07	1.5E-07

Table 4-15: Small strain elastic compressibility (C_b) calibration.

Soil	Depth	σ'_{v0}	G_{max}	ω_n	e	σ'	C_b	Avg. C_b
[-]	[m]	[kPa]	[kPa]	[-]	[-]	[kPa]	[-]	[-]
UMC	16	133	36000	0.59	1.61	90	486	510
LMC	28	226	48000	0.56	1.55	154	534	

Table 4-16: CRS tests, effective vertical stresses for specific void ratios and β values.

Test	SC-15	SC-16	SC-17	SC-18	β
$\dot{\epsilon}$ [%/hr]	0.45%	0.25%	0.18%	0.13%	
e	σ'_v	σ'_v	σ'_v	σ'_v	
[-]	[psf]	[psf]	[psf]	[psf]	[-]
1.70	3391	2921	2791	2786	0.169
1.65	3669	3197	3188	3149	0.126
1.60	3972	3538	3599	3506	0.098
1.55	4485	3938	4013	3963	0.099
1.50	4930	4362	4518	4621	0.054
1.45	5511	5013	5200	5278	0.034
1.40	6286	5779	5755	5936	0.053
1.35	7219	6638	6425	6767	0.066
1.30	8374	7529	7738	7979	0.042
1.25	9656	8792	9771	9502	Neg.
1.20	11067	10055	11804	11065	Neg.
1.15	13149	11803	13837	13188	Neg.
1.10	15619	13975	15870	15311	Neg.
				Avg.:	0.082

Table 4-17: Series 4 tests, calculated values for $C_{\alpha\epsilon}$, $\hat{C}_{\alpha\epsilon}$ and $\dot{\epsilon}_1$.

Stage	$C_{\alpha\epsilon}$ [-]	$\hat{C}_{\alpha\epsilon}$ [-]				$\dot{\epsilon}_1$ [1/hr]		
[psf]	SC-11	SC-12	SC-13	SC-14	SC-12	SC-13	SC-14	
1000	0.00094	0.00025	0.00018	0.00022	0.00009	0.00009	0.00005	
2000	0.01173	0.00523	0.00264	0.00089	0.00110	0.00027	0.00010	
4000	0.01062	0.00500	0.00116	0.00040	0.00075	0.00011	0.00009	
8000	0.00915	0.00475	0.00175	0.00042	0.00064	0.00011	0.00010	

Table 4-18: Series 4 tests, OCR, $\hat{C}_{\alpha\epsilon}/C_{\alpha\epsilon}$ and $\dot{\epsilon}_1/\dot{\epsilon}_{100}$ for β_2 calibration.

Test	OCR	$\hat{C}_{\alpha\epsilon}/C_{\alpha\epsilon}$	$\dot{\epsilon}_1/\dot{\epsilon}_{100}$
[-]	[-]	[-]	[-]
SC-12	1.25	0.2646	0.0237
	1.20	0.4455	0.2884
	1.20	0.4703	0.1985
	1.20	0.5196	0.1689
SC-13	1.50	0.1963	0.0246
	1.40	0.2251	0.0722
	1.40	0.1094	0.0300

	1.40	0.1916	0.0284
SC-14	1.75	0.2337	0.0123
	1.60	0.0761	0.0252
	1.60	0.0378	0.0230
	1.60	0.0459	0.0257

Table 4-19: Calibration of non-linear variation of rate dependency with stress history (β_2) and reduction of creep rate during unloading parameter (β_3).

β_2	5	6	7	8	β_3	8	9	10	11
OCR	$\hat{C}_{\alpha\epsilon}/C_{\alpha\epsilon}$	$\hat{C}_{\alpha\epsilon}/C_{\alpha\epsilon}$	$\hat{C}_{\alpha\epsilon}/C_{\alpha\epsilon}$	$\hat{C}_{\alpha\epsilon}/C_{\alpha\epsilon}$	OCR	$\dot{\epsilon}_1/\dot{\epsilon}_{100}$	$\dot{\epsilon}_1/\dot{\epsilon}_{100}$	$\dot{\epsilon}_1/\dot{\epsilon}_{100}$	$\dot{\epsilon}_1/\dot{\epsilon}_{100}$
[-]	[-]	[-]	[-]	[-]	[-]	[-]	[-]	[-]	[-]
1.00	1.000	1.000	1.000	1.000	1.00	1.000	1.000	1.000	1.000
1.10	0.766	0.722	0.678	0.636	1.10	0.467	0.424	0.386	0.350
1.20	0.573	0.502	0.436	0.377	1.20	0.233	0.194	0.162	0.135
1.30	0.424	0.343	0.275	0.218	1.30	0.123	0.094	0.073	0.056
1.40	0.314	0.234	0.173	0.127	1.40	0.068	0.048	0.035	0.025
1.50	0.233	0.161	0.111	0.075	1.50	0.039	0.026	0.017	0.012
1.60	0.174	0.113	0.072	0.046	1.60	0.023	0.015	0.009	0.006
1.70	0.132	0.080	0.048	0.028	1.70	0.014	0.008	0.005	0.003
1.80	0.101	0.057	0.032	0.018	1.80	0.009	0.005	0.003	0.002
1.90	0.078	0.042	0.022	0.012	1.90	0.006	0.003	0.002	0.001
2.00	0.061	0.031	0.016	0.008	2.00	0.004	0.002	0.001	0.000
2.10	0.048	0.023	0.011	0.005	2.10	0.003	0.001	0.001	0.000
3.00	0.008	0.003	0.001	0.000	3.00	0.000	0.000	0.000	0.000

Table 4-20: Calculated values of secondary compression (ρ_α) and reference strain rate ($\dot{\epsilon}_{ref}$).

Test	BH8-U4-S3	BH8-U4-S4	BH8-U6-S3	BH8-U6-S4	Average
ρ_α	0.0056	0.0075	0.0068	0.0079	0.007
$\dot{\epsilon}_{ref}$ [day ⁻¹]	3.8E-03	5.1E-03	4.0E-03	4.8E-03	4.4E-03

Table 4-21: PLAXIS predictions of settlements and settlement rates, 1985-2012, PLX01 to PLX23.

PLAXIS N°	H MC	H UMC	H LMC	31-Dec-85		31-Dec-87		31-Dec-92		31-Dec-97		31-Dec-02		31-Dec-05		31-Dec-07		31-Dec-12	
				u	$\Delta u/\Delta t$	u	$\Delta u/\Delta t$	u	$\Delta u/\Delta t$	u	$\Delta u/\Delta t$	u	$\Delta u/\Delta t$	u	$\Delta u/\Delta t$	u	$\Delta u/\Delta t$	u	$\Delta u/\Delta t$
[-]	[m]	[m]	[m]	[m]	[mm/yr]	[m]	[mm/yr]	[m]	[mm/yr]	[m]	[mm/yr]	[m]	[mm/yr]	[m]	[mm/yr]	[m]	[mm/yr]	[m]	[mm/yr]
PLX01	6.0	4.5	1.5	1.7	180.3	1.9	50.1	2.1	12.1	2.1	4.9	2.1	2.7	2.1	2.4	2.1	1.6	2.1	1.5
PLX02	8.0	4.5	3.5	1.8	207.9	2.1	76.3	2.3	22.8	2.4	9.1	2.4	5.1	2.4	3.4	2.4	3.1	2.5	2.5
PLX03	10.0	4.5	5.5	1.8	221.5	2.2	95.5	2.5	37.0	2.6	16.4	2.7	8.9	2.7	6.5	2.7	5.1	2.7	3.3
PLX04	12.0	4.5	7.5	1.8	227.4	2.2	104.5	2.6	48.6	2.8	25.1	2.9	13.8	2.9	10.3	2.9	8.4	3.0	5.4
PLX05	14.0	4.5	9.5	1.8	229.7	2.3	110.3	2.7	57.6	2.9	32.8	3.0	19.7	3.1	14.9	3.1	12.8	3.1	8.4
PLX06	16.0	4.5	11.5	1.8	233.5	2.3	114.1	2.7	62.1	3.0	38.1	3.1	25.0	3.2	19.6	3.2	16.7	3.3	11.6
PLX07	18.0	4.5	13.5	1.9	235.6	2.3	117.1	2.7	65.9	3.0	42.2	3.2	28.6	3.2	23.6	3.3	20.4	3.4	14.7
PLX08	20.0	4.5	15.5	1.9	235.8	2.3	120.5	2.8	68.2	3.0	45.2	3.2	32.1	3.3	26.5	3.4	23.3	3.5	17.3
PLX09	22.0	4.5	17.5	1.9	237.5	2.3	122.2	2.8	70.3	3.1	47.4	3.3	34.0	3.4	28.4	3.4	25.1	3.5	19.1
PLX10	8.0	6.5	1.5	1.8	203.6	2.2	69.9	2.3	19.6	2.4	8.3	2.4	4.5	2.4	3.2	2.5	3.1	2.5	2.6
PLX11	10.0	6.5	3.5	1.9	221.3	2.3	90.9	2.5	33.2	2.7	14.4	2.7	7.5	2.7	6.1	2.7	4.6	2.7	3.4
PLX12	12.0	6.5	5.5	1.9	229.8	2.3	102.6	2.7	44.5	2.8	22.0	2.9	12.2	2.9	8.8	3.0	7.2	3.0	4.8
PLX13	14.0	6.5	7.5	1.9	235.6	2.4	109.0	2.7	54.6	3.0	29.9	3.1	17.8	3.1	13.1	3.1	11.0	3.2	7.3
PLX14	16.0	6.5	9.5	1.9	237.0	2.4	113.6	2.8	60.7	3.0	36.2	3.2	22.7	3.2	17.6	3.3	15.1	3.3	10.5
PLX15	18.0	6.5	11.5	2.0	238.6	2.4	116.9	2.8	64.6	3.1	40.9	3.3	27.1	3.3	21.7	3.4	18.6	3.5	13.3
PLX16	20.0	6.5	13.5	2.0	243.5	2.4	119.4	2.9	67.3	3.1	43.9	3.3	30.2	3.4	25.1	3.4	21.9	3.5	16.1
PLX17	22.0	6.5	15.5	2.0	244.1	2.4	121.8	2.9	70.1	3.2	46.2	3.4	32.6	3.5	27.1	3.5	23.9	3.6	18.4
PLX18	24.0	6.5	17.5	2.0	244.1	2.4	123.4	2.9	72.0	3.2	48.2	3.4	34.7	3.5	29.3	3.5	26.0	3.7	19.9
PLX19	10.0	8.5	1.5	2.0	225.1	2.3	86.8	2.6	30.6	2.7	12.9	2.8	6.9	2.8	5.3	2.8	4.5	2.8	3.3
PLX20	12.0	8.5	3.5	2.0	239.0	2.4	102.0	2.7	42.6	2.9	20.2	3.0	11.0	3.0	8.4	3.0	6.5	3.0	4.6
PLX21	14.0	8.5	5.5	2.0	245.2	2.5	111.0	2.8	52.7	3.0	28.3	3.1	16.1	3.2	12.0	3.2	10.0	3.2	6.7
PLX22	16.0	8.5	7.5	2.0	249.7	2.5	115.6	2.9	59.5	3.1	34.5	3.3	21.6	3.3	16.3	3.3	14.1	3.4	9.6
PLX23	18.0	8.5	9.5	2.0	254.1	2.5	119.5	2.9	63.7	3.2	39.6	3.4	25.8	3.4	20.4	3.5	17.7	3.5	12.4

Table 4-22: PLAXIS predictions of settlements and settlement rates, 2017-2047, PLX01 to PLX23.

PLAXIS N°	H MC	H UMC	H LMC	31-Dec-17		31-Dec-22		31-Dec-27		31-Dec-32		31-Dec-37		31-Dec-42		31-Dec-47	
				u	$\Delta u/\Delta t$	u	$\Delta u/\Delta t$	u	$\Delta u/\Delta t$	U	$\Delta u/\Delta t$	u	$\Delta u/\Delta t$	u	$\Delta u/\Delta t$	u	$\Delta u/\Delta t$
[-]	[m]	[m]	[m]	[m]	[mm/yr]	[m]	[mm/yr]	[m]	[mm/yr]	[m]	[mm/yr]	[m]	[mm/yr]	[m]	[mm/yr]	[m]	[mm/yr]
PLX01	6.0	4.5	1.5	2.1	1.4	2.1	1.2	2.1	0.6	2.2	0.6	2.2	0.6	2.2	0.6	2.2	0.5
PLX02	8.0	4.5	3.5	2.5	1.5	2.5	1.5	2.5	1.3	2.5	1.1	2.5	1.1	2.5	0.8	2.5	0.7
PLX03	10.0	4.5	5.5	2.7	2.8	2.8	2.1	2.8	1.6	2.8	1.6	2.8	0.9	2.8	0.9	2.8	0.9
PLX04	12.0	4.5	7.5	3.0	4.0	3.0	3.0	3.0	2.2	3.0	2.1	3.0	1.8	3.0	1.6	3.0	1.2
PLX05	14.0	4.5	9.5	3.2	5.9	3.2	4.6	3.2	3.3	3.2	3.1	3.2	2.3	3.3	2.0	3.3	1.9
PLX06	16.0	4.5	11.5	3.3	8.3	3.4	6.2	3.4	4.9	3.4	3.8	3.4	3.2	3.4	2.7	3.4	2.2
PLX07	18.0	4.5	13.5	3.4	10.9	3.5	8.3	3.5	6.5	3.6	5.1	3.6	4.2	3.6	3.5	3.6	3.0
PLX08	20.0	4.5	15.5	3.5	13.1	3.6	10.1	3.6	8.0	3.7	6.4	3.7	5.4	3.7	4.5	3.7	3.8
PLX09	22.0	4.5	17.5	3.6	15.0	3.7	11.9	3.7	9.6	3.8	7.8	3.8	6.4	3.8	5.4	3.9	4.6
PLX10	8.0	6.5	1.5	2.5	1.6	2.5	1.4	2.5	1.3	2.5	1.1	2.5	0.8	2.5	0.7	2.5	0.7
PLX11	10.0	6.5	3.5	2.8	2.7	2.8	2.0	2.8	1.5	2.8	1.5	2.8	1.0	2.8	1.0	2.8	0.9
PLX12	12.0	6.5	5.5	3.0	3.9	3.0	2.7	3.0	2.1	3.0	1.8	3.1	1.7	3.1	1.0	3.1	1.0
PLX13	14.0	6.5	7.5	3.2	5.2	3.2	3.9	3.3	3.2	3.3	2.6	3.3	2.2	3.3	2.0	3.3	1.8
PLX14	16.0	6.5	9.5	3.4	7.4	3.4	5.4	3.4	4.2	3.4	3.4	3.5	2.9	3.5	2.4	3.5	2.3
PLX15	18.0	6.5	11.5	3.5	9.8	3.6	7.4	3.6	5.7	3.6	4.7	3.6	3.9	3.6	3.3	3.7	2.7
PLX16	20.0	6.5	13.5	3.6	12.0	3.7	9.2	3.7	7.2	3.7	5.9	3.8	4.9	3.8	4.1	3.8	3.8
PLX17	22.0	6.5	15.5	3.7	14.0	3.7	11.0	3.8	8.8	3.8	7.2	3.9	5.9	3.9	5.0	3.9	4.4
PLX18	24.0	6.5	17.5	3.7	15.5	3.8	12.4	3.9	10.0	3.9	8.2	4.0	6.9	4.0	5.8	4.0	5.1
PLX19	10.0	8.5	1.5	2.8	2.5	2.8	1.9	2.8	1.5	2.8	1.4	2.8	1.0	2.8	1.0	2.8	0.9
PLX20	12.0	8.5	3.5	3.1	3.7	3.1	2.5	3.1	2.0	3.1	1.9	3.1	1.7	3.1	1.3	3.1	1.2
PLX21	14.0	8.5	5.5	3.3	4.8	3.3	3.6	3.3	2.6	3.3	2.4	3.3	2.0	3.3	1.8	3.3	1.7
PLX22	16.0	8.5	7.5	3.4	6.7	3.5	5.1	3.5	4.0	3.5	3.2	3.5	2.8	3.5	2.2	3.5	2.1
PLX23	18.0	8.5	9.5	3.6	9.0	3.6	6.8	3.6	5.5	3.7	4.2	3.7	3.5	3.7	2.9	3.7	2.8

Table 4-23: PLAXIS predictions of settlements and settlement rates, 1985-2012, PLX24 to PLX46.

PLAXIS N°	H MC	H UMC	H LMC	31-Dec-85		31-Dec-87		31-Dec-92		31-Dec-97		31-Dec-02		31-Dec-05		31-Dec-07		31-Dec-12	
				u	$\Delta u/\Delta t$	u	$\Delta u/\Delta t$	u	$\Delta u/\Delta t$	u	$\Delta u/\Delta t$	u	$\Delta u/\Delta t$	u	$\Delta u/\Delta t$	u	$\Delta u/\Delta t$	u	$\Delta u/\Delta t$
[-]	[m]	[m]	[m]	[m]	[mm/yr]	[m]	[mm/yr]	[m]	[mm/yr]	[m]	[mm/yr]	[m]	[mm/yr]	[m]	[mm/yr]	[m]	[mm/yr]	[m]	[mm/yr]
PLX24	20.0	8.5	11.5	2.0	254.7	2.5	122.5	3.0	67.5	3.2	43.3	3.4	29.3	3.5	23.8	3.5	20.7	3.6	15.0
PLX25	22.0	8.5	13.5	2.0	251.4	2.5	125.2	3.0	70.2	3.3	45.7	3.5	32.4	3.6	26.7	3.6	23.5	3.7	17.5
PLX26	24.0	8.5	15.5	2.1	261.7	2.5	127.3	3.0	72.4	3.3	47.9	3.5	34.1	3.6	28.8	3.7	25.4	3.8	19.3
PLX27	26.0	8.5	17.5	2.1	261.8	2.5	129.0	3.0	74.3	3.3	49.8	3.5	36.0	3.6	30.1	3.7	26.8	3.8	20.7
PLX28	12.0	10.5	1.5	2.0	251.2	2.5	106.5	2.8	41.0	2.9	19.2	3.0	10.4	3.0	7.5	3.1	6.3	3.1	4.2
PLX29	14.0	10.5	3.5	2.0	255.4	2.5	116.3	2.9	51.6	3.1	27.1	3.2	15.1	3.2	11.1	3.3	9.2	3.3	6.3
PLX30	16.0	10.5	5.5	2.1	261.8	2.6	122.3	3.0	60.4	3.2	33.8	3.3	20.2	3.4	15.3	3.4	12.9	3.5	8.6
PLX31	18.0	10.5	7.5	2.1	262.7	2.6	125.8	3.0	64.8	3.3	38.8	3.4	25.2	3.5	19.7	3.5	16.7	3.6	11.8
PLX32	20.0	10.5	9.5	2.1	266.3	2.6	129.7	3.1	68.5	3.3	43.0	3.5	28.6	3.6	23.0	3.6	19.9	3.7	14.3
PLX33	22.0	10.5	11.5	2.1	266.9	2.6	132.1	3.1	71.4	3.4	46.0	3.6	31.6	3.7	25.6	3.7	23.0	3.8	16.9
PLX34	24.0	10.5	13.5	2.1	269.6	2.6	134.0	3.1	74.0	3.4	48.5	3.6	34.1	3.7	28.0	3.8	24.7	3.9	19.0
PLX35	26.0	10.5	15.5	2.1	270.5	2.6	135.6	3.1	75.9	3.4	50.4	3.6	35.7	3.7	30.1	3.8	26.7	3.9	20.4
PLX36	28.0	10.5	17.5	2.1	269.2	2.6	137.3	3.1	78.5	3.5	52.4	3.7	37.6	3.8	31.7	3.8	28.9	4.0	22.4
PLX37	14.0	12.5	1.5	2.1	263.3	2.6	122.6	3.0	53.5	3.2	26.3	3.3	14.4	3.3	10.7	3.3	9.3	3.3	6.0
PLX38	16.0	12.5	3.5	2.1	266.4	2.6	129.0	3.0	61.3	3.3	33.3	3.4	19.9	3.4	14.7	3.5	12.5	3.5	8.3
PLX39	18.0	12.5	5.5	2.1	268.2	2.6	133.3	3.1	67.7	3.3	39.3	3.5	24.5	3.6	19.0	3.6	16.3	3.7	11.1
PLX40	20.0	12.5	7.5	2.1	272.2	2.6	136.6	3.1	71.1	3.4	43.2	3.6	28.7	3.7	22.5	3.7	19.8	3.8	14.1
PLX41	22.0	12.5	9.5	2.1	274.0	2.7	139.5	3.2	74.8	3.5	46.6	3.6	31.5	3.7	25.7	3.8	22.3	3.9	16.3
PLX42	24.0	12.5	11.5	2.1	275.5	2.7	141.2	3.2	77.0	3.5	49.5	3.7	34.3	3.8	28.4	3.8	24.9	3.9	18.5
PLX43	26.0	12.5	13.5	2.1	275.7	2.7	143.8	3.2	79.4	3.5	51.3	3.7	36.1	3.8	30.1	3.9	26.6	4.0	20.1
PLX44	28.0	12.5	15.5	2.1	277.7	2.7	145.4	3.2	80.3	3.5	52.9	3.8	38.5	3.9	32.4	3.9	28.0	4.1	21.5
PLX45	30.0	12.5	17.5	2.1	278.6	2.7	146.1	3.2	82.8	3.6	54.7	3.8	39.4	3.9	33.2	4.0	29.6	4.1	23.4
PLX46	16.0	14.5	1.5	2.1	269.3	2.6	133.5	3.1	63.5	3.3	34.6	3.5	20.2	3.5	14.9	3.5	12.3	3.6	8.1

Table 4-24: PLAXIS predictions of settlements and settlement rates, 2017-2047, PLX24 to PLX46.

PLAXIS N°	H MC	H UMC	H LMC	31-Dec-17		31-Dec-22		31-Dec-27		31-Dec-32		31-Dec-37		31-Dec-42		31-Dec-47	
				u	$\Delta u/\Delta t$	u	$\Delta u/\Delta t$	u	$\Delta u/\Delta t$	U	$\Delta u/\Delta t$	u	$\Delta u/\Delta t$	u	$\Delta u/\Delta t$	u	$\Delta u/\Delta t$
[-]	[m]	[m]	[m]	[m]	[mm/yr]	[m]	[mm/yr]	[m]	[mm/yr]	[m]	[mm/yr]	[m]	[mm/yr]	[m]	[mm/yr]	[m]	[mm/yr]
PLX24	20.0	8.5	11.5	3.7	11.2	3.7	8.6	3.8	6.9	3.8	5.6	3.8	4.8	3.9	3.7	3.9	3.2
PLX25	22.0	8.5	13.5	3.8	13.3	3.8	10.4	3.9	8.3	3.9	6.7	4.0	5.7	4.0	4.6	4.0	4.0
PLX26	24.0	8.5	15.5	3.9	15.0	3.9	11.9	4.0	9.6	4.0	7.9	4.0	6.6	4.1	5.7	4.1	4.8
PLX27	26.0	8.5	17.5	3.9	16.4	4.0	13.2	4.0	10.8	4.1	8.9	4.1	7.4	4.2	6.3	4.2	5.5
PLX28	12.0	10.5	1.5	3.1	3.2	3.1	2.5	3.1	2.0	3.1	1.9	3.1	1.3	3.1	1.3	3.2	1.2
PLX29	14.0	10.5	3.5	3.3	4.4	3.3	3.4	3.4	2.9	3.4	2.3	3.4	2.0	3.4	1.8	3.4	1.4
PLX30	16.0	10.5	5.5	3.5	6.2	3.5	4.7	3.6	3.7	3.6	3.0	3.6	2.4	3.6	2.1	3.6	2.0
PLX31	18.0	10.5	7.5	3.7	8.4	3.7	6.4	3.7	5.0	3.7	4.0	3.8	3.3	3.8	3.0	3.8	2.5
PLX32	20.0	10.5	9.5	3.8	10.7	3.8	8.1	3.8	6.4	3.9	5.2	3.9	4.2	3.9	3.6	3.9	3.1
PLX33	22.0	10.5	11.5	3.9	12.8	3.9	9.8	4.0	7.8	4.0	6.5	4.0	5.4	4.1	4.4	4.1	3.7
PLX34	24.0	10.5	13.5	3.9	14.5	4.0	11.5	4.1	9.2	4.1	7.5	4.1	6.1	4.2	5.2	4.2	4.8
PLX35	26.0	10.5	15.5	4.0	16.0	4.1	12.8	4.1	10.4	4.2	8.6	4.2	7.1	4.2	6.1	4.3	5.2
PLX36	28.0	10.5	17.5	4.1	17.5	4.1	14.4	4.2	11.7	4.2	9.8	4.3	8.4	4.3	6.9	4.4	6.1
PLX37	14.0	12.5	1.5	3.4	4.3	3.4	3.3	3.4	2.7	3.4	2.2	3.4	1.9	3.4	1.8	3.4	1.4
PLX38	16.0	12.5	3.5	3.6	5.9	3.6	4.5	3.6	3.5	3.6	3.1	3.6	2.4	3.6	2.0	3.7	1.9
PLX39	18.0	12.5	5.5	3.7	8.1	3.7	6.1	3.8	4.8	3.8	3.8	3.8	3.1	3.8	2.9	3.8	2.4
PLX40	20.0	12.5	7.5	3.8	10.2	3.9	8.2	3.9	6.0	3.9	4.9	4.0	4.0	4.0	3.3	4.0	3.1
PLX41	22.0	12.5	9.5	3.9	12.4	4.0	9.6	4.0	7.6	4.1	6.1	4.1	5.2	4.1	4.3	4.1	3.7
PLX42	24.0	12.5	11.5	4.0	14.2	4.1	11.1	4.1	8.9	4.2	7.4	4.2	6.0	4.2	5.2	4.3	4.5
PLX43	26.0	12.5	13.5	4.1	15.7	4.2	12.5	4.2	10.1	4.3	8.3	4.3	6.9	4.3	5.9	4.4	5.1
PLX44	28.0	12.5	15.5	4.1	17.2	4.2	14.1	4.3	11.4	4.3	9.6	4.4	8.1	4.4	6.7	4.4	5.9
PLX45	30.0	12.5	17.5	4.2	18.3	4.3	14.8	4.3	12.1	4.4	10.2	4.4	8.5	4.5	7.4	4.5	6.4
PLX46	16.0	14.5	1.5	3.6	5.8	3.6	4.4	3.7	3.4	3.7	2.7	3.7	2.2	3.7	2.0	3.7	1.9

Table 4-25: PLAXIS predictions of settlements and settlement rates, 1985-2012, PLX47 to PLX54.

PLAXIS N°	H MC	H UMC	H LMC	31-Dec-85		31-Dec-87		31-Dec-92		31-Dec-97		31-Dec-02		31-Dec-05		31-Dec-07		31-Dec-12	
				u	$\Delta u/\Delta t$	u	$\Delta u/\Delta t$	u	$\Delta u/\Delta t$	u	$\Delta u/\Delta t$	u	$\Delta u/\Delta t$	u	$\Delta u/\Delta t$	u	$\Delta u/\Delta t$	u	$\Delta u/\Delta t$
[-]	[m]	[m]	[m]	[m]	[mm/yr]	[m]	[mm/yr]	[m]	[mm/yr]	[m]	[mm/yr]	[m]	[mm/yr]	[m]	[mm/yr]	[m]	[mm/yr]	[m]	[mm/yr]
PLX47	18.0	14.5	3.5	2.1	271.7	2.6	138.3	3.1	70.5	3.4	40.9	3.6	25.0	3.6	19.3	3.7	16.2	3.7	11.0
PLX48	20.0	14.5	5.5	2.1	275.7	2.7	141.7	3.2	74.4	3.5	44.6	3.7	28.8	3.7	22.8	3.8	20.1	3.8	14.1
PLX49	22.0	14.5	7.5	2.1	278.0	2.7	145.1	3.2	78.3	3.5	48.3	3.7	32.1	3.8	25.9	3.8	23.1	3.9	16.7
PLX50	24.0	14.5	9.5	2.1	278.6	2.7	147.6	3.2	80.2	3.6	51.0	3.8	34.7	3.9	28.4	3.9	25.5	4.0	18.8
PLX51	26.0	14.5	11.5	2.1	279.1	2.7	148.7	3.2	83.0	3.6	53.1	3.8	36.7	3.9	30.3	4.0	27.4	4.1	20.5
PLX52	28.0	14.5	13.5	2.1	281.8	2.7	149.8	3.3	84.6	3.6	55.3	3.8	38.9	3.9	32.4	4.0	28.6	4.1	21.8
PLX53	30.0	14.5	15.5	2.1	281.7	2.7	151.3	3.3	86.2	3.6	56.4	3.9	41.0	4.0	33.4	4.0	30.4	4.2	23.3
PLX54	32.0	14.5	17.5	2.1	280.0	2.7	152.1	3.3	87.4	3.6	57.7	3.9	41.7	4.0	35.0	4.1	31.2	4.2	24.1

Table 4-26: PLAXIS predictions of settlements and settlement rates, 2017-2047, PLX47 to PLX54.

PLAXIS N°	H MC	H UMC	H LMC	31-Dec-17		31-Dec-22		31-Dec-27		31-Dec-32		31-Dec-37		31-Dec-42		31-Dec-47	
				u	$\Delta u/\Delta t$	u	$\Delta u/\Delta t$	u	$\Delta u/\Delta t$	u	$\Delta u/\Delta t$	u	$\Delta u/\Delta t$	u	$\Delta u/\Delta t$	u	$\Delta u/\Delta t$
[-]	[m]	[m]	[m]	[m]	[mm/yr]	[m]	[mm/yr]	[m]	[mm/yr]	[m]	[mm/yr]	[m]	[mm/yr]	[m]	[mm/yr]	[m]	[mm/yr]
PLX47	18.0	14.5	3.5	3.8	7.9	3.8	5.9	3.8	4.6	3.9	3.8	3.9	3.2	3.9	2.5	3.9	2.4
PLX48	20.0	14.5	5.5	3.9	10.1	4.0	7.6	4.0	6.0	4.0	4.9	4.0	3.8	4.1	3.3	4.1	2.8
PLX49	22.0	14.5	7.5	4.0	12.3	4.1	9.6	4.1	7.4	4.1	6.1	4.2	4.9	4.2	4.2	4.2	3.6
PLX50	24.0	14.5	9.5	4.1	14.2	4.2	11.0	4.2	8.8	4.2	7.2	4.3	5.9	4.3	5.0	4.3	4.4
PLX51	26.0	14.5	11.5	4.2	15.8	4.2	12.5	4.3	9.9	4.3	8.2	4.4	6.8	4.4	5.8	4.4	5.0
PLX52	28.0	14.5	13.5	4.2	17.1	4.3	13.7	4.4	11.0	4.4	9.3	4.5	7.6	4.5	6.5	4.5	5.6
PLX53	30.0	14.5	15.5	4.3	18.2	4.3	14.7	4.4	11.9	4.5	10.0	4.5	8.3	4.5	7.2	4.6	6.2
PLX54	32.0	14.5	17.5	4.3	19.3	4.4	15.4	4.5	12.9	4.5	10.6	4.6	9.1	4.6	7.7	4.6	6.7

Table 4-27: PLAXIS predictions of settlement rates [mm/yr], 2017-2047.

H MC	31-Dec-17			31-Dec-22			31-Dec-27			31-Dec-32			31-Dec-37			31-Dec-42			31-Dec-47		
[m]	Min	Avg	Max	Min	Avg	Max	Min	Avg	Max	Min	Avg	Max	Min	Avg	Max	Min	Avg	Max	Min	Avg	Max
6	1.4	1.4	1.4	1.2	1.2	1.2	0.6	0.6	0.6	0.6	0.6	0.6	0.6	0.6	0.6	0.6	0.6	0.6	0.5	0.5	0.5
8	1.5	1.5	1.6	1.4	1.4	1.5	1.3	1.3	1.3	1.1	1.1	1.1	0.8	0.9	1.1	0.7	0.8	0.8	0.7	0.7	0.7
10	2.5	2.7	2.8	1.9	2.0	2.1	1.5	1.6	1.6	1.4	1.5	1.6	0.9	1.0	1.0	0.9	0.9	1.0	0.9	0.9	0.9
12	3.2	3.7	4.0	2.5	2.7	3.0	2.0	2.1	2.2	1.8	1.9	2.1	1.3	1.6	1.8	1.0	1.3	1.6	1.0	1.2	1.2
14	4.3	4.9	5.9	3.3	3.7	4.6	2.6	2.9	3.3	2.2	2.5	3.1	1.9	2.1	2.3	1.8	1.9	2.0	1.4	1.6	1.9
16	5.8	6.7	8.3	4.4	5.0	6.2	3.4	4.0	4.9	2.7	3.2	3.8	2.2	2.7	3.2	2.0	2.2	2.7	1.9	2.1	2.3
18	7.9	9.0	10.9	5.9	6.8	8.3	4.6	5.4	6.5	3.8	4.2	5.1	3.1	3.5	4.2	2.5	3.0	3.5	2.4	2.6	3.0
20	10.1	11.2	13.1	7.6	8.6	10.1	6.0	6.8	8.0	4.9	5.5	6.4	3.8	4.5	5.4	3.3	3.8	4.5	2.8	3.3	3.8
22	12.3	13.3	15.0	9.6	10.4	11.9	7.4	8.2	9.6	6.1	6.7	7.8	4.9	5.6	6.4	4.2	4.7	5.4	3.6	4.0	4.6
24	14.2	14.7	15.5	11.0	11.6	12.4	8.8	9.3	10.0	7.2	7.6	8.2	5.9	6.3	6.9	5.0	5.4	5.8	4.4	4.7	5.1
26	15.7	16.0	16.4	12.5	12.7	13.2	9.9	10.3	10.8	8.2	8.5	8.9	6.8	7.0	7.4	5.8	6.0	6.3	5.0	5.2	5.5
28	17.1	17.3	17.5	13.7	14.1	14.4	11.0	11.4	11.7	9.3	9.5	9.8	7.6	8.0	8.4	6.5	6.7	6.9	5.6	5.9	6.1
30	18.2	18.3	18.3	14.7	14.8	14.8	11.9	12.0	12.1	10.0	10.1	10.2	8.3	8.4	8.5	7.2	7.3	7.4	6.2	6.3	6.4
32	19.3	19.3	19.3	15.4	15.4	15.4	12.9	12.9	12.9	10.6	10.6	10.6	9.1	9.1	9.1	7.7	7.7	7.7	6.7	6.7	6.7

Table 4-28: PLAXIS predictions of settlements [m], 2017-2047.

H MC	31-Dec-17			31-Dec-22			31-Dec-27			31-Dec-32			31-Dec-37			31-Dec-42			31-Dec-47			
	[m]	Min	Avg	Max	Min	Avg	Max	Min	Avg	Max	Min	Avg	Max	Min	Avg	Max	Min	Avg	Max	Min	Avg	Max
6	2.1	2.1	2.1	2.1	2.1	2.1	2.1	2.1	2.1	2.2	2.2	2.2	2.2	2.2	2.2	2.2	2.2	2.2	2.2	2.2	2.2	2.2
8	2.5	2.5	2.5	2.5	2.5	2.5	2.5	2.5	2.5	2.5	2.5	2.5	2.5	2.5	2.5	2.5	2.5	2.5	2.5	2.5	2.5	2.5
10	2.7	2.8	2.8	2.8	2.8	2.8	2.8	2.8	2.8	2.8	2.8	2.8	2.8	2.8	2.8	2.8	2.8	2.8	2.8	2.8	2.8	2.8
12	3.0	3.0	3.1	3.0	3.1	3.1	3.0	3.1	3.1	3.0	3.1	3.1	3.0	3.1	3.1	3.0	3.1	3.1	3.0	3.1	3.1	3.2
14	3.2	3.3	3.4	3.2	3.3	3.4	3.2	3.3	3.4	3.2	3.3	3.4	3.2	3.3	3.4	3.3	3.3	3.4	3.3	3.3	3.3	3.4
16	3.3	3.5	3.6	3.4	3.5	3.6	3.4	3.5	3.7	3.4	3.5	3.7	3.4	3.6	3.7	3.4	3.6	3.7	3.4	3.6	3.7	3.7
18	3.4	3.6	3.8	3.5	3.7	3.8	3.5	3.7	3.8	3.6	3.7	3.9	3.6	3.7	3.9	3.6	3.7	3.9	3.6	3.8	3.9	3.9
20	3.5	3.7	3.9	3.6	3.8	4.0	3.6	3.8	4.0	3.7	3.8	4.0	3.7	3.9	4.0	3.7	3.9	4.1	3.7	3.9	4.1	4.1
22	3.6	3.8	4.0	3.7	3.9	4.1	3.7	3.9	4.1	3.8	4.0	4.1	3.8	4.0	4.2	3.8	4.0	4.2	3.9	4.0	4.2	4.2
24	3.7	3.9	4.1	3.8	4.0	4.2	3.9	4.0	4.2	3.9	4.1	4.2	4.0	4.1	4.3	4.0	4.2	4.3	4.0	4.2	4.3	4.3
26	3.9	4.0	4.2	4.0	4.1	4.2	4.0	4.2	4.3	4.1	4.2	4.3	4.1	4.3	4.4	4.2	4.3	4.4	4.2	4.3	4.4	4.4
28	4.1	4.1	4.2	4.1	4.2	4.3	4.2	4.3	4.4	4.2	4.3	4.4	4.3	4.4	4.5	4.3	4.4	4.5	4.4	4.4	4.4	4.5
30	4.2	4.2	4.3	4.3	4.3	4.3	4.3	4.4	4.4	4.4	4.4	4.5	4.4	4.5	4.5	4.5	4.5	4.5	4.5	4.5	4.5	4.6
32	4.3	4.3	4.3	4.4	4.4	4.4	4.5	4.5	4.5	4.5	4.5	4.5	4.6	4.6	4.6	4.6	4.6	4.6	4.6	4.6	4.6	4.6

Table 4-29: PLAXIS average predictions of settlements [m] and of settlement rates [mm/yr], 1985-2012.

H MC	31-Dec-85		31-Dec-87		31-Dec-92		31-Dec-97		31-Dec-02		31-Dec-05		31-Dec-07		31-Dec-12	
	u	$\Delta u/\Delta t$	u	$\Delta u/\Delta t$	u	$\Delta u/\Delta t$	u	$\Delta u/\Delta t$	u	$\Delta u/\Delta t$	u	$\Delta u/\Delta t$	u	$\Delta u/\Delta t$	u	$\Delta u/\Delta t$
[m]	[m]	[mm/yr]	[m]	[mm/yr]	[m]	[mm/yr]	[m]	[mm/yr]	[m]	[mm/yr]	[m]	[mm/yr]	[m]	[mm/yr]	[m]	[mm/yr]
6	1.7	180.3	1.9	50.1	2.1	12.1	2.1	4.9	2.1	2.7	2.1	2.4	2.1	1.6	2.1	1.5
8	1.8	205.8	2.1	73.1	2.3	21.2	2.4	8.7	2.4	4.8	2.4	3.3	2.4	3.1	2.5	2.5
10	1.9	222.6	2.3	91.0	2.5	33.6	2.7	14.6	2.7	7.7	2.7	6.0	2.7	4.7	2.8	3.4
12	1.9	236.9	2.4	103.9	2.7	44.2	2.9	21.6	2.9	11.8	3.0	8.7	3.0	7.1	3.0	4.8
14	2.0	245.9	2.4	113.8	2.8	54.0	3.0	28.9	3.1	16.6	3.2	12.4	3.2	10.5	3.2	7.0
16	2.0	253.0	2.5	121.4	2.9	61.3	3.1	35.1	3.3	21.6	3.3	16.4	3.4	13.9	3.4	9.5
18	2.0	255.1	2.5	125.1	3.0	66.2	3.2	40.3	3.4	26.0	3.4	20.6	3.5	17.6	3.6	12.4
20	2.0	258.0	2.5	128.4	3.0	69.5	3.3	43.9	3.4	29.6	3.5	24.0	3.6	21.0	3.7	15.1
22	2.0	258.7	2.5	131.0	3.0	72.5	3.3	46.7	3.5	32.4	3.6	26.6	3.6	23.5	3.7	17.5
24	2.1	265.9	2.6	134.7	3.1	75.1	3.4	49.0	3.6	34.4	3.7	28.6	3.7	25.3	3.8	19.1
26	2.1	271.8	2.6	139.3	3.1	78.1	3.5	51.1	3.7	36.1	3.8	30.2	3.8	26.9	4.0	20.4
28	2.1	276.2	2.7	144.2	3.2	81.1	3.5	53.5	3.8	38.3	3.9	32.2	3.9	28.5	4.0	21.9
30	2.1	280.2	2.7	148.7	3.2	84.5	3.6	55.6	3.8	40.2	3.9	33.3	4.0	30.0	4.1	23.3
32	2.1	280.0	2.7	152.1	3.3	87.4	3.6	57.7	3.9	41.7	4.0	35.0	4.1	31.2	4.2	24.1

Table 4-30: PLAXIS average predictions of settlements [m] and of settlement rates [mm/yr], 2017-2047.

H MC	31-Dec-17		31-Dec-22		31-Dec-27		31-Dec-32		31-Dec-37		31-Dec-42		31-Dec-47	
	u	$\Delta u/\Delta t$	u	$\Delta u/\Delta t$	u	$\Delta u/\Delta t$	u	$\Delta u/\Delta t$	u	$\Delta u/\Delta t$	u	$\Delta u/\Delta t$	u	$\Delta u/\Delta t$
[m]	[m]	[mm/yr]	[m]	[mm/yr]	[m]	[mm/yr]	[m]	[mm/yr]	[m]	[mm/yr]	[m]	[mm/yr]	[m]	[mm/yr]
6	2.1	1.4	2.1	1.2	2.1	0.6	2.2	0.6	2.2	0.6	2.2	0.6	2.2	0.5
8	2.5	1.5	2.5	1.4	2.5	1.3	2.5	1.1	2.5	0.9	2.5	0.8	2.5	0.7
10	2.8	2.7	2.8	2.0	2.8	1.6	2.8	1.5	2.8	1.0	2.8	0.9	2.8	0.9
12	3.0	3.7	3.1	2.7	3.1	2.1	3.1	1.9	3.1	1.6	3.1	1.3	3.1	1.2
14	3.3	4.9	3.3	3.7	3.3	2.9	3.3	2.5	3.3	2.1	3.3	1.9	3.3	1.6
16	3.5	6.7	3.5	5.0	3.5	4.0	3.5	3.2	3.6	2.7	3.6	2.2	3.6	2.1
18	3.6	9.0	3.7	6.8	3.7	5.4	3.7	4.2	3.7	3.5	3.7	3.0	3.8	2.6
20	3.7	11.2	3.8	8.6	3.8	6.8	3.8	5.5	3.9	4.5	3.9	3.8	3.9	3.3
22	3.8	13.3	3.9	10.4	3.9	8.2	4.0	6.7	4.0	5.6	4.0	4.7	4.0	4.0
24	3.9	14.7	4.0	11.6	4.0	9.3	4.1	7.6	4.1	6.3	4.2	5.4	4.2	4.7
26	4.0	16.0	4.1	12.7	4.2	10.3	4.2	8.5	4.3	7.0	4.3	6.0	4.3	5.2
28	4.1	17.3	4.2	14.1	4.3	11.4	4.3	9.5	4.4	8.0	4.4	6.7	4.4	5.9
30	4.2	18.3	4.3	14.8	4.4	12.0	4.4	10.1	4.5	8.4	4.5	7.3	4.6	6.3
32	4.3	19.3	4.4	15.4	4.5	12.9	4.5	10.6	4.6	9.1	4.6	7.7	4.6	6.7

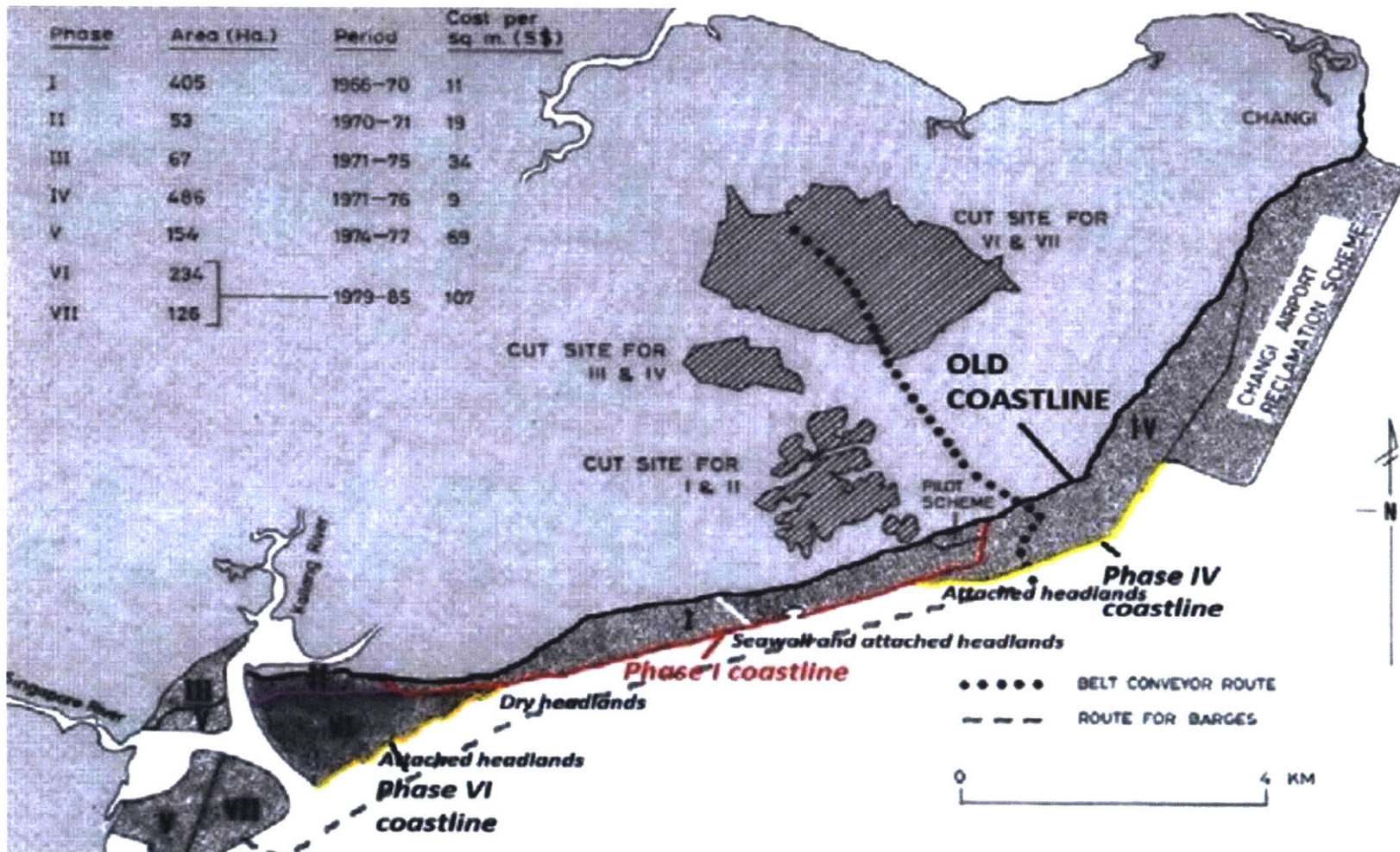


Figure 4-1: Marina bay reclaimed areas and phases (Mott MacDonald, 2015).

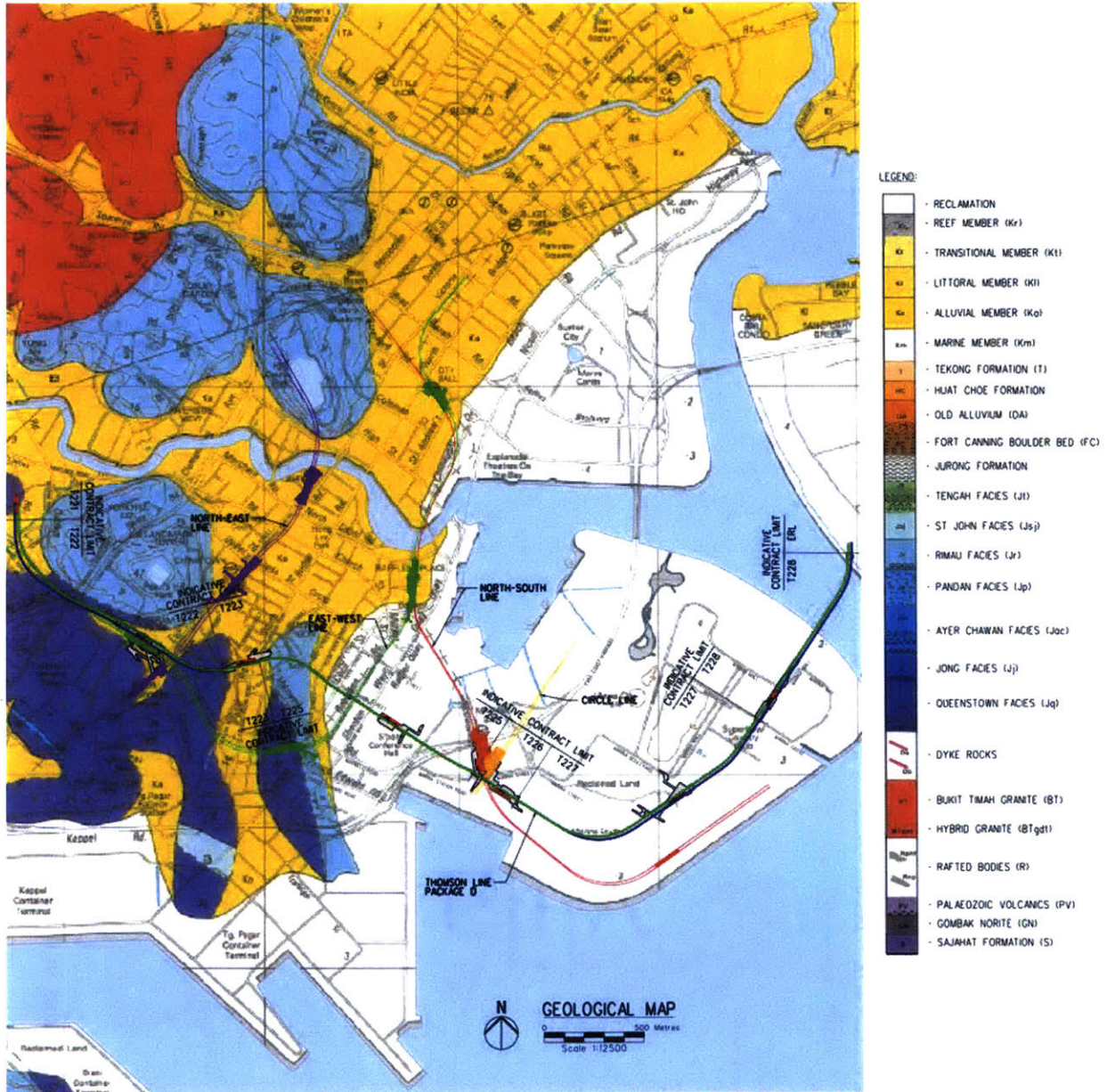


Figure 4-2: Marina bay reclaimed areas (Arup, 2014).

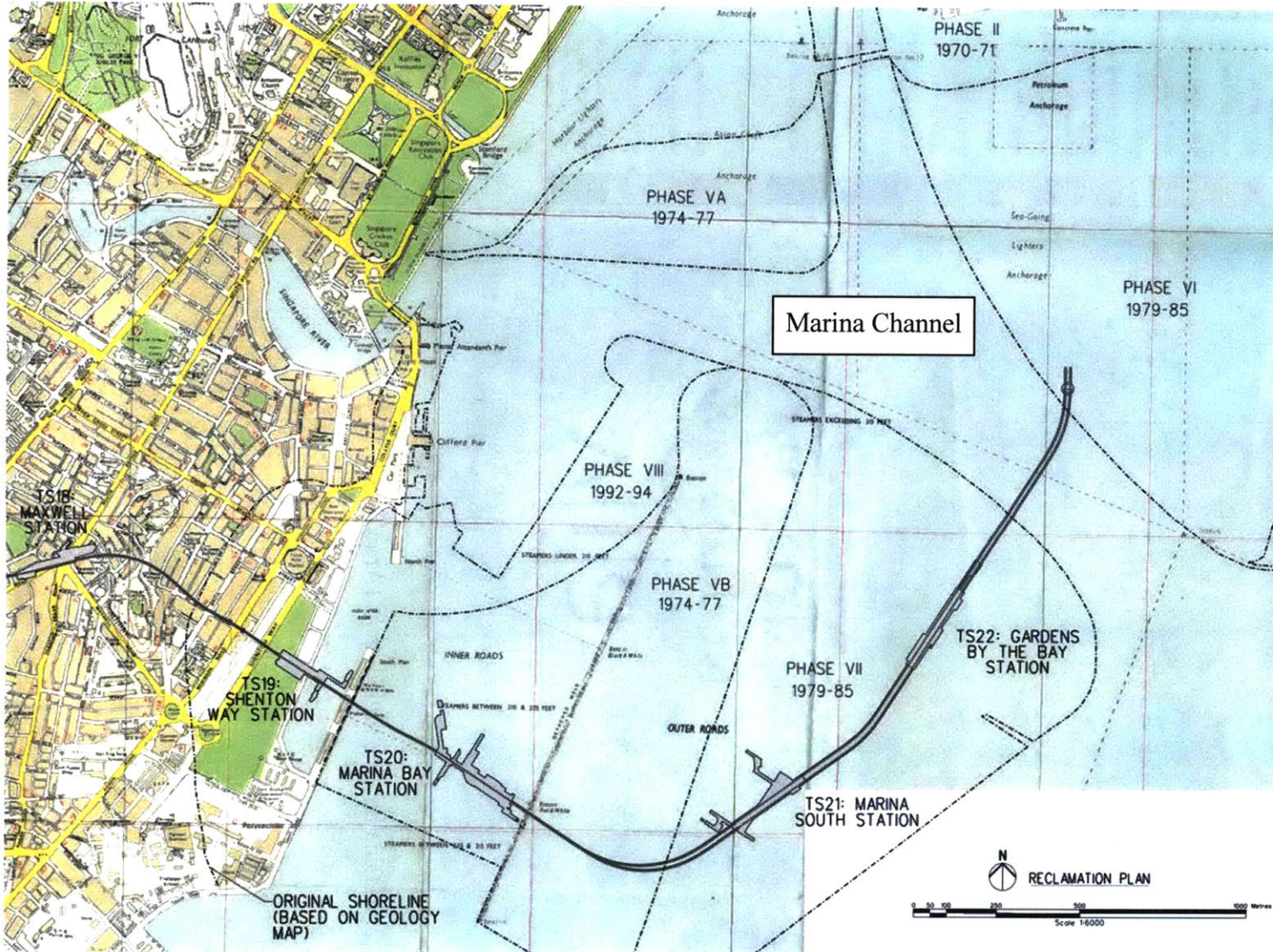


Figure 4-3: Reclamation stages, areas and dates in the Marina bay Area (Arup, 2014).

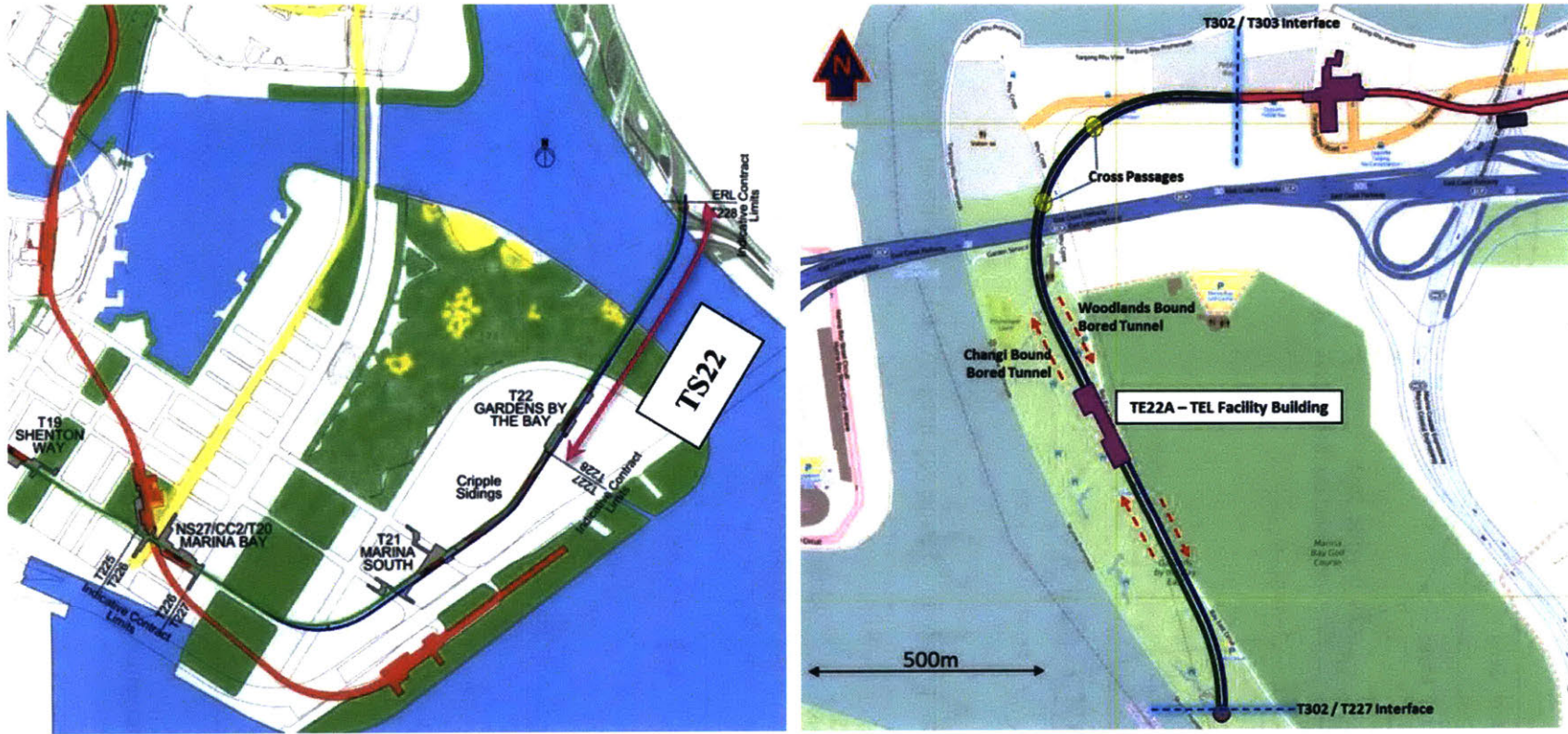


Figure 4-4: Areas included in contracts T228 (left) and T302 (right).

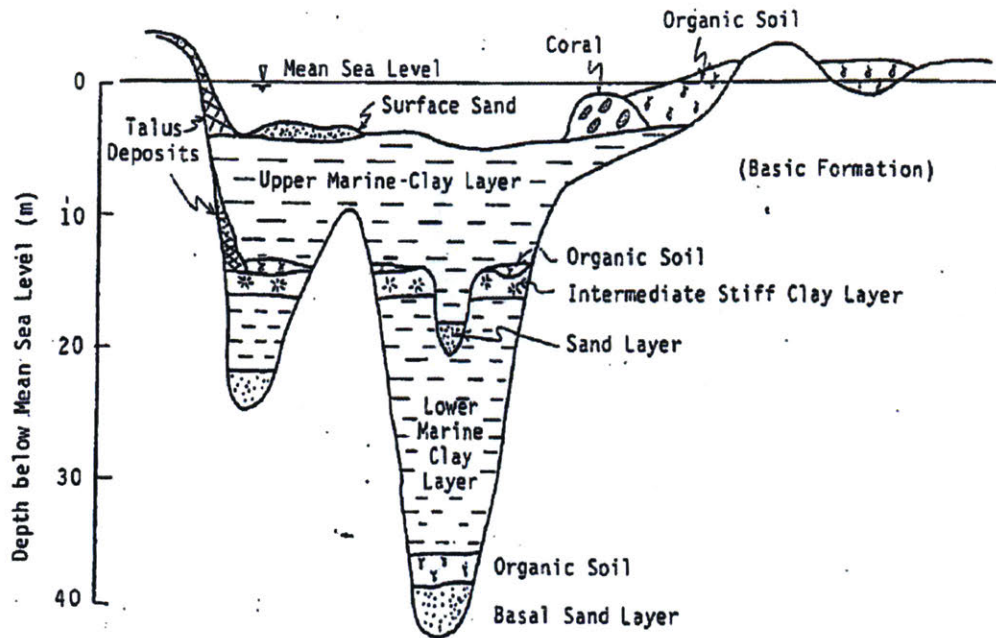


Figure 4-5: Schematic geotechnical profile in Marina bay area (Adachi & Mizuni, 1979).

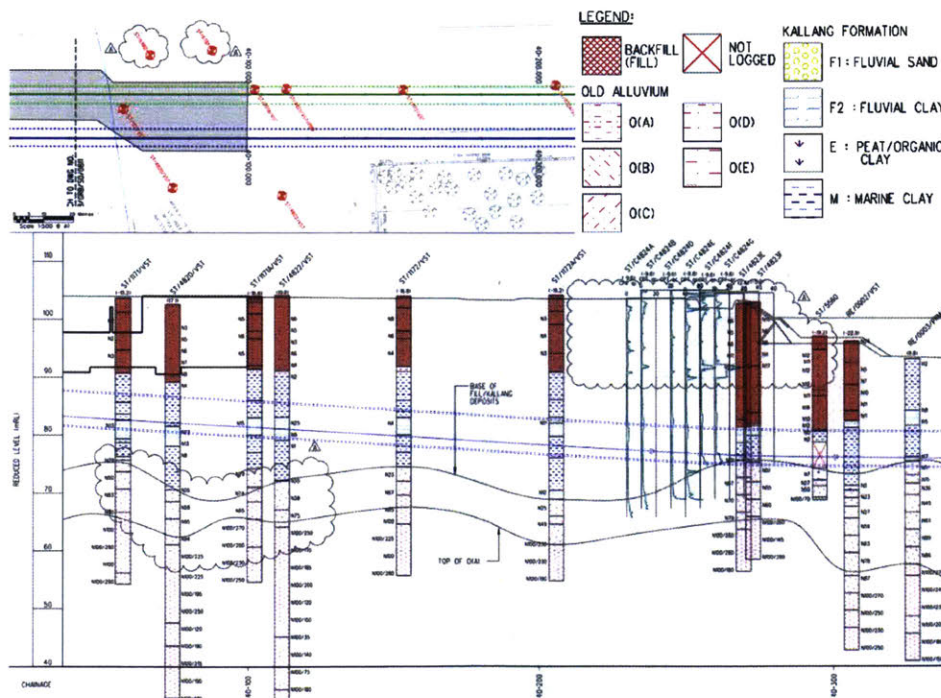


Figure 4-6: Typical soil profile encountered in T228 (Arup, 2014).

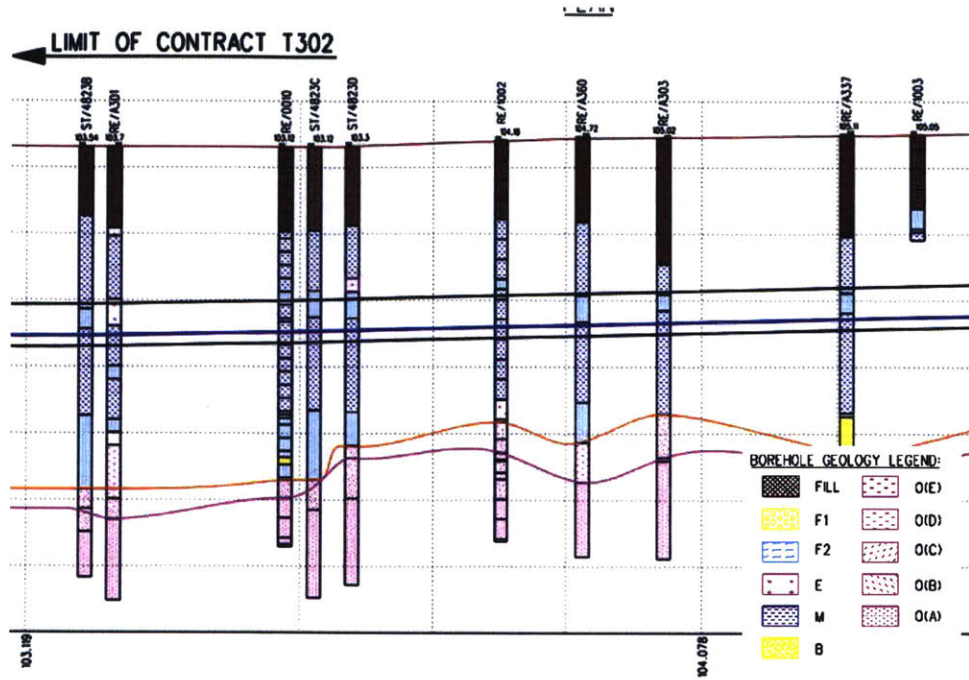


Figure 4-7: Typical soil profile encountered in T302 (Mott MacDonald, 2015).

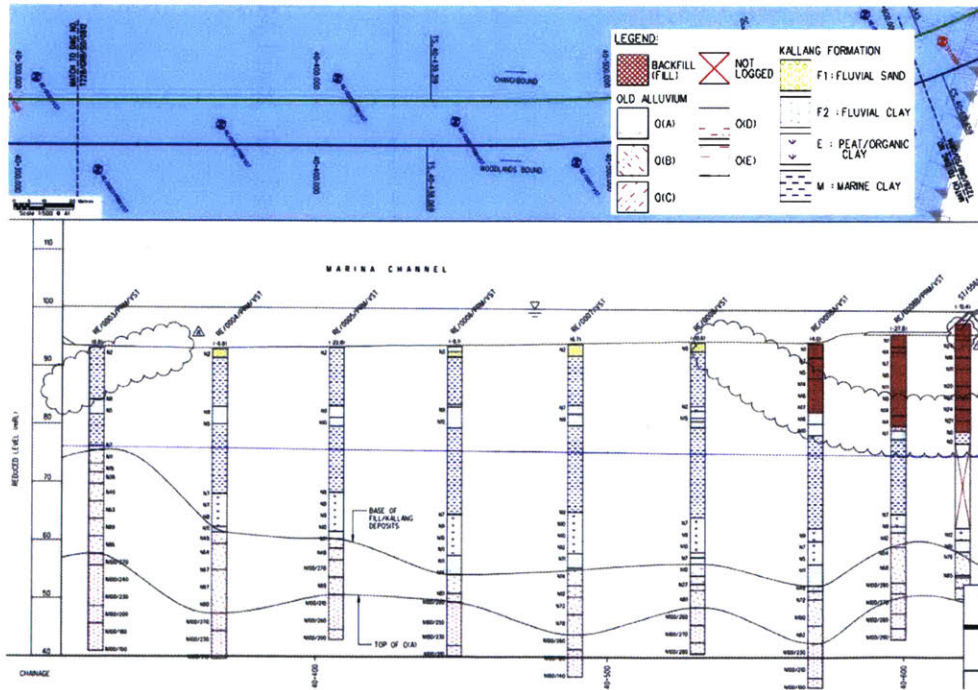


Figure 4-8: Soil profile in the Marina Bay channel (Arup, 2014).

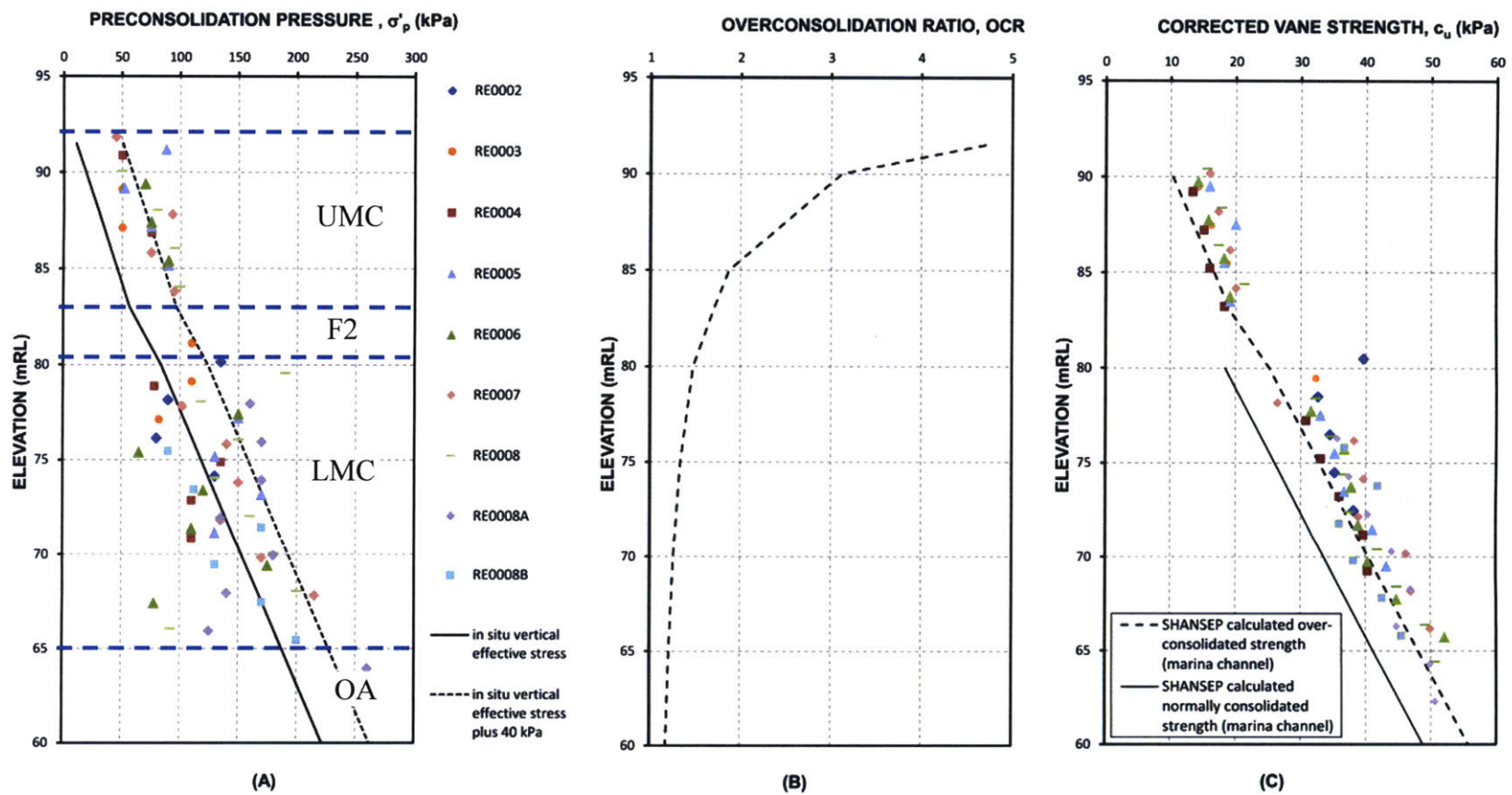


Figure 4-9: Undrained shear strength and OCR profile for UMC and LMC in the canal in T228 (Arup, 2014).

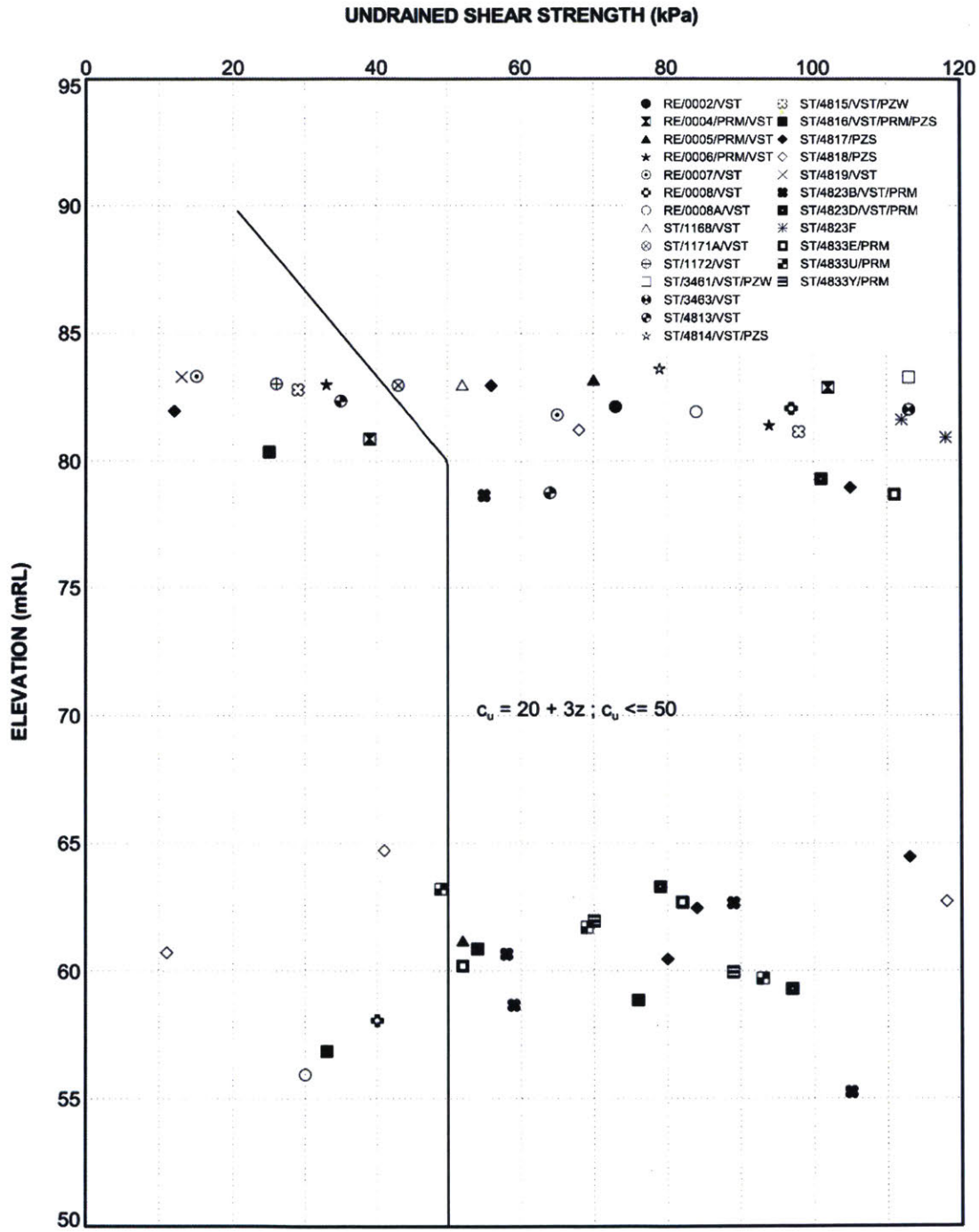


Figure 4-10: Undrained shear strength for F2 in T228 (Arup, 2014).

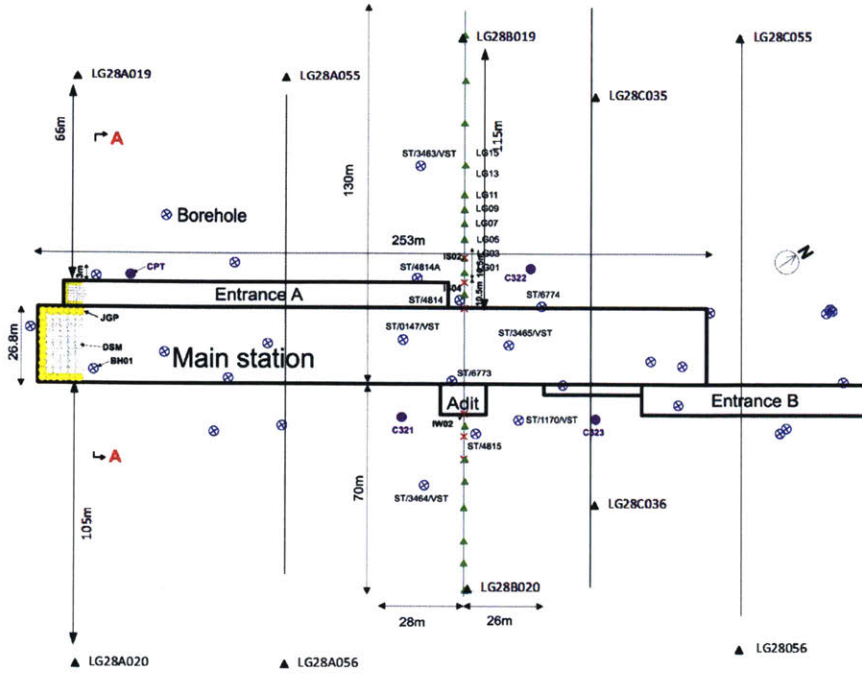


Figure 4-11: Location of settlement markers in TS22 (T228).

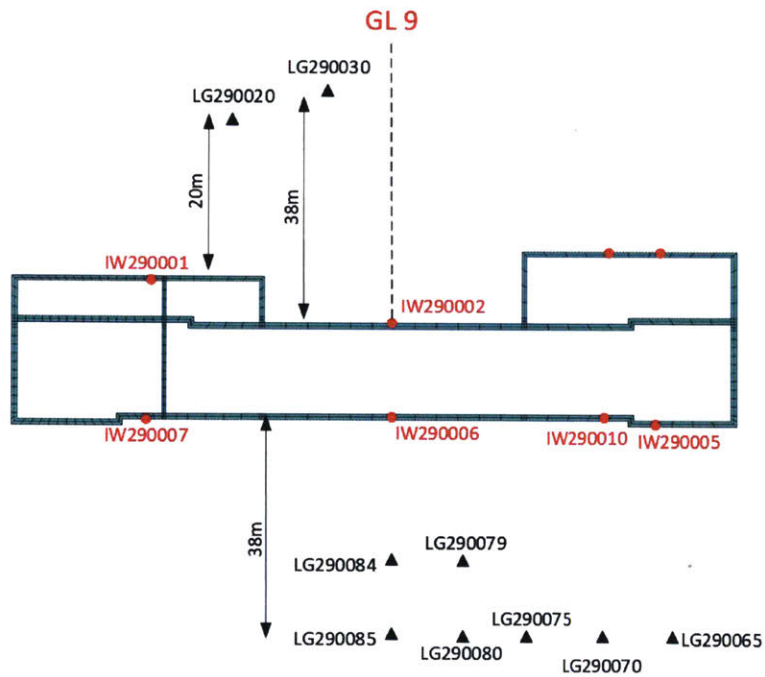


Figure 4-12: Location of settlement markers in TE22A (T302).

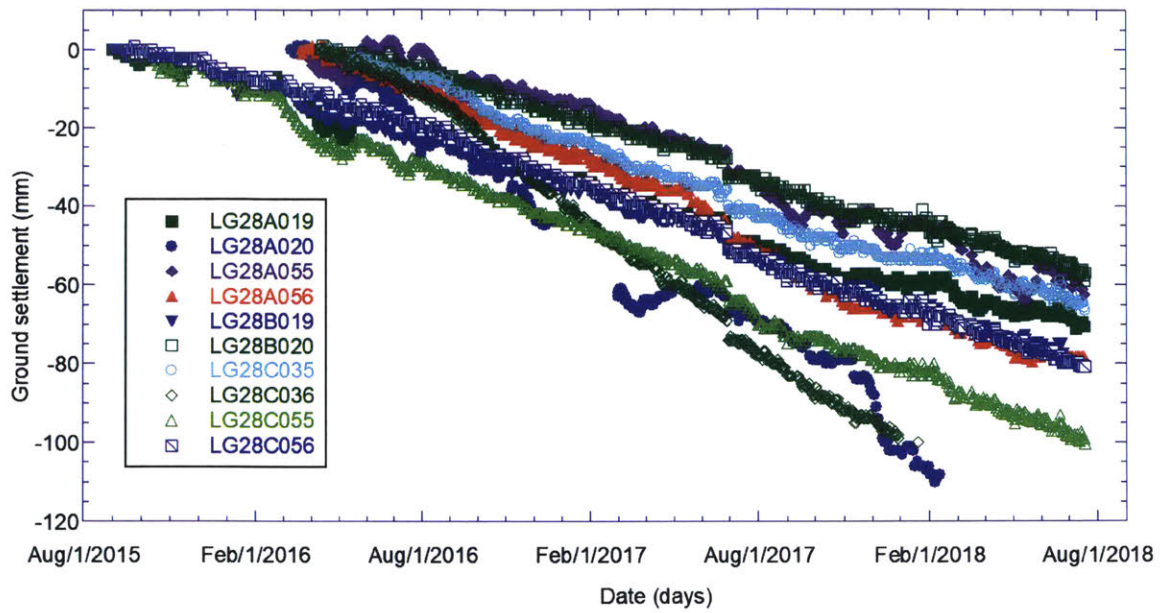


Figure 4-13: Settlement vs. time in markers in TS22 (T228).

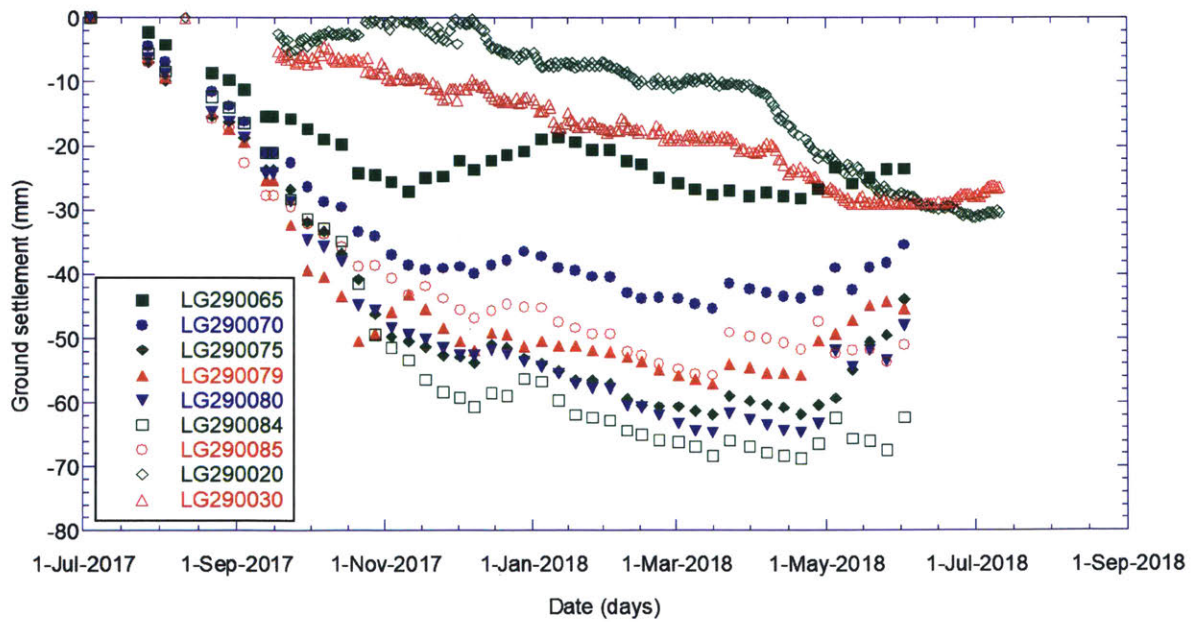


Figure 4-14: Settlement vs. time in markers in TE22A (T302).

Boundary conditions:

- x_{min} & x_{max} :
 - Normally fixed
 - Flow closed
- y_{max} :
 - Free displacement.
 - Free flow.
- y_{min} :
 - Fully fixed,
 - Flow closed.

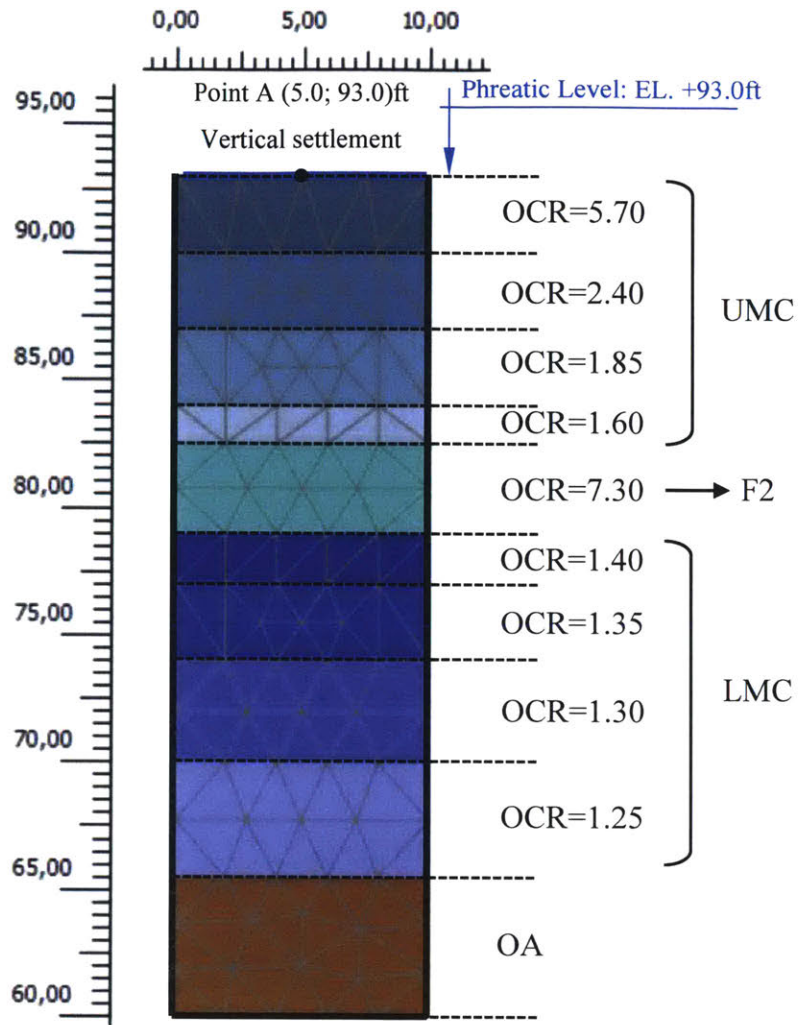


Figure 4-15: PLAXIS Model, example of geometry and materials (PLX34).

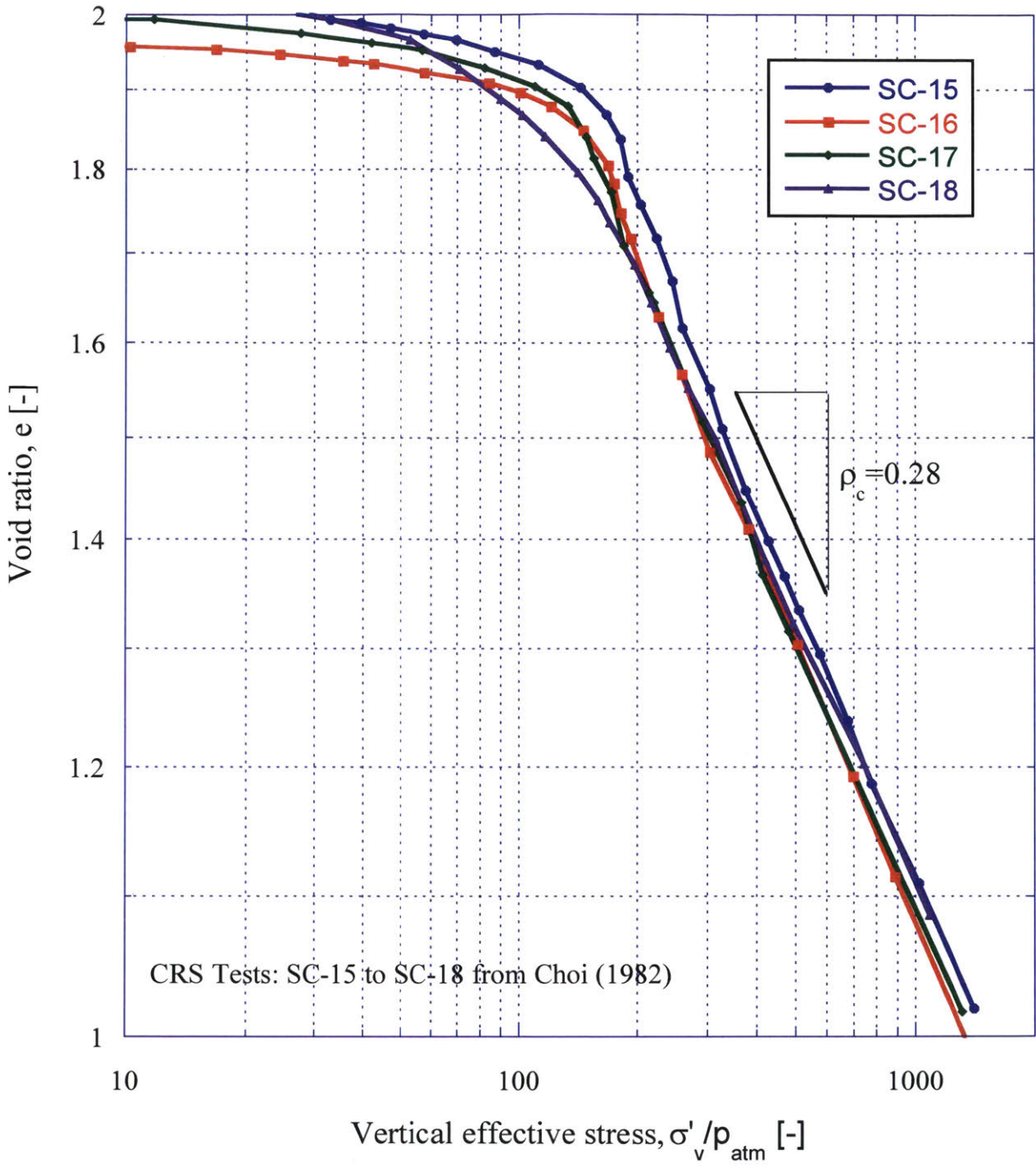


Figure 4-16: ρ_c selection in $\log(e) - \log(\sigma'_v)$ space.

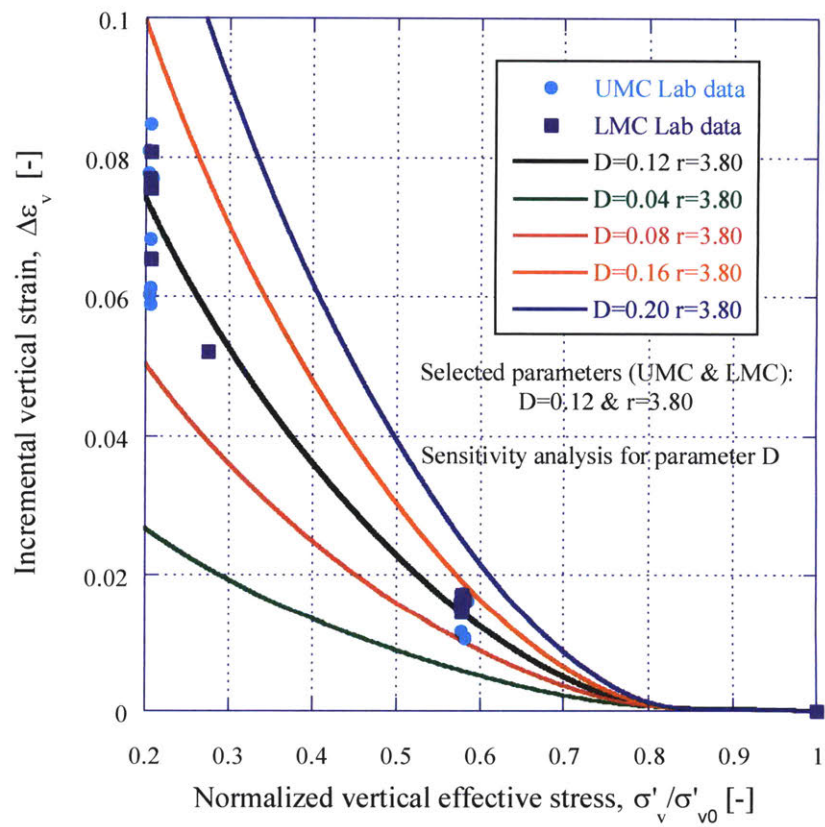
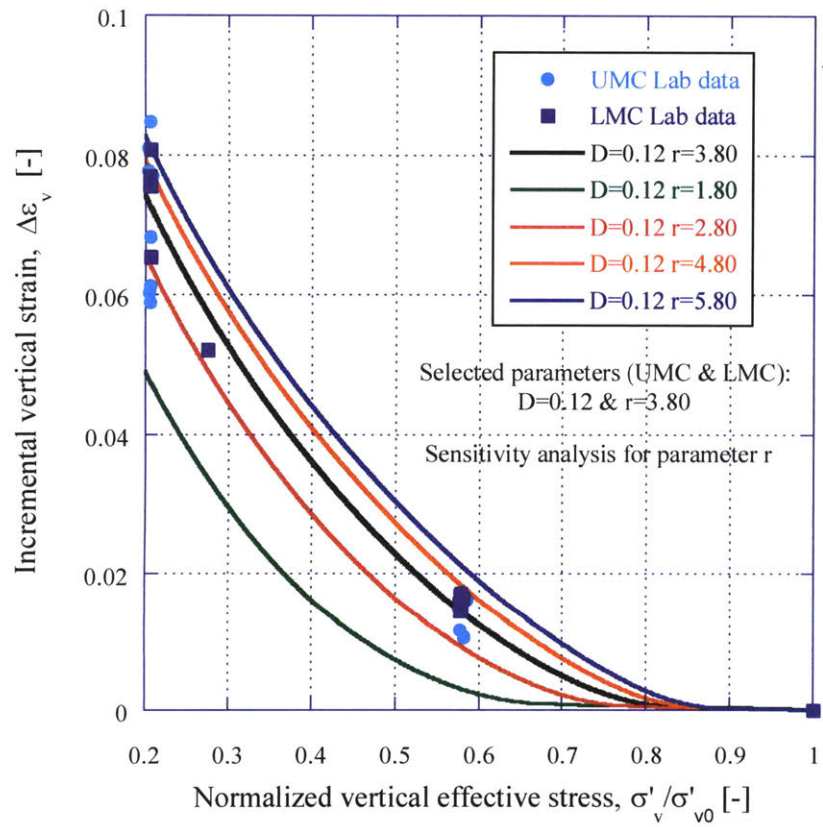


Figure 4-17: D & r selection for UMC and LMC and sensitivity analyses.

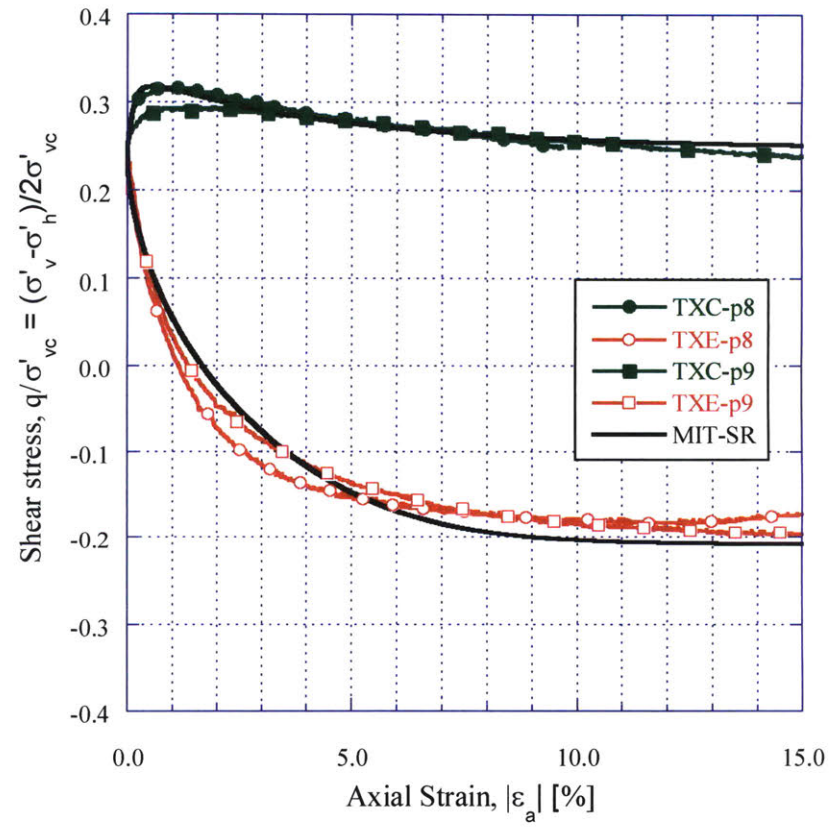
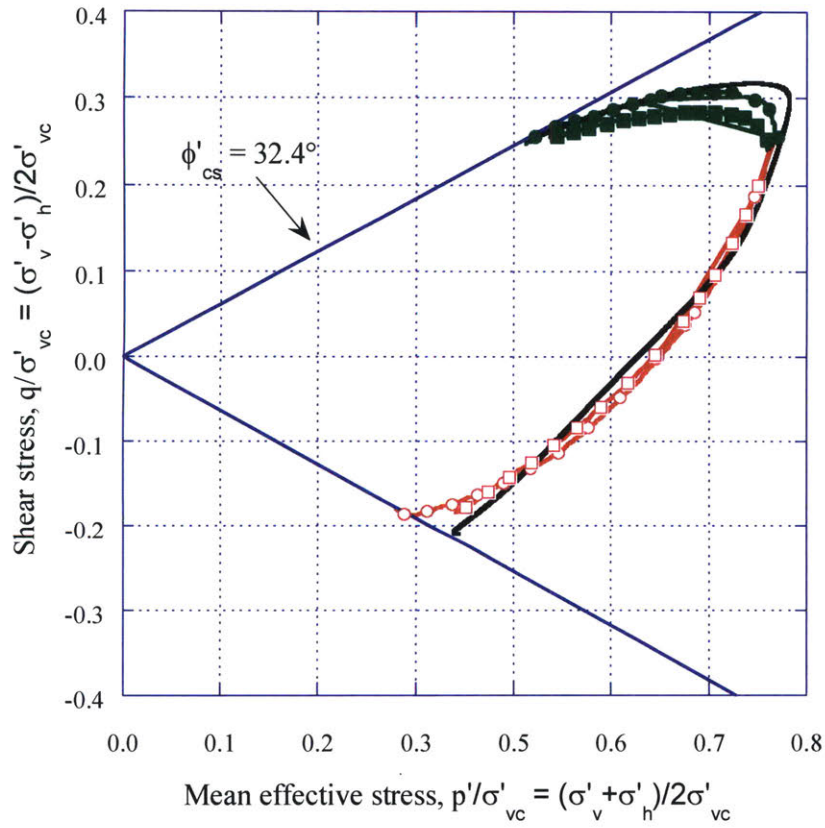


Figure 4-18: ϕ'_m , m , w_s & ψ selection for UMC in q/σ'_{vc} vs. p'/σ'_{vc} and q/σ'_{vc} vs. ϵ_a spaces.

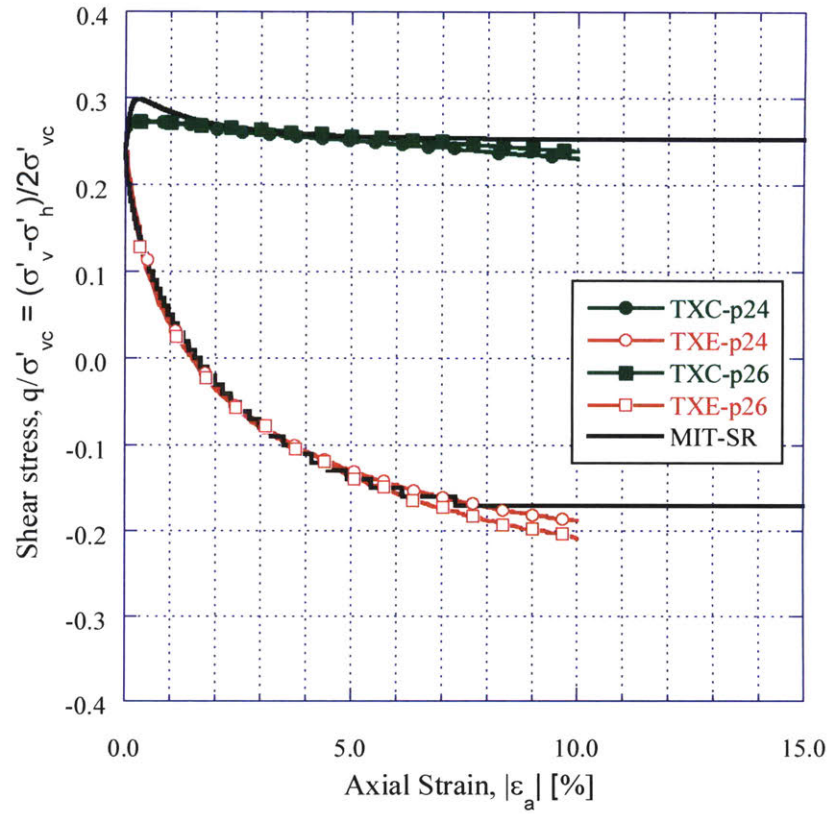
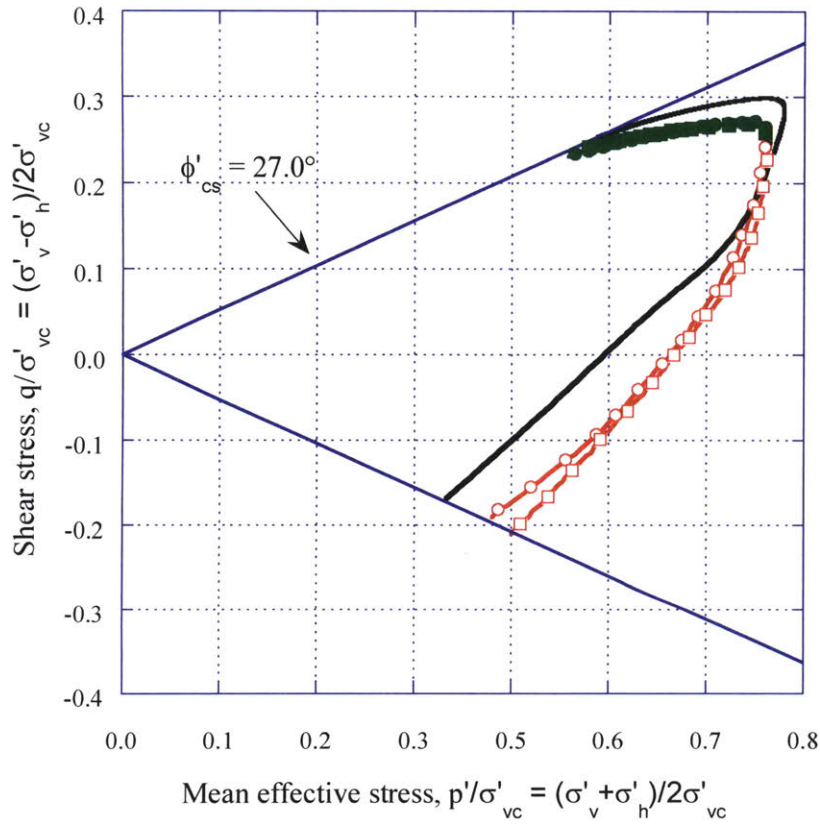


Figure 4-19: ϕ'_m , m , w_s & ψ selection for LMC in q/σ'_{vc} vs. p'/σ'_{vc} and q/σ'_{vc} vs. ϵ_a spaces.

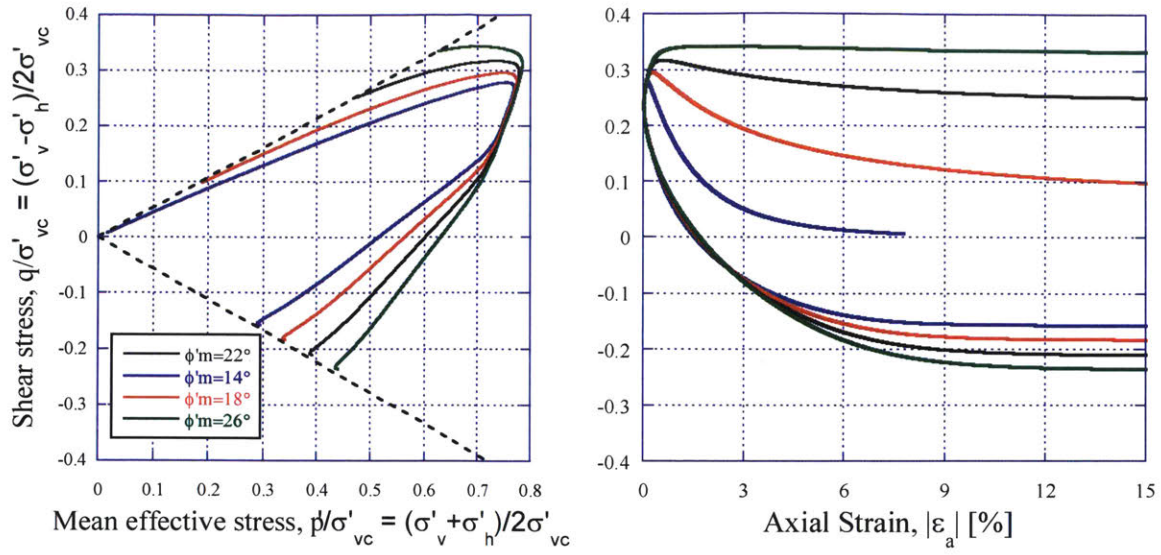


Figure 4-20: ϕ'_m , m , w_s and ψ parameters, ϕ'_m sensitivity analyses.

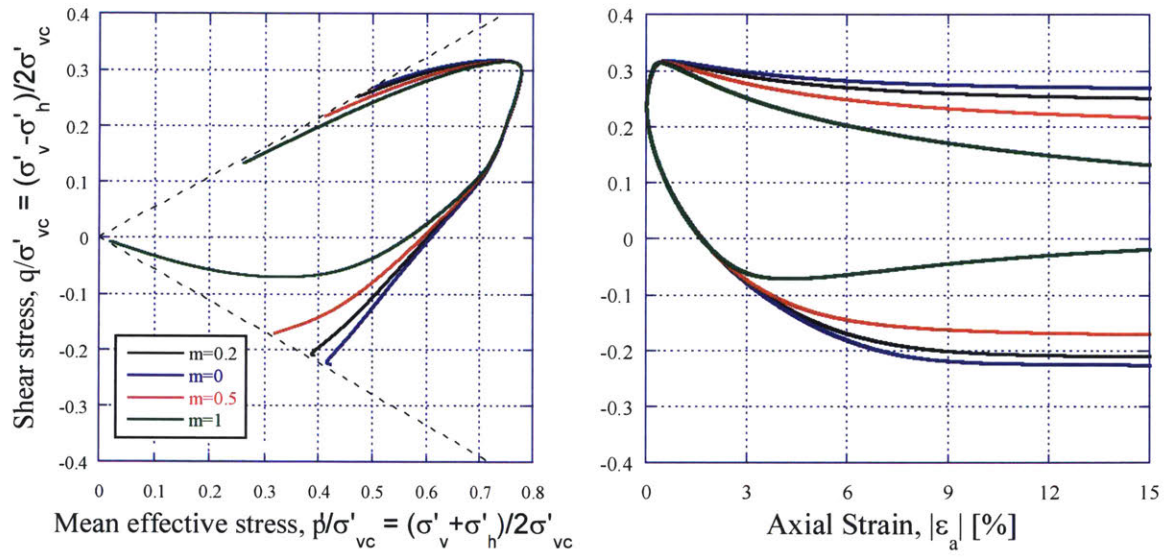


Figure 4-21: ϕ'_m , m , w_s and ψ parameters, m sensitivity analyses.

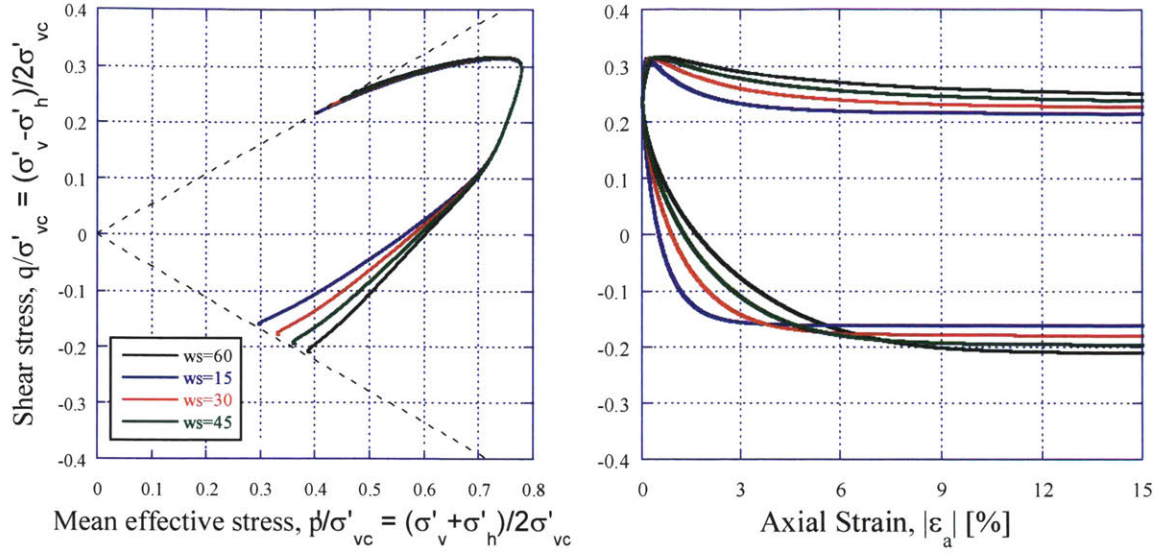


Figure 4-22: ϕ'_m , m , w_s and ψ parameters, w_s sensitivity analyses.

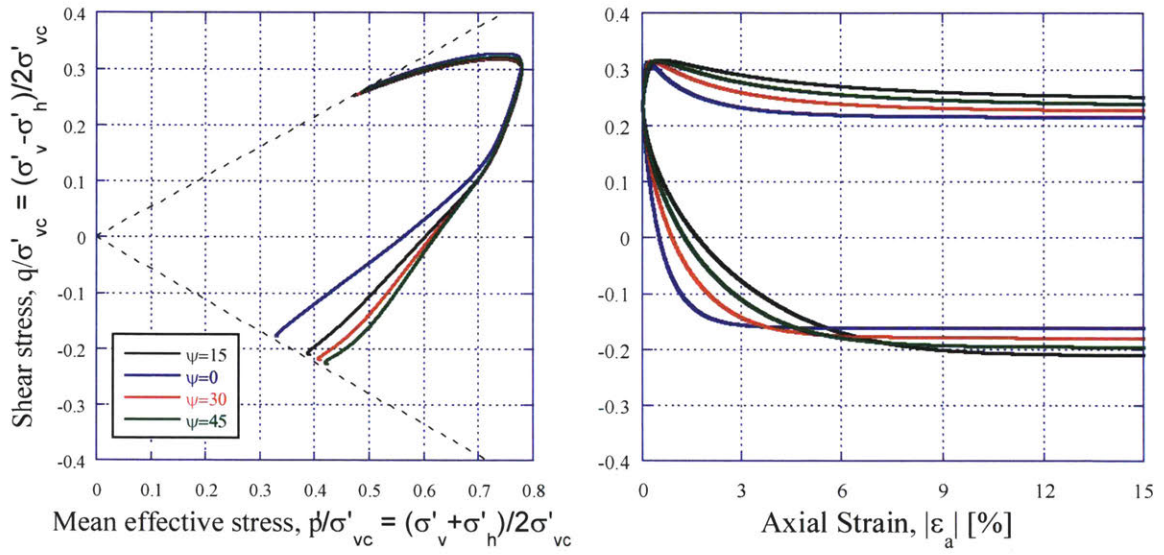


Figure 4-23: ϕ'_m , m , w_s and ψ parameters, ψ sensitivity analyses.

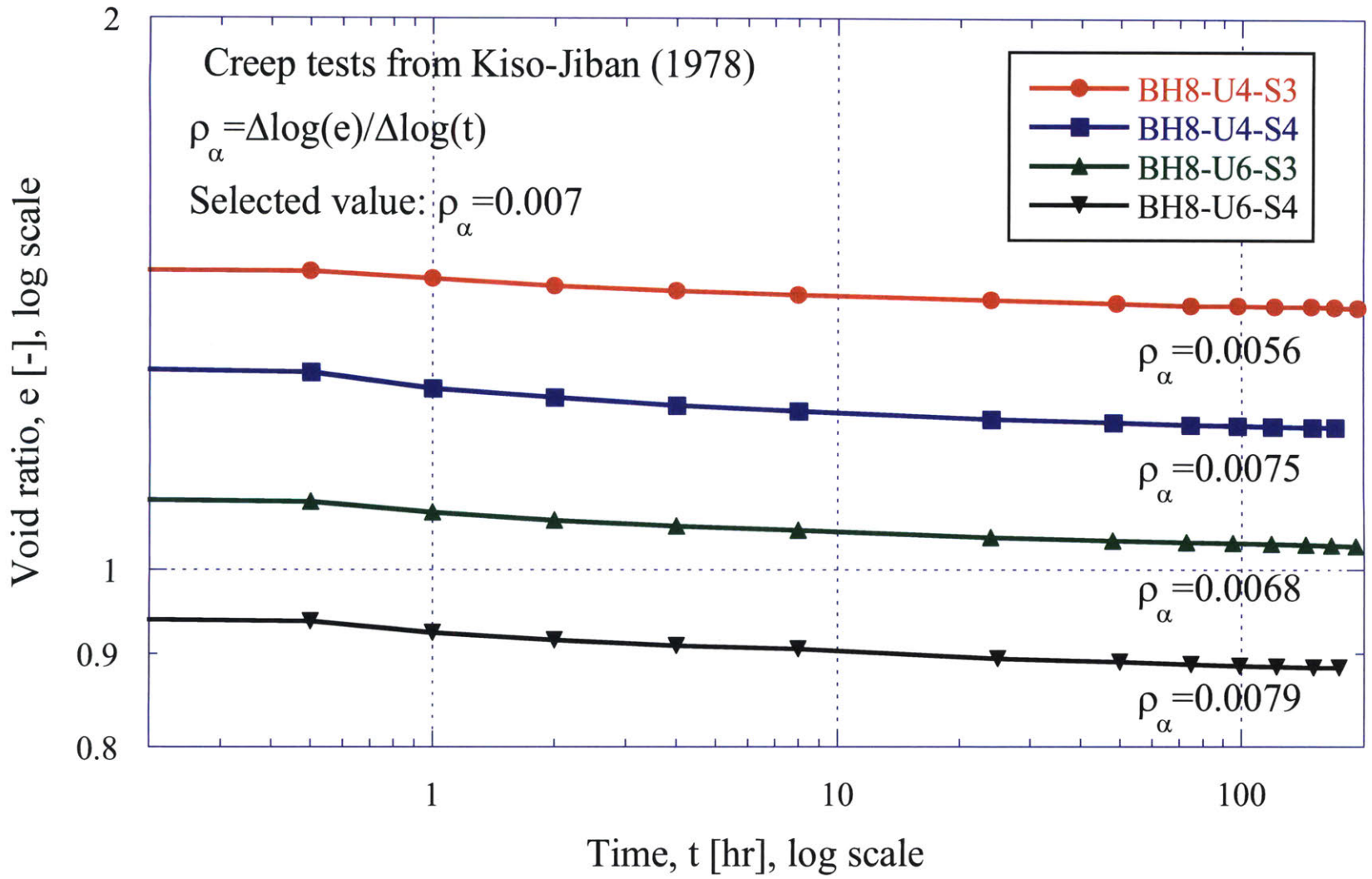


Figure 4-24: Creep tests, ρ_{α} determination for UMC and LMC.

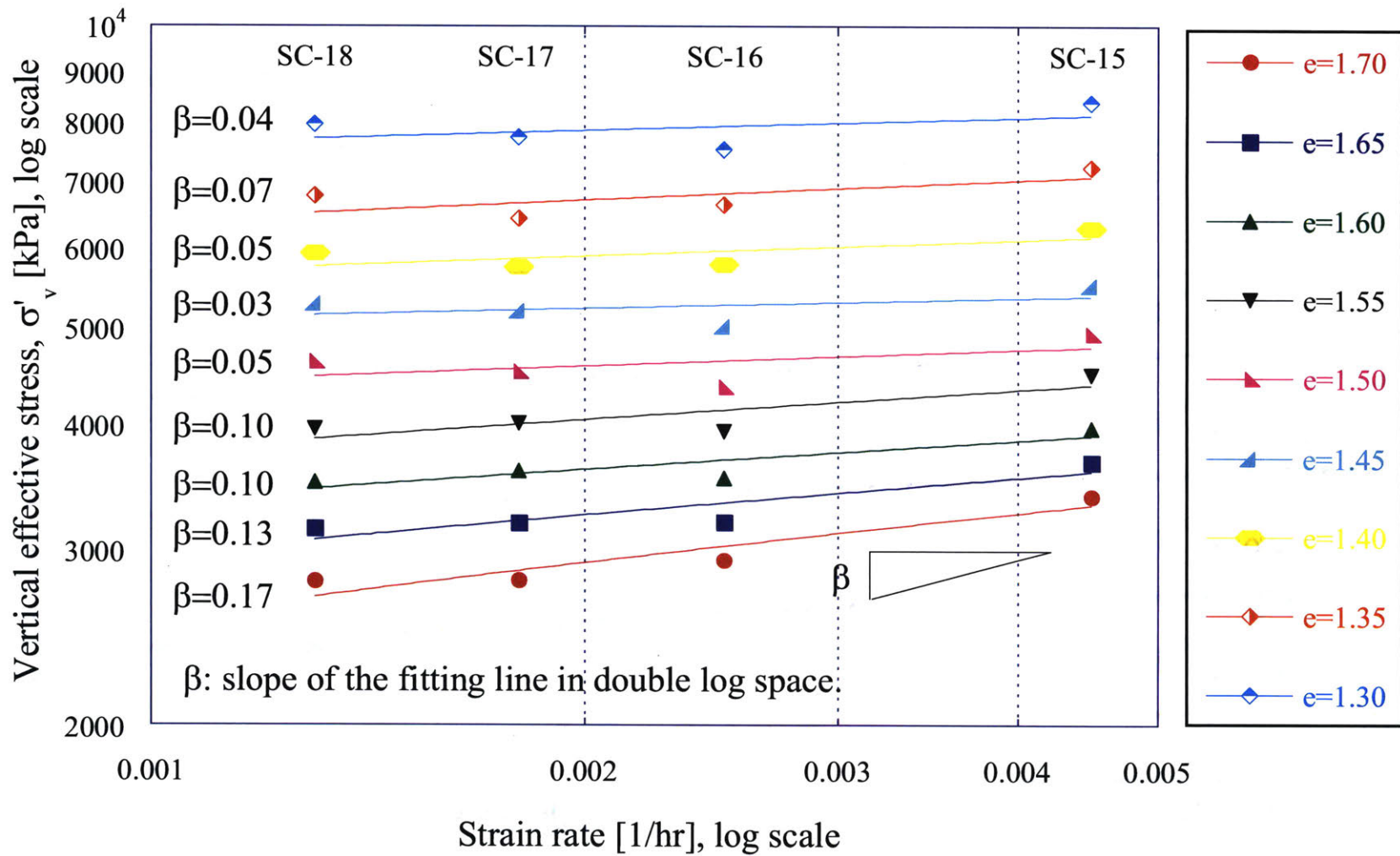


Figure 4-25: β selection in $\log(\dot{\epsilon}) - \log(\sigma'_{vc})$ space.

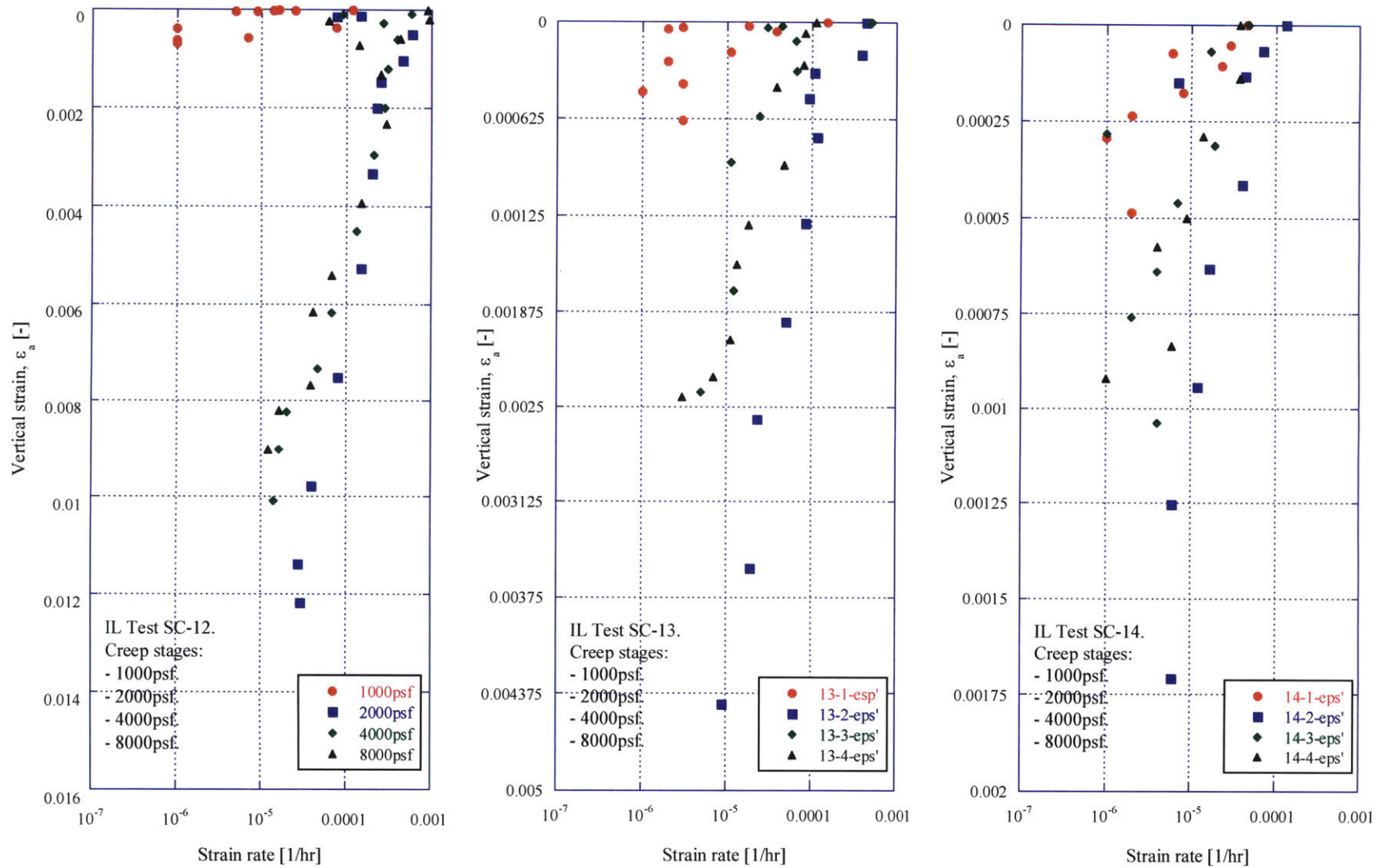


Figure 4-26: Series 4 IL tests on Marine Clay (Choi, 1982): $\dot{\epsilon}' - \epsilon'$. SC-13 detail (left) and SC-14 detail (right).

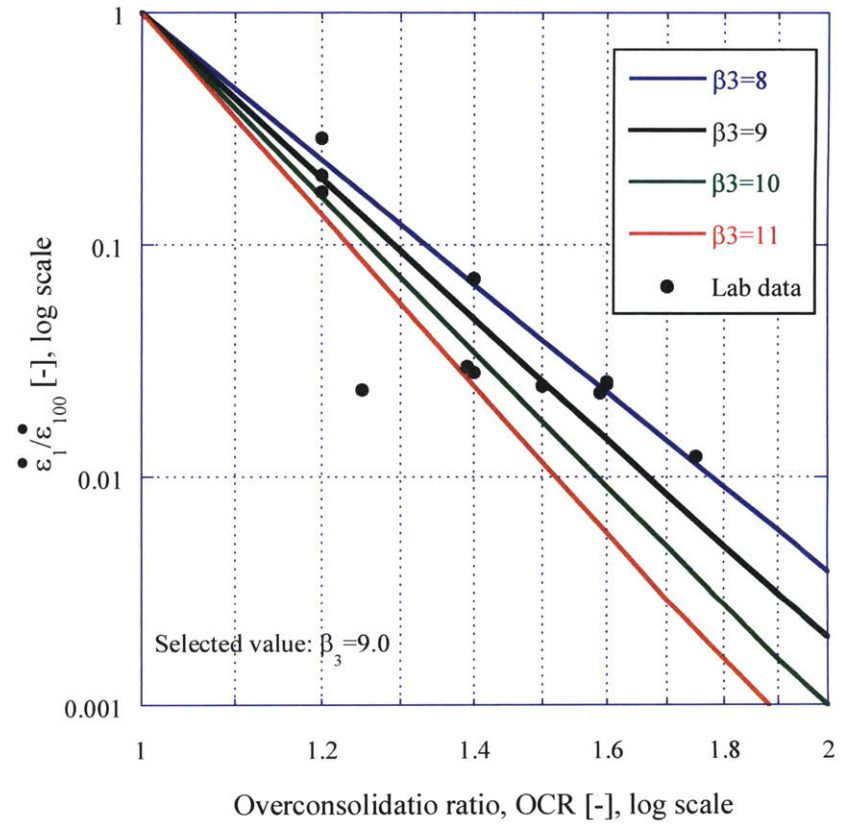
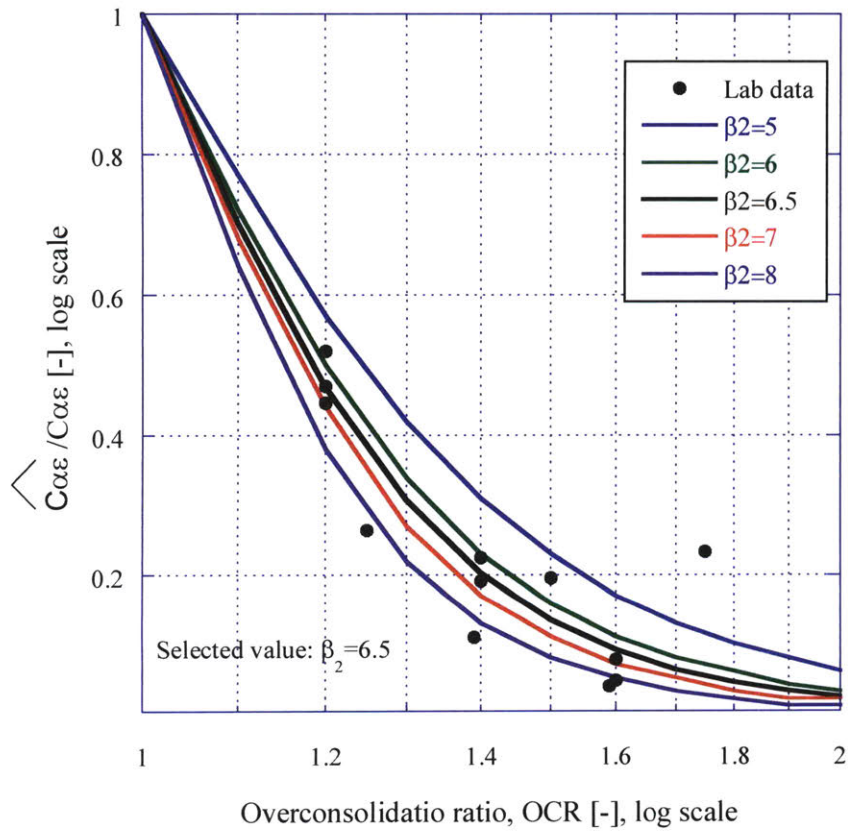


Figure 4-27: Calibration curves for β_2 (left) and β_3 (right).

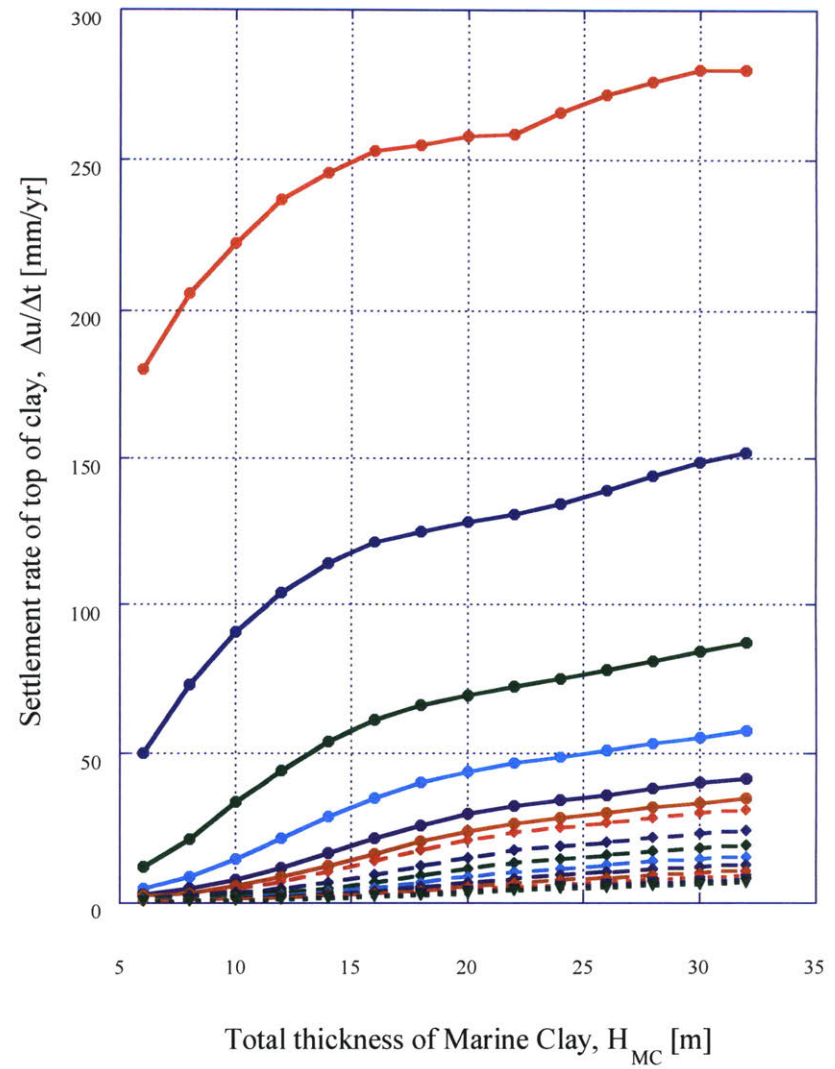
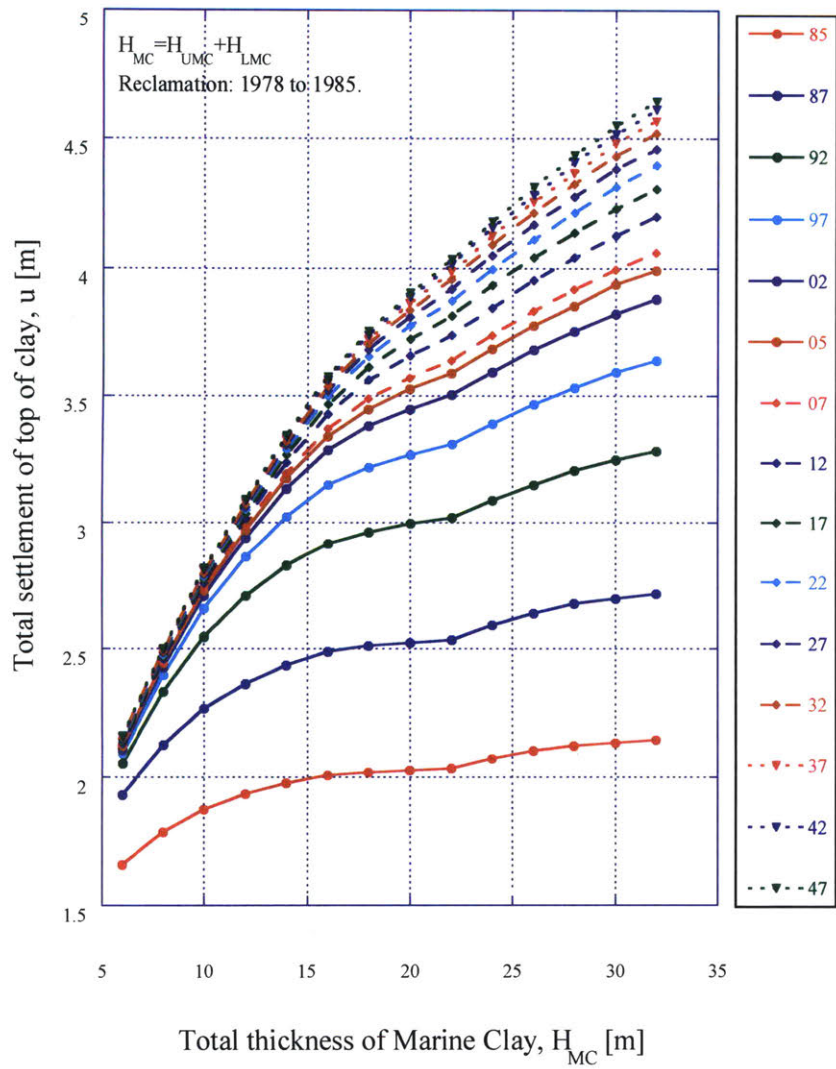


Figure 4-28: PLAXIS results, total settlements (left) and settlement rates (right) from 1985 to 2047.

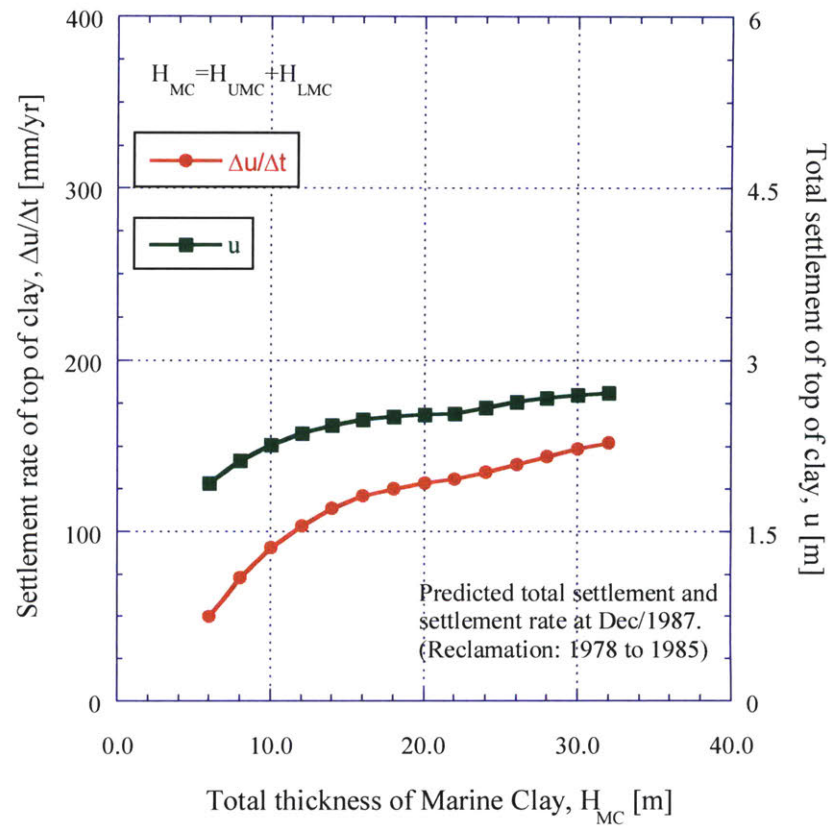
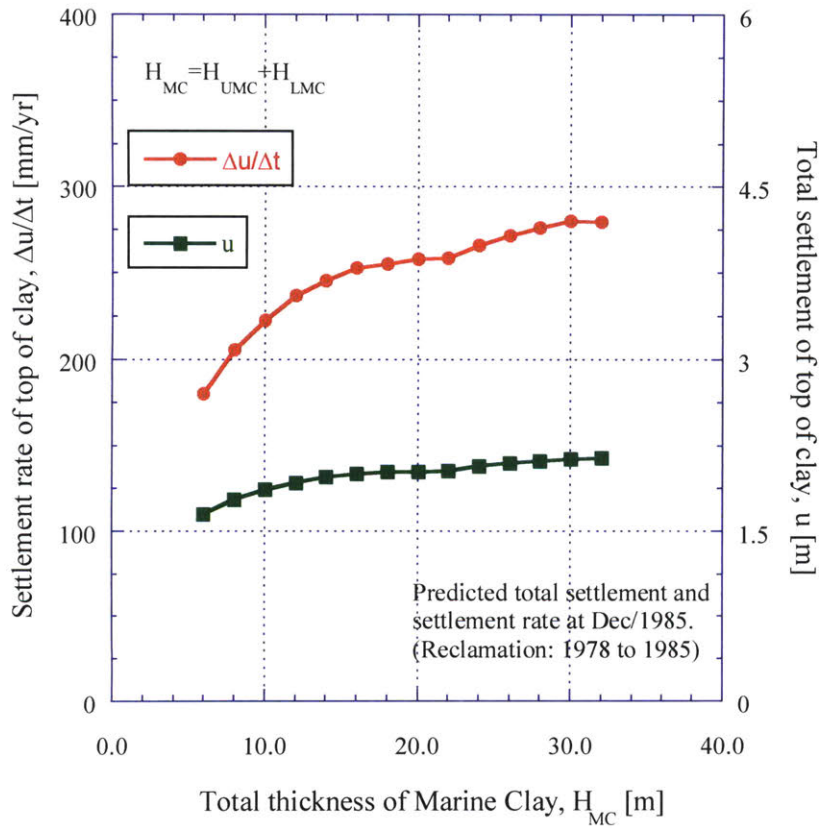


Figure 4-29: PLAXIS results, total settlement and settlement rates at Dec/1985 (left) and Dec/1987 (right).

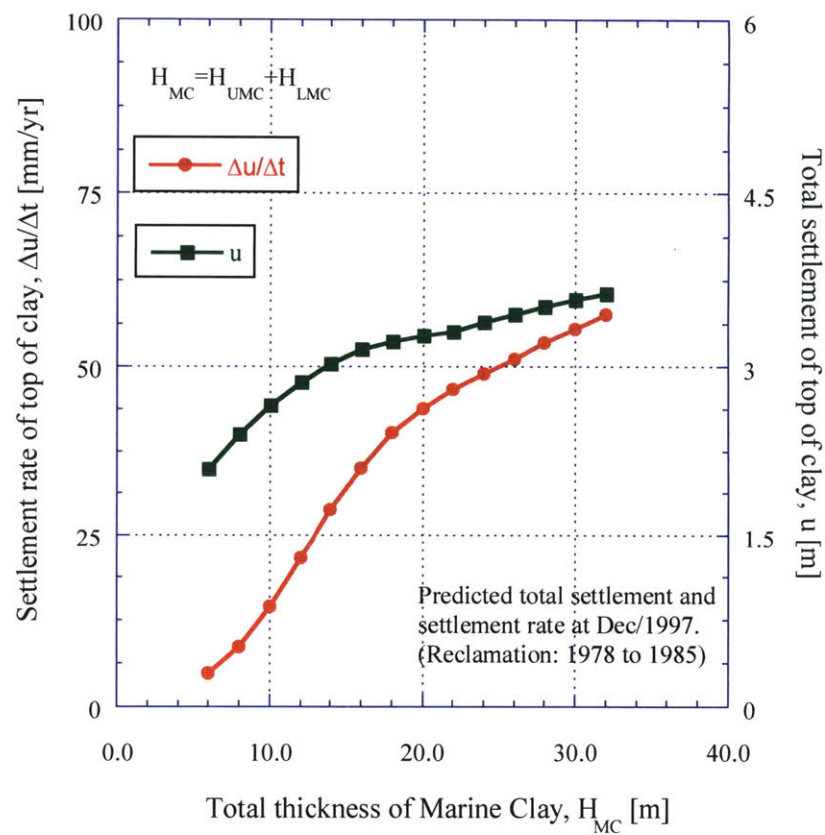
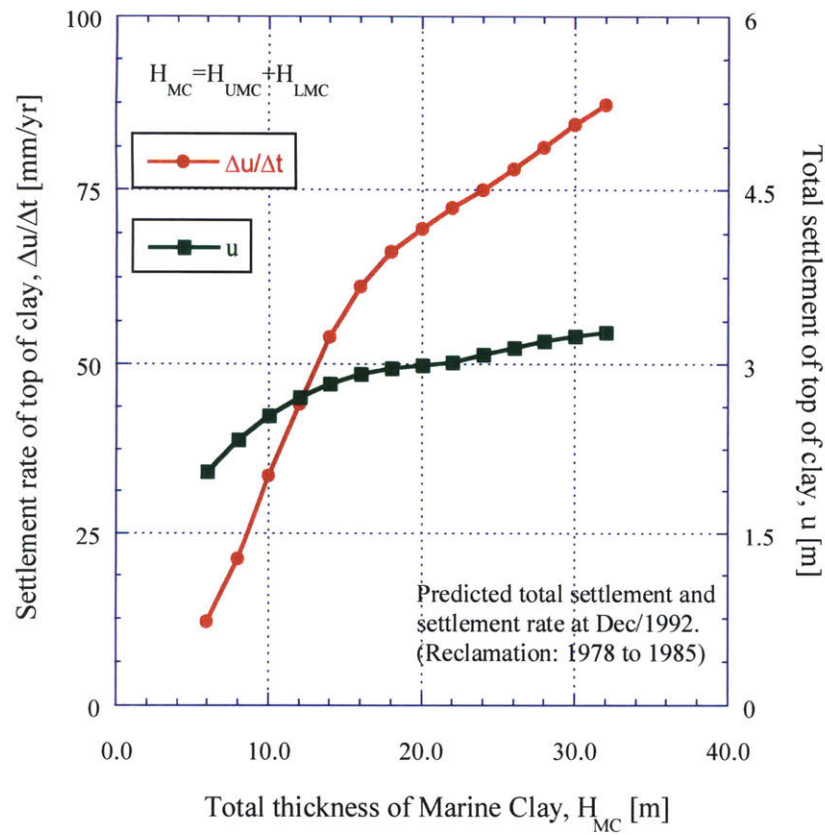


Figure 4-30: PLAXIS results, total settlement and settlement rates at Dec/1992 (left) and Dec/1997 (right).

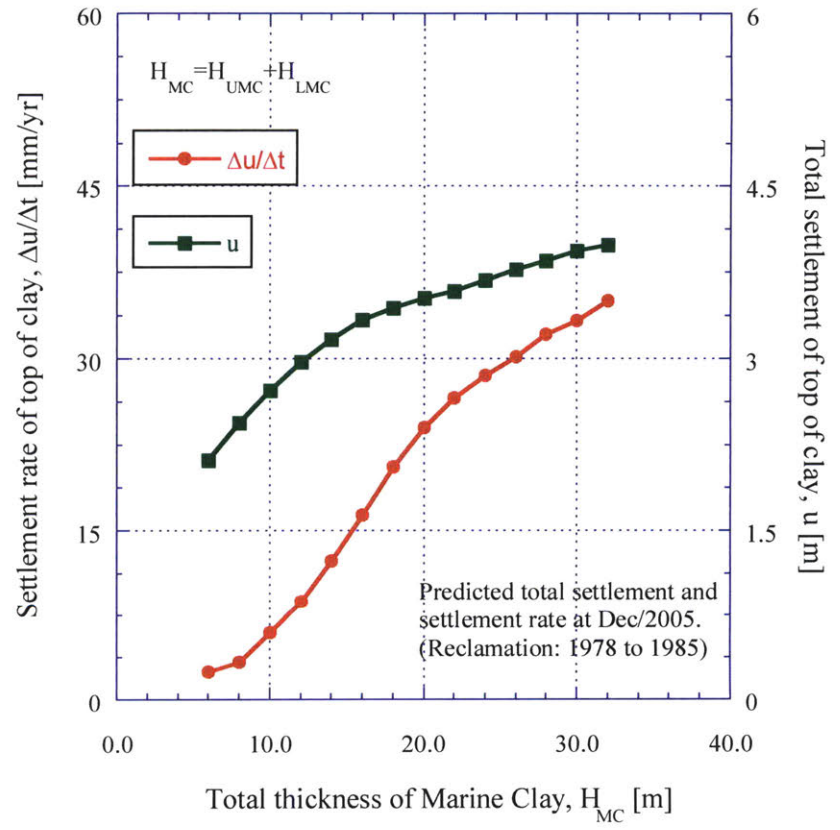
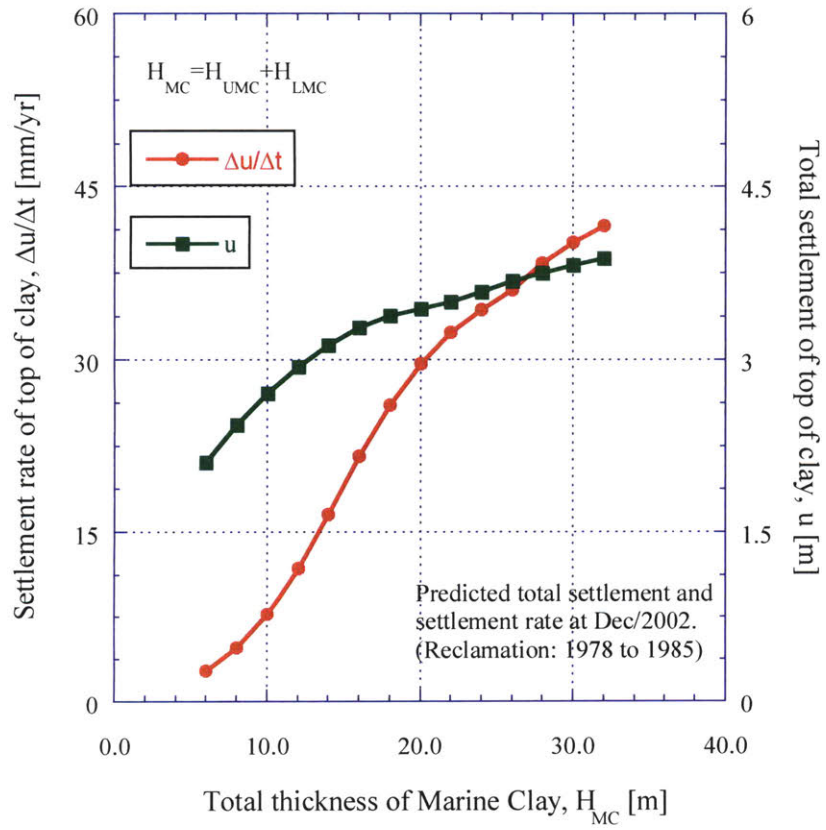


Figure 4-31: PLAXIS results, total settlement and settlement rates at Dec/2002 (left) and Dec/2005 (right).

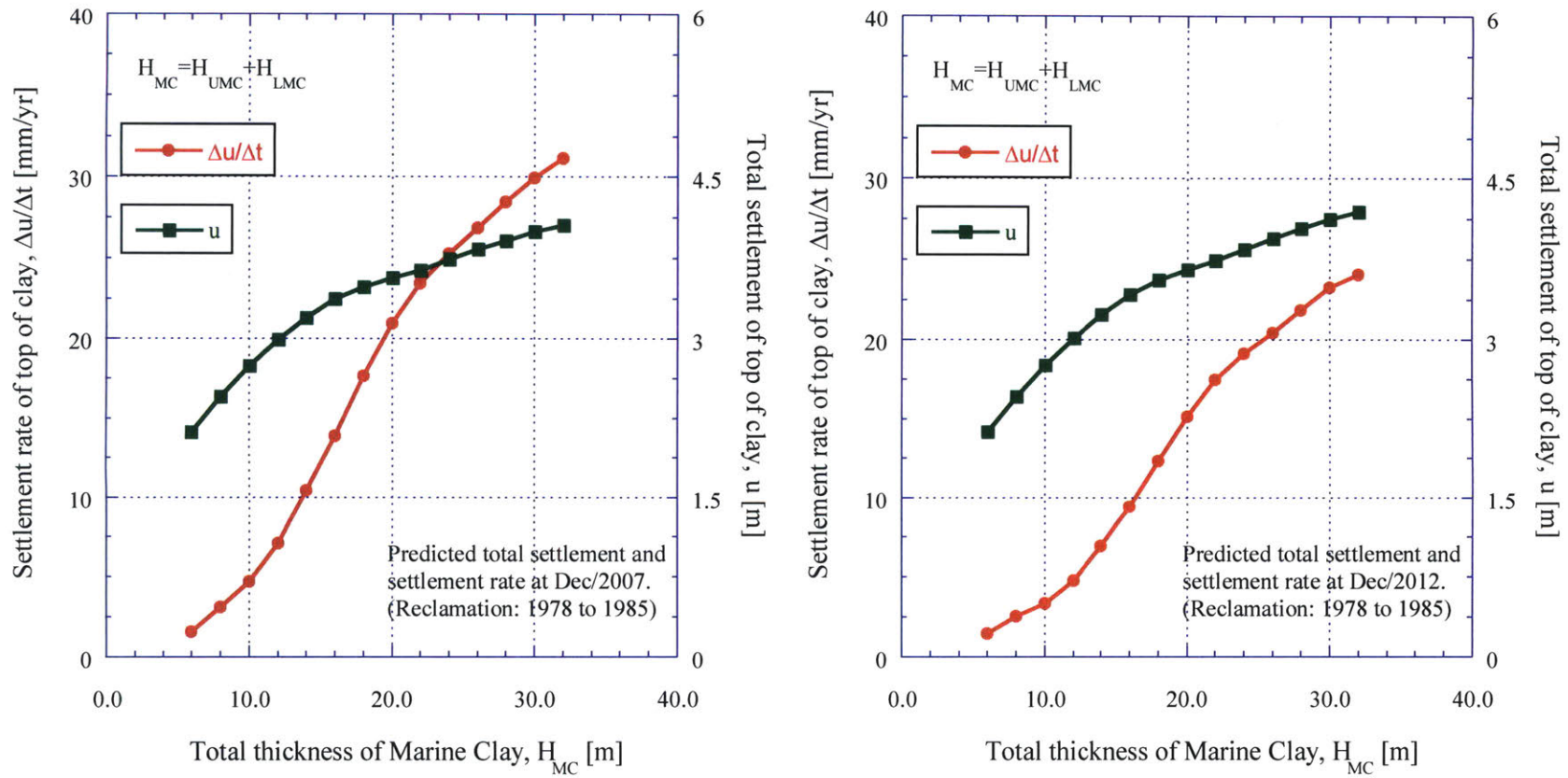


Figure 4-32: PLAXIS results, total settlement and settlement rates at Dec/2007 (left) and Dec/2012 (right).

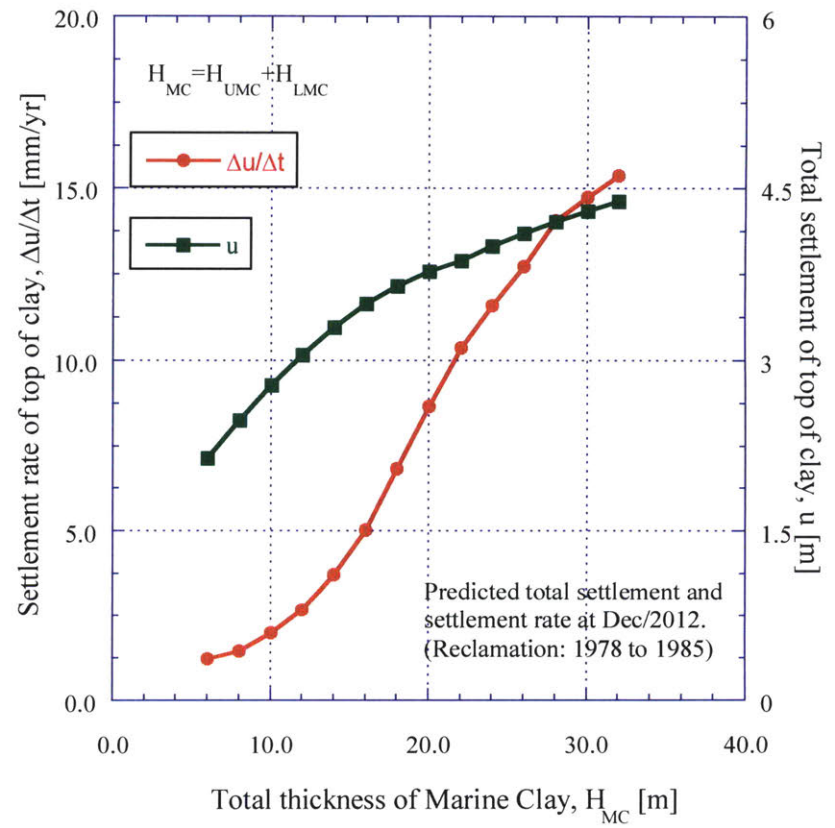
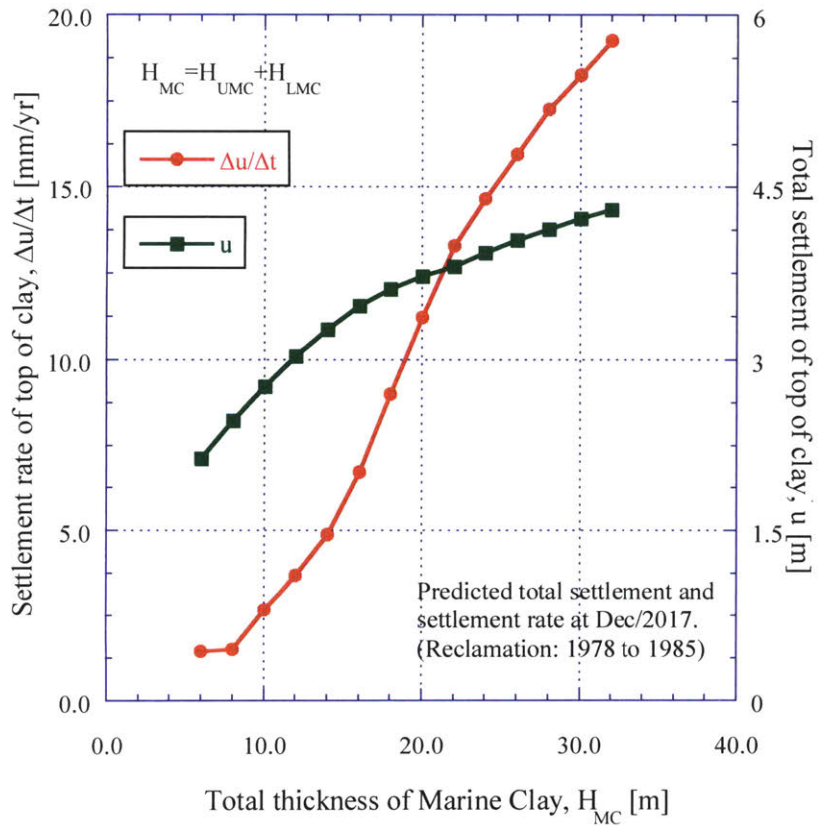


Figure 4-33: PLAXIS results, total settlement and settlement rates at Dec/2017 (left) and Dec/2022 (right).

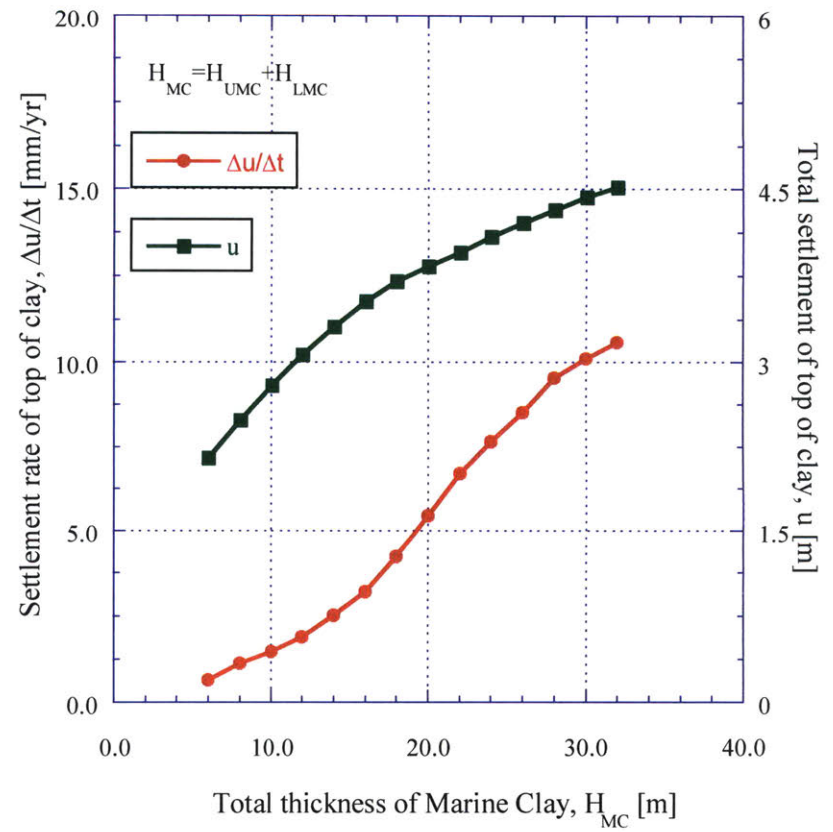
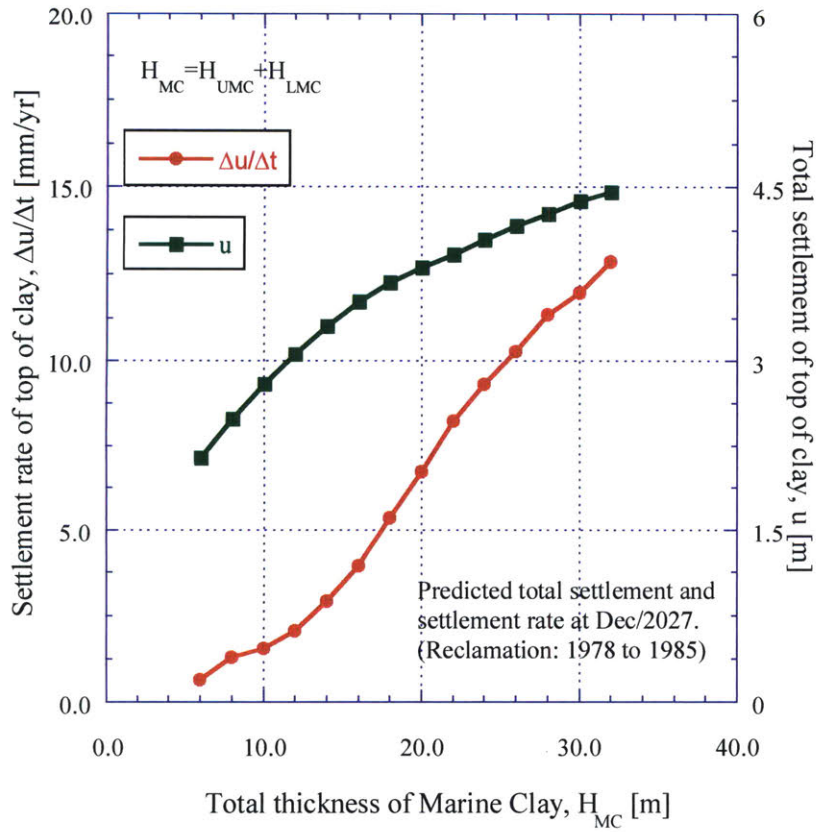


Figure 4-34: PLAXIS results, total settlement and settlement rates at Dec/2027 (left) and Dec/2032 (right).

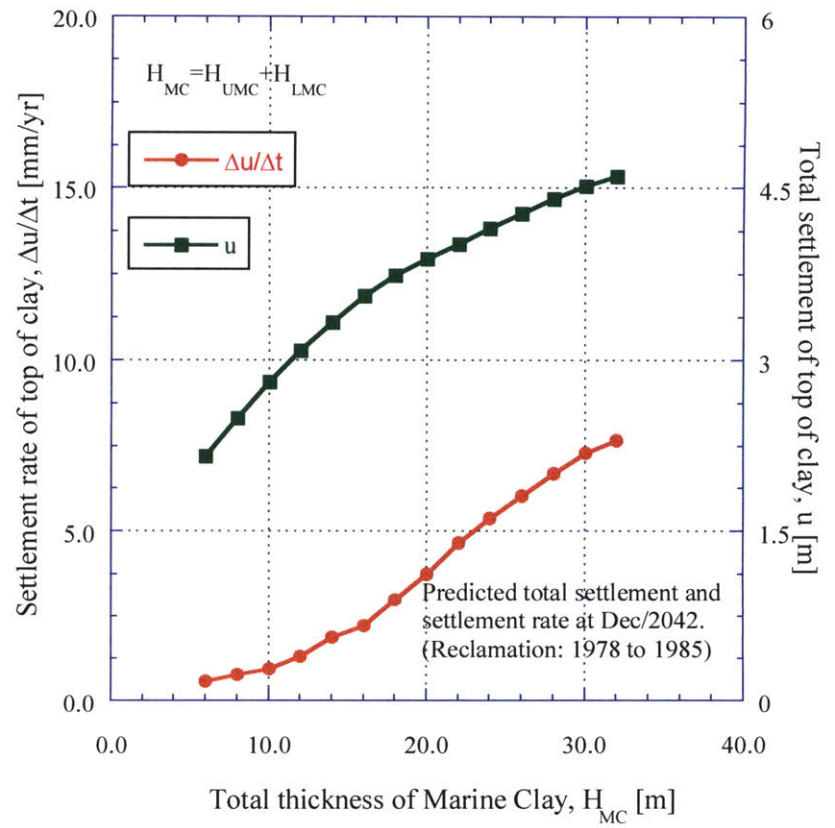
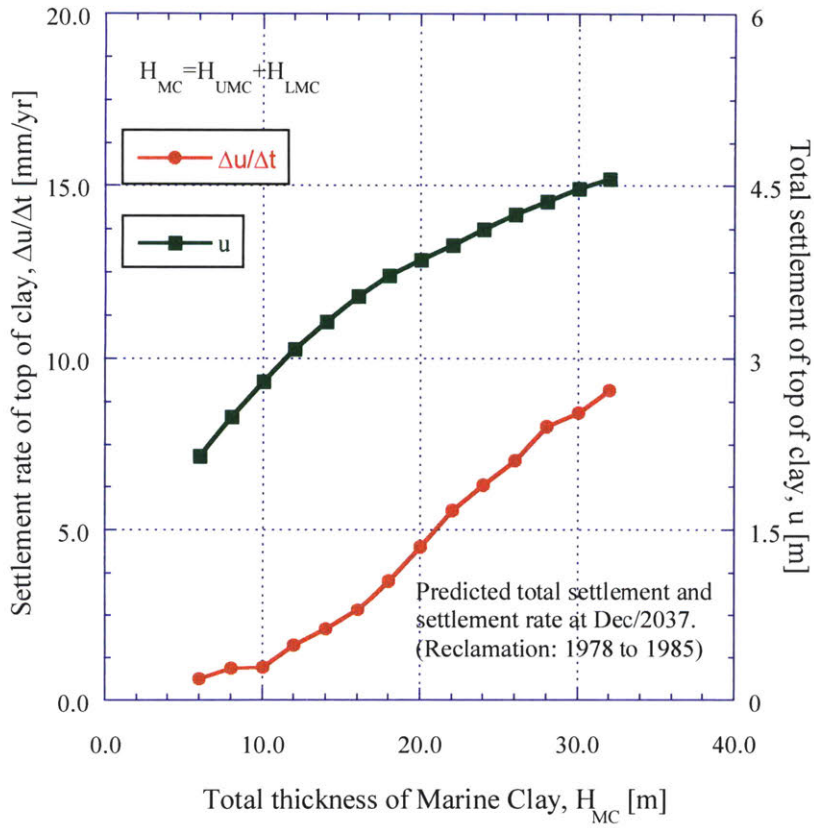


Figure 4-35: PLAXIS results, total settlement and settlement rates at Dec/2037 (left) and Dec/2042 (right).

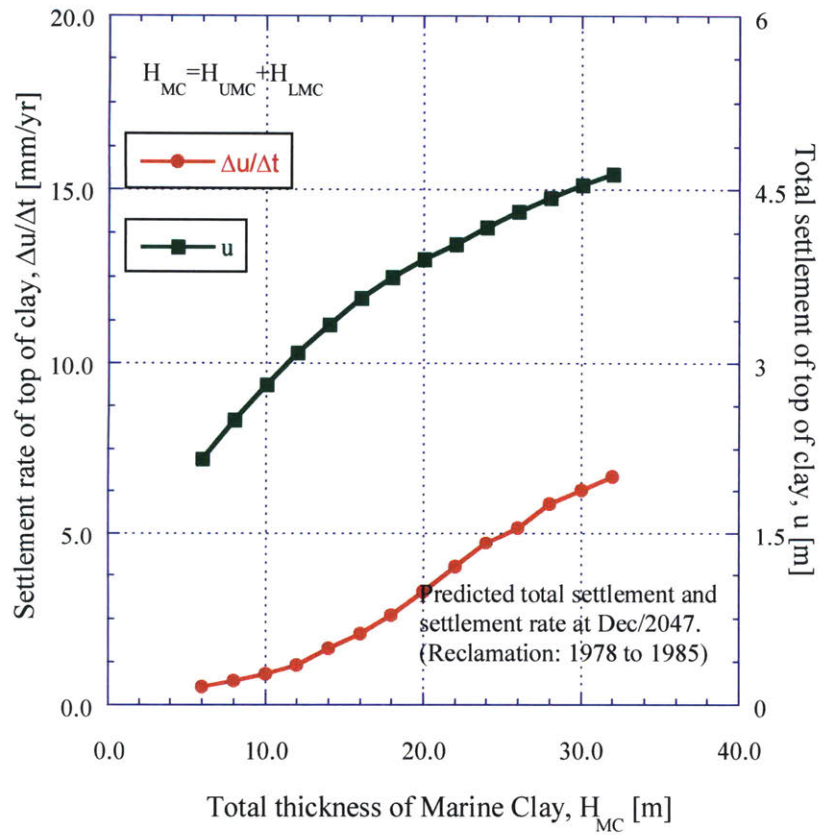


Figure 4-36: PLAXIS results, total settlement and settlement rates at Dec/2047.

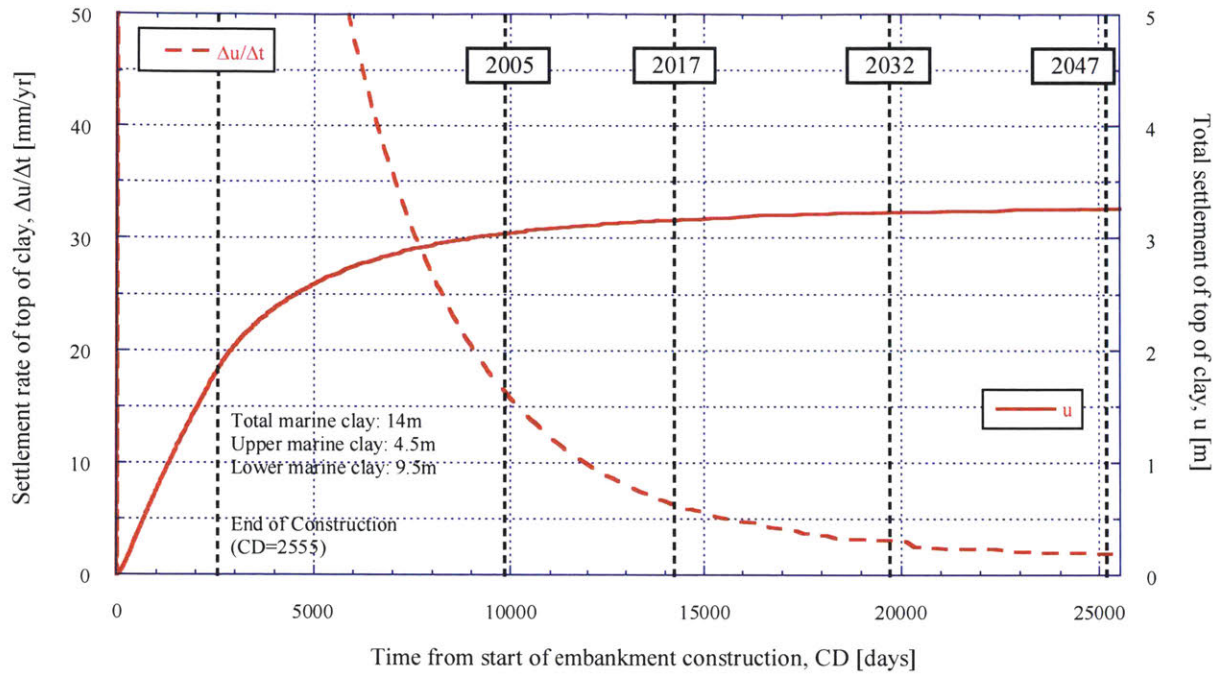


Figure 4-37: PLAXIS settlement rates and settlement for 14m of marine clay (UMC=4.5m).

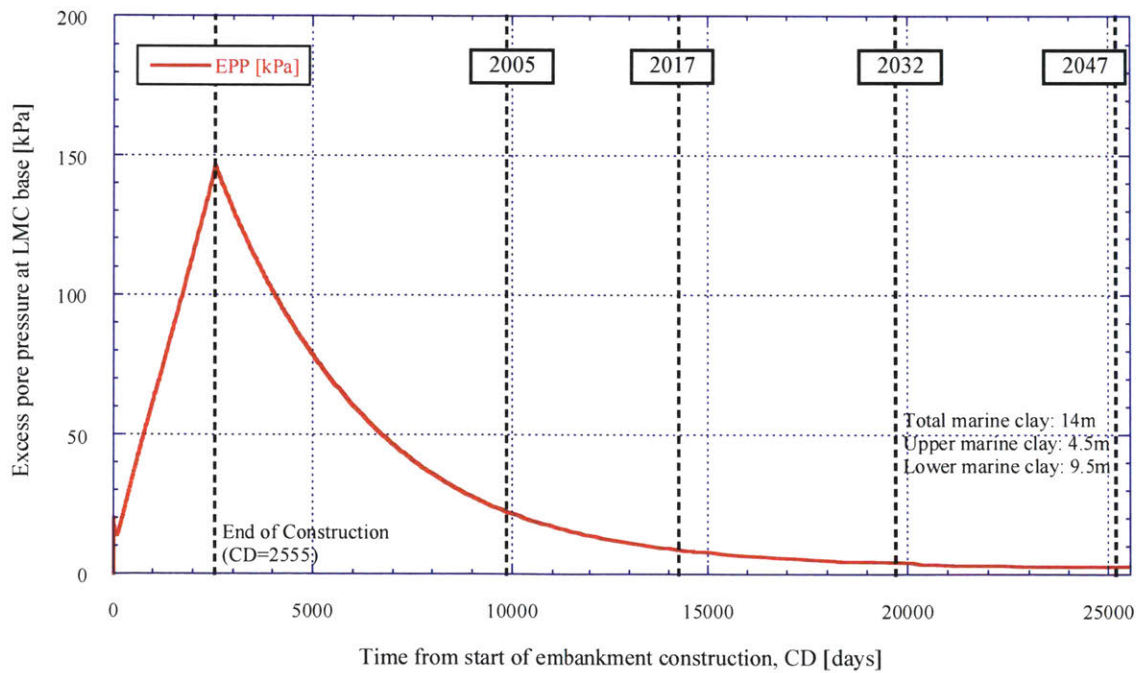


Figure 4-38: PLAXIS excess pore pressure for 14m of marine clay (UMC=4.5m).

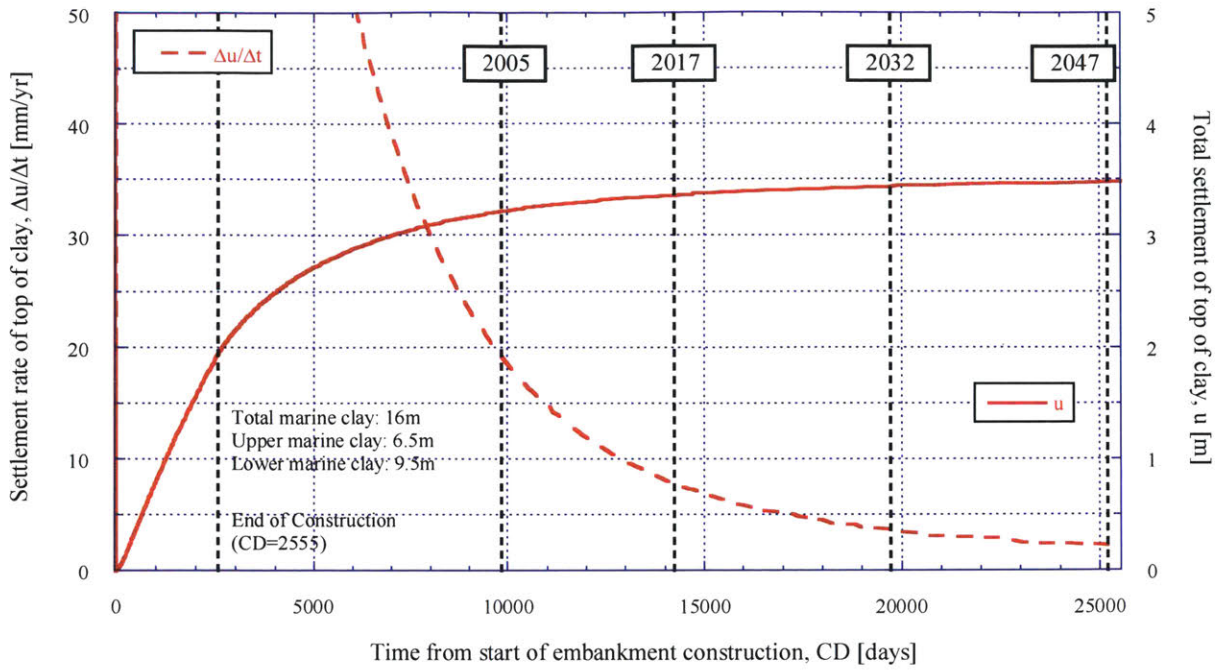


Figure 4-39: PLAXIS settlement rates and settlement for 16m of marine clay (UMC=6.5m).

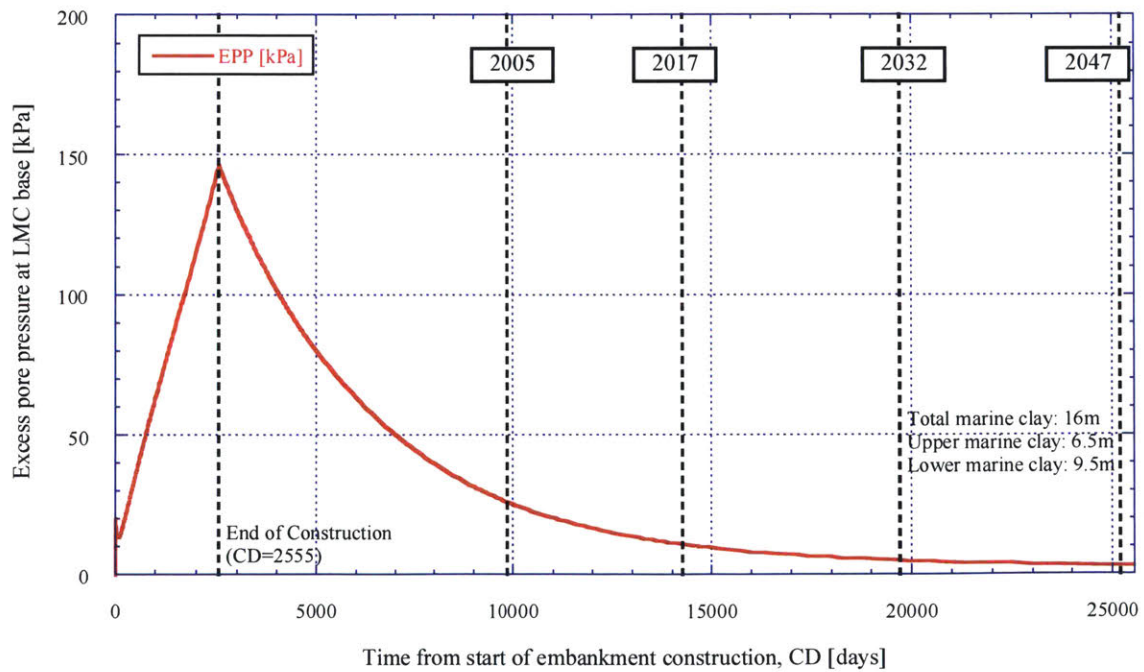


Figure 4-40: PLAXIS excess pore pressure for 16m of marine clay (UMC=6.5m).

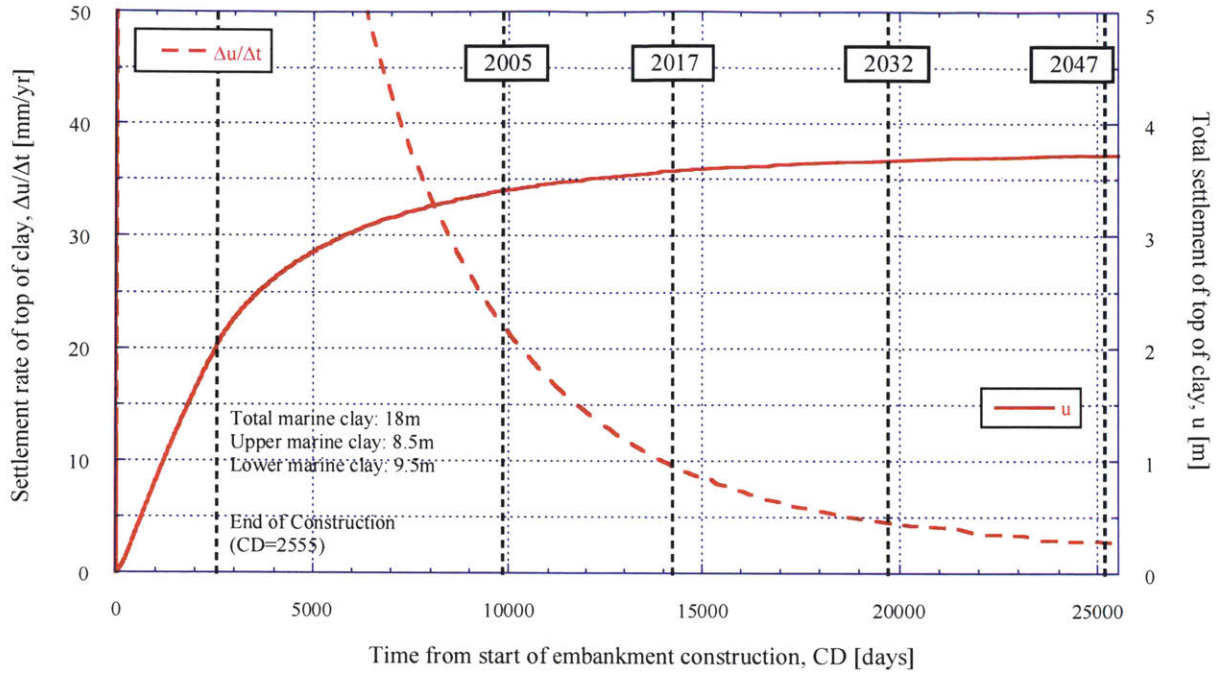


Figure 4-41: PLAXIS settlement rates and settlement for 18m of marine clay (UMC=8.5m).

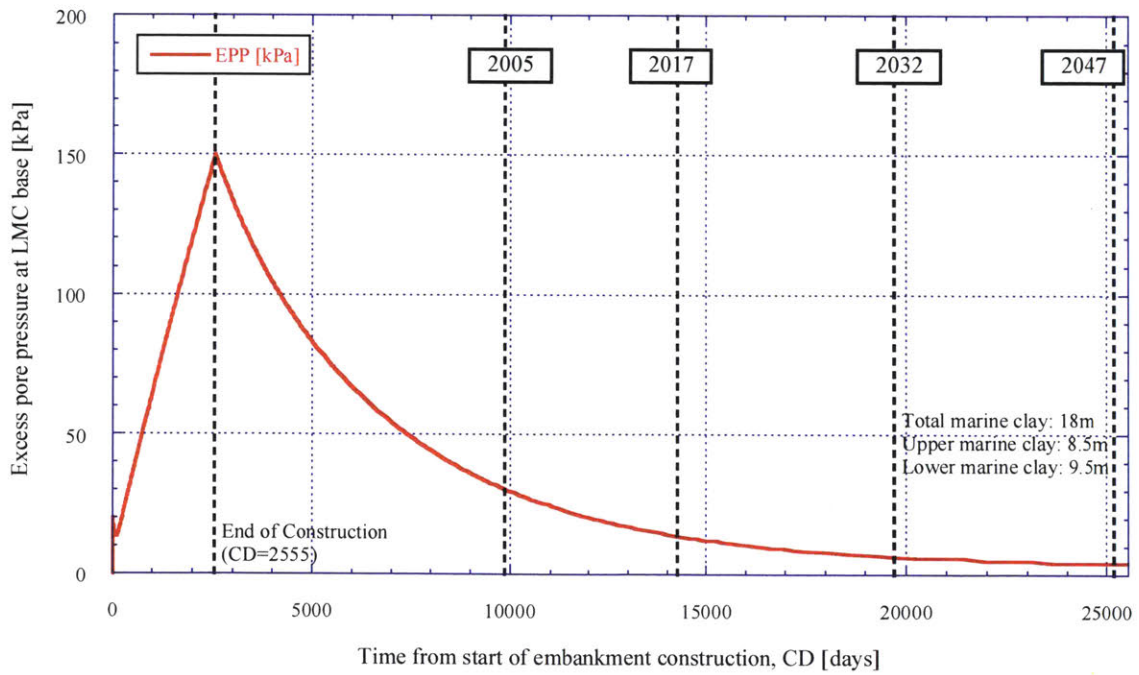


Figure 4-42: PLAXIS excess pore pressure for 18m of marine clay (UMC=8.5m).

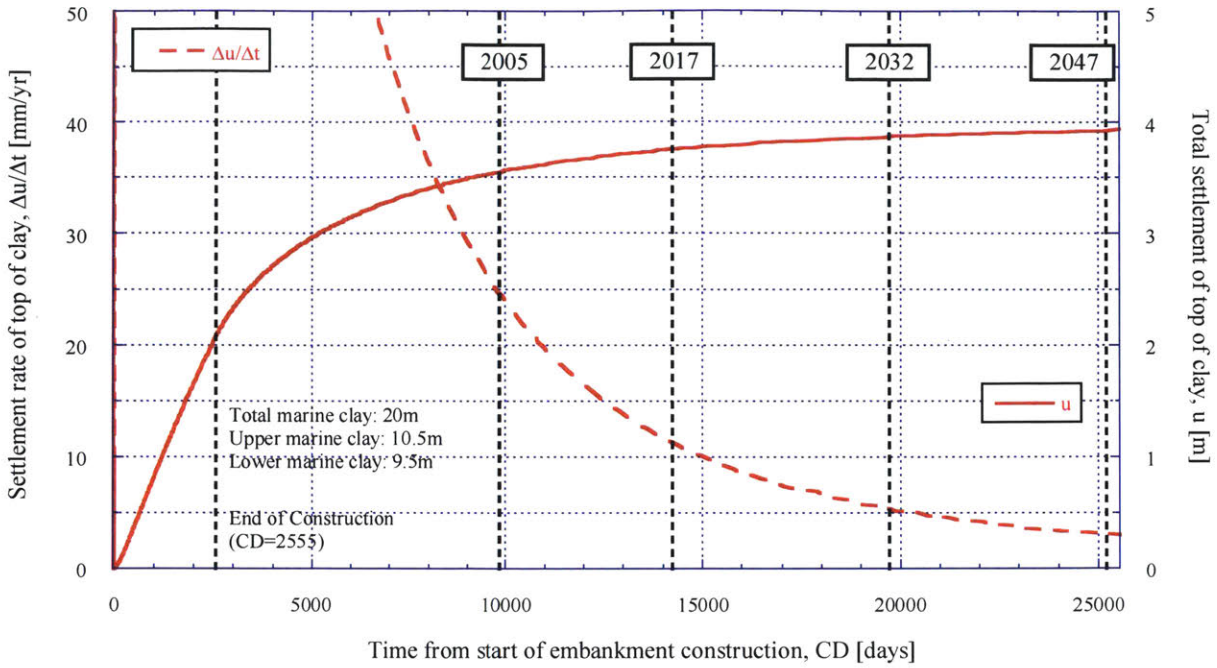


Figure 4-43: PLAXIS settlement rates and settlement for 20m of marine clay (UMC=10.5m).

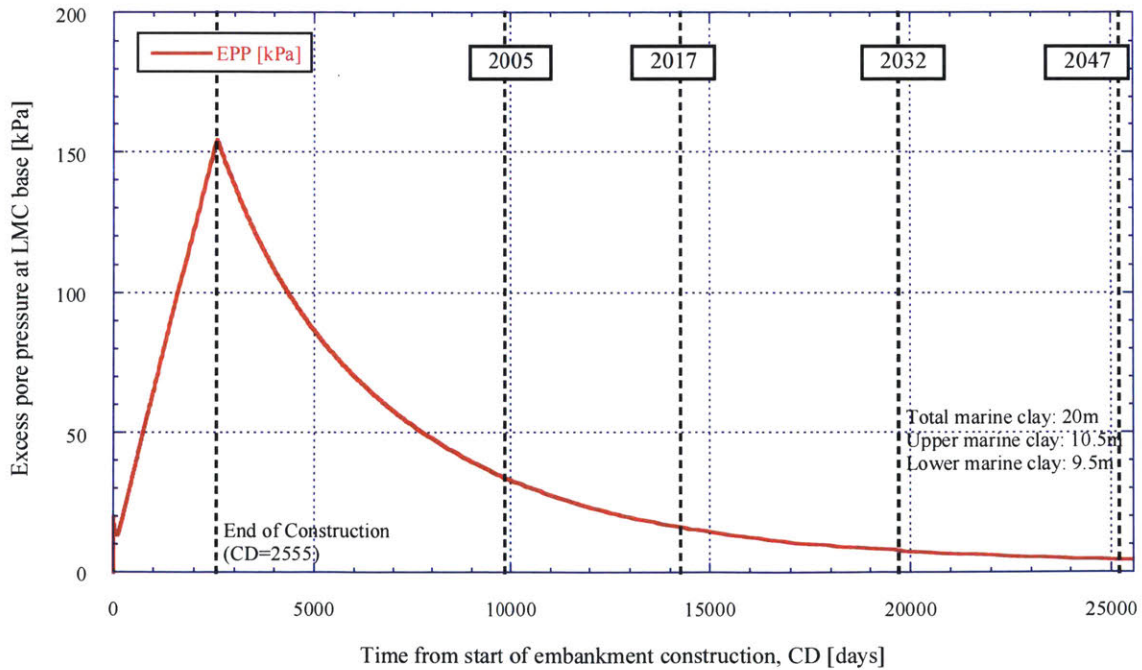


Figure 4-44: PLAXIS excess pore pressure for 20m of marine clay (UMC=10.5m).

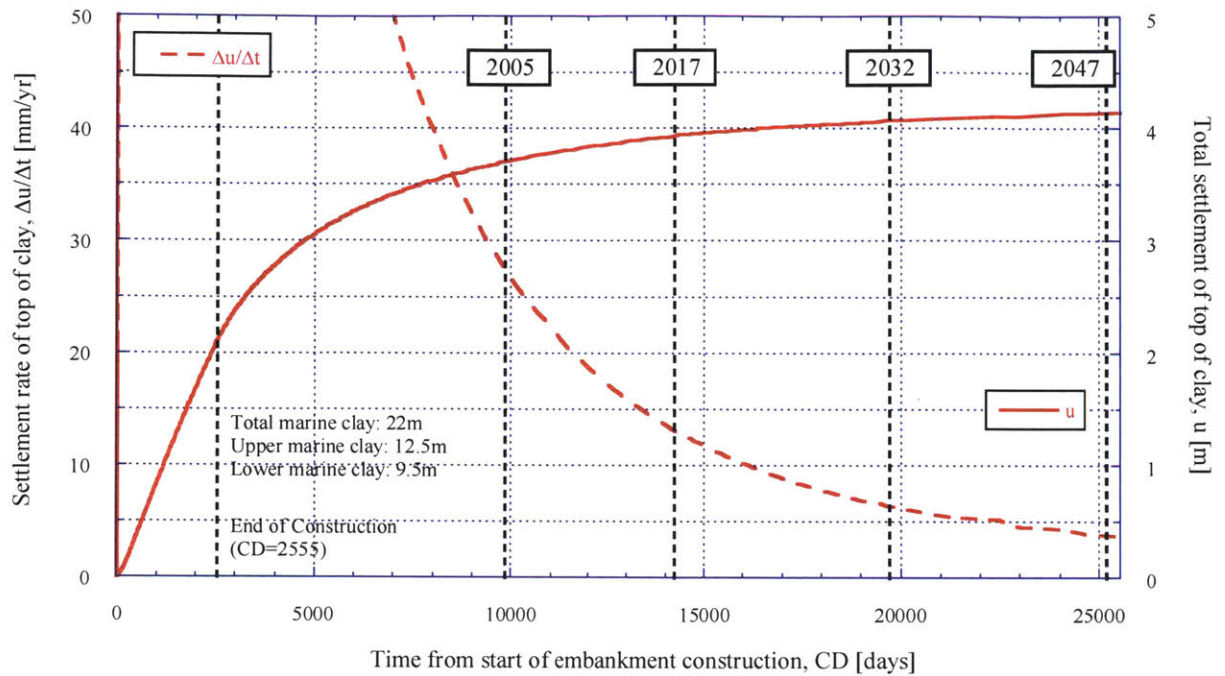


Figure 4-45: PLAXIS settlement rates and settlement for 22m of marine clay (UMC=12.5m).

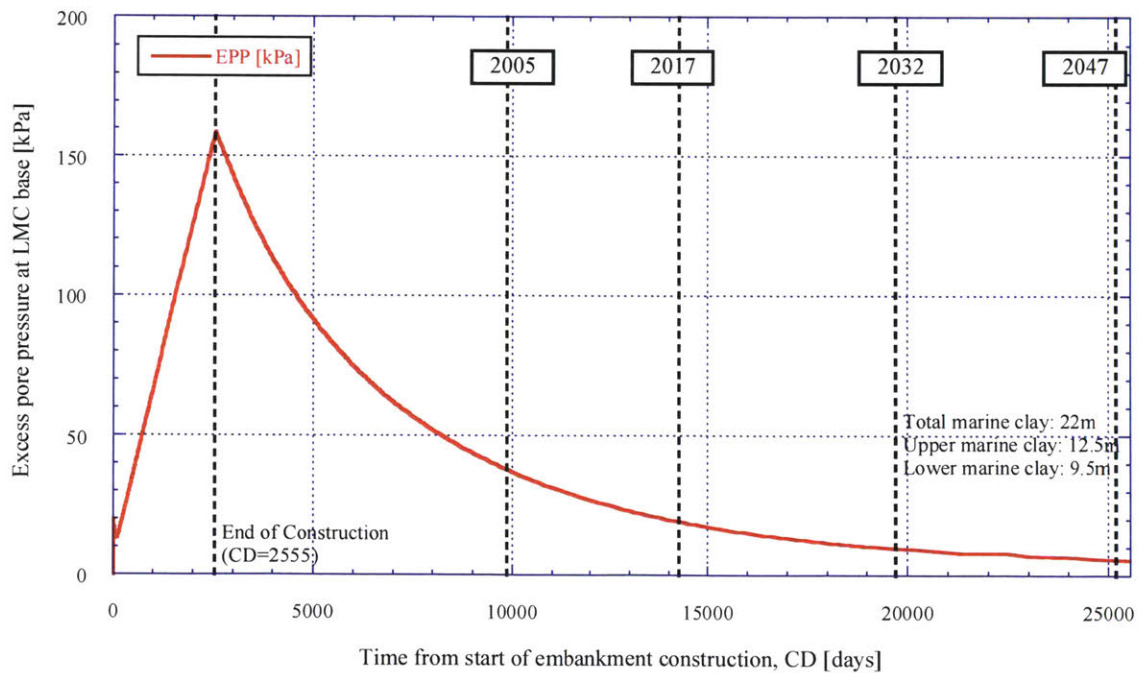


Figure 4-46: PLAXIS excess pore pressure for 22m of marine clay (UMC=12.5m).

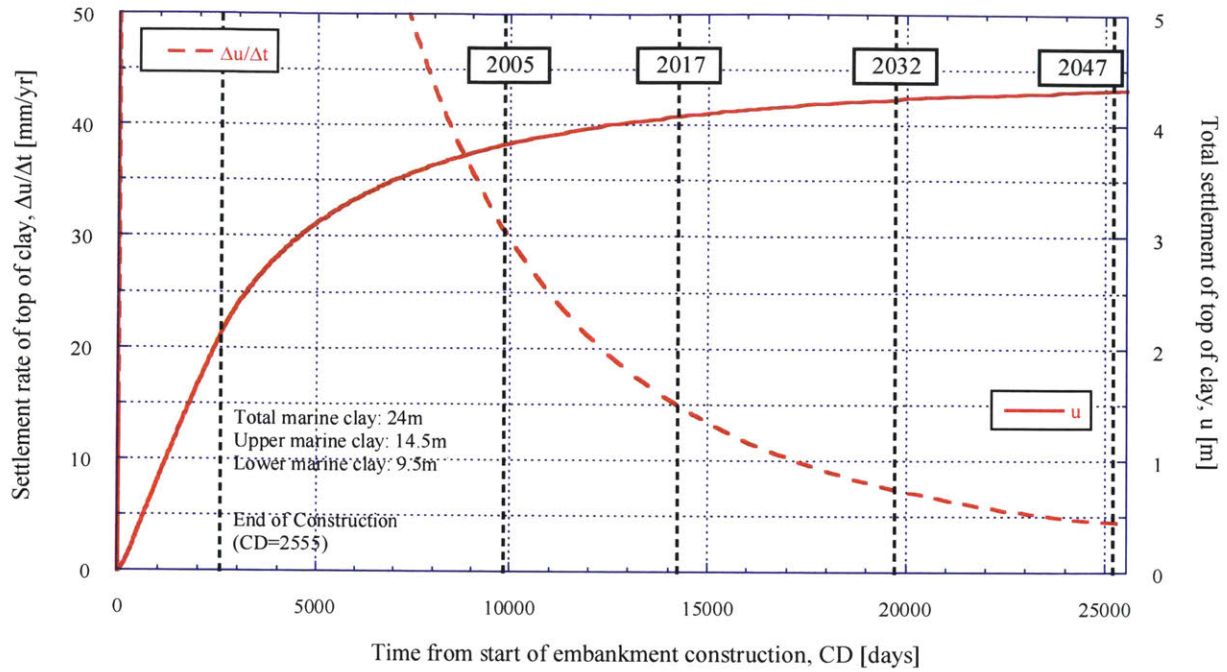


Figure 4-47: PLAXIS settlement rates and settlement for 24m of marine clay (UMC=14.5m).

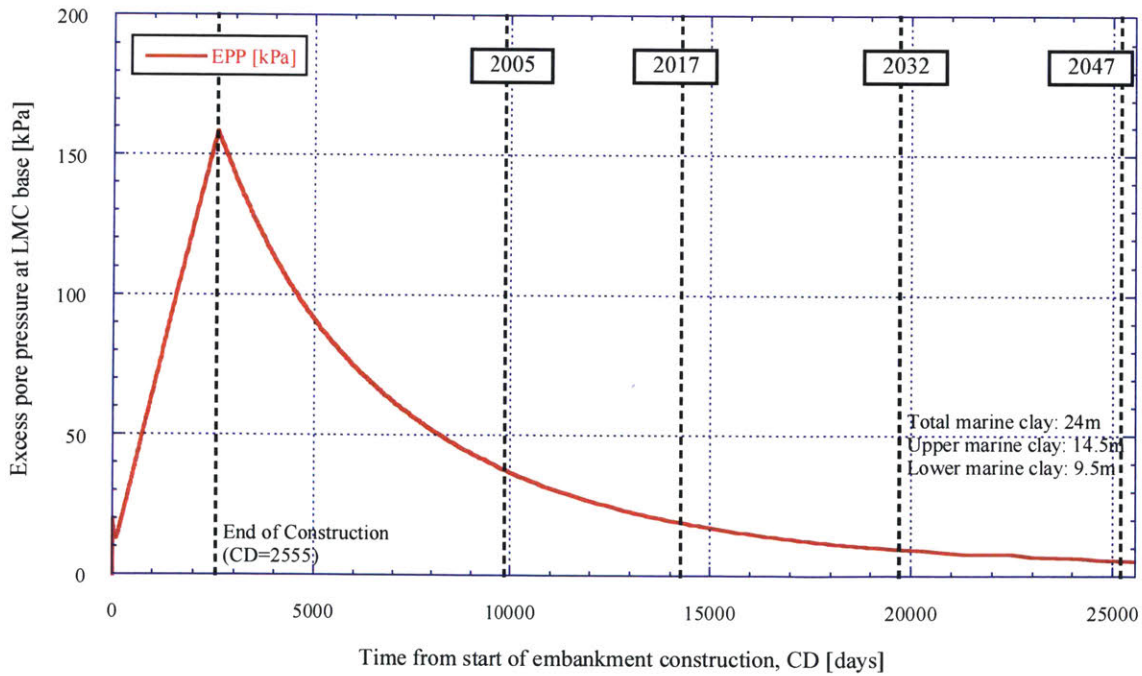


Figure 4-48: PLAXIS excess pore pressure for 24m of marine clay (UMC=14.5m).

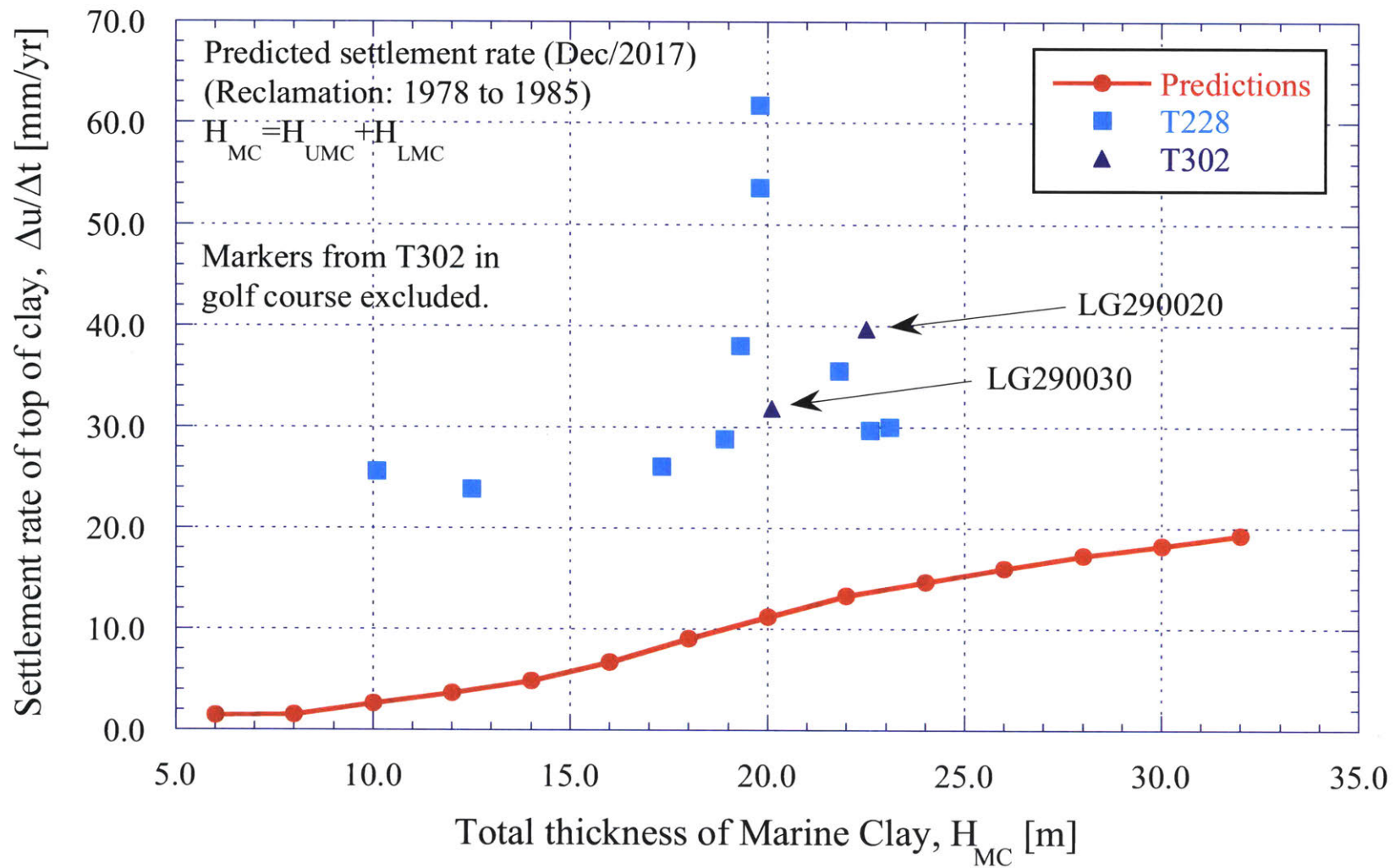


Figure 4-49: Comparison between PLAXIS predictions at Dec/2017 and site measurements.

5. SUMMARY, CONCLUSIONS AND RECOMMENDATIONS

5.1. SUMMARY

This thesis has investigated the application of a new rate dependent constitutive model, MIT-SR, for predicting long-term deformations of clays. MIT-SR (Yuan, 2016) introduces a novel elasto-viscoplastic formulation in which viscoplastic strain rates are controlled by the prior history of straining. This enables the model to capture a wide range of time dependent behavior, encompassing the extreme scaling of creep and consolidation with length scale envisaged by Hypotheses A and B (Ladd et al., 1977). The current thesis presents two detailed case studies using MIT-SR. In each case, the model is calibrated using results of available laboratory tests and is then applied directly in predictions of performance through finite element analyses using the Plaxis 2D program.

The first project analyzed was the New Hamilton Partnership Levee (NHPL) in California. It consisted of an 11ft high embankment, constructed between Apr/96 and Nov/96 approximately, on +30ft of a highly compressive clay known as San Francisco Bay Mud (SFBM). Settlements of the levee were monitored for a period of 5.5 years after construction. The original settlement predictions were presented prior to construction and grossly underestimated the settlements of the levee. This result motivated a series of site investigations, monitoring programs and re-analyses, including a prior SM thesis at MIT (Nguyen, 2006). The study by Nguyen (2006) utilized the Soft Soil Model (SSM) to represent SFBM and calibrated its parameters to match the observed post-construction levee's behavior. The SSM does not include creep and was only able to match the measured post-construction settlements after scaling the measured pre-consolidation pressures by a factor of $0.8 \sigma'_p$.

Our re-analyses consisted on the calibration of MIT-SR parameters for SFBM considering the original preconsolidation profile utilizing laboratory and field tests data only. The model predictions are compared with results obtained using both SSM and Soft Soil Creep Model (SSCM) where creep parameter (μ^*) was calculated independently. Two-dimensional FEM simulations of the construction and long-term consolidation processes (from Apr/96 to Apr/26, 30yrs from construction) of the NHPL were executed with each model (SSM, SSCM and MIT-SR) and the predictions of the embankment's performance (vertical and horizontal displacements and total pore pressure) were analyzed and compared against available monitoring measurements.

The second project concerns long-term settlements of reclamation fills for Marina Bay in Singapore. This land reclamation process occurred between 1979 and 1985 and consisted on the deposition of 13m of granular, dredged fill on the original seabed, principally composed by soft compressive clays (Upper and Lower Marine Clay; UMC and LMC). The recent development of the Thomson Line for the Singapore Mass Rapid Transit system includes the construction of new underground stations associated with projects T228 and T302 on the west and east banks of the Marina channel. Ongoing works at these sites are revealing significant on-going settlements at free-field locations (afar from the tunnel excavations).

MIT-SR was utilized to represent the UMC and LMC present in the area and a series of 1D FEM simulations were conducted to represent the full range of subsurface stratigraphies found on both banks of the channel. Between Dec/87 and Dec/47, results were calculated every 5 years to track their progression. The preconsolidation profile prior to the reclamation works was determined and a relationship between creep rates and settlement with total Marine Clay thickness was determined. The UMC thicknesses considered varied between 4.5 and 14.5m whereas for LMC they ranged between 1.5 and 17.5m. All simulations considered 13.0m of Fill over UMC, 3.5m of fluvial clay (F2) between UMC and LMC and Old Alluvium below LMC. From top to bottom, the geotechnical layers considered in the 54 studied stratigraphies were Fill, UMC, F2, LMC and OA.

The performance of MIT-SR model was analyzed by comparing the predicted creep rates and total settlement at Dec/17 against site measurements and current ground elevations. In addition, the results from these simulations pretend to serve as a robust, reference tool to estimate creep rate based on total thickness of the Marine Clay area and complement numerical simulations which do not account for creep phenomena.

5.2. CONCLUSIONS

The results from MIT-SR simulations in both projects were very encouraging and confirmed the strong predictive capabilities of the model with a calibration procedure based on laboratory and site tests data.

The conclusions from the NHPL project are:

- The models predictions of displacements are very different, especially in the undrained response during levee construction and the long-term response. All models predicted very similar pore pressures during construction and consolidation.
- The long-term maximum settlement (u_{yA}) predictions (April/2026) were 3.47ft (SSM), 4.91ft (SSCM) and 3.07ft (MIT-SR) while the post-construction settlements responses were 1.98ft (SSM), 3.37ft (SSCM) and 2.57ft (MIT-SR). The larger discrepancies occurred in the undrained response during construction and illustrate the differences in the modelling of the undrained shear behavior: MIT-SR predicted at the end of construction a settlement of 0.51m while SSM and SSCM predicted settlements equal to 1.49 and 1.54ft, respectively.
- The predictions of maximum horizontal displacement (u_{xB}) exhibited also major differences between models and again, the undrained response had strong influence in the differences observed: u_{xB} at the end of construction (EOC) were approximately 0.70ft (SSM and SSCM) and 0.10ft (MIT-SR). The predictions of the ratio u_{xB}/u_{yA} , at EOC were 0.45 (SSM and SSCM) and 0.20 (MIT-SR) and decayed during consolidation to values between 0.20 and 0.25 (SSM and SSCM) and 0.174 (MIT-SR). If considering only post-construction displacements, these relationships converge in the long-term to 0.07-0.10 (SSM and SSCM) 0.168 (MIT-SR).
- Empirical data by Ladd (1991) showed that $u_{xB}/u_{yA} \sim 0.20$ are normal while higher ratios are abnormal for most embankments. MIT-SR can correctly track the continuous increment of horizontal displacement due to construction and consolidation and therefore, the ratio u_{xB}/u_{yA} can correctly be registered even during construction. On the other hand. SSM and SSCM exhibit limitations in predicting both undrained and consolidation responses with a unique set of parameters.
- The predictions of pore pressure presented the higher similarities although there was a general trend: SSCM predicted the higher pore pressures, followed by SSM while MIT-SR always predicted the lowest values. SSM and MIT-SR were very similar and accurately matched the monitored values on site.
- Last but not least, regarding creep and the long-term response, SSM and MIT-SR converge to long-term, steady responses while SSCM continues to exhibit increment in settlement due to creep. MIT-SR reaches a steady condition because its framework contains a decay

mechanism to control viscoplastic strains in time and reduce creep rate while SSCM considers constant creep rate and settlement increases indefinitely.

The conclusions from the Marina Bay reclamation analyses are as follows:

- There is a direct relationship between total thickness of marine clay and the settlement and creep rates observed. Slight differences were encountered between minimum, average and maximum settlement and creep rates calculated for each specific thickness of marine clay. Therefore, average values were considered for later comparisons against site information.
- For 9m and 30m of MC (values that define the calculated 95% confidence interval), current settlement and creep rate would be 2.62m and 2mm/yr and 4.23m and 18mm/yr, respectively. For 19.3m (the mean thickness of MC) current settlement and creep rate would be 3.67m and 10mm/yr.
- By the end of the reclamation, maximum excess pore pressure is approximately 150kPa while in 2017 the excess pore pressure is lower than 20kPa. Therefore, the settlement rate from 2017 onwards can be attributed principally to creep.
- Settlement rates in T228 are more consistent and data shows settlement increasing linearly with time and annual rates of settlement are consistent. On the other hand, most of the markers in T302 are located within a golf course which construction ended in 2006 and included additional fillings. These points exhibit a higher settlement rate until in November 2017 and around May 2018, some points show rebound which could be explained by material removed in the golf course. Their behavior does not represent free field behavior. The comparison is mostly focused against T228 markers.
- The first comparison against site measurements was in terms of ground elevations. Simulations considered an initial ground elevation of +106mRL (Jan/1985) and ground elevations at Dec/17 were calculated from the predicted total settlement. Predicted ground elevations ranged between +101.7 and +103.9mRL while ground elevations at T228 and T302 varied between +103.2 and +106.5mRL.
- The second comparison with field information was in term of creep rates. All the markers considered had marine clay thicknesses between 10.1 and 23.1m and calculated settlement rates were 24-62mm/yr. For these marine clay values, predictions estimate current settlement rate between 9 and 15mm/yr.

- In both comparisons, predictions fall short to accurately describe current ground elevations and creep rates. The main issue to be addressed is that the 1D problem modelled is sensitive to the hydraulic conductivities of UMC, F2 and LMC. The limitation of the information available to select this parameter conditioned the analyses. If selecting lower values than the considered in these analyses ($k_v=2.1E-8m/s$ for UMC and $k_v=6.4E-9m/s$ for F2 and LMC), predictions by 2017 would change and lower settlements and higher rates would be expected.

As stated, MIT-SR exhibited a strong predictive capability in both projects, particularly in the NHPL comparisons. The comparison with Singapore Bay project was strongly limited by the information available.

5.3. RECOMMENDATIONS

The current thesis studied the predictive capability of MIT-SR model with materials calibrated with laboratory and field tests data and with projects that included soil loading, consolidation and creep response.

Other proposed applications and validations of the MIT-SR model could be:

1. Problem with stress relaxation to study the soil-structure interaction. Two proposed cases would be deep excavations (already proposed by Sottile, 2016) and tunnel excavations. In these projects, potential optimization of the structural design and construction procedure would signify reduction in costs and construction time.
2. Dynamic analyses to test the pore pressure development and dissipation together with the potential liquefaction of sands considering that MIT-SR includes the framework of MIT-S1 (originally proposed to unify sands and clays constitutive modelling).
3. Validate the models proposed framework for β_2 and β_3 parameters (already proposed by Yuan, 2016) at element scale by simulating laboratory tests with creep stages after surcharge phases. Examples of tests with these characteristics are included in Choi (1982).

6. REFERENCES

- Amberg & TTI (2004): "Final Geotechnical Interpretative Report." Report dated August 12th, 2004. Submitted to Nishimatsu Construction Co. Ltd, Singapore Branch, Singapore.
- ARUP (2014): "Tender Addendum 2 – Geotechnical Interpretative Baseline Report – Contract T228." Report dated January 28th, 2014. Submitted to Land Transport Authority, Singapore.
- Berre & Iversen, 1972; Berre, T., and Iversen, K. (1972). "Oedometer tests with different specimen heights on a clay exhibiting large secondary compression." *Géotechnique*, 22(1), 53–70.
- Bjerrum, L. (1972). "Embankments on soft ground." *Proceedings of the ASCE Conference on Performance of Earth-Supported Structures*, Purdue University, 2, 1-54.
- Bjerrum, L. (1973). "Problems of soil mechanics and construction on soft clays." *Proceedings of the 8th International Conference on Soil Mechanics and Foundation Engineering*, Moscow, 3, 111-159.
- Bodas Freitas, T. M., Potts, D. M., and Zdravkovic, L. (2011). "A time dependent constitutive model for soils with isotache viscosity." *Computers and Geotechnics*, Elsevier Ltd, 38(6), 809–820.
- Choi, Y. (1982). "Consolidation behavior of natural clays." Ph.D. thesis, Dept. of Civil Eng., University of Illinois at Urbana-Champaign, Urbana, IL.
- Corral & Whittle (2010): "Re-analysis of deep excavation collapse using a generalized effective stress soil model" ASCE Earth Retention Conference, Bellevue, WA.
- Crawford, C. B. (1965). "The resistance of soil structure to consolidation." *Canadian Geotechnical Journal*, 2(2), 90–97.
- Degago, S. A., Grimstad, G., and Jostad, H. P. (2011). "Use and misuse of the isotache concept with respect to creep Hypotheses A and B." *Géotechnique*, (10), 897–908.
- Germaine, J.T. (2002, 2004). Database of laboratory tests on Bay Mud. Dept. of Civil and Environmental Engineering, Massachusetts Institute of Technology, Cambridge, MA.
- Gonzalez, J. H. (2000). "Experimental and theoretical investigation of constant rate of strain consolidation." S.M. Thesis, Massachusetts Institute of Technology, Cambridge, MA.
- Kabbaj, M., Tavenas, F., and Leroueil, S. (1988). "In situ and laboratory stress-strain." *Géotechnique*, 38(1), 83–100.
- Kavvadas, M. (1982). "Non-linear Consolidation around Driven Piles in Clays." Ph.D. thesis, Dept. of Civil and Environmental Eng., Massachusetts Institute of Technology, Cambridge, MA.
- Kiso-Jiban Consultants Co. Ltd. (1978): "Laboratory soil test results for B747 Hangar Complex at Changi Volume 1 – Summary of soil tests." Report dated February 4th, 1978. Submitted to Singapore Airlines Limited, Singapore.
- Korchaiyapruk, A. (2007) "Experimental and numerical study of primary consolidation of soft clay." Ph.D. thesis, Dept. of Civil and Environmental Eng., Massachusetts Institute of Technology, Cambridge, MA.

Ladd, C.C. (1991). “Stability evaluation during staged construction, 22nd Terzaghi Lecture.” *Journal of Geotechnical Engineering*, ASCE, 117(4), 537-615.

Ladd, C. C., and DeGroot, D. J. (2003, June). “Recommended practice for soft ground site characterization: Arthur Casagrande Lecture.” *Proceedings of the 12th Pan American Conference on Soil Mechanics and Geotechnical Engineering*, Massachusetts Institute of Technology, Cambridge, MA.

Ladd, C. C., Foott, R., Ishihara, K., Schlosser, F., and Poulos, H. G. (1977). “Stress Deformation and Strength Characteristics.” *Proceedings of the 9th International Conference on Soil Mechanics and Foundation Engineering*, Tokyo, 421-494.

Leroueil, S. (2006). “The isotache approach. Where are we 50 years after its development by Professor Šuklje? (2006 Prof. Šuklje’s Memorial Lecture).” *Proceedings of the 13th Danube-European Conference on Geotechnical Engineering*, Ljubljana, 2, 55–88.

Matsuoka, H., and Nakai, T. (1974). “Stress-deformation and strength characteristics under three different principal stresses.” *Proceeding of Japanese Society of Civil Engineering*, 232, 59-70.

Mesri, G. (2001). “Primary compression and secondary compression.” *Proceedings of the Soil Behavior and Soft Ground Construction Symposia in Honor of Charles C. “Chuck” Ladd*, ASCE, Reston, VA, 122–166.

Mesri, G., and Choi, Y. K. (1985). “The uniqueness of the end-of-primary (EOP) void ratio-effective stress relationship.” *Proceedings of the 11th International Conference on Soil Mechanics and Foundation Engineering*, San Francisco, 587–590.

Mesri, G. and Choi, Y. K. (1985b). “Settlement analysis of embankments on soft clays.” *ASCE, Journal of Geotechnical Engineering*, 111(4), 441-464.

Mesri, G., and Godlewski, P.M. (1977). “Time-and stress-compressibility interrelationship.” *ASCE, Journal of Geotechnical Engineering*, 105(5), 417-430.

Mott MacDonald (2015): “Geotechnical Interpretative Baseline Report – Contract T302.” Report dated May 25th, 2015. Submitted to Land Transport Authority, Singapore.

Neher, H. P., M. Wehnert, and Bonnier, P. G. (2001). “An evaluation of soft soil models based on trial embankments.” *Computer Methods and Advances in Geomechanics, Proceedings of the 10th International Conference on Computer Methods and Advances in Geomechanics, Tucson/Arizona*, 373–378.

Ng, N.S.Y. (1998). “Characterization of consolidation and creep properties of Salt Lake City clays.” S.M. Thesis, Massachusetts Institute of Technology, Cambridge, MA.

Nguyen, H.Q. (2002). “Reanalysis of the settlement of a levee on soft bay mud.” S.M. Thesis, Massachusetts Institute of Technology, Cambridge, MA.

Panteghini, A. and Lagioia, R. (2014). “A fully convex reformulation of the original Matsuoka-Nakai failure criterion and its implicit numerically efficient integration algorithm.” *International Journal for Numerical and Analytical Methods in Geomechanics*, 38, 593-614.

Pestana, J.M. (1994). “A unified constitutive model for clays and sands.” Ph.D. thesis, Dept. of Civil and Environmental Eng., Massachusetts Institute of Technology, Cambridge, MA.

Pestana, J.M. and Whittle, A.J., (1995). "Compression model for cohesionless soils" *Géotechnique*, 45(5), 611-631.

Pestana, J.M. and Whittle, A.J., (1999). "Formulation of a unified constitutive model for clays and sands." *International Journal for Numerical and Analytical Methods in Geomechanics*, 23, 1215-1243.

Sheahan, T.C. (1991). "An experimental study of the time-dependent undrained shear behavior of resedimented clay using automated stress path triaxial equipment." Ph.D. thesis, Dept. of Civil and Environmental Eng., Massachusetts Institute of Technology, Cambridge, MA.

Sottile, M. G. (2016). "Implementation and evaluation of a recently developed rate-dependent effective stress soil model 'MIT-SR'." S.M. Thesis, Massachusetts Institute of Technology, Cambridge, MA.

Tan, T. S., Phoon, K. K., Lee, F. H., Tanaka, H., Locat, J., Chong, P.T. (2003). "A characterisation study of Singapore Lower Marine Clay." *Characterisation and Engineering Properties of Natural Soils*, 1, 429-454.

URS (2003). "Report: Geotechnical investigation and design recommendations for the New Hamilton partnership levee, Hamilton army air field base, wetlands restoration project." URS Corporation, San Francisco, CA. Draft report dated February 14, 2003. Final report was issued April 30th, 2004.

Vaid, Y. P., and Campanella, R. G. (1977). "Time-dependent behavior of undisturbed clay." *ASCE, Journal of Geotechnical Engineering*, 103(7), 693-709.

Vermeer, P.A. and Neher, H.P. (1999). "A soft soil model that accounts for creep." *Beyond 2000 in computational geotechnics: 10 years of PLAXIS International. Proceeding of the International Symposium beyond 2000 in Computational Geotechnics*, Amsterdam, 249-262.

Watabe, Y., Udaka, K., Kobayashi, M., Tabata, T., and Emura, T. (2008). "Effects of friction and thickness on long-term consolidation behavior of Osaka Bay clays." *Soils and Foundations*, 48(4), 547-561.

Whittle, A. J. and Kavvas, M.J. (1994) "Formulation of MIT-E3 Constitutive Model for Overconsolidated Clays." *ASCE Journal of Geotechnical Engineering*, 120(1), 173-198.

Wissa, A. E. Z., Christian, J. T., Davis, E. H., and Heiberg, S. (1971). "Consolidation Testing at Constant Rate of Strain." *ASCE, Journal of Soil Mechanics and Foundations*, 97(10), 1393-1413.

Yin, Z.Y., Chang, C. S., Karstunen, M., and Hicher, P.Y. (2010). "An anisotropic elastic-viscoplastic model for soft clays." *International Journal of Solids and Structures*, 47(5), 665-677.

Yuan, Y. (2016). "A new elasto-viscoplastic model for rate-dependent behaviour of clays." Ph.D. thesis, Dept. of Civil and Environmental Eng., Massachusetts Institute of Technology, Cambridge, MA.

7. APPENDICES

7.1. APPENDIX A: NEW HAMILTON PARTNERSHIP LEVEE PROJECT

7.1.1. URS (2003) site investigation and monitoring information

Table 7-1: Summary of field testing on Bay Mud for NHPL (Nguyen, 2006).

Tasks	Technique/Contractor	Quantity	Remarks
Borings with sampling along the alignment of NHPL	Rotary wash drilling; Dames Moore U-sampler, Pitcher sampler, Dames & Moore Piston Sampler, and SPT	19 boreholes	Taking undisturbed samples typically at 5ft depth intervals in Bay Mud borehole logs; Dames&More Piston Sampler used to get undisturbed sample (2.5 inches in diameter and 18 inches long –brass tubes) for laboratory tests. Also some 3” ϕ Osterberg sampler for MIT DSS tests
Field vane tests	Geonor device	20 locations	- Undrained shear strength and stress history spatial variations under and adjacent to levee. - Field vane correction factor $\mu = 0.8$.
CPTU tests (piezocone penetration tests)	Nk = 16	7 locations	- Tip resistance, side friction, pore pressures used mainly to provide information on stratigraphy and strength. - Pore pressure dissipation proved the sandy layer under the Bay Mud is a draining layer
Downhole geophysical tests	Redpath Geophysics of Murphys, California	4 locations, in the area of the proposed new test fill	- Compression and shear wave velocities; SFBM has shear wave velocity = 255 to 270 ft/sec (free field) -Deposit stratigraphy.
Instrumentation	URS	30 devices	- 6 test sections. - 26 piezometers, 2 inclinometers, 2 Sondex systems - Pore pressures, lateral deformation, vertical settlement profiles. -TS3 and 5 at proposed test fill area.
Settlement monitoring program after construction of NHPL	City of Novato (From Oct. 96 to Jan. 31, 2002)	32 points, 200ft spacing along the NHPL alignment	- Settlement markers were installed on the floodwall (about 3.0ft away from center of the levee crest). - Baseline readings were taken between Oct. 7 and Dec. 4, 1996. - Between baseline and Jan. 2002, 11 sets of readings were taken.

Table 7-2: Summary of laboratory testing on Bay Mud for NHPL (Nguyen, 2006).

Tasks	Technique/Contractor	Quantity	Remarks
Index tests	- ASTM D422, D1140, D4318, D2216, D2937	All tubes	Atterberg limits, grain size analyses, moisture content, specific gravity and density.
X-rays	MIT	All tubes tested at MIT	All tubes sent to MIT for X-rays for assessing microfabric and sample quality
Consolidation tests	ASTM D 4186, MIT ASTM D 2435, Signet	22 CRSC 16 IL OED	Compressibility and hydraulic conductivity parameters and stress history. Casagrande and Becker et al. (1987) strain energy techniques for σ'_p
CK0U-DSS	ASTM D 6528, MIT	7 DSS	SHANSEP technique with values of S & m; DSS also provided compressibility and σ'_p
CK0UTC/TE	ASTM D 4767, MIT	3 TC 2 TE	

Table 7-3: Monitoring information, settlement (URS, 2003).

Date	Δt	P16 ρ_t	P17 ρ_t	P18 ρ_t	P19 ρ_t
[-]	[day]	[ft]	[ft]	[ft]	[ft]
11/11/1996	0	0.00	0.00	0.00	0.00
7/1/1997	57	0.17	0.13	0.07	0.11
3/2/1997	84	0.23	0.17	0.11	0.17
4/3/1997	113	0.28	0.22	0.16	0.23
31/3/1997	140	0.37	0.30	0.24	0.31
6/5/1997	176	0.44	0.36	0.31	0.39
4/6/1997	205	0.44	0.36	0.30	0.40
9/7/1997	240	0.52	0.43	0.35	0.46
29/10/1998	717	1.12	0.95	0.83	1.00
24/8/1999	1016	1.35	1.17	1.01	1.25
25/8/2000	1383	1.63	1.45	1.27	1.54
31/1/2002	1907	1.92	1.74	1.52	1.86

Table 7-4: Monitoring information, inclinometers and Sondex in 20/Nov/2002 (URS, 2003).

Inclinometers				Sondex			
TS3-14'		TS5-14'		TS3-S1		TS3-S3	
EL	ρ_h	EL	ρ_h	EL	ρ_v	EL	ρ_v
[ft]	[ft]	[ft]	[ft]	[ft]	[ft]	[ft]	[ft]
-4.1	-0.002	-4.3	-0.003	-5.8	0.14	4.9	0.24
-6.0	0.003	-6.5	0.000	-11.0	0.08	-0.1	0.16
-8.1	0.007	-8.7	0.003	-16.1	0.08	-5.0	0.14
-10.2	0.009	-10.6	0.005	-21.1	0.09	-10.3	0.17
-12.2	0.012	-12.6	0.009	-26.0	0.10	-14.4	0.16
-14.1	0.015	-14.5	0.010	-31.1	0.11	-19.4	0.12
-16.2	0.017	-16.2	0.010	-36.1	0.10	-24.3	0.09
-18.1	0.020	-18.4	0.013	-41.2	0.00	-29.6	0.08
-20.0	0.019	-20.6	0.012	-46.2	0.00	-33.9	0.00
-21.9	0.019	-22.5	0.012	-50.3	0.00	-38.8	0.00
-23.8	0.019	-24.3	0.010	-55.3	0.00	-43.6	0.00
-25.8	0.017	-26.3	0.010	-60.4	0.00	-48.3	0.00
-27.7	0.017	-28.3	0.009	-65.4	0.00	-52.6	0.00
-29.5	0.014	-30.3	0.009	-70.3	0.00	-57.8	0.00
-31.5	0.013	-32.0	0.007	-75.2	0.00	-68.1	0.00
-33.4	0.010	-34.0	0.006	-80.4	0.00	-77.4	0.00
-35.3	0.008	-36.1	0.004	-5.8	0.14	4.9	0.24
-37.3	0.005	-38.1	0.001				
-39.2	0.003	-40.0	0.001				
-42.8	0.002	-43.9	0.001				
-46.7	0.002	-47.7	0.002				
-50.2	0.002	-51.6	0.001				
-54.3	0.002	-55.6	0.002				
-58.1	0.002	-59.5	0.002				
-60.1	0.001	-61.7	0.001				
-64.0	0.001	-65.7	0.001				
-68.0	0.001	-69.7	0.002				

Table 7-5: Monitoring information, piezometers in Line 1 in TS3 (URS, 2003).

Piezometer	EL	Pore pressure, Hw [ft]							
		[-]	[ft]	1-feb-02	16-feb-02	15-mar-02	23-mar-02	31-mar-02	12-may-02
TS3P1-P1	-13.5		10.46	8.94	9.45	9.48	9.52	8.52	8.16
TS3P1-P2	-23.5		20.42	19.49	20.40	20.33	19.97	19.56	19.11
TS3P1-P3	-33.5		30.57	28.76	29.47	29.70	29.54	28.93	29.75
TS3P1-P4	-44.5		40.63	40.20	40.12	40.15	39.89	39.48	39.32

Table 7-6: Monitoring information, piezometers in Line 2 in TS3 (URS, 2003).

Piezometer	EL	Pore pressure, Hw [ft]						
		[-]	[ft]	16-feb-02	15-mar-02	23-mar-02	31-mar-02	12-may-02
TS3P2-P1	-10.8		13.50	11.00	11.00	10.50	9.50	9.00
TS3P2-P2	-17.8		16.36	15.83	15.80	15.06	13.46	14.15
TS3P2-P3	-24.8		21.93	20.83	21.23	21.20	20.90	20.58
TS3P2-P4	-32.8		29.93	30.54	30.80	30.50	30.00	29.87
TS3P2-P5	-39.8		35.50	35.40	35.81	35.49	35.33	34.58
TS3P2-P6	-47.8		42.65	42.55	42.52	42.49	42.33	41.58
TS3P2-P7	-57.8		52.50	51.98	52.38	51.92	51.05	51.45
TS3P2-P8	-67.8		64.22	63.98	64.38	63.78	63.48	63.45

Table 7-7: Monitoring information, piezometers in Line 3 in TS3 (URS, 2003).

Piezometer		EL						Pore pressure, Hw [ft]			
[-]	[ft]	1-feb-02	16-feb-02	15-mar-02	23-mar-02	31-mar-02	12-may-02	5-jul-02	18-ago-02	20-nov-02	20-dic-02
TS3P3-P1	-10.1	13.87	6.50	6.60	6.73	6.77	7.14	6.61	6.68	8.50	9.00
TS3P3-P2	-17.1	21.97	18.32	17.22	17.45	16.99	17.46	16.13	16.09	16.38	16.16
TS3P3-P3	-24.1	30.00	28.54	27.43	27.46	27.31	27.17	27.64	27.21	24.69	25.27
TS3P3-P4	-31.1	36.40	35.15	34.25	34.17	34.12	33.79	32.85	32.61	32.59	32.47
TS3P3-P5	-38.1	36.90	35.45	37.15	37.08	37.13	36.79	36.45	36.52	36.40	36.57
TS3P3-P6	-45.1	41.51	40.66	41.06	40.99	40.33	40.39	39.96	40.12	40.40	40.48

Table 7-8: Monitoring information, piezometers in Line 4 in TS3 (URS, 2003).

Piezometer	EL	Pore pressure, Hw [ft]							
		16-feb-02	15-mar-02	23-mar-02	31-mar-02	12-may-02	5-jul-02	5-dic-02	20-dic-02
[-]	[ft]								
TS5P1-P1	-10.1	2.80	4.51	4.04	4.07	5.71	5.79	5.50	5.50
TS5P1-P2	-19.1	14.90	14.51	14.44	14.37	14.50	17.29	16.50	16.50
TS5P1-P3	-27.1	23.40	23.31	22.94	23.16	22.80	27.48	25.00	25.00
TS5P1-P4	-35.9	34.70	35.10	34.84	32.86	31.20	30.48	30.00	30.00
TS5P1-P5	-45.1	40.50	40.60	40.33	40.46	40.19	42.27	40.50	40.50

Table 7-9: Monitoring information, piezometers in Line 1 in TS5 (URS, 2003).

Piezometer	EL	Pore pressure, Hw [ft]				
		15-mar-02	23-mar-02	31-mar-02	12-may-02	20-nov-02
[-]	[ft]					
TS5P1-P1	-11.5	6.67	6.15	6.14	5.37	7.03
TS5P1-P2	-20	17.56	17.55	18.26	17.18	16.20
TS5P1-P3	-35	31.11	31.40	31.49	31.33	30.46
TS5P1-P4	-40	35.69	35.48	35.36	35.10	35.34
TS5P1-P5	-46.5	42.01	42.20	41.98	41.42	41.00

Table 7-10: Monitoring information, piezometers in Line 2 in TS5 (URS, 2003).

Piezometer	EL	Pore pressure, Hw [ft]					
		20-ene-02	1-feb-02	15-mar-02	23-mar-02	12-may-02	20-nov-02
[-]	[ft]						
TS5P2-P1	-9.8	5.12	4.81	5.60	5.29	4.02	4.61
TS5P2-P2	-17.8	14.86	14.95	14.92	14.82	14.47	15.37
TS5P2-P3	-26.3	27.66	25.30	23.33	23.32	23.29	23.97
TS5P2-P4	-34.3	33.50	31.96	31.32	31.93	30.77	30.84
TS5P2-P5	-41.8	37.60	37.39	36.65	36.64	36.50	36.17

Table 7-11: Monitoring information, piezometers in Line 3 in TS5 (URS, 2003).

Piezometer	EL [ft]	Pore pressure, Hw [ft]							
		20-ene-02	16-feb-02	15-mar-02	31-mar-02	12-may-02	5-jul-02	18-ago-02	20-nov-02
TS5P3-P1	-11.6	16.47	11.55	11.14	11.85	10.50	10.40	10.30	10.00
TS5P3-P2	-17.6	17.47	16.67	16.47	16.67	15.66	16.16	16.57	16.67
TS5P3-P3	-24.1	23.59	25.70	26.10	27.61	24.00	23.90	23.39	23.19
TS5P3-P4	-30.6	34.94	31.43	31.22	31.43	31.63	31.22	30.72	31.63
TS5P3-P5	-36.6	36.75	36.04	35.94	35.64	35.44	35.14	35.44	35.14
TS5P3-P6	-43.1	40.16	39.46	39.16	38.76	38.15	38.05	38.25	38.76

7.1.2. Korchaiyapruk (2007)

Table 7-12: Oedometer tests – Load applied, strain and void ratio (Korchaiyapruk, 2007).

ALL	Oed 112		Oed 113		Oed 116		Oed 117		Oed 122	
	e ₀ =2.579		e ₀ =2.371		e ₀ =2.581		e ₀ =2.137		e ₀ =2.435	
σ'_v	ϵ	e	ϵ	e	ϵ	e	ϵ	e	ϵ	e
[ksc]	[%]	[-]	[%]	[-]	[%]	[-]	[%]	[-]	[%]	[-]
0.1	0.1	2.58	0.1	2.37	0.0	2.58	0.0	2.14	2.2	2.36
0.2	0.6	2.56	0.4	2.36	0.5	2.56	0.4	2.12	4.6	2.28
0.4	2.0	2.51	1.9	2.31	1.3	2.53	1.5	2.09	13.3	1.98
1.0	14.1	2.07	13.4	1.92	9.8	2.23	11.4	1.78	25.7	1.55
2.0	24.8	1.69	22.6	1.61	19.8	1.87	20.7	1.49	33.9	1.27
4.0	33.8	1.37	30.7	1.34	27.4	1.60	27.8	1.26	40.5	1.05
8.0	40.2	1.14	38.1	1.09	34.6	1.34	34.6	1.05	46.6	0.83
16.0	46.4	0.92	44.1	0.88	40.3	1.14	39.8	0.89	51.4	0.67

Table 7-13: Oedometer test 112 – Secondary compression stages (Korchaiyapruk, 2007).

Stage: 1-2ksc			Stage: 2-4ksc			Stage: 4-8ksc			Stage: 8-16ksc		
t	ϵ	e	t	ϵ	e	t	ϵ	e	t	ϵ	e
[min]	[%]	[-]	[min]	[%]	[-]	[min]	[%]	[-]	[min]	[%]	[-]
0.04	16.53	1.988	0.24	27.23	1.604	0.13	35.00	1.326	0.03	41.06	1.110
0.06	16.56	1.986	0.33	27.33	1.601	0.16	35.04	1.325	0.05	41.13	1.107
0.08	16.62	1.984	0.44	27.43	1.597	0.20	35.09	1.323	0.08	41.18	1.105
0.12	16.68	1.982	0.59	27.57	1.592	0.25	35.15	1.321	0.11	41.23	1.103
0.17	16.75	1.980	0.80	27.73	1.587	0.31	35.22	1.319	0.15	41.31	1.100

0.24	16.85	1.976	1.07	27.92	1.580	0.39	35.29	1.316	0.22	41.39	1.098
0.34	16.95	1.972	1.44	28.11	1.573	0.49	35.38	1.313	0.31	41.49	1.094
0.49	17.09	1.968	1.97	28.37	1.564	0.62	35.47	1.309	0.43	41.61	1.090
0.70	17.25	1.962	2.47	28.54	1.558	0.78	35.58	1.306	0.61	41.75	1.085
0.99	17.45	1.954	3.26	28.88	1.545	0.98	35.70	1.301	0.87	41.93	1.078
1.42	17.72	1.945	4.38	29.26	1.532	1.24	35.84	1.296	1.26	42.07	1.073
2.01	18.01	1.934	5.79	29.64	1.518	1.55	35.99	1.291	1.58	42.23	1.068
2.94	18.25	1.926	7.51	30.00	1.505	1.95	36.16	1.285	1.91	42.44	1.060
3.72	18.58	1.914	9.92	30.46	1.489	2.46	36.35	1.278	2.65	42.71	1.051
4.46	18.93	1.902	13.11	30.92	1.472	3.09	36.57	1.270	3.60	43.02	1.039
5.88	19.32	1.887	17.00	31.34	1.457	3.89	36.79	1.262	4.68	43.31	1.029
7.48	19.77	1.871	22.46	31.77	1.442	4.89	37.05	1.253	6.35	43.69	1.015
9.51	20.19	1.856	30.22	32.20	1.426	6.10	37.33	1.243	8.43	44.03	1.003
12.36	20.77	1.836	40.66	32.59	1.413	7.42	37.57	1.235	10.95	44.36	0.991
16.07	21.25	1.819	54.71	32.89	1.402	9.07	37.83	1.225	14.23	44.68	0.980
19.99	21.71	1.802	69.88	33.24	1.389	11.09	38.10	1.215	18.90	44.99	0.969
25.42	22.17	1.786	95.43	33.36	1.385	13.56	38.37	1.206	25.65	45.31	0.957
32.33	22.65	1.768	128.39	33.57	1.377	16.58	38.64	1.196	35.59	45.60	0.947
41.12	23.11	1.752	172.72	33.75	1.371	20.56	38.90	1.187	52.71	45.86	0.938
53.47	23.56	1.736	232.36	33.91	1.365	25.87	39.16	1.177	74.73	46.05	0.931
72.66	24.04	1.719	312.58	34.06	1.360	32.54	39.43	1.168	105.95	46.23	0.924
103.26	24.42	1.705	420.49	34.20	1.355	40.94	39.62	1.161	150.22	46.37	0.920
147.86	24.76	1.693	565.65	34.34	1.350	48.45	39.88	1.152	212.98	46.49	0.915
208.69	25.05	1.682	760.90	34.45	1.346	61.15	39.95	1.149	301.97	46.62	0.910
296.77	25.31	1.673	1023.56	34.57	1.342	76.91	40.12	1.143	428.13	46.74	0.906
422.11	25.54	1.665	1376.85	34.67	1.338	96.73	40.25	1.138	607.01	46.84	0.903
600.49	25.73	1.658	1719.85	34.79	1.334	121.63	40.37	1.134	860.62	46.95	0.899
835.74	25.89	1.652	-	-	-	152.96	40.49	1.130	1220.20	47.06	0.895
1041.72	26.01	1.648	-	-	-	192.35	40.59	1.126	1730.01	47.15	0.891
-	-	-	-	-	-	241.87	40.69	1.123	2317.54	47.22	0.889
-	-	-	-	-	-	304.14	40.78	1.119	2985.05	47.31	0.886
-	-	-	-	-	-	382.43	40.87	1.116	-	-	-
-	-	-	-	-	-	441.30	40.93	1.114	-	-	-

Table 7-14: Oedometer test 113 – Secondary compression stages (Korchaiyapruk, 2007).

Stage: 1-2ksc			Stage: 2-4ksc			Stage: 4-8ksc			Stage: 8-16ksc		
t	ϵ	e	t	ϵ	e	t	ϵ	e	t	ϵ	e
[min]	[%]	[-]	[min]	[%]	[-]	[min]	[%]	[-]	[min]	[%]	[-]
0.21	15.89	1.84	0.20	24.09	1.56	0.12	34.01	1.22	0.13	39.57	1.04
0.28	16.00	1.83	0.29	24.24	1.55	0.15	34.06	1.22	0.18	39.63	1.04
0.37	16.10	1.83	0.41	24.39	1.55	0.20	34.12	1.22	0.26	39.72	1.03

0.50	16.22	1.82	0.58	24.57	1.54	0.27	34.18	1.22	0.36	39.82	1.03
0.66	16.35	1.82	0.82	24.78	1.54	0.36	34.26	1.22	0.50	39.94	1.02
0.89	16.49	1.82	1.15	25.02	1.53	0.49	34.36	1.21	0.71	40.09	1.02
1.19	16.67	1.81	1.63	25.29	1.52	0.65	34.47	1.21	0.99	40.27	1.01
1.59	16.87	1.80	2.31	25.64	1.51	0.86	34.59	1.20	1.41	40.45	1.01
2.13	17.11	1.79	3.24	25.99	1.49	1.15	34.72	1.20	1.95	40.70	1.00
2.86	17.37	1.79	4.33	26.32	1.48	1.57	34.84	1.20	2.68	40.95	0.99
3.83	17.70	1.77	5.50	26.69	1.47	2.03	35.03	1.19	3.53	41.22	0.98
5.13	18.04	1.76	6.98	27.05	1.46	2.67	35.25	1.18	4.74	41.53	0.97
6.88	18.43	1.75	8.67	27.41	1.45	3.44	35.49	1.17	6.51	41.94	0.96
8.90	18.83	1.74	10.76	27.77	1.43	4.42	35.72	1.17	8.56	42.26	0.95
11.29	19.25	1.72	13.37	28.14	1.42	5.69	35.98	1.16	11.03	42.56	0.94
14.33	19.65	1.71	16.61	28.50	1.41	7.32	36.24	1.15	14.21	42.88	0.93
17.86	20.04	1.70	20.63	28.87	1.40	9.24	36.50	1.14	18.70	43.20	0.91
22.26	20.42	1.68	26.19	29.24	1.39	11.46	36.74	1.13	25.14	43.52	0.90
27.74	20.82	1.67	33.97	29.61	1.37	14.22	36.98	1.12	34.52	43.79	0.89
34.57	21.18	1.66	46.01	29.95	1.36	17.96	37.24	1.12	48.43	44.01	0.89
43.87	21.55	1.64	65.06	30.28	1.35	23.10	37.50	1.11	67.95	44.20	0.88
56.69	21.93	1.63	92.00	30.55	1.34	29.18	37.72	1.10	95.36	44.38	0.88
61.80	22.24	1.62	130.08	30.75	1.33	38.89	37.99	1.09	133.83	44.54	0.87
80.31	22.46	1.61	183.94	30.96	1.33	52.98	38.24	1.08	187.85	44.66	0.87
107.60	22.72	1.61	260.05	31.12	1.32	77.91	38.45	1.08	263.69	44.76	0.86
144.14	22.95	1.60	367.67	31.27	1.32	106.37	38.60	1.07	370.14	44.88	0.86
193.09	23.17	1.59	519.81	31.41	1.31	141.80	38.74	1.07	519.59	44.99	0.85
258.62	23.35	1.58	734.89	31.54	1.31	189.02	38.86	1.06	729.39	45.09	0.85
346.38	23.53	1.58	1038.95	31.66	1.30	251.97	38.98	1.06	1023.94	45.19	0.85
423.43	23.63	1.57	1468.81	31.78	1.30	335.89	39.09	1.05	1437.45	45.28	0.84
-	-	-	1863.58	31.86	1.30	409.28	39.16	1.05	2018.04	45.36	0.84
-	-	-	-	-	-	-	-	-	2658.56	45.43	0.84

Table 7-15: Oedometer test 116 – Secondary compression stages (Korchaiyapruk, 2007).

Stage: 1-2ksc			Stage: 2-4ksc			Stage: 4-8ksc			Stage: 8-16ksc		
t	ϵ	e	t	ϵ	e	t	ϵ	e	t	ϵ	e
[min]	[%]	[-]	[min]	[%]	[-]	[min]	[%]	[-]	[min]	[%]	[-]
0.12	9.44	2.24	0.15	21.54	1.81	0.13	28.83	1.55	0.05	35.90	1.30
0.17	9.47	2.24	0.20	21.58	1.81	0.18	28.88	1.55	0.08	35.94	1.29
0.24	9.57	2.24	0.26	21.63	1.81	0.26	28.95	1.54	0.11	35.98	1.29
0.34	9.66	2.24	0.34	21.69	1.80	0.36	29.02	1.54	0.15	36.04	1.29
0.47	9.76	2.23	0.45	21.75	1.80	0.49	29.12	1.54	0.22	36.10	1.29
0.67	9.90	2.23	0.59	21.82	1.80	0.68	29.23	1.53	0.31	36.17	1.29
0.94	10.07	2.22	0.78	21.91	1.80	0.95	29.35	1.53	0.43	36.24	1.28
1.33	10.27	2.21	1.03	22.02	1.79	1.32	29.49	1.52	0.61	36.33	1.28

1.88	10.51	2.20	1.34	22.13	1.79	1.83	29.67	1.52	0.85	36.43	1.28
2.65	10.78	2.19	1.77	22.25	1.78	2.53	29.87	1.51	1.25	36.57	1.27
3.75	11.12	2.18	2.32	22.41	1.78	3.60	30.04	1.51	1.77	36.73	1.27
5.29	11.55	2.17	3.06	22.59	1.77	4.90	30.34	1.49	2.53	36.86	1.26
7.48	12.06	2.15	4.02	22.80	1.76	6.48	30.63	1.48	3.55	37.06	1.25
10.38	12.54	2.13	5.39	22.96	1.76	8.80	30.98	1.47	4.84	37.30	1.25
14.92	13.27	2.11	6.94	23.27	1.75	11.24	31.29	1.46	6.78	37.58	1.24
19.77	13.90	2.08	8.63	23.51	1.74	14.66	31.66	1.45	8.76	37.82	1.23
27.35	14.78	2.05	11.02	23.80	1.73	18.34	31.99	1.44	11.56	38.13	1.22
35.46	15.42	2.03	13.77	24.09	1.72	22.49	32.28	1.42	15.59	38.43	1.20
45.98	16.13	2.00	19.07	24.58	1.70	27.57	32.59	1.41	20.13	38.71	1.19
59.61	16.78	1.98	23.82	24.90	1.69	34.50	32.90	1.40	26.01	38.99	1.18
77.28	17.43	1.96	29.25	25.23	1.68	44.07	33.24	1.39	34.32	39.28	1.17
104.60	18.08	1.93	35.93	25.55	1.67	56.29	33.53	1.38	46.27	39.56	1.16
147.76	18.62	1.91	44.89	25.90	1.65	74.90	33.86	1.37	63.74	39.84	1.15
182.13	19.14	1.90	57.05	26.24	1.64	138.25	34.31	1.35	80.11	40.06	1.15
248.03	19.30	1.89	72.50	26.57	1.63	199.74	34.52	1.34	111.09	40.17	1.14
350.23	19.64	1.88	93.72	26.90	1.62	277.03	34.68	1.34	156.40	40.33	1.14
494.44	19.89	1.87	120.74	27.21	1.61	384.26	34.82	1.33	220.21	40.47	1.13
698.02	20.13	1.86	173.51	27.46	1.60	533.03	34.94	1.33	310.04	40.61	1.13
985.32	20.33	1.85	236.06	27.67	1.59	739.39	35.07	1.33	436.57	40.72	1.12
1390.98	20.56	1.84	310.35	27.83	1.58	1025.67	35.18	1.32	614.73	40.83	1.12
1963.42	20.73	1.84	408.00	27.98	1.58	1422.84	35.28	1.32	865.63	40.93	1.12
2771.46	20.91	1.83	536.37	28.11	1.57	1973.83	35.38	1.31	1193.21	41.01	1.11
3911.83	21.06	1.83	693.18	28.23	1.57	2738.31	35.47	1.31	-	-	-
5288.21	21.16	1.82	-	-	-	3798.79	35.56	1.31	-	-	-
-	-	-	-	-	-	5270.14	35.65	1.30	-	-	-

Table 7-16: Oedometer test 117 – Secondary compression stages (Korchaiyapruk, 2007).

Stage: 1-2ksc			Stage: 2-4ksc			Stage: 4-8ksc			Stage: 8-16ksc		
t	ϵ	e	t	ϵ	e	t	ϵ	e	t	ϵ	e
[min]	[%]	[-]	[min]	[%]	[-]	[min]	[%]	[-]	[min]	[%]	[-]
0.10	12.32	1.75	0.11	22.57	1.43	0.08	29.32	1.22	0.11	36.03	1.01
0.14	12.35	1.75	0.15	22.59	1.43	0.10	29.35	1.22	0.15	36.06	1.01
0.20	12.40	1.75	0.21	22.64	1.43	0.15	29.38	1.22	0.21	36.11	1.00
0.27	12.47	1.75	0.29	22.68	1.43	0.20	29.44	1.21	0.30	36.16	1.00
0.38	12.55	1.74	0.41	22.74	1.42	0.28	29.49	1.21	0.42	36.22	1.00
0.53	12.64	1.74	0.58	22.81	1.42	0.39	29.56	1.21	0.58	36.28	1.00
0.74	12.76	1.74	0.81	22.89	1.42	0.54	29.64	1.21	0.81	36.36	1.00
1.02	12.90	1.73	1.14	22.99	1.42	0.75	29.74	1.20	1.13	36.46	0.99
1.42	13.07	1.73	1.60	23.12	1.41	1.05	29.84	1.20	1.58	36.57	0.99

1.98	13.27	1.72	2.24	23.26	1.41	1.45	29.98	1.20	2.20	36.70	0.99
2.75	13.51	1.71	3.14	23.44	1.40	2.02	30.13	1.19	3.12	36.86	0.98
3.83	13.80	1.70	4.40	23.66	1.39	2.81	30.31	1.19	4.47	37.07	0.97
5.32	14.13	1.69	6.17	23.94	1.39	3.90	30.54	1.18	5.99	37.24	0.97
7.25	14.50	1.68	8.47	24.22	1.38	5.41	30.77	1.17	7.85	37.48	0.96
9.71	14.89	1.67	11.38	24.52	1.37	7.37	31.06	1.16	10.08	37.68	0.95
12.63	15.26	1.66	14.97	24.88	1.36	9.63	31.36	1.15	13.79	38.00	0.94
15.82	15.68	1.65	19.09	25.22	1.35	11.83	31.60	1.15	18.46	38.28	0.94
19.43	16.03	1.63	23.83	25.53	1.34	15.46	31.97	1.13	23.71	38.53	0.93
25.37	16.61	1.62	30.06	25.86	1.33	20.20	32.31	1.12	30.44	38.78	0.92
31.78	17.08	1.60	37.92	26.22	1.31	25.32	32.61	1.11	39.92	39.02	0.91
39.02	17.49	1.59	48.85	26.58	1.30	31.75	32.90	1.10	53.45	39.26	0.91
47.90	17.93	1.57	62.94	26.90	1.29	40.63	33.21	1.10	74.61	39.53	0.90
58.79	18.39	1.56	82.82	27.25	1.28	53.08	33.52	1.09	103.72	39.74	0.89
72.18	18.78	1.55	112.10	27.53	1.27	72.25	33.84	1.08	159.14	39.90	0.89
88.63	19.18	1.54	146.48	27.85	1.26	98.80	34.08	1.07	225.27	40.03	0.88
113.40	19.58	1.52	205.37	28.02	1.26	151.45	34.32	1.06	314.46	40.15	0.88
154.41	19.95	1.51	287.92	28.22	1.25	228.48	34.53	1.05	438.96	40.26	0.87
214.66	20.30	1.50	403.66	28.39	1.25	317.47	34.69	1.05	612.76	40.37	0.87
298.48	20.59	1.49	565.93	28.55	1.24	441.13	34.81	1.05	855.38	40.46	0.87
415.09	20.86	1.48	793.43	28.69	1.24	612.94	34.92	1.04	1145.29	40.54	0.87
577.44	21.04	1.48	1066.37	28.80	1.23	851.69	35.02	1.04	-	-	-
803.29	21.22	1.47	-	-	-	1183.42	35.13	1.04	-	-	-
1117.58	21.38	1.47	-	-	-	1644.36	35.22	1.03	-	-	-
1554.78	21.55	1.46	-	-	-	2284.84	35.31	1.03	-	-	-
2163.24	21.69	1.46	-	-	-	3174.78	35.40	1.03	-	-	-
3009.94	21.82	1.45	-	-	-	4411.36	35.47	1.02	-	-	-
4188.31	21.94	1.45	-	-	-	5762.96	35.53	1.02	-	-	-
5478.24	22.02	1.45	-	-	-	-	-	-	-	-	-

Table 7-17: Oedometer test 122 – Secondary compression stages (Korchaiyapruk, 2007).

Stage: 1-2ksc			Stage: 2-4ksc			Stage: 4-8ksc			Stage: 8-16ksc		
t	ϵ	e	t	ϵ	e	t	ϵ	e	t	ϵ	e
[min]	[%]	[-]	[min]	[%]	[-]	[min]	[%]	[-]	[min]	[%]	[-]
0.09	28.17	1.47	0.05	36.36	1.19	0.10	42.47	0.98	0.07	48.66	0.76
0.13	28.37	1.46	0.07	36.45	1.18	0.14	42.64	0.97	0.09	48.73	0.76
0.18	28.57	1.45	0.09	36.55	1.18	0.20	42.86	0.96	0.11	48.82	0.76
0.25	28.85	1.44	0.13	36.68	1.18	0.27	43.09	0.95	0.14	48.91	0.75
0.34	29.15	1.43	0.17	36.82	1.17	0.38	43.36	0.95	0.18	49.02	0.75
0.47	29.52	1.42	0.22	36.97	1.17	0.51	43.64	0.94	0.23	49.11	0.75
0.63	29.85	1.41	0.29	37.10	1.16	0.66	43.92	0.93	0.28	49.21	0.74

0.84	30.26	1.40	0.36	37.29	1.15	0.92	44.33	0.91	0.32	49.32	0.74
1.14	30.77	1.38	0.47	37.54	1.15	1.22	44.67	0.90	0.39	49.45	0.74
1.45	31.15	1.36	0.62	37.77	1.14	1.55	44.97	0.89	0.50	49.63	0.73
1.82	31.54	1.35	0.78	38.03	1.13	2.02	45.30	0.88	0.61	49.78	0.72
2.27	31.92	1.34	1.02	38.32	1.12	2.73	45.63	0.87	0.78	50.00	0.72
2.85	32.29	1.33	1.31	38.60	1.11	3.77	45.96	0.86	0.99	50.18	0.71
3.63	32.65	1.31	1.69	38.89	1.10	5.21	46.21	0.85	1.25	50.39	0.70
4.64	33.01	1.30	2.18	39.18	1.09	7.01	46.44	0.84	1.59	50.61	0.70
6.17	33.33	1.29	2.81	39.45	1.08	9.93	46.59	0.83	2.02	50.81	0.69
8.36	33.62	1.28	3.68	39.72	1.07	13.72	46.73	0.83	2.57	51.00	0.68
12.29	33.91	1.27	4.81	39.98	1.06	18.95	46.87	0.82	3.26	51.18	0.68
16.99	34.12	1.26	6.50	40.20	1.05	26.17	47.00	0.82	4.12	51.35	0.67
23.48	34.31	1.26	9.78	40.44	1.05	36.13	47.10	0.82	6.16	51.60	0.66
32.46	34.45	1.25	12.81	40.57	1.04	49.90	47.20	0.81	8.19	51.70	0.66
44.86	34.60	1.25	16.77	40.73	1.04	68.90	47.31	0.81	10.40	51.80	0.66
61.99	34.74	1.24	21.97	40.84	1.03	95.15	47.41	0.81	13.20	51.88	0.65
85.67	34.86	1.24	28.78	40.94	1.03	131.40	47.51	0.80	16.76	51.96	0.65
118.38	34.98	1.23	37.70	41.06	1.02	181.45	47.60	0.80	21.28	52.04	0.65
163.59	35.11	1.23	49.38	41.16	1.02	250.56	47.69	0.80	27.02	52.11	0.64
226.04	35.22	1.23	64.69	41.26	1.02	346.00	47.78	0.79	34.31	52.18	0.64
312.35	35.34	1.22	84.74	41.36	1.01	477.79	47.87	0.79	43.56	52.25	0.64
431.60	35.45	1.22	111.01	41.45	1.01	659.79	47.96	0.79	55.30	52.31	0.64
596.34	35.55	1.21	135.92	41.51	1.01	911.08	48.04	0.78	70.21	52.38	0.64
823.99	35.66	1.21	-	-	-	1232.97	48.11	0.78	89.15	52.45	0.63
1138.53	35.77	1.21	-	-	-	-	-	-	113.19	52.51	0.63
1480.43	35.84	1.20	-	-	-	-	-	-	143.71	52.57	0.63
-	-	-	-	-	-	-	-	-	182.46	52.63	0.63
-	-	-	-	-	-	-	-	-	231.66	52.68	0.63

Table 7-18: CRS 654/656/662/674 tests information (Korchaiyapruk, 2007).

CRS-654		CRS-656		CRS-662		CRS-674	
$\dot{\epsilon}$ [%/hr]	0.090	$\dot{\epsilon}$ [%/hr]	0.100	$\dot{\epsilon}$ [%/hr]	0.088	$\dot{\epsilon}$ [%/hr]	0.375
e_0	2.548	e_0	2.081	e_0	2.301	e_0	2.294

σ'_v	e	σ'_v	e	σ'_v	e	σ'_v	e
[psf]	[-]	[psf]	[-]	[psf]	[-]	[psf]	[-]
0.92	2.23	1.21	1.82	0.86	2.04	0.97	2.07
1.01	2.19	1.33	1.79	0.94	2.01	1.05	2.03
1.08	2.15	1.49	1.75	1.00	1.99	1.14	1.99
1.19	2.12	1.67	1.71	1.09	1.95	1.24	1.95
1.29	2.07	1.87	1.68	1.17	1.92	1.34	1.91

1.37	2.04	2.11	1.64	1.29	1.89	1.47	1.87
1.48	2.00	2.37	1.60	1.38	1.86	1.60	1.83
1.61	1.96	2.69	1.56	1.50	1.83	1.77	1.78
1.74	1.92	3.03	1.52	1.57	1.81	1.89	1.75
1.92	1.88	3.40	1.48	1.68	1.78	2.08	1.71
2.10	1.84	3.83	1.44	1.84	1.75	2.26	1.67
2.30	1.79	4.32	1.40	2.00	1.72	2.45	1.64
2.50	1.75	4.88	1.36	-	-	0.97	2.07
2.73	1.70	5.43	1.33	-	-	1.05	2.03
2.87	1.68	6.12	1.29	-	-	-	-
-	-	6.53	1.27	-	-	-	-

Table 7-19: CRS 680/683/686/687 tests information (Korchaiyapruk, 2007).

CRS-680		CRS-683		CRS-686		CRS-687	
$\dot{\epsilon}$ [%/hr]	0.500	$\dot{\epsilon}$ [%/hr]	0.500	$\dot{\epsilon}$ [%/hr]	3.000	$\dot{\epsilon}$ [%/hr]	1.450
e_0	2.854	e_0	2.776	e_0	2.533	e_0	2.752

σ'_v	e	σ'_v	e	σ'_v	e	σ'_v	e
[psf]	[-]	[psf]	[-]	[psf]	[-]	[psf]	[-]
0.88	2.48	0.84	2.46	0.90	2.21	0.87	2.37
0.95	2.42	0.90	2.41	0.99	2.16	0.96	2.30
1.01	2.39	0.97	2.36	1.09	2.10	1.03	2.25
1.06	2.34	1.04	2.31	1.18	2.05	1.13	2.20
1.13	2.30	1.11	2.27	1.28	2.01	1.26	2.13
1.21	2.25	1.17	2.23	1.39	1.97	1.40	2.07
1.32	2.19	1.27	2.18	1.51	1.93	1.57	2.01
1.43	2.13	1.38	2.13	1.62	1.89	1.76	1.95
1.51	2.10	1.49	2.09	1.73	1.86	1.90	1.91
1.59	2.07	1.58	2.06	1.87	1.82	2.07	1.87
1.71	2.03	1.72	2.02	2.04	1.79	2.26	1.83
1.86	1.99	1.80	1.99	2.25	1.74	2.45	1.80
2.02	1.95	1.97	1.95	2.46	1.71	2.69	1.75
2.18	1.92	2.16	1.90	2.68	1.67	2.96	1.71
2.31	1.89	2.29	1.87	2.90	1.64	3.21	1.68
2.54	1.84	2.52	1.83	3.16	1.61	3.61	1.64
2.76	1.80	2.73	1.79	3.49	1.57	-	-
2.98	1.76	2.95	1.75	3.80	1.54	-	-
3.23	1.72	3.30	1.70	4.20	1.51	-	-
3.46	1.69	3.53	1.67	4.54	1.48	-	-
3.77	1.65	3.78	1.65	5.15	1.44	-	-

-	-	4.12	1.61	-	-	-	-
---	---	------	------	---	---	---	---

Table 7-20: CRS 672 test information (Korchaiyapruk, 2007).

CRS-672-1		CRS-672-2		CRS-672-3	
$\dot{\epsilon}$ [%/hr]	0.100	$\dot{\epsilon}$ [%/hr]	0.750	$\dot{\epsilon}$ [%/hr]	1.500
e_0	2.371	e_0	2.371	e_0	2.371

σ'_v	e	σ'_v	e	σ'_v	e
[psf]	[-]	[psf]	[-]	[psf]	[-]
0.94	2.16	1.00	2.18	1.07	2.17
1.00	2.12	1.06	2.15	1.12	2.14
1.06	2.08	1.11	2.12	1.18	2.10
1.14	2.05	1.16	2.09	1.26	2.07
1.21	2.01	1.22	2.06	1.31	2.04
1.28	1.98	1.38	1.99	1.44	1.99
1.35	1.95	1.54	1.93	1.58	1.94
1.43	1.92	1.63	1.90	1.69	1.90
1.52	1.89	1.75	1.87	1.78	1.88
1.64	1.85	1.87	1.84	1.94	1.84
1.76	1.82	1.98	1.81	2.10	1.80
1.90	1.79	2.08	1.79	2.38	1.75
2.05	1.75	2.17	1.77	2.52	1.72
2.23	1.72	2.32	1.74	2.68	1.70
2.43	1.69	2.49	1.72	2.93	1.66
2.85	1.62	2.94	1.65	3.36	1.61
3.12	1.59	3.20	1.62	3.73	1.58
3.42	1.56	3.49	1.59	4.08	1.55

Table 7-21: CRS 691 test information (Korchaiyapruk, 2007).

CRS-691-1		CRS-691-2		CRS-691-3	
$\dot{\epsilon}$ [%/hr]	0.750	$\dot{\epsilon}$ [%/hr]	1.500	$\dot{\epsilon}$ [%/hr]	3.000
e_0	2.786	e_0	2.786	e_0	2.786

σ'_v	e	σ'_v	e	σ'_v	e
[psf]	[-]	[psf]	[-]	[psf]	[-]
0.63	2.51	0.69	2.50	0.76	2.47
0.67	2.48	0.73	2.46	0.81	2.43
0.72	2.44	0.77	2.43	0.86	2.39
0.81	2.36	0.82	2.39	0.90	2.36

0.86	2.33	0.87	2.35	0.94	2.33
0.92	2.29	0.97	2.28	0.99	2.30
0.98	2.25	1.02	2.25	1.05	2.27
1.05	2.21	1.15	2.19	1.12	2.23
1.12	2.18	1.22	2.16	1.21	2.19
1.19	2.14	1.30	2.12	1.30	2.15
1.28	2.11	1.40	2.09	1.39	2.11
1.37	2.07	1.58	2.02	1.48	2.08
1.48	2.03	1.67	1.99	1.59	2.04
1.59	2.00	1.76	1.97	1.71	2.00
1.72	1.96	1.88	1.94	1.83	1.97
1.85	1.93	2.01	1.91	1.97	1.93
1.99	1.90	2.17	1.87	2.12	1.90
2.14	1.86	2.32	1.84	2.28	1.87
2.32	1.82	2.52	1.81	2.43	1.84
2.52	1.79	2.67	1.78	2.60	1.81
2.72	1.76	2.88	1.75	2.78	1.78
2.94	1.73	3.03	1.73	3.01	1.75
3.19	1.70	3.24	1.70	3.25	1.72
3.45	1.66	3.44	1.67	3.54	1.68
3.75	1.63	3.73	1.64	3.84	1.65
4.08	1.60	3.93	1.61	4.15	1.62

7.1.3. PLAXIS Contour plots

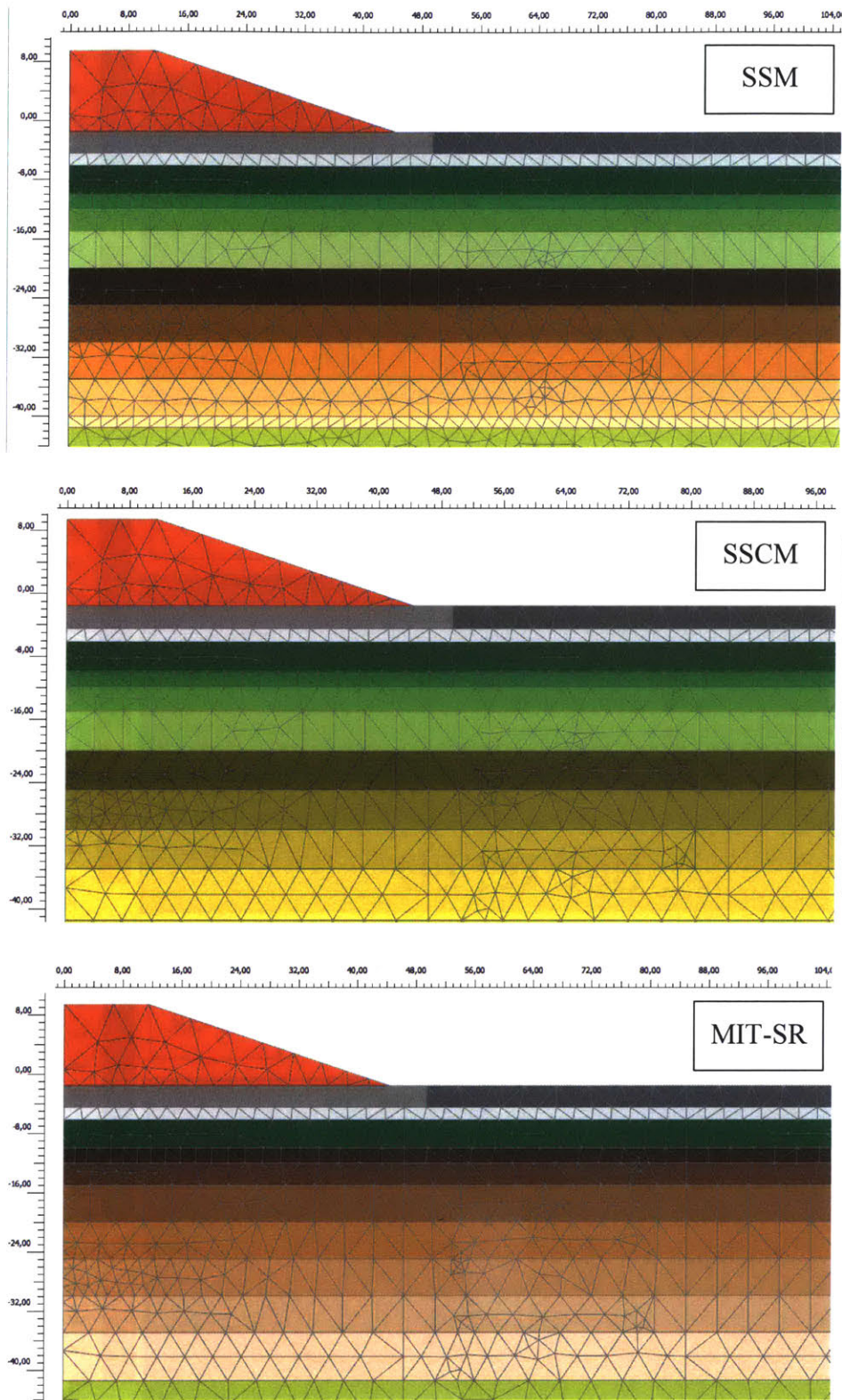


Figure 7-1: Geometries and meshes considered, SSM, SSCM & MIT-SR.

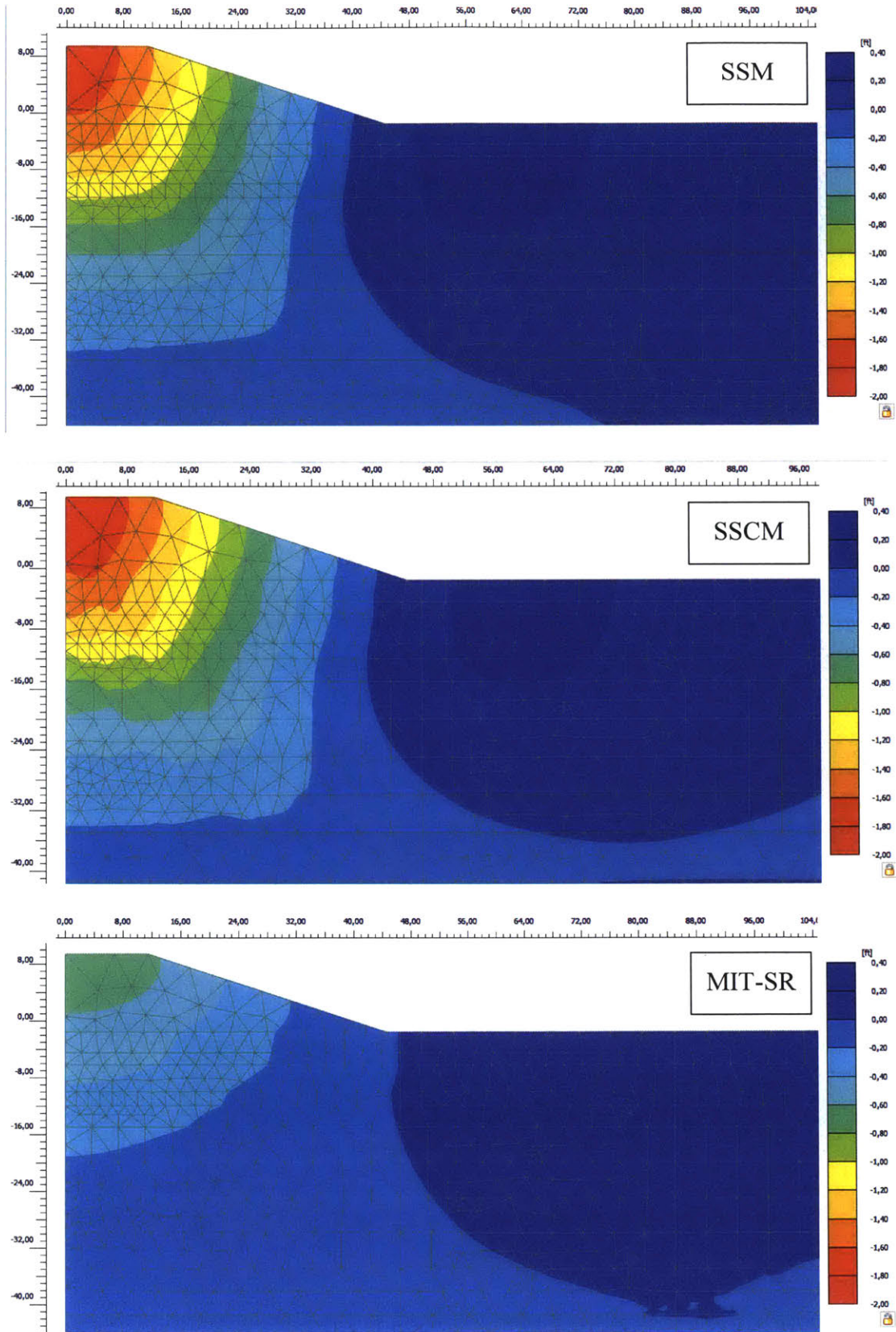


Figure 7-2: Vertical settlements (u_y) CD=215 (11/Nov/96), SSM, SSCM & MIT-SR.

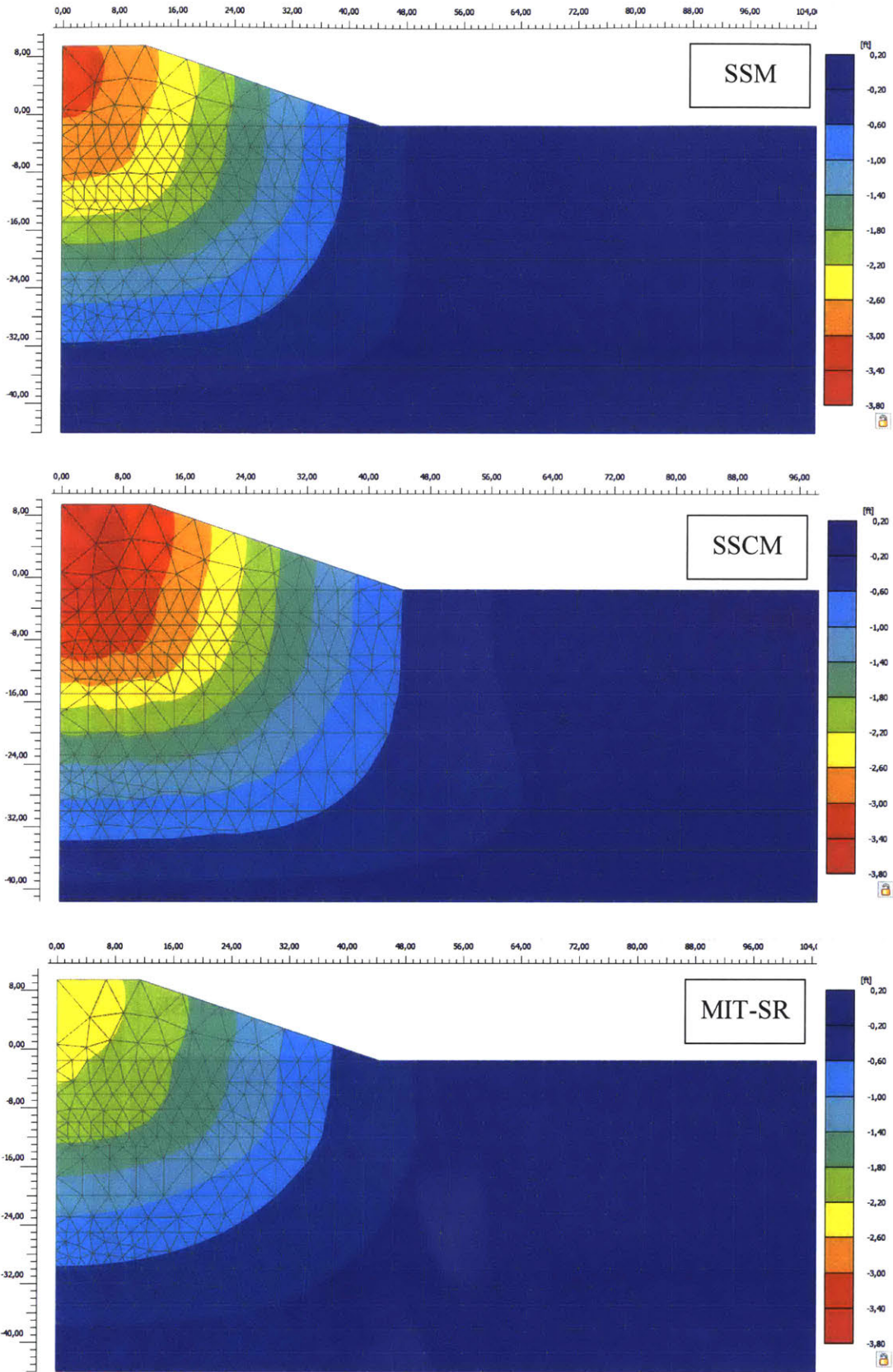


Figure 7-3: Vertical settlements (u_y) CD=2140 (17/Feb/02), SSM, SSCM & MIT-SR.

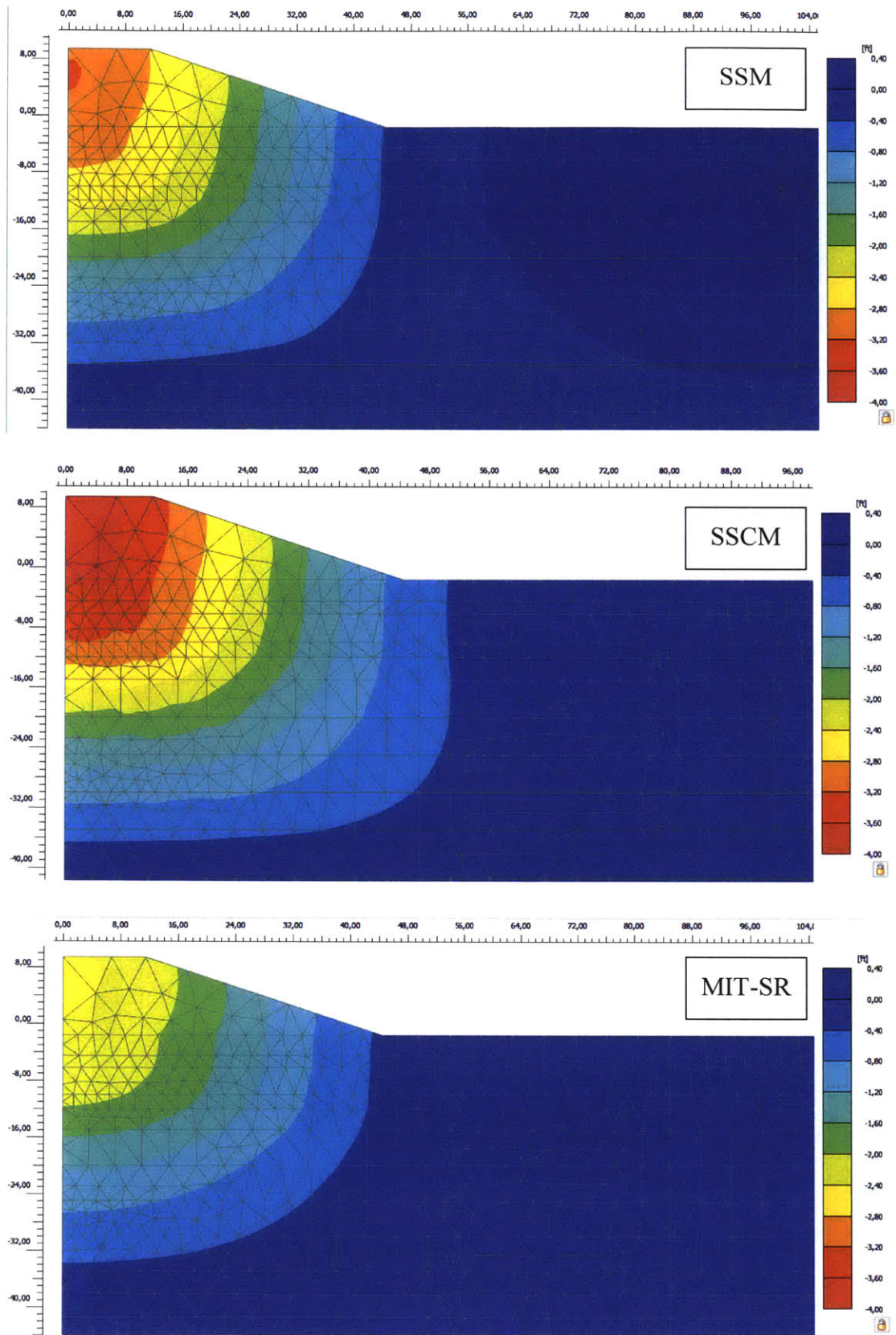


Figure 7-4: Vertical settlements (u_y) CD=2417 (20/Nov/02), SSM, SSCM & MIT-SR.

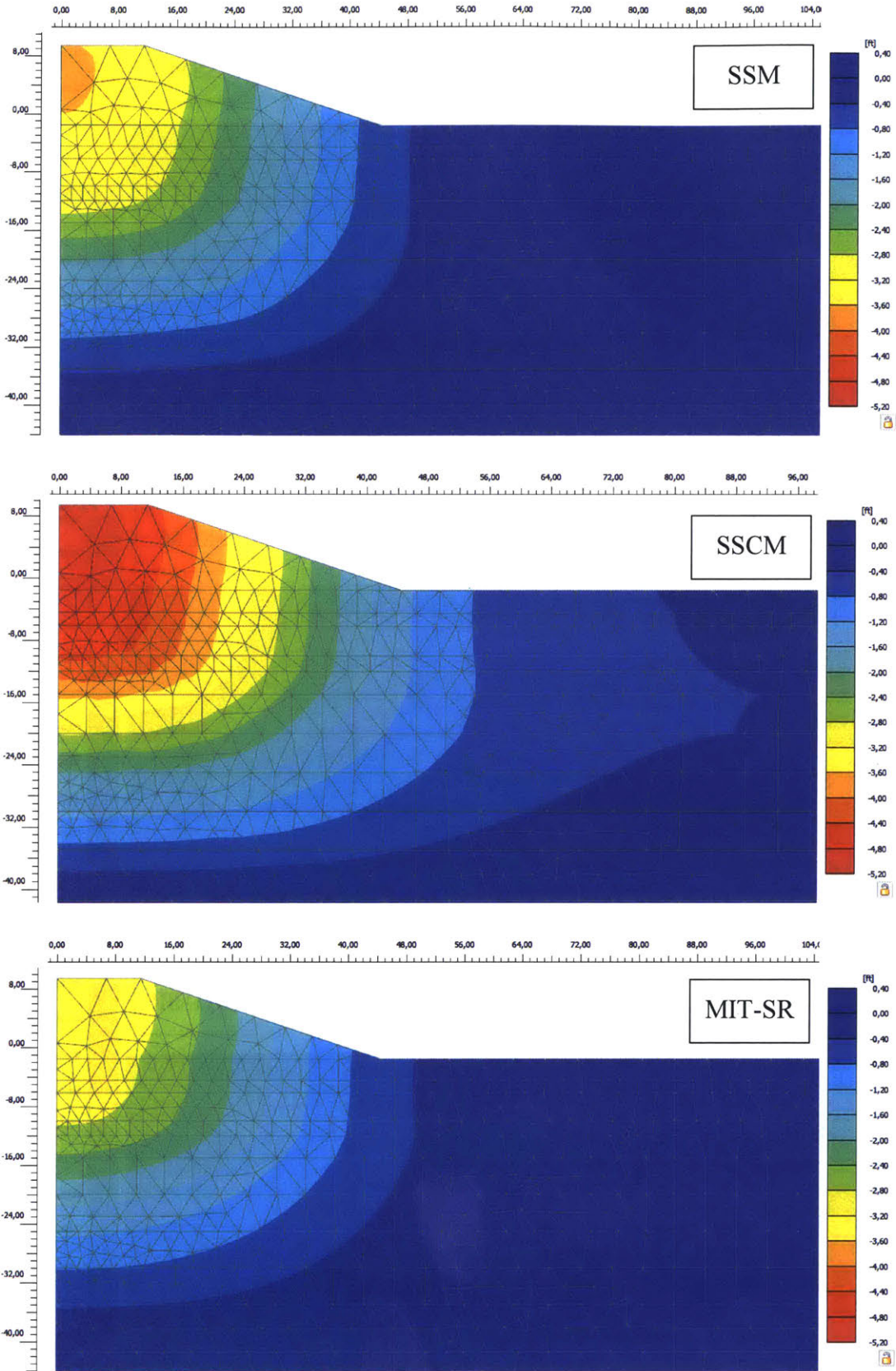


Figure 7-5: Vertical settlements (u_y) CD=10960 (10/Apr/26), SSM, SSCM & MIT-SR.

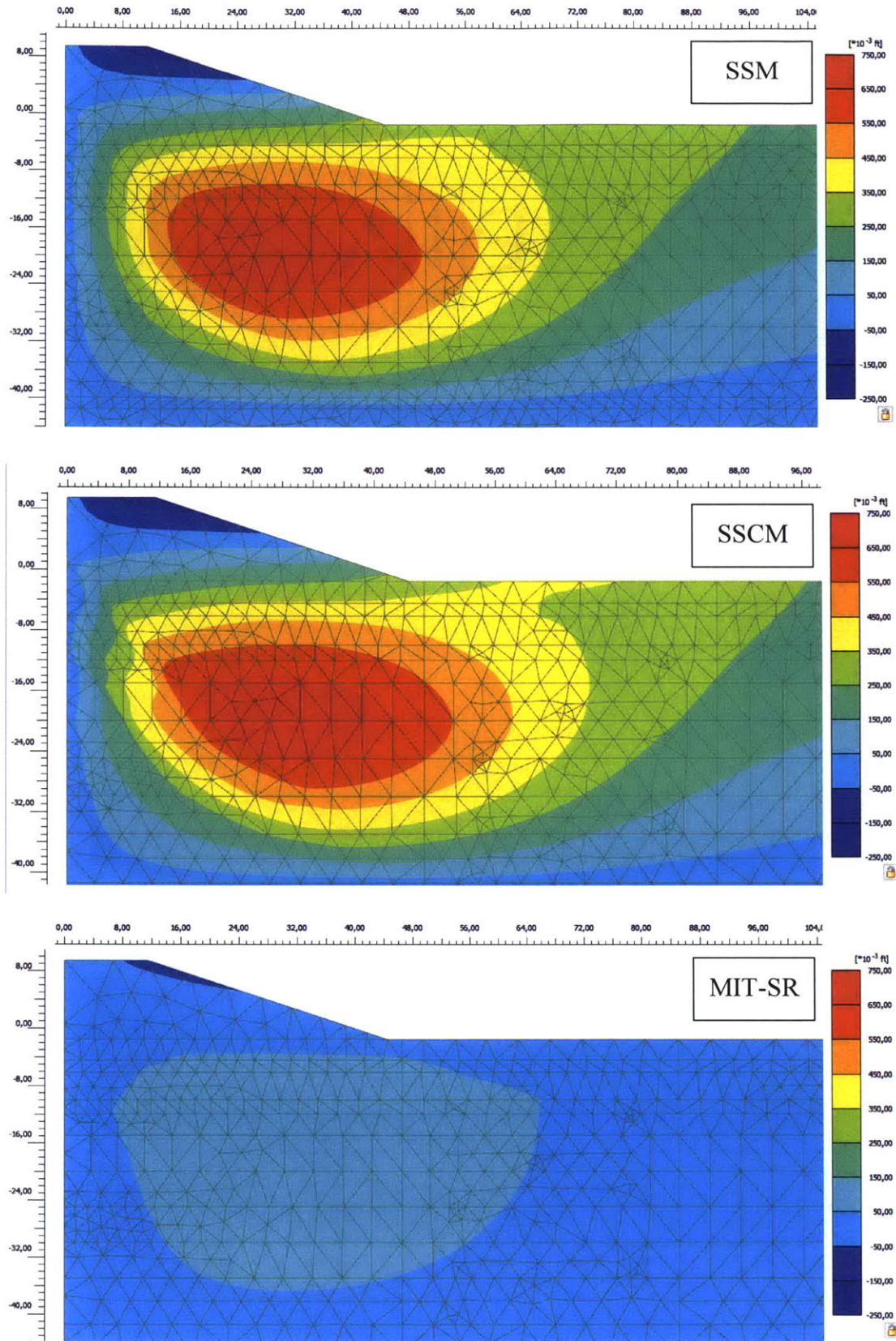


Figure 7-6: Horizontal settlements (u_x) CD=215 (11/Nov/96), SSM, SSCM & MIT-SR.

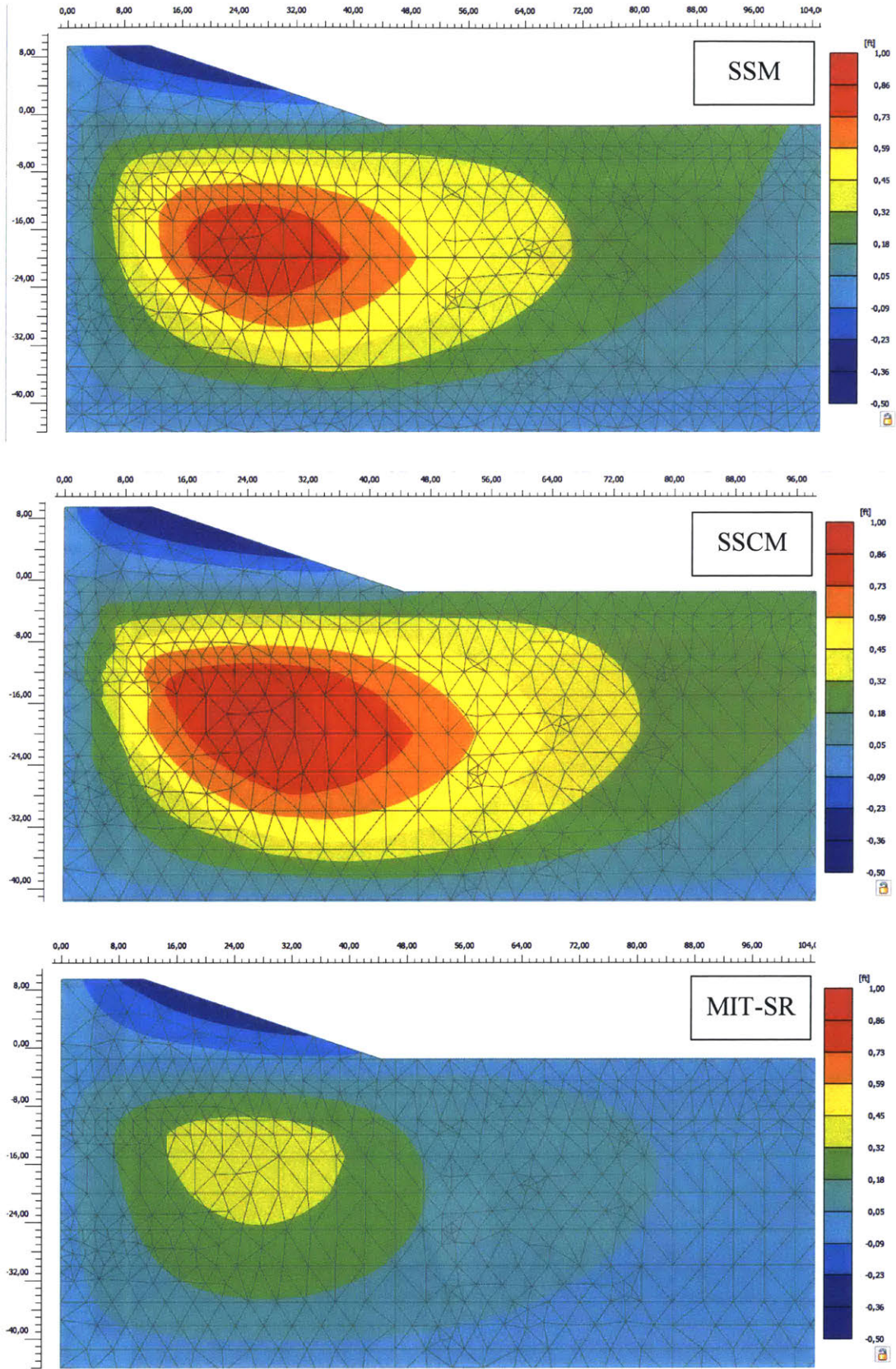


Figure 7-7: Horizontal settlements (u_x) CD=2140 (17/Feb/02), SSM, SSCM & MIT-SR.

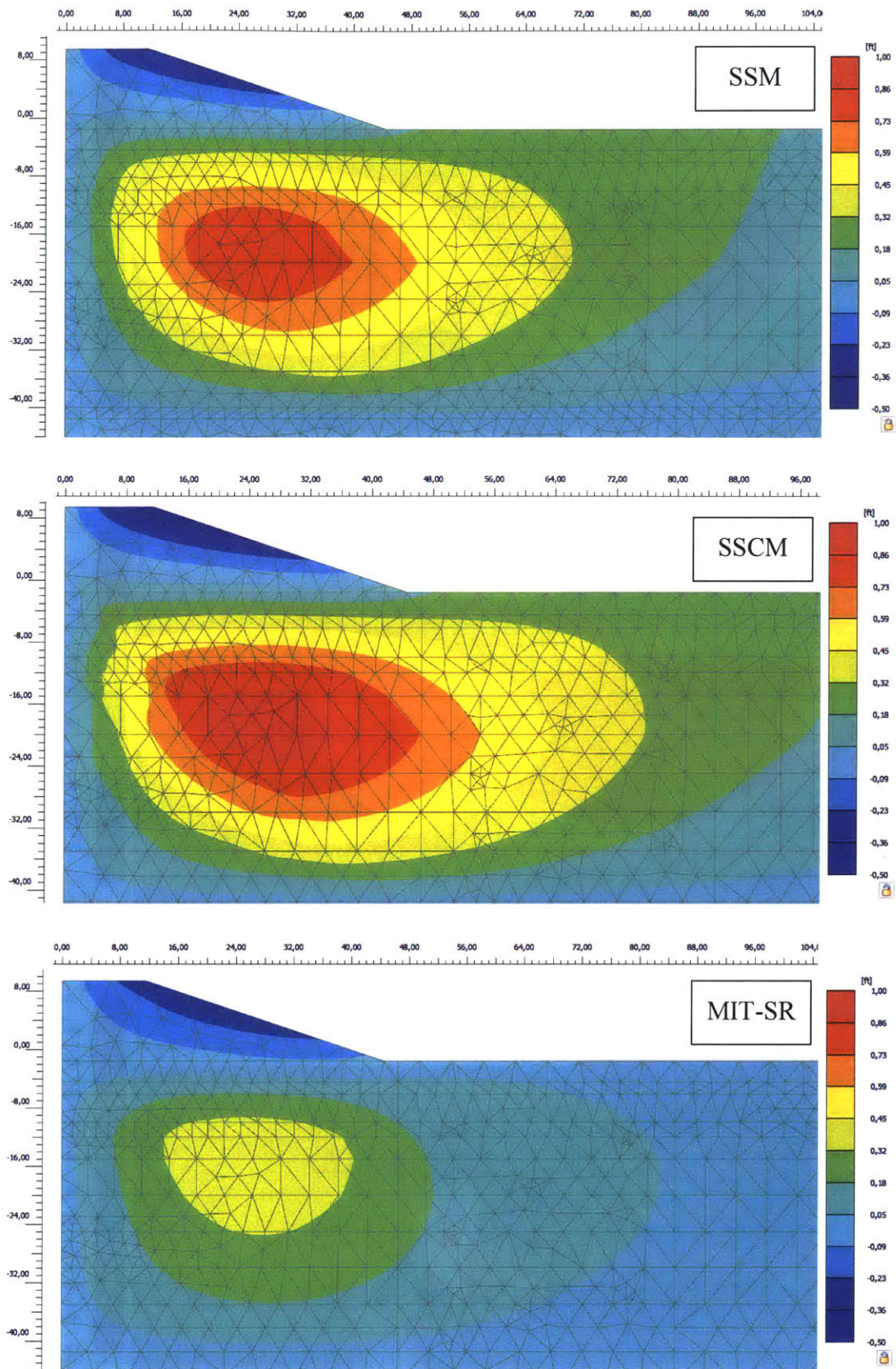


Figure 7-8: Horizontal settlements (u_x) CD=2417 (20/Nov/02), SSM, SSCM & MIT-SR.

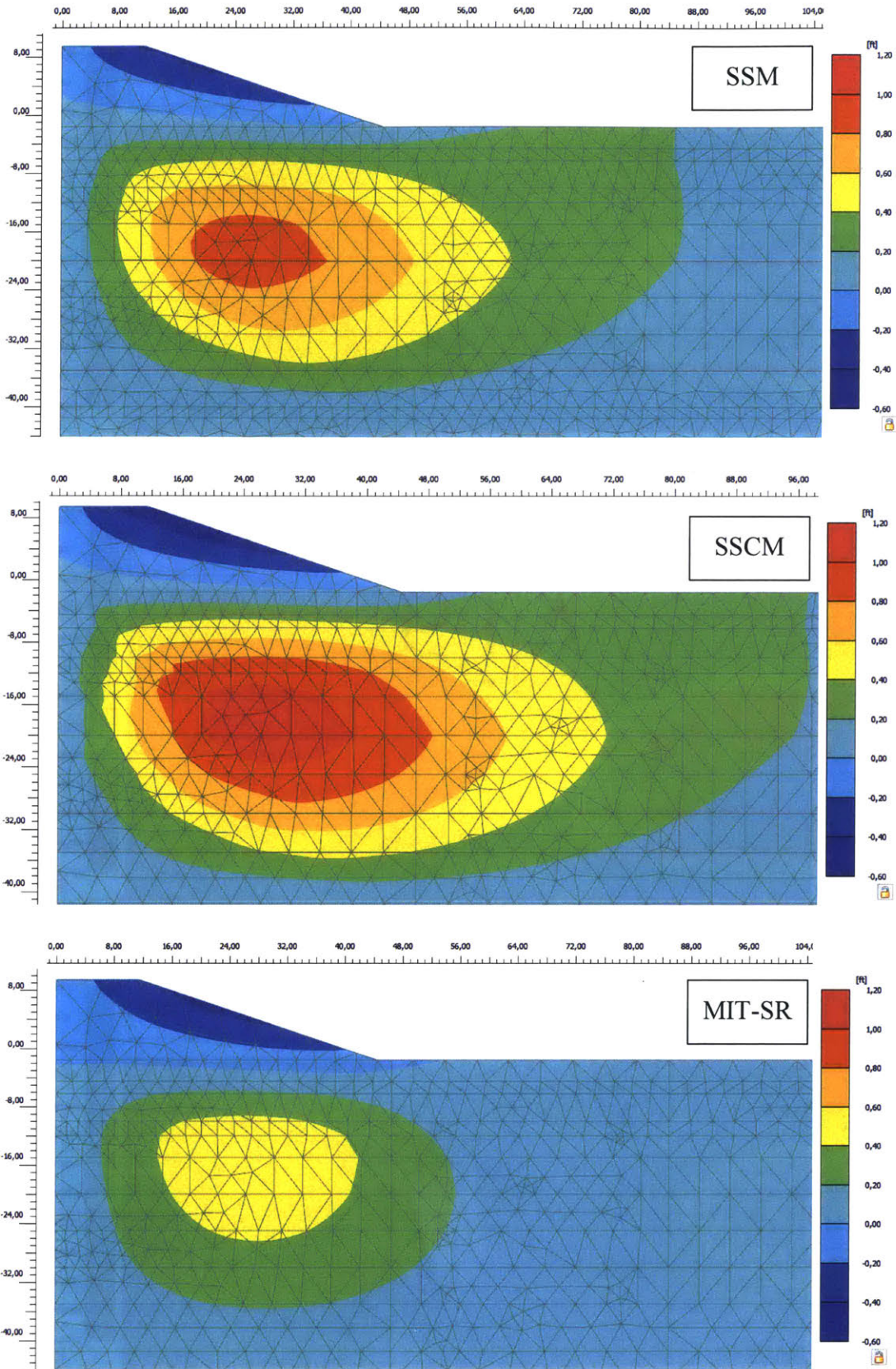


Figure 7-9: Horizontal settlements (u_x) CD=10960 (10/Apr/26), SSM, SSCM & MIT-SR.

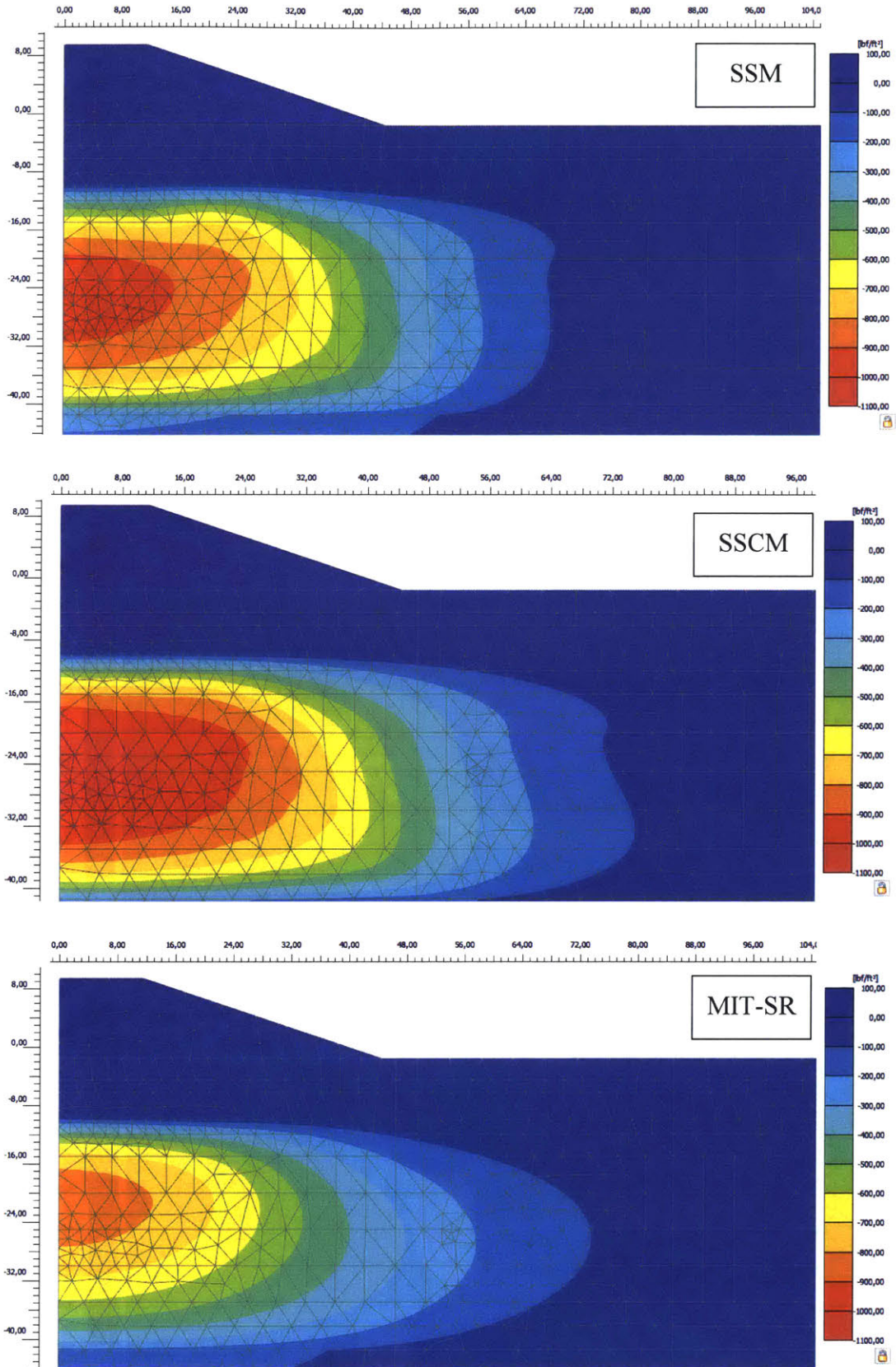


Figure 7-10: Excess pore pressure (p_{excess}) CD=215 (11/Nov/96), SSM, SSCM & MIT-SR.

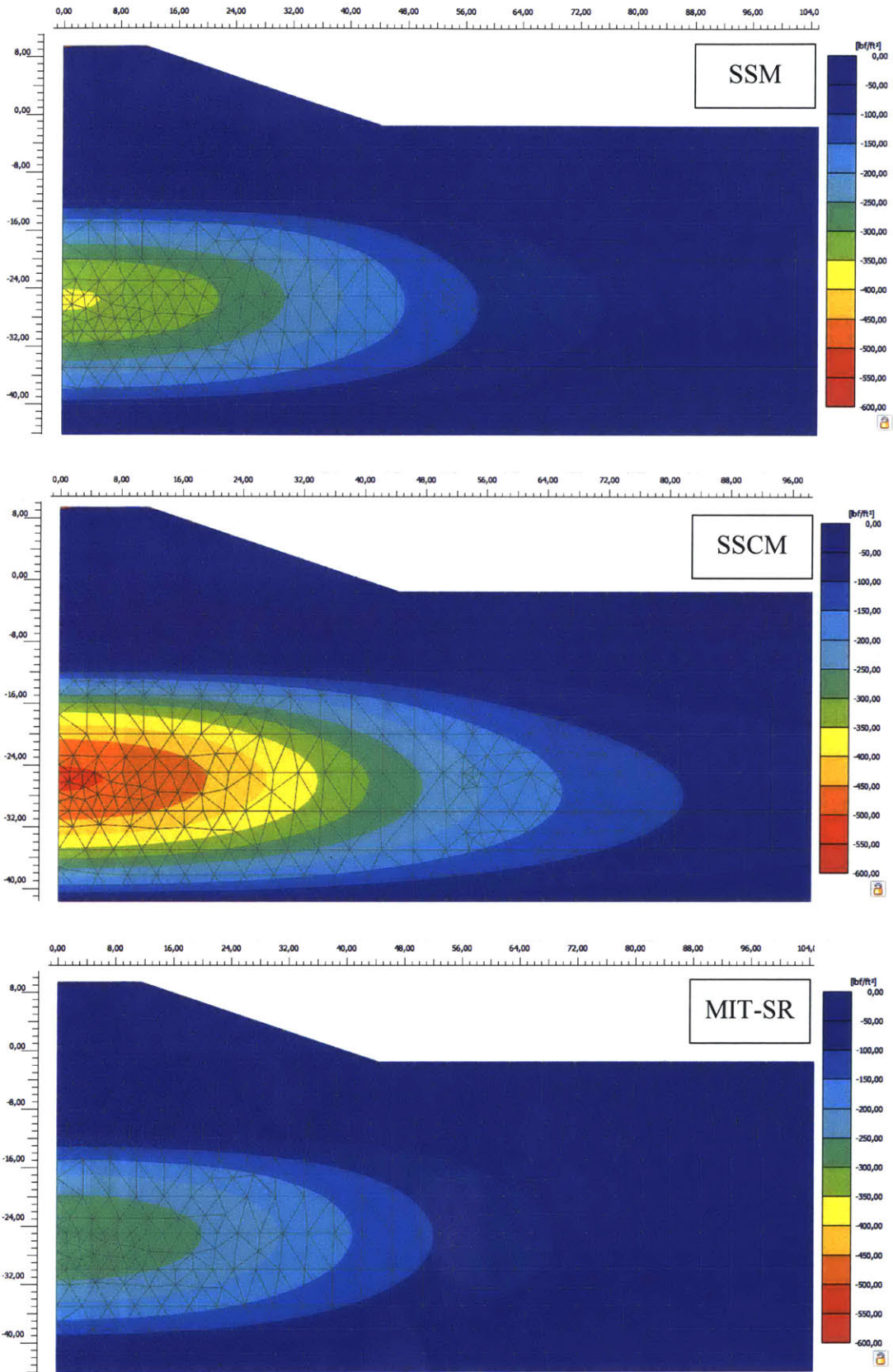


Figure 7-11: Excess pore pressure (p_{excess}) CD=2140 (17/Feb/02), SSM, SSCM & MIT-SR.

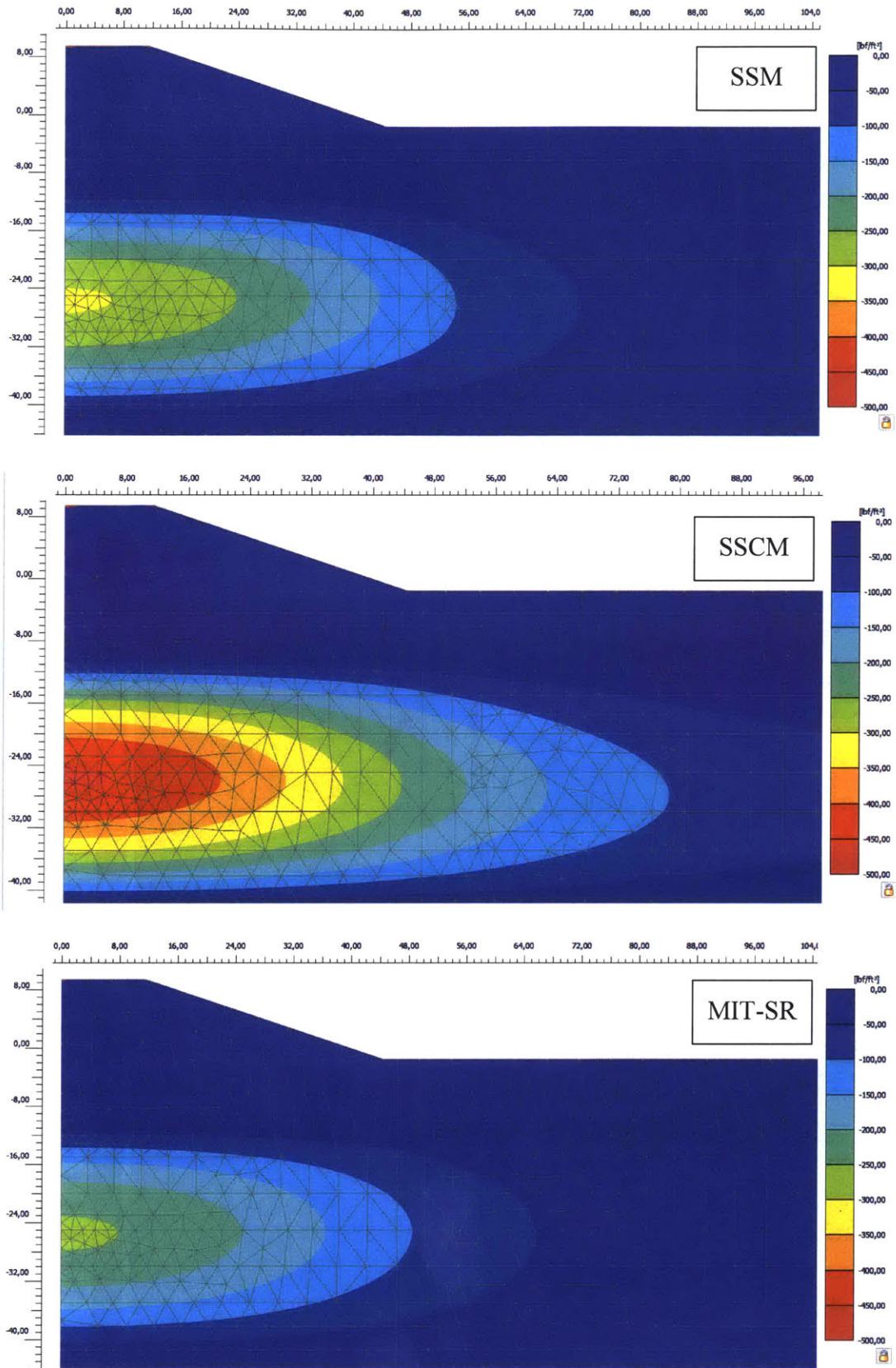


Figure 7-12: Excess pore pressure (p_{excess}) CD=2417 (20/Nov/02), SSM, SSCM & MIT-SR.

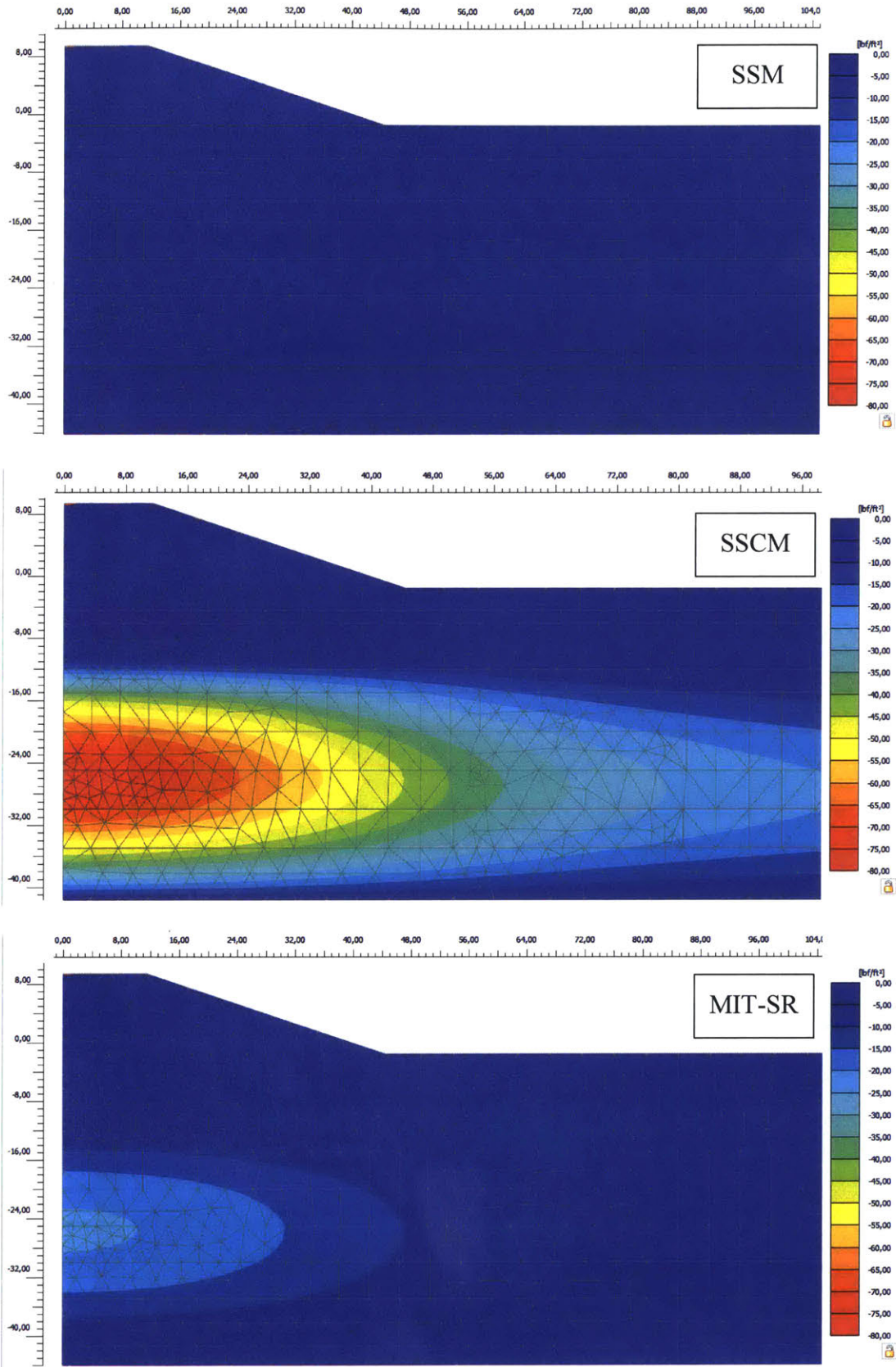


Figure 7-13: Excess pore pressure (p_{excess}) CD=10960 (10/Apr/26), SSM, SSCM & MIT-SR.

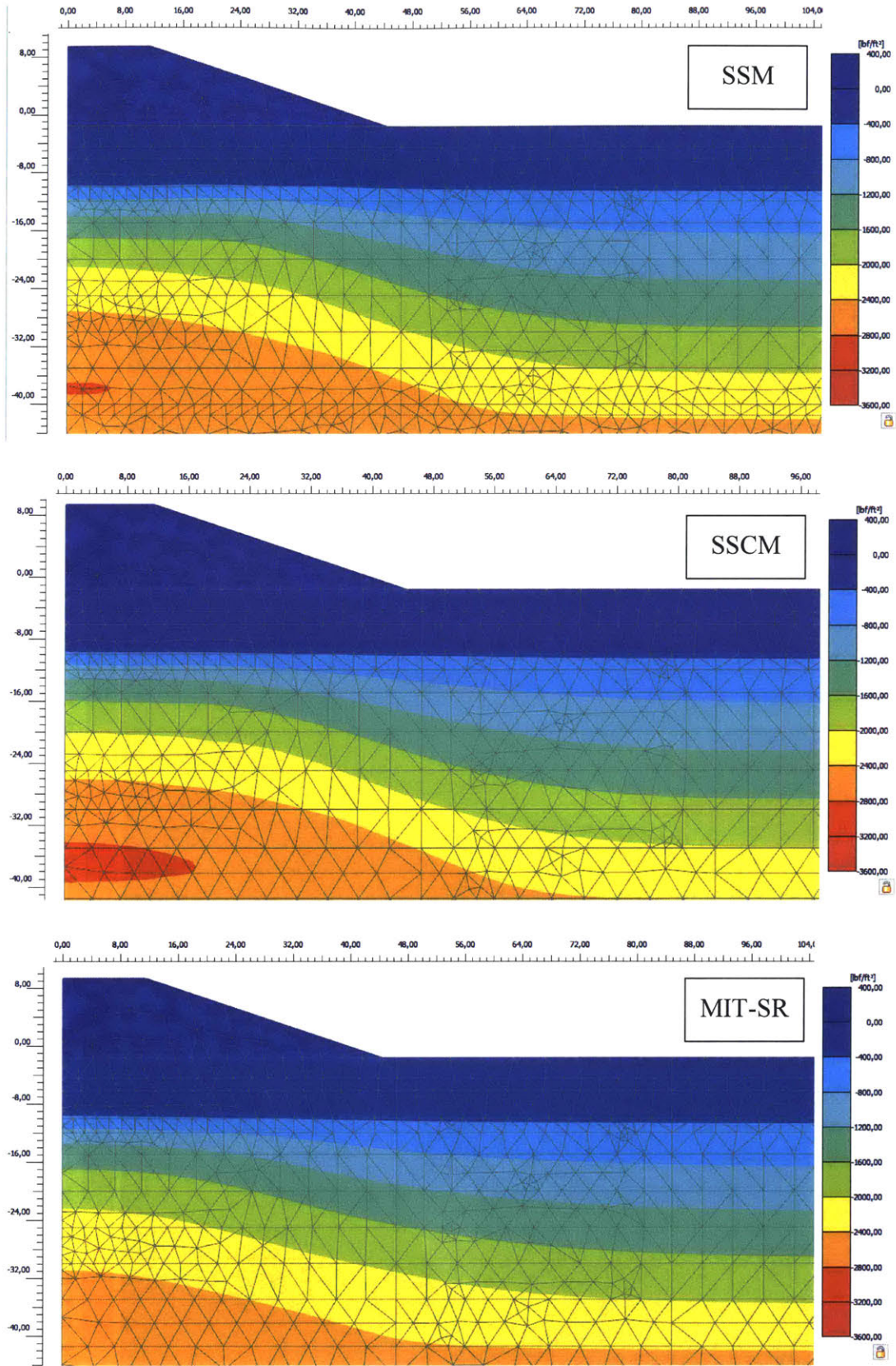


Figure 7-14: Active pore pressure (p_{active}) CD=215 (11/Nov/96), SSM, SSCM & MIT-SR.

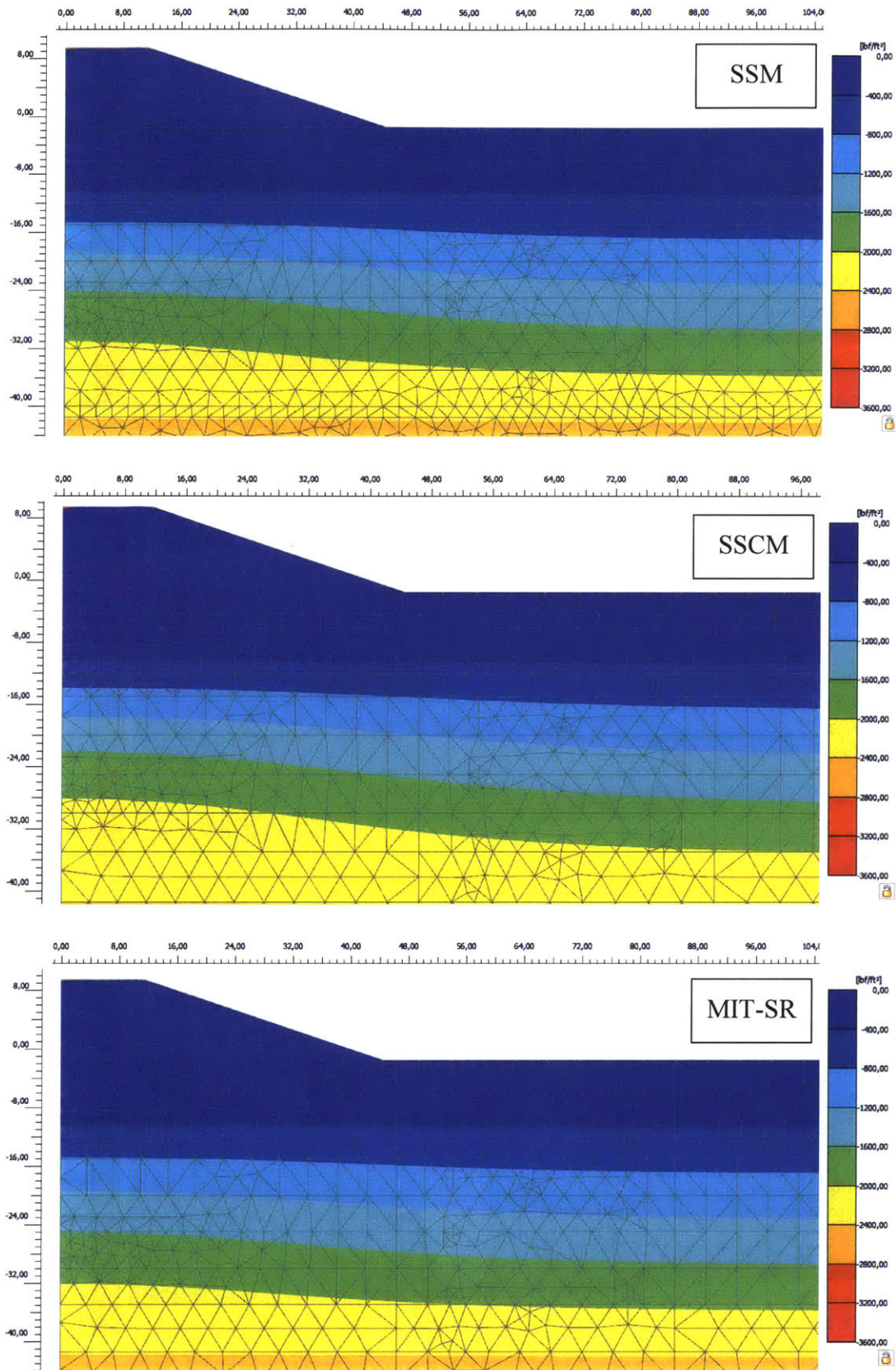


Figure 7-15: Active pore pressure (p_{active}) CD=2140 (17/Feb/02), SSM, SSCM & MIT-SR.

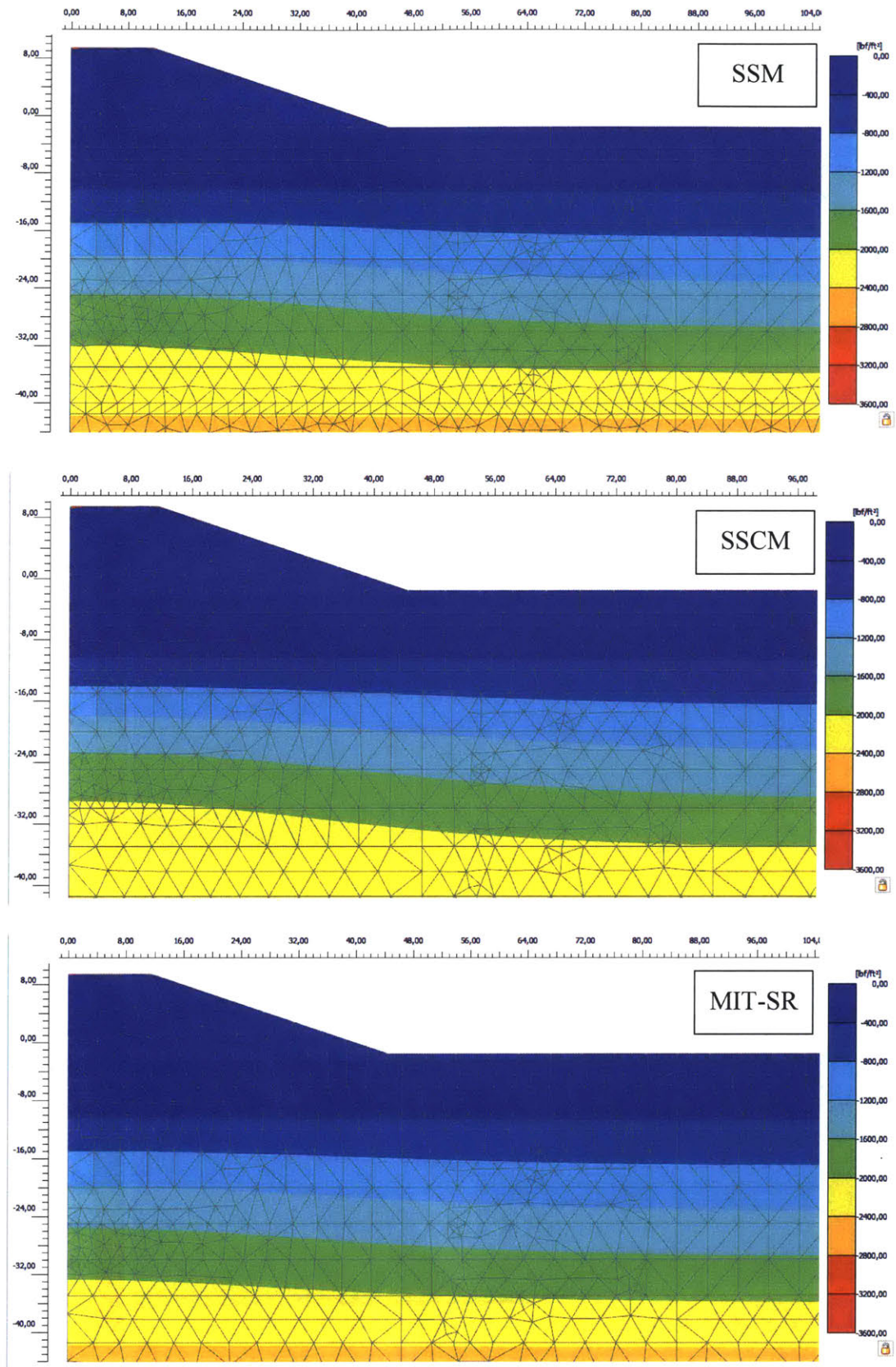


Figure 7-16: Active pore pressure (p_{active}) CD=2417 (20/Nov/02), SSM, SSCM & MIT-SR.

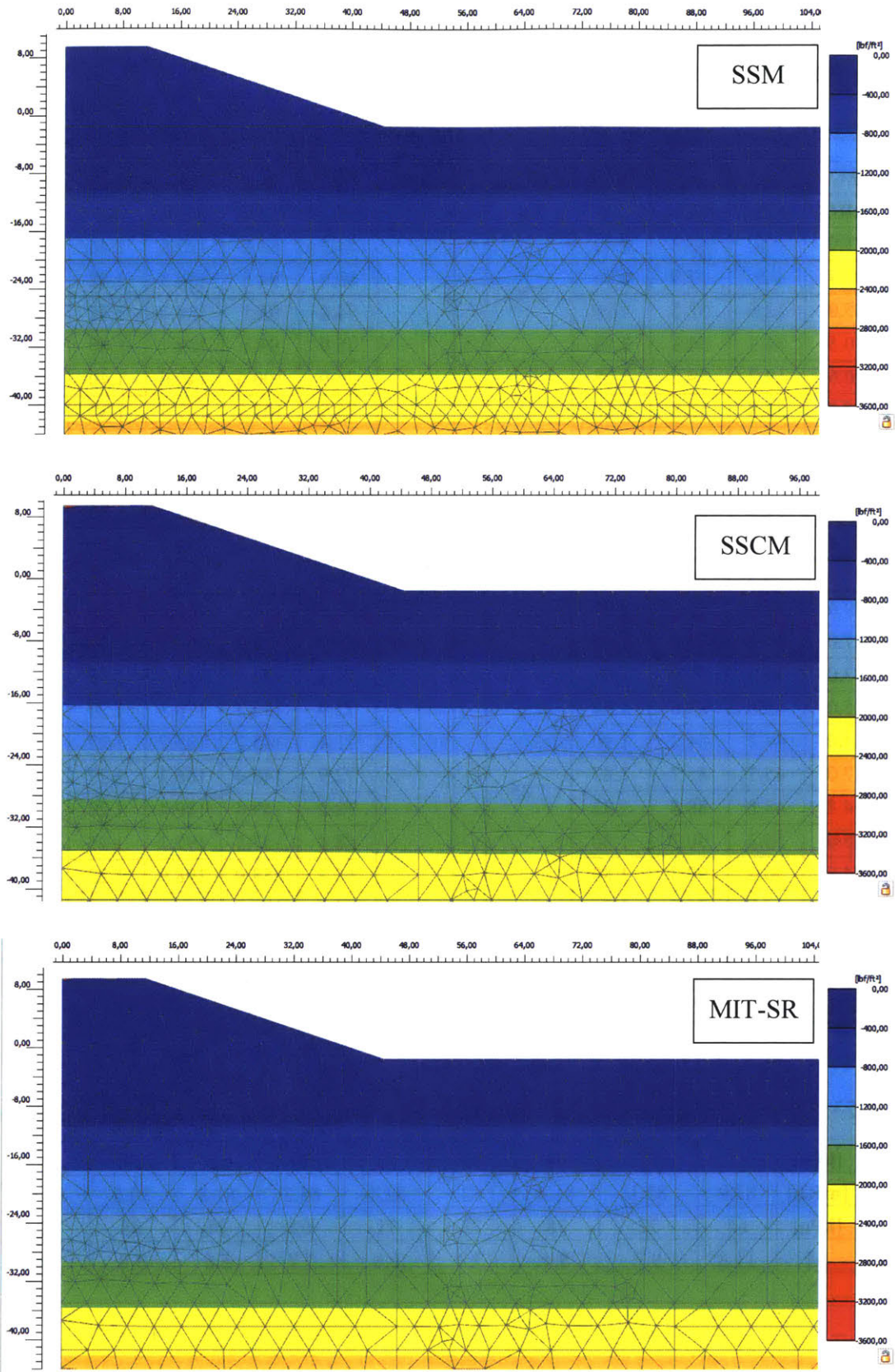


Figure 7-17: Active pore pressure (p_{active}) CD=10960 (10/Apr/26), SSM, SSCM & MIT-SR.

7.2. APPENDIX B: MARINA BAY AREA PROJECTS

7.2.1. Arup (2014) & Mott MacDonald (2015)

Table 7-22: Digitized effective vertical stress and preconsolidation pressure (Arup, 2014).

Layer	EL	σ'_v	σ'_p	OCR	OCR _{avg}	Layer	EL	σ'_v	σ'_p	OCR	OCR _{avg}
[-]	[mRL]	[kPa]	[kPa]	[-]	[-]	[-]	[mRL]	[kPa]	[kPa]	[-]	[-]
UMC	91.0	5.2	45.2	8.72	5.70	LMC	81.8	87.8	127.8	1.46	1.40
	91.4	7.9	47.9	6.05			80.6	94.5	134.5	1.42	
	85.0	12.5	52.5	4.20			74.4	95.1	135.1	1.42	
	90.5	14.3	54.3	3.79			75.9	99.1	139.1	1.40	
	90.6	19.2	59.2	3.08	75.9		100.6	140.6	1.40		
	87.7	23.8	63.8	2.68	75.9		107.3	147.3	1.37		
	90.6	25.0	65.0	2.60	73.0		107.9	147.9	1.37		
	90.3	25.3	65.3	2.58	77.4		108.5	148.5	1.37		
	86.3	31.7	71.7	2.26	78.8		113.1	153.1	1.35		
	84.4	33.2	73.2	2.20	78.0		114.6	154.6	1.35		
	87.0	36.3	76.3	2.10	73.0		120.7	160.7	1.33		
	90.6	37.5	77.5	2.07	75.9		121.0	161.0	1.33		
	87.0	37.8	77.8	2.06	73.0	125.9	165.9	1.32			
	87.0	39.0	79.0	2.02	74.4	132.3	172.3	1.30			
	85.0	43.6	83.6	1.92	72.9	136.3	176.3	1.29			
	84.0	44.2	84.2	1.90	71.4	145.7	185.7	1.27			
	87.0	45.7	85.7	1.87	72.9	146.4	186.4	1.27			
	84.8	48.8	88.8	1.82	72.2	149.4	189.4	1.27			
	85.0	50.3	90.3	1.80	68.4	157.3	197.3	1.25			
	84.6	50.3	90.3	1.80	66.3	158.9	198.9	1.25			
	83.3	56.7	96.7	1.71	68.5	173.8	213.8	1.23			
	84.0	58.2	98.2	1.69	59.7	183.2	223.2	1.22			
	81.8	75.3	115.3	1.53							
	78.1	81.7	121.7	1.49							

Table 7-23: Digitized undrained shear strength of F2 (Arup, 2014) and calculated OCR values.

s_u	[kPa]	102	97	94	84	73	70	65	54	50
EL	[mRL]	82.9	82.1	81.4	82	82.1	83.2	81.8	80.6	80.9
σ'_v	[kPa]	64	72	78	73	71	62	74	85	82
OCR	[-]	11.8	9.7	8.4	7.9	6.8	7.7	5.6	3.8	3.6

7.2.2. Choi (1982)

Table 7-24: CRS tests information (Choi, 1982).

SC-15		SC-16		SC-17		SC-18	
$\dot{\epsilon}$ [%/hr]	0.45%	$\dot{\epsilon}$ [%/hr]	0.25%	$\dot{\epsilon}$ [%/hr]	0.18%	$\dot{\epsilon}$ [%/hr]	0.13%
e_0	2.015	e_0	1.963	e_0	2.000	e_0	2.056

σ'_v	e	σ'_v	e	σ'_v	e	σ'_v	e
[psf]	[-]	[psf]	[-]	[psf]	[-]	[psf]	[-]
51	2.015	52	1.962	68	1.995	39	2.053
98	2.013	89	1.962	137	1.994	70	2.051
175	2.010	150	1.957	172	1.993	130	2.048
256	2.006	247	1.954	406	1.975	229	2.037
385	2.001	357	1.948	616	1.961	322	2.017
484	1.994	521	1.939	837	1.952	774	1.966
579	1.989	624	1.934	1210	1.928	1041	1.927
689	1.981	848	1.923	1616	1.904	1325	1.888
845	1.974	1237	1.909	1964	1.878	1501	1.867
1020	1.966	1481	1.896	2186	1.839	1712	1.840
1281	1.950	1773	1.878	2286	1.813	2077	1.796
1646	1.932	2136	1.848	2524	1.772	2331	1.762
2113	1.902	2472	1.805	2717	1.709	2496	1.736
2447	1.868	2567	1.783	3141	1.656	2888	1.687
2661	1.837	2662	1.747	3238	1.644	3188	1.644
2779	1.791	2828	1.717	4288	1.517	3544	1.595
2999	1.757	3312	1.629	5394	1.436	3943	1.552
3285	1.717	3796	1.567	6083	1.367	4633	1.499
3595	1.668	4483	1.486	7091	1.316	6187	1.381
3812	1.616	5599	1.410	19259	1.017	7265	1.323
4474	1.551	7427	1.304	-	-	10920	1.203
4823	1.509	10243	1.193	-	-	15908	1.086
5529	1.448	13095	1.115	-	-	-	-
6296	1.399	20942	0.983	-	-	-	-
6901	1.366	-	-	-	-	-	-
7506	1.335	-	-	-	-	-	-

8486	1.295	-	-	-	-	-	-
9964	1.238	-	-	-	-	-	-
11434	1.187	-	-	-	-	-	-
14967	1.110	-	-	-	-	-	-
20680	1.019	-	-	-	-	-	-

Table 7-25: SC-12 test, creep stage at 1000psf (Choi, 1982).

Time	Δe	e	ϵ	ϵ'	$\dot{\epsilon}'$
[mins]	[-]	[-]	[-]	[-]	[1/hr]
0	0.000	1.909	0.00002	-	-
1	0.000	1.909	-0.00015	-	-
1	-0.001	1.910	-0.00036	-	-
2	-0.002	1.910	-0.00052	-	-
4	-0.002	1.911	-0.00073	-	-
9	-0.002	1.911	-0.00076	-	-
16	-0.002	1.911	-0.00084	-	-
32	-0.003	1.911	-0.00087	0.000000	0.00012
64	-0.002	1.911	-0.00086	0.000013	0.000025
104	-0.002	1.911	-0.00085	0.000023	0.000014
170	-0.002	1.911	-0.00084	0.000032	0.000009
287	-0.002	1.911	-0.00083	0.000042	0.000005
427	-0.003	1.911	-0.00087	0.000005	0.000016
714	-0.001	1.910	-0.00050	0.000373	0.000077
1576	-0.001	1.910	-0.00048	0.000388	0.000001
3280	-0.001	1.910	-0.00029	0.000581	0.000007
5985	-0.001	1.909	-0.00023	0.000637	0.000001
9430	-0.001	1.909	-0.00018	0.000690	0.000001

Table 7-26: SC-12 test, creep stage at 2000psf (Choi, 1982).

Time	Δe	e	ϵ	ϵ'	$\dot{\epsilon}'$
[mins]	[-]	[-]	[-]	[-]	[1/hr]
0	0.000	1.783	-0.00006	-	-
1	0.000	1.784	-0.00014	-	-
1	-0.001	1.784	-0.00021	-	-
2	-0.001	1.784	-0.00042	-	-
4	-0.002	1.785	-0.00063	0.000000	0.005636

9	-0.001	1.785	-0.00052	0.000114	0.001548
17	-0.001	1.785	-0.00050	0.000133	0.000147
33	-0.001	1.785	-0.00048	0.000154	0.000076
68	0.000	1.784	-0.00013	0.000503	0.000590
138	0.001	1.782	0.00041	0.001038	0.000460
241	0.002	1.781	0.00084	0.001474	0.000254
380	0.004	1.779	0.00137	0.002002	0.000228
779	0.008	1.776	0.00270	0.003330	0.000200
1553	0.013	1.770	0.00463	0.005264	0.000150
3280	0.019	1.764	0.00689	0.007527	0.000079
6730	0.025	1.758	0.00916	0.009788	0.000039
10298	0.030	1.753	0.01076	0.011388	0.000027
11924	0.032	1.751	0.01155	0.012185	0.000029

Table 7-27: SC-12 test, creep stage at 4000psf (Choi, 1982).

Time [mins]	Δe [-]	e [-]	ϵ [-]	ϵ' [-]	$\dot{\epsilon}'$ [1/hr]
0	0.000	1.433	-0.00007	-	-
1	-0.001	1.433	-0.00026	-	-
1	-0.001	1.433	-0.00044	-	-
2	-0.002	1.434	-0.00068	-	-
4	-0.002	1.434	-0.00086	-	-
8	-0.003	1.435	-0.00105	0.000000	0.003006
16	-0.002	1.435	-0.00097	0.000076	0.000571
31	-0.002	1.435	-0.00095	0.000099	0.000090
72	-0.002	1.434	-0.00077	0.000283	0.000269
122	-0.001	1.433	-0.00044	0.000614	0.000397
239	0.000	1.432	0.00016	0.001209	0.000306
409	0.002	1.430	0.00096	0.002008	0.000282
680	0.005	1.428	0.00191	0.002962	0.000211
1383	0.008	1.424	0.00345	0.004495	0.000131
2898	0.012	1.420	0.00514	0.006185	0.000067
4410	0.015	1.417	0.00630	0.007344	0.000046
7122	0.018	1.415	0.00720	0.008245	0.000020
10087	0.019	1.413	0.00799	0.009038	0.000016
14484	0.022	1.410	0.00904	0.010091	0.000014

Table 7-28: SC-12 test, creep stage at 8000psf (Choi, 1982).

Time	Δe	e	ϵ	ϵ'	$\dot{\epsilon}'$
------	------------	-----	------------	-------------	-------------------

[mins]	[-]	[-]	[-]	[-]	[1/hr]
0	0.000	1.189	-0.00008	-	-
0	-0.001	1.189	-0.00028	-	-
1	-0.001	1.190	-0.00049	-	-
2	-0.002	1.190	-0.00075	-	-
7	-0.002	1.191	-0.00105	-	-
13	-0.002	1.191	-0.00114	0.000000	0.000893
26	-0.002	1.191	-0.00094	0.000199	0.000938
50	-0.002	1.191	-0.00092	0.000225	0.000062
103	-0.001	1.190	-0.00054	0.000599	0.000428
159	-0.001	1.190	-0.00041	0.000731	0.000141
302	0.000	1.188	0.00019	0.001333	0.000254
507	0.003	1.186	0.00120	0.002336	0.000293
1139	0.006	1.183	0.00279	0.003928	0.000151
2448	0.009	1.179	0.00426	0.005403	0.000068
3563	0.011	1.178	0.00503	0.006169	0.000041
5972	0.014	1.174	0.00655	0.007692	0.000038
7973	0.016	1.173	0.00708	0.008223	0.000016
12118	0.017	1.171	0.00791	0.009049	0.000012

Table 7-29: SC-13 test, creep stage at 1000psf (Choi, 1982).

Time	Δe	e	ϵ	ϵ'	$\dot{\epsilon}'$
[mins]	[-]	[-]	[-]	[-]	[1/hr]
0	-0.001	1.910	-0.00025	-	-
1	-0.002	1.911	-0.00059	-	-
1	-0.003	1.913	-0.00116	-	-
2	-0.005	1.914	-0.00164	-	-
4	-0.006	1.916	-0.00207	-	-
9	-0.007	1.916	-0.00237	-	-
16	-0.007	1.917	-0.00254	-	-
32	-0.008	1.917	-0.00261	-	-
63	-0.008	1.917	-0.00269	0.000000	0.000152
162	-0.008	1.917	-0.00262	0.000063	0.000038
275	-0.008	1.917	-0.00266	0.000029	0.000018
421	-0.008	1.917	-0.00265	0.000037	0.000003
724	-0.008	1.917	-0.00264	0.000047	0.000002
1553	-0.007	1.917	-0.00249	0.000196	0.000011
3329	-0.007	1.917	-0.00243	0.000256	0.000002
6074	-0.007	1.916	-0.00229	0.000401	0.000003
9430	-0.006	1.916	-0.00223	0.000454	0.000001
12832	-0.006	1.915	-0.00205	0.000639	0.000003

Table 7-30: SC-13 test, creep stage at 2000psf (Choi, 1982).

Time	Δe	e	ϵ	ϵ'	$\dot{\epsilon}'$
[mins]	[-]	[-]	[-]	[-]	[1/hr]
0	-0.001	1.714	-0.00026	-	-
1	-0.001	1.715	-0.00047	-	-
1	-0.002	1.716	-0.00088	-	-
2	-0.004	1.717	-0.00134	-	-
4	-0.005	1.718	-0.00175	-	-
9	-0.005	1.719	-0.00197	-	-
16	-0.006	1.719	-0.00204	-	-
33	-0.006	1.719	-0.00216	0.000000	0.000434
66	-0.005	1.719	-0.00195	0.000213	0.000387
132	-0.005	1.719	-0.00183	0.000330	0.000107
238	-0.005	1.718	-0.00167	0.000492	0.000092
369	-0.004	1.717	-0.00142	0.000745	0.000116
757	-0.002	1.716	-0.00087	0.001294	0.000085
1530	-0.001	1.714	-0.00023	0.001938	0.000050
3233	0.001	1.712	0.00042	0.002584	0.000023
6347	0.004	1.710	0.00140	0.003562	0.000019
12461	0.006	1.707	0.00228	0.004444	0.000009

Table 7-31: SC-13 test, creep stage at 4000psf (Choi, 1982).

Time	Δe	e	ϵ	ϵ'	$\dot{\epsilon}'$
[mins]	[-]	[-]	[-]	[-]	[1/hr]
0	-0.001	1.371	-0.00039	-	-
1	-0.002	1.372	-0.00074	-	-
1	-0.003	1.373	-0.00125	-	-
2	-0.004	1.375	-0.00187	-	-
4	-0.006	1.376	-0.00233	-	-
8	-0.007	1.377	-0.00294	-	-
15	-0.007	1.377	-0.00308	-	-
31	-0.008	1.378	-0.00322	0.000000	0.000509
68	-0.008	1.378	-0.00319	0.000027	0.000044
121	-0.008	1.378	-0.00322	-0.000006	0.000037
241	-0.007	1.377	-0.00309	0.000125	0.000065
415	-0.008	1.378	-0.00318	0.000037	0.000030
671	-0.007	1.377	-0.00290	0.000320	0.000066
1393	-0.006	1.376	-0.00261	0.000613	0.000024

2932	-0.005	1.376	-0.00231	0.000906	0.000011
7029	-0.004	1.374	-0.00148	0.001737	0.000012
14999	-0.002	1.372	-0.00081	0.002405	0.000005

Table 7-32: SC-13 test, creep stage at 8000psf (Choi, 1982).

Time	Δe	e	ϵ	ϵ'	$\dot{\epsilon}'$
[mins]	[-]	[-]	[-]	[-]	[1/hr]
0	-0.001	1.136	-0.00038	-	-
0	-0.001	1.137	-0.00059	-	-
1	-0.003	1.138	-0.00121	-	-
2	-0.004	1.140	-0.00196	-	-
7	-0.007	1.142	-0.00321	-	-
12	-0.007	1.143	-0.00336	-	-
25	-0.008	1.143	-0.00357	-	-
50	-0.007	1.143	-0.00349	-	-
100	-0.008	1.143	-0.00358	0.000000	0.000111
155	-0.007	1.143	-0.00350	0.000076	0.000083
308	-0.007	1.143	-0.00330	0.000280	0.000080
529	-0.007	1.142	-0.00316	0.000420	0.000038
1179	-0.006	1.141	-0.00265	0.000925	0.000047
2478	-0.005	1.140	-0.00227	0.001309	0.000018
3672	-0.004	1.140	-0.00202	0.001562	0.000013
6380	-0.003	1.139	-0.00152	0.002057	0.000011
8533	-0.003	1.138	-0.00127	0.002306	0.000007
10932	-0.002	1.138	-0.00115	0.002434	0.000003

Table 7-33: SC-14 test, creep stage at 1000psf (Choi, 1982).

Time	Δe	e	ϵ	ϵ'	$\dot{\epsilon}'$
[mins]	[-]	[-]	[-]	[-]	[1/hr]
0	-0.002	1.915	-0.00065	-	-
1	-0.003	1.916	-0.00108	-	-
1	-0.005	1.919	-0.00178	-	-
2	-0.007	1.921	-0.00253	-	-
4	-0.010	1.923	-0.00340	-	-
8	-0.012	1.925	-0.00406	-	-
16	-0.012	1.926	-0.00423	-	-
32	-0.013	1.926	-0.00448	-	-
60	-0.013	1.927	-0.00456	-	-
153	-0.013	1.927	-0.00463	0.000000	0.000046
267	-0.013	1.927	-0.00457	0.000055	0.000029

403	-0.013	1.927	-0.00452	0.000108	0.000023
714	-0.013	1.927	-0.00455	0.000074	0.000006
1530	-0.013	1.926	-0.00445	0.000178	0.000008
3233	-0.013	1.926	-0.00439	0.000237	0.000002
6074	-0.013	1.926	-0.00433	0.000294	0.000001
12461	-0.012	1.925	-0.00414	0.000486	0.000002

Table 7-34: SC-14 test, creep stage at 2000psf (Choi, 1982).

Time [mins]	Δe [-]	e [-]	ϵ [-]	ϵ' [-]	$\dot{\epsilon}'$ [1/hr]
0	-0.001	1.686	-0.00036	-	-
1	-0.002	1.687	-0.00087	-	-
1	-0.004	1.688	-0.00138	-	-
2	-0.005	1.690	-0.00203	-	-
4	-0.007	1.692	-0.00269	-	-
9	-0.008	1.693	-0.00315	-	-
16	-0.009	1.694	-0.00342	-	-
32	-0.009	1.694	-0.00345	-	-
66	-0.009	1.694	-0.00352	0.000000	0.000131
125	-0.009	1.694	-0.00345	0.000068	0.000070
218	-0.009	1.694	-0.00339	0.000134	0.000043
358	-0.009	1.694	-0.00337	0.000150	0.000007
746	-0.008	1.693	-0.00311	0.000415	0.000041
1530	-0.008	1.692	-0.00289	0.000631	0.000017
3093	-0.007	1.692	-0.00258	0.000943	0.000012
6163	-0.006	1.691	-0.00227	0.001255	0.000006
10761	-0.005	1.690	-0.00181	0.001708	0.000006

Table 7-35: SC-14 test, creep stage at 4000psf (Choi, 1982).

Time [mins]	Δe [-]	e [-]	ϵ [-]	ϵ' [-]	$\dot{\epsilon}'$ [1/hr]
0	-0.001	1.351	-0.00061	-	-
1	-0.003	1.352	-0.00107	-	-
1	-0.004	1.354	-0.00191	-	-
2	-0.007	1.356	-0.00280	-	-
4	-0.009	1.358	-0.00369	-	-
8	-0.011	1.360	-0.00448	-	-
15	-0.011	1.361	-0.00483	-	-

30	-0.012	1.362	-0.00508	-	-
61	-0.012	1.362	-0.00505	-	-
122	-0.012	1.362	-0.00508	-	-
233	-0.012	1.362	-0.00512	-	-
412	-0.012	1.362	-0.00526	0.000000	0.000047
667	-0.012	1.362	-0.00519	0.000071	0.000017
1424	-0.012	1.361	-0.00494	0.000313	0.000019
2916	-0.012	1.361	-0.00497	0.000284	0.000001
4519	-0.011	1.361	-0.00480	0.000461	0.000007
7210	-0.011	1.361	-0.00462	0.000639	0.000004
10087	-0.011	1.360	-0.00450	0.000759	0.000002
14524	-0.010	1.360	-0.00422	0.001041	0.000004

Table 7-36: SC-14 test, creep stage at 8000psf (Choi, 1982).

Time	Δe	e	ϵ	ϵ'	$\dot{\epsilon}'$
[mins]	[-]	[-]	[-]	[-]	[1/hr]
0	-0.002	1.122	-0.00074	-	-
0	-0.003	1.123	-0.00137	-	-
1	-0.005	1.125	-0.00218	-	-
2	-0.006	1.127	-0.00305	-	-
7	-0.011	1.131	-0.00514	-	-
14	-0.012	1.133	-0.00583	-	-
25	-0.012	1.133	-0.00587	-	-
51	-0.013	1.133	-0.00602	-	-
96	-0.013	1.133	-0.00605	-	-
153	-0.013	1.133	-0.00616	-	-
305	-0.013	1.134	-0.00625	0.000000	0.000037
531	-0.013	1.133	-0.00611	0.000141	0.000037
1151	-0.013	1.133	-0.00596	0.000290	0.000014
2495	-0.012	1.132	-0.00575	0.000500	0.000009
3647	-0.012	1.132	-0.00567	0.000574	0.000004
6440	-0.011	1.132	-0.00541	0.000835	0.000006
8378	-0.011	1.132	-0.00540	0.000845	0.000000
12610	-0.011	1.132	-0.00533	0.000921	0.000001

7.2.3. Kiso-Jiban (1978)

Table 7-37: Consolidation test BH8-U4-S3 (Kiso-Jiban, 1978).

Time	Δe	e	ϵ	ϵ'	$\dot{\epsilon}'$
[mins]	[-]	[-]	[-]	[-]	[1/hr]
0.1	0.000	1.528	0.00000	0.00000	0.000000
0.2	0.003	1.526	0.00100	0.00000	1.187111
0.2	0.004	1.525	0.00141	0.00000	0.250886
0.5	0.006	1.522	0.00250	0.00000	0.264170
1.0	0.011	1.517	0.00427	0.00000	0.206206
2.0	0.016	1.512	0.00647	0.00000	0.133499
4.0	0.025	1.503	0.00978	0.00000	0.099828
8.0	0.037	1.491	0.01457	0.00000	0.071282
15.1	0.052	1.476	0.02061	0.00000	0.051168
30.6	0.067	1.461	0.02644	0.00000	0.022549
61.0	0.080	1.448	0.03182	0.00000	0.010615
120.7	0.093	1.435	0.03669	0.00000	0.004890
242.8	0.102	1.426	0.04044	0.00000	0.001847
488.3	0.110	1.418	0.04339	0.00294	0.000719
1451.1	0.119	1.409	0.04725	0.00681	0.000241
2919.8	0.124	1.404	0.04916	0.00872	0.000078
4528.9	0.128	1.400	0.05053	0.01009	0.000051
5874.7	0.129	1.399	0.05114	0.01070	0.000027
7257.5	0.131	1.397	0.05175	0.01131	0.000026
8966.7	0.131	1.397	0.05199	0.01155	0.000008
10212.3	0.132	1.396	0.05237	0.01193	0.000018
11631.4	0.133	1.395	0.05261	0.01216	0.000010

Table 7-38: Consolidation test BH8-U4-S4 (Kiso-Jiban, 1978).

Time	Δe	e	ϵ	ϵ'	$\dot{\epsilon}'$
[mins]	[-]	[-]	[-]	[-]	[1/hr]
0.1	0.000	1.392	0.00000	0.00000	0.000000
0.2	0.001	1.391	0.00050	0.00000	0.595472
0.3	0.004	1.388	0.00163	0.00000	0.641903
0.5	0.008	1.384	0.00325	0.00000	0.387293
1.0	0.015	1.377	0.00646	0.00000	0.375606
2.0	0.024	1.368	0.01015	0.00000	0.218239
4.1	0.038	1.354	0.01606	0.00000	0.175703
8.1	0.058	1.335	0.02404	0.00000	0.117152
15.3	0.080	1.313	0.03328	0.00000	0.077458

30.2	0.107	1.285	0.04491	0.00000	0.046818
60.6	0.133	1.259	0.05559	0.00000	0.021059
121.8	0.148	1.245	0.06166	0.00000	0.005956
242.6	0.160	1.232	0.06694	0.00000	0.002619
491.5	0.168	1.224	0.07030	0.00337	0.000812
1452.7	0.181	1.211	0.07576	0.00882	0.000340
2895.6	0.186	1.206	0.07785	0.01092	0.000087
4437.8	0.190	1.202	0.07946	0.01253	0.000063
5819.3	0.191	1.201	0.07995	0.01302	0.000021
7087.3	0.192	1.200	0.08028	0.01334	0.000015
7145.8	0.192	1.200	0.08028	0.01335	0.000000
8919.6	0.194	1.199	0.08093	0.01399	0.000022
10171.9	0.195	1.198	0.08141	0.01447	0.000023

Table 7-39: Consolidation test BH8-U6-S3 (Kiso-Jiban, 1978).

Time	Δe	e	ϵ	ϵ'	ϵ'
[mins]	[-]	[-]	[-]	[-]	[1/hr]
0.1	0.000	1.166	0.00000	0.00000	0.000000
0.1	0.002	1.164	0.00083	0.00000	1.030413
0.3	0.003	1.163	0.00134	0.00000	0.299938
0.5	0.006	1.159	0.00300	0.00000	0.406942
1.0	0.010	1.155	0.00481	0.00000	0.215955
2.0	0.018	1.148	0.00825	0.00000	0.205590
4.0	0.026	1.140	0.01218	0.00000	0.119050
8.0	0.040	1.126	0.01854	0.00000	0.093929
15.0	0.058	1.108	0.02667	0.00000	0.070471
30.0	0.075	1.090	0.03482	0.00000	0.032510
60.1	0.091	1.075	0.04182	0.00000	0.013963
118.5	0.102	1.064	0.04704	0.00000	0.005368
237.4	0.109	1.057	0.05048	0.00344	0.001735
479.5	0.115	1.051	0.05327	0.00623	0.000691
1422.6	0.124	1.042	0.05738	0.01034	0.000261
2850.4	0.128	1.038	0.05904	0.01199	0.000070
4360.6	0.131	1.035	0.06035	0.01331	0.000052
5711.1	0.132	1.034	0.06085	0.01381	0.000022
7063.8	0.133	1.033	0.06135	0.01430	0.000022
8665.8	0.134	1.032	0.06185	0.01480	0.000019
9957.9	0.135	1.031	0.06234	0.01529	0.000023
11536.7	0.136	1.030	0.06267	0.01563	0.000013

Table 7-40: Consolidation test BH8-U6-S4 (Kiso-Jiban, 1978).

Time	Δe	e	ϵ	ϵ'	$\dot{\epsilon}'$
[mins]	[-]	[-]	[-]	[-]	[1/hr]
0.1	0.000	1.019	0.00000	0.00000	0.000000
0.2	0.001	1.018	0.00071	0.00000	0.826131
0.3	0.004	1.016	0.00176	0.00000	0.632402
0.5	0.007	1.012	0.00366	0.00000	0.460633
1.0	0.013	1.006	0.00657	0.00000	0.342158
2.0	0.021	0.999	0.01031	0.00000	0.221300
4.1	0.033	0.987	0.01622	0.00000	0.174419
8.2	0.049	0.970	0.02429	0.00000	0.117064
15.3	0.064	0.955	0.03186	0.00000	0.064270
30.6	0.082	0.937	0.04078	0.00000	0.034877
60.8	0.095	0.924	0.04702	0.00000	0.012378
122.0	0.104	0.915	0.05142	0.00000	0.004320
244.8	0.111	0.909	0.05483	0.00341	0.001664
491.3	0.115	0.905	0.05673	0.00531	0.000464
1484.3	0.125	0.894	0.06185	0.01042	0.000309
2978.1	0.129	0.890	0.06409	0.01266	0.000090
4522.7	0.132	0.888	0.06513	0.01370	0.000040
5926.8	0.133	0.886	0.06582	0.01440	0.000030
7333.8	0.134	0.885	0.06634	0.01492	0.000022
9000.9	0.135	0.884	0.06686	0.01544	0.000019
10431.2	0.136	0.884	0.06721	0.01579	0.000015